# INJURY SIMULATION OF REAR SEAT CHILD OCCUPANT IN OFFSET DEFORMABLE BARRIER FRONTAL IMPACT

**Tomoshi Takahashi**
**Satoshi Fukushima**
**Yuichi Kitagawa**
**Tsuyoshi Yasuki**
Toyota Motor Corporation
Japan

Paper Number 15-0048

## ABSTRACT

From 2016, Euro NCAP plans to assess child occupant protection performance with Q6 and Q10 dummies in a 64 km/h offset deformable barrier (ODB) frontal impact test. This paper describes research simulating this frontal impact test using a ten-year old (10YO) version of the Total Human Model for Safety (THUMS) and an FE model of the Q10 dummy. The changes in impact kinematics and injury values of the 10YO THUMS model were compared with the Q10 dummy under various load limiter (L/L) values ranging from 2 to 5 kN, and the differences between the two were examined.

Differences in the kinematics between the two mostly appeared during the second half of the test. As a result, the displacement of the head and chest of the Q10 dummy was smaller than that of the 10YO THUMS model. This result was probably because the thoracic plate of the Q10 dummy hindered the flexion of the thoracic spine. In addition, the chest upper deflection of the Q10 dummy resulted in higher injury values. This result was assumed to be because the shoulder belt was positioned close to the chest upper deflection gauge. In addition, the change in the chest upper deflection of the Q10 dummy was greater than that of the 10YO THUMS model, with a sensitivity of approximately four times as large. This result was due to the high force transmission ratio from the clavicle to the sternum.

## INTRODUCTION

According to European accident statistics, the rate of child (0 to 14 year-old) occupant fatalities in the EU in 2009 amounted to 2.5 people in 100,000 (Kirk et al., 2012). As one measure to help improve the safety of child occupants, the EU enacted ECE R44 in 1981 to specify safety criteria for child seats. Euro NCAP then began assessing child occupant protection performance from 2003.

The development of the Q-series of child dummies began in 1993. Five completed dummies have already been completed, ranging in age from 0 to 6 years old, and the 10-year old Q10 dummy is due to be completed in the near future. Currently, Euro NCAP assesses child occupant protection performance using the 1.5-year old Q1.5 dummy and the 3-year old Q3 dummy. In addition, Euro NCAP has also announced plans to adopt the 6-year old Q6 dummy and the 10-year old Q10 dummy from 2016. Although various researches have examined the injury states, tolerances, and thresholds of child occupants, little information is available compared to research into adults. Physical tests on live subjects have been carried out at low force levels, assuming playground accidents. However, there is very little information related to tolerance and threshold at high forces such as in impact tests. For this reason, research using human finite element (FE) models is regarded as an effective means to better understand pediatric injuries.

The research described in this paper compared the occupant kinematics and injury values in a frontal impact using a ten-year old (10YO) version of the THUMS human FE model and an FE model of the Q10 dummy. Assuming the same conditions as the 64 km/h offset deformable barrier (ODB) frontal impact test used in Euro NCAP, the simulation placed the child occupant models in a junior seat (JRS) located in the rear. The impact kinematics and injury values of rear seat occupants are affected by the load limiter (L/L) device of the seatbelts. Therefore, this

research also examined changes in the displacement and injury value for each part of the occupant (i.e., the sensitivity) under various L/L values. After describing these simulations, this paper details the differences in impact kinematics and injury values of the 10YO THUMS and Q10 dummy models.

## METHOD

The first section of this paper describes an outline of the FE models used in the research.

### Vehicle FE Model

The simulated test vehicle was a B-segment compact car with a weight of 1,070 kg. The FE model of the test vehicle was created to represent its geometry and structure, including component parts. It was verified that the floor deceleration pulse, forward displacement, and yawing motion matched those measured in an ODB frontal impact test of this vehicle. The seatbelts in the rear seats for child occupants were equipped with a pretensioner to remove slack and an L/L function to control the occupant restraining force.

### JRS FE Model

A high-backed JRS in the 2-3 weight group was used. The FE model was created using external geometrical data obtained using optical measurement. The plastic and metal parts were modeled with shell elements, while solid elements were used for the foam parts. The average mesh size was 5 mm. It was verified that the deformation stiffness and strength of the head and lateral supports were consistent with those of actual JRS.

### 10YO THUMS Model

The 10YO THUMS model was created by changing the 6YO THUMS pedestrian model created by Nishimura et al. (2002) to a seated posture and scaling up the physique to that of a 10-year old child. The seated height of the 10YO THUMS model was changed to match that of the Q10 dummy. Both models had a weight of 35 kg. The impact response of the 10YO THUMS head was previously verified by Nishimura et al.(2002), while the chest response was verified in the research by comparison with the chest loading tests on post mortem human subjects (PMHS) of a 10-year old (Kent et al., 2012). The head displacement was measured at the center of gravity of the head and the chest displacement was measured at the fourth thoracic vertebra (T4). The displacement data was transferred to the vehicle (the rear floor) coordinate system. The upper and lower chest deflections were calculated in accordance with the measuring points on the Q10 dummy.

### Q10 Dummy FE Model

The Ver. 1.2.1 Q10 dummy FE model (Humanetics Innovative Solutions, Inc. ,2013) was used for the comparison with the 10YO THUMS model. The head and chest response were verified based on the details of Humanetics Technical Reports. The displacement and injury values of each part were outputted following the Humanetics User Manual from the sensors set inside the model. The displacement data was transferred to the vehicle coordinate system as processed in the 10YO THUMS model.

## Calculation Model and Conditions

The JRS model was placed on the right rear seat (i.e., the far side of the vehicle) assuming fixation through the ISOFIX anchors. Both the 10YO THUMS and Q10 dummy occupant models were seated so that their backs were in contact with the seatbacks. The seatbelts were wrapped around the torsos of the dummies passing through the belt guides. The pretensioner was activated at 20 msec after the impact, based on the specifications of the tested vehicle. Eight cases were simulated with the 10YO THUMS and Q10 dummy models, changing the L/L value from 2 to 5 kN. The kinematics of each part of the models and the injury values were compared for each case. Table 1 shows the calculation conditions for all eight cases.

***Table 1.*** **Simulation Matrix**

| CASE | | 1 | 2 | 3 | 4 | 5 | 6 | 7 | 8 |
|---|---|---|---|---|---|---|---|---|---|
| Test Condition | | 64kph ODB | | | | 64kph ODB | | | |
| Vehicle Type | | Compact Car | | | | Compact Car | | | |
| Occupant Position | | Rear Seat (Far Side) | | | | Rear Seat (Far Side) | | | |
| Child Occupant Model | | **10YO THUMS** | | | | **Q10 dummy** | | | |
| JRS | Seat Back | Available | | | | Available | | | |
| | Mount | ISO-FIX | | | | ISO-FIX | | | |
| Seatbelt | P/T | Available | | | | Available | | | |
| | L/L | 2kN | 3kN | 4kN | 5kN | 2kN | 3kN | 4kN | 5kN |

## RESULTS

This section compares the impact responses and injury values of the 10YO THUMS and Q10 dummy models between cases 3 and 7 (L/L value: 4 kN).

### Kinematics

Figure 1(a) superimposes the kinematics of the 10YO THUMS and Q10 dummy models at 0, 60 and 120 msec after the impact. In both models, the upper body flexed after the pelvis stopped. The head positions of two models were almost identical up to 60 msec but diverged after that. The upper body flexion and lateral bending of spine were greater in the 10YO THUMS model than those in the Q10 dummy. At 120 msec, the head forward displacement of the 10YO THUMS model was 547 mm and the chest (T4) forward displacement was 327 mm. These values were 179 mm (head) and 92 mm (chest) larger than those of the Q10 dummy, respectively. The lateral displacement of the 10YO THUMS model (chest) was 101 mm, larger than the 80 mm recorded by the Q10 dummy.

Figure 1(b) shows the changes in the maximum forward displacement of the head and chest under different L/L values. The maximum lateral displacement of the chest is also shown. Under the same L/L value, the 10YO THUMS model exhibited greater displacement than the Q10 dummy. The maximum forward displacement increased as the L/L value decreased. In contrast, there was little difference in the sensitivity of the maximum forward displacement against the L/L value. Under the impact conditions assumed in the research, the head of the 10YO THUMS model contacted the back of the front seat in case 1 (L/L value = 2 kN).

The maximum lateral displacement of the chest in the 10YO THUMS model was larger than that in the Q10 dummy. In this model, the lateral displacement increased as the L/L value decreased. However, in case 1 only, the lateral displacement of the 10YO THUMS model was smaller than that in case 2 even though the L/L value was smaller.

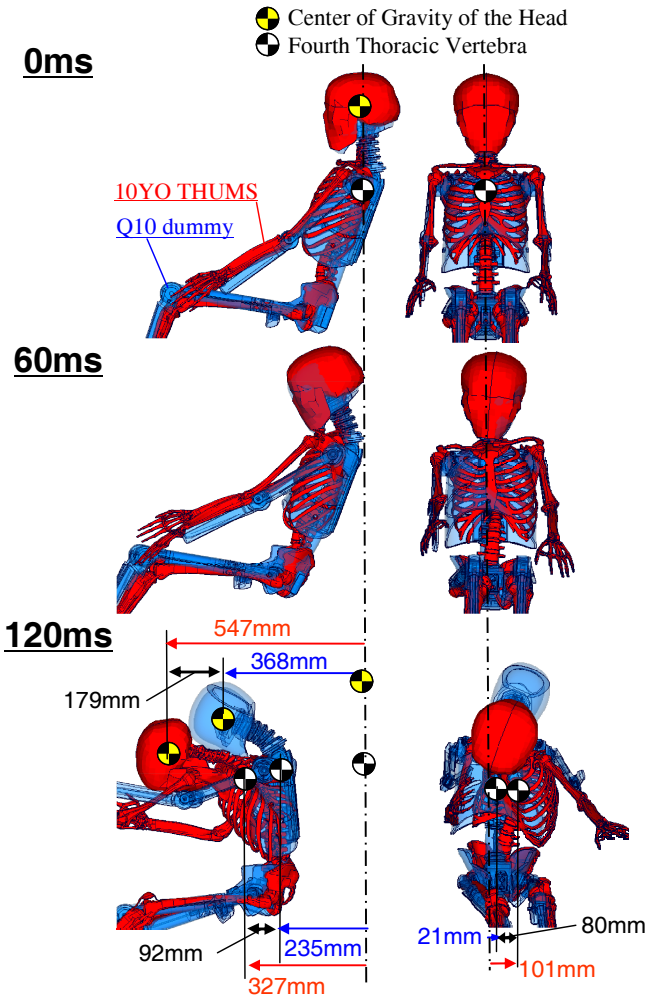


*(a)* Comparison of 10YO THUMS and Q10 dummy models (cases 3 and 7)

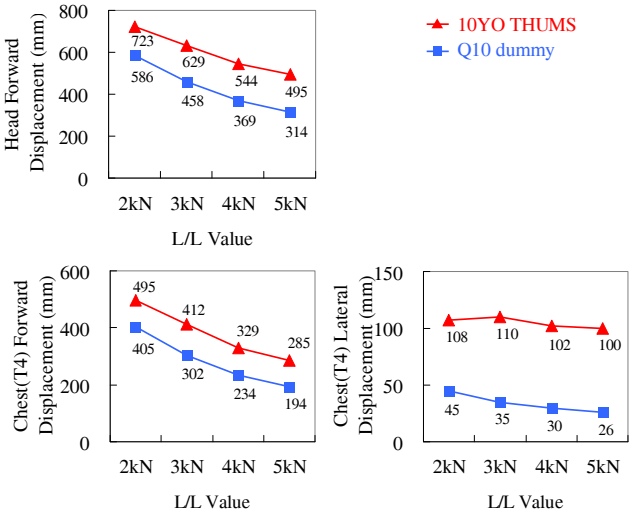


*(b)* Maximum displacement of head and chest at each L/L value

***Figure 1.*** Occupant displacement and sensitivity of displacement of each part to L/L value.

**Injury Values**

Figure 2(a) compares the time history curves of the head resultant acceleration, upper neck tension force, and chest deflections (upper and lower) of the 10YO THUMS and Q10 dummy models. The head resultant acceleration and upper neck tension force reached the maximum peaks at 116 msec, which was close to the timing of the maximum head forward displacement (120 msec). It should be noted that the maximum values in all cases were higher for the 10YO THUMS model. The chin and clavicle of the Q10 dummy came into contact at 85 msec, generating an initial peak for head resultant acceleration. Initial peaks for the chest upper and lower deflections appeared at 76 msec and the maximum values appeared after 116 msec. At 76 msec, the shoulder belt restrained the Q10 dummy from the chest to the abdomen. At 116 msec, the upper body flexed, causing the clavicle to be restrained by the shoulder belt. Although the maximum chest upper deflection of the 10YO THUMS model was smaller than that of the Q10 dummy, the chest lower deflection was greater.

Figure 2(b) shows the relationship between the L/L value and the head injury criteria (HIC), as well as the injury values for the neck (upper neck force) and chest (chest upper and lower deflections). Apart from the chest upper deflection, the injury values of the 10YO THUMS model were higher in all cases than the Q10 dummy. In the 10YO THUMS model, the HIC increased as the L/L value decreased. In contrast, the HIC of the Q10 dummy decreased as the L/L value decreased. The HIC was particularly high in case 1, in which the head contacted the back of the front seat. Although the upper neck force of the 10YO THUMS model increased as the L/L value decreased, the upper neck force of the Q10 dummy model decreased under the same conditions. The chest upper and lower chest deflection of both the 10YO THUMS and Q10 dummy models also decreased as the L/L value decreased. However, the change in the chest upper deflection of the Q10 dummy was greater than in the 10YO THUMS model, with a sensitivity of approximately four times as high.

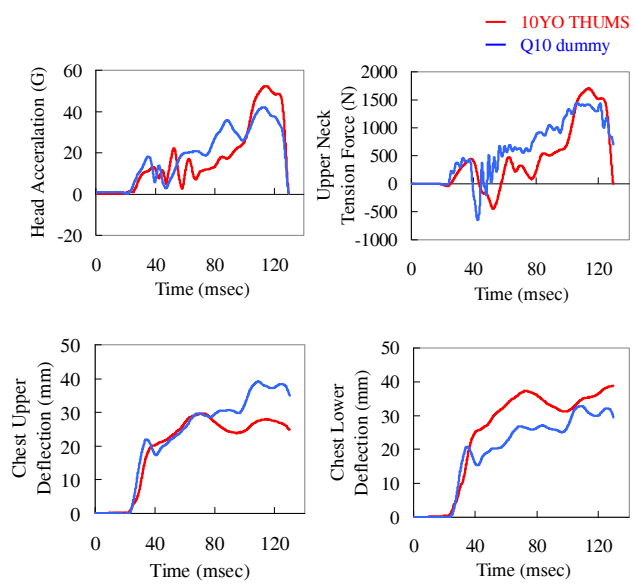


*(a)* Time history comparison of head resultant acceleration, upper neck tension force, and chest deflection (cases 3 and 7)

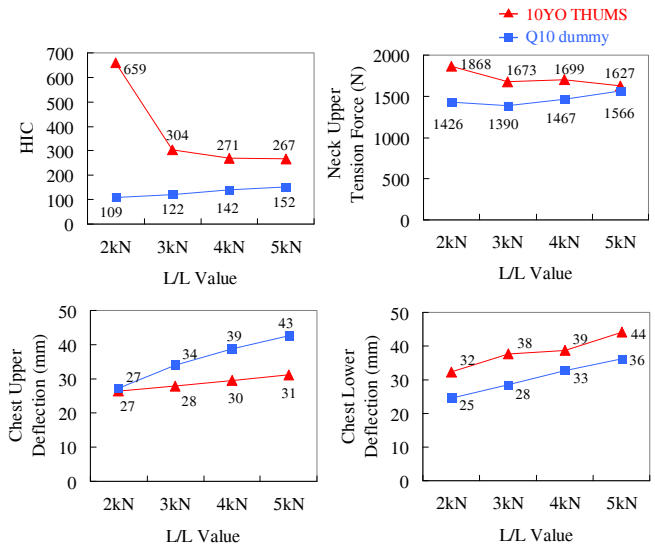


*(b)* Injury values of each part at each L/L value

***Figure 2.*** Injury value time history and sensitivity of displacement of each part to L/L value.

## DISCUSSIONS

### Cause of Smaller Head and Chest Displacement in Q10 Dummy Compared to 10YO THUMS Model

The mass distribution, dimensions and stiffness of body parts of the Q10 dummy closely match the average values of a 10-year old (Lemmen et al., 2012). However, the Q10 dummy has a rigid block, called a thoracic plate, for supporting the measurement instrumentation. The flexion range of the thoracic spine was relatively small due to the higher rigidity of this part compared to an actual human spine.

The smaller forward displacement of the Q10 dummy head compared to the 10YO THUMS head was analyzed comparing cases 3 and 7. The head forward displacement is mostly determined by the pelvis displacement and the flexion of the cervical, thoracic, and lumbar spines. Figure 3 compares the contributions of pelvis displacement and spine flexions between the 10YO THUMS and Q10 dummy. In the 10YO THUMS model, 328 mm (60%) of the head displacement amount of 544 mm was caused by the flexion of the thoracic spine. In contrast, the Q10 dummy had little flexion of the thoracic spine. This suggests that the thoracic plate of the Q10 dummy hindered the flexion of the thoracic spine. The rigidity of the thoracic plate was also a possible factor of the smaller chest forward displacement of the Q10 dummy.

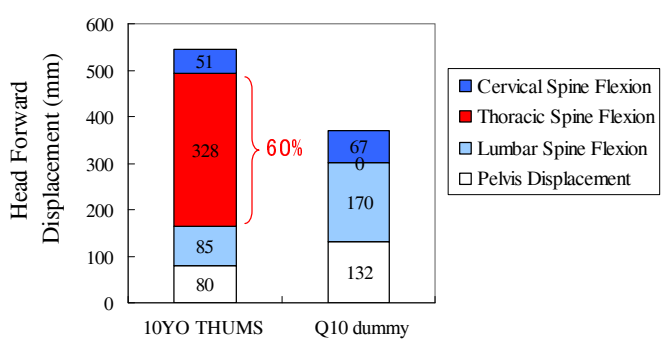


***Figure 3.*** Contributions of pelvis displacement and spine flexions to head forward displacement.

**Cause of Higher Chest Deflection in Q10 Dummy Compared to 10YO THUMS Model**

The contact force of the shoulder belt acting on the chest of the Q10 dummy (6,500 N, case 7) was lower than that of the 10YO THUMS model (8,300 N, case 3). Lemmen et al. (2012) reported that the chest deflection responses of the Q10 dummy are within the test corridor. These points indicate that the cause of the difference in chest deflection is neither the force of the shoulder belt nor the chest deflection responses of the Q10 dummy. This research focused on the relationship between the chest deflection measurement points and the position of the shoulder belt.
Figure 4 shows the positional relationship at the maximum chest deflection. The distance between the chest upper deflection measurement point and the center of the shoulder belt in the width direction was 89 mm in the 10YO THUMS model (case 3). This differed greatly from the distance in the Q10 dummy, which was only 7 mm (case 7). The shoulder belt contacted the area around the chest upper deflection measurement point in the Q10 dummy, while the belt was at the lower area in the 10YO THUMS model. This is thought to be the reason why the chest upper deflection of the Q10 dummy was greater than that of the 10YO THUMS model.

As shown in Figure 1(a), the Q10 dummy model exhibited much smaller chest lateral displacement (21 mm at 120 msec) compared to the 10YO THUMS model (101 mm), while there was little difference in the chest vertical displacement. The shoulder belt kept in contact with the area around chest upper deflection measurement point in the Q10 dummy while the chest upper deflection measurement point deviated from the shoulder belt contact in the 10YO THUMS model.

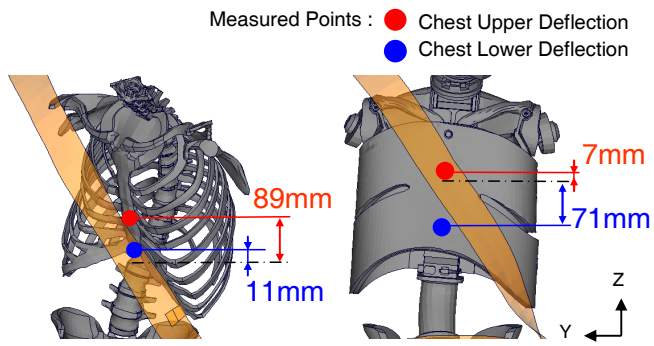


***Figure 4.*** Positional relationship between chest and shoulder belt.

**Cause of Higher Chest Upper Deflection Sensitivity to Changes in L/L value in Q10 Dummy**

In the 10YO THUMS model, the chest upper deflection decreased by 5.3 mm for each 1 kN of the L/L value. However, in the Q10 dummy, the chest upper deflection decreased by only 1.3 mm. The sensitivity of the chest upper deflection to the L/L value was roughly four times higher for the Q10 dummy than the 10YO THUMS model.

In cases 3 and 7, the shoulder belt contact area was divided into three regions (the clavicle, chest, and abdomen) for analyzing the force contribution to chest deflection. The clavicle region covers the right shoulder and the right rib 1, the chest region covered the area from the right rib 2 to the left rib 9, and the abdominal region covered the area below the left rib 9. At the maximum chest upper deflection, 48% of the force was generated at the clavicle region, 37% at the chest region, and 15% at the abdominal region. Of these, the forces at the clavicle and abdominal regions do not directly cause an increase in upper chest deflection. There were little differences in the change in clavicle force between both models with different L/L values.

The ratio of force transmission from the clavicle to the sternum (force transmission rate) was compared between the 10YO THUMS and Q10 dummy models. This ratio was 22% in the Q10 dummy but only 8% in the 10YO THUMS model, approximately 2.6 times higher (Figure 5(a)) than the rate for the Q10 dummy. In the human body, the left and right clavicles are completely separate and join to the sternum through ligaments. On the other hand, the clavicle

of the Q10 dummy is a single part extending laterally from the left to the right and bolted to the ribcage (Figure 5(b)). The high sensitivity of the chest upper deflection of the Q10 dummy is due to the smaller freedom of deformation of the joint between the clavicle and sternum, which facilitates transmission of the shoulder belt load acting on the clavicle to the sternum.

It is considered that the impact kinematics and responses of the Q10 dummy could be made closer to those of the 10YO THUMS model by improving the flexibility of the thoracic spine and the joint between the clavicle and sternum.

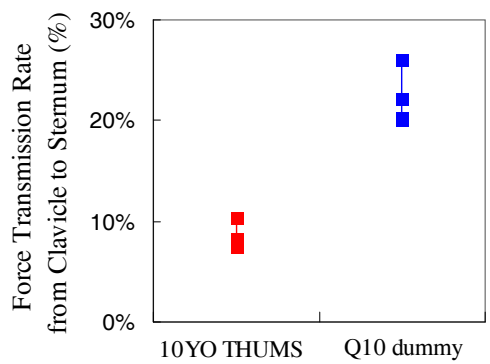


***(a)*** Force transmission rate from clavicle to sternum

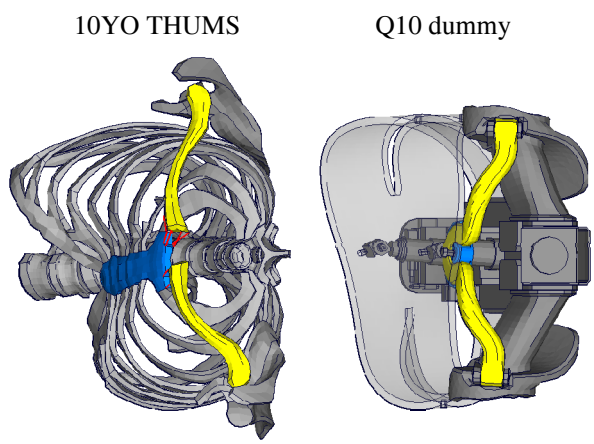


***(b)*** Deformation of clavicle and sternum with fixed spine (116 msec)

***Figure 5.*** Clavicle force transmission rate and structural differences.

Limitation

This research was conducted assuming particular impact conditions (vehicle, impact pattern, and speed). The investigation does not comprehensively cover all the types of accidents that occur in the real world and is not directly related to accident results.

## CONCLUSIONS

This paper described a simulated 64 km/h ODB frontal impact test using 10YO THUMS and Q10 dummy models. The changes in impact kinematics and injury values of the two models were compared under various L/L values ranging from 2 to 5 kN.

The kinematics of the 10YO THUMS and Q10 dummy models were almost identical up to 60 msec after the impact. However, the forward and lateral displacements of the 10YO THUMS model were larger than those of the Q10 dummy after 60 msec. The Q10 dummy exhibited lower head resultant acceleration, smaller upper neck tension force, greater chest upper deflection, and smaller chest lower deflection. The changes in the injury values under different L/L values were similar between the 10YO THUMS and Q10 dummy models. However, the change in the chest upper deflection of the Q10 dummy was greater than that of the 10YO THUMS model, with a sensitivity of approximately four times as high.

The smaller head and chest displacement in the Q10 dummy compared to the 10YO THUMS model was probably due to the thoracic plate of the Q10 dummy hindering the flexion of the thoracic spine. The greater chest upper deflection of the Q10 dummy was assumed to be because the shoulder belt was positioned close to the chest upper deflection gauge. The high sensitivity of the chest upper deflection of the Q10 dummy to the L/L changes was probably due to the high force transmission ratio from the clavicle to the sternum.

These results showed that the impact kinematics and responses of the Q10 dummy could be made closer to those of the 10YO THUMS model by improving the flexibility of the thoracic spine and the joint between the clavicle and sternum.

## REFERENCES


Humanetics Innovative Solutions, Inc. (2013). *Q10 Child Dummy Model LS-DYNA Model Version 1.2 User's Manual.* Humanetics Innovative Solutions, Inc. U.S.A.

Kent, R., Lopez-Valdes, F., Lamp, J., Lau, S., Parent, D., Kerrigan, J., et al. (2011). *Characterization of the Pediatric Chest and Abdomen Using Three Post-Mortem Human Subjects.* Proceedings of the 22nd ESV Conference. Paper No. 11-0394. Washington, D.C, U.S.A. : NHTSA

Kirk, A., Lesire, P., & Schick, S. (2012). *Project Deliverable 3.2.1 of the EC FP7 Project CASPER.* Retrieved from http://casper-project.eu/

Lemmen, P., Waagmeester, K., Burleigh, M., Lakshminarayana, A., & Korschdon, K. (2013). *Development of the Q10 10 Year-old Child Crash Test Dummy.* Proceedings of the 23rd ESV Conference. Paper No. 13-0348. Seoul, Republic of Korea. : NHTSA

Nishimura, R., & Hasegawa, J. (2002). *Development of the Human FEM Model for Child Pedestrian.* Proceedings of 2002 JSAE Autumn Congress. Paper No. 78-02. Kyoto, Japan. : JSAE

# INJURIES AND KINEMATICS: RESPONSE OF THE CERVICAL SPINE IN INVERTED IMPACTS

**Carolyn Roberts**
**Jason R. Kerrigan**
University of Virginia, Center for Applied Biomechanics
United States of America

Paper Number 15-0432

## ABSTRACT

Given the frequency and severity of cervical spine injuries resulting from rollover crashes, it is critical to analyze the mechanism of cervical spine injury in this loading condition. In rollover crashes, roof-to-ground impacts can generate axial compression of the cervical spine, which can result in paralysis and death. This study was performed to compare injury type and severity between component and full body inverted vertex impact tests with post-mortem human surrogates (PMHS); a secondary aim was to determine how changes in vertebral kinematics resulted in changes in hear reaction loads. Five PMHS were suspended in an inverted seated position and then dropped from two heights to achieve 2 m/s (one subjects once and another twice) and 4.4 m/s (all subjects) at impact. The subjects were dropped on a padded five-axis load cell to record the reaction force from impact. Each PMHS was instrumented with three blocks (each containing three accelerometers and three angular rate sensors) rigidly mounted along the upper thoracic spine and on the head. Injuries were determined using both CT scans and dissection following testing. Vertical force traces from the load cell reflect a similar two peak shape seen in previous full-body and component tests. High-speed (1000 Hz) X-ray video analysis shows the neck retains in its initial orientation but becomes increasingly compressed during the loading portion of the first peak. At the first peak, the cervical spine begins to curve, putting the cervical spine into extension, with the center of curvature around C3 or C4, and continues into bending during the unloading of the first peak. The head then translates forward and the neck moves into flexion during the second peak. Each PMHS achieved a flexion injury in the upper thoracic spine or the lower cervical spine during the testing, which occurred during the second peak of the force trace, contradicting previous theories that injury occurs at the first peak, where maximum force occurs. These tests suggest that the direction of torso loading, impact velocity, and boundary conditions at the ends of the cervical spine all affect the kinematics during impact as well as the resulting injuries, and should all be taken into account when determining appropriate injury criteria and developing biofidelic ATDs to predict injuries in crash tests.

## INTRODUCTION

Occupant-to-roof impact can cause some of the most severe injuries in rollover crashes; these injuries have been shown to be related to the amount of roof intrusion into the occupant compartment and the post-crash headroom in the vehicle (Ridella et al. 2008). Occupant-roof interaction generates axial compression in the cervical spine, which is responsible for many rollover crash-induced injuries. Although there are multiple head-neck PMHS compoment studies focused on cervical spine injuries caused by axial compression, few full-body PMHS tests have been performed (Sances et al., 1981; Nusholtz, 1983; Yoganandan et al., 1991; Kerrigan et al. 2014). Viano combines the data from studies by Sances, Nusholtz, and Yoganandan and reports full-body PMHS testing consistently produced injury above 4.0 m/s and consistently resulted in no injury below 2.0 m/s, and more data is needed between the 2.0 and 4.0 m/s range (Sances et al., 1981; Nusholtz, 1983; Yoganandan et al., 1991; Viano & Parenteau , 2008).

Previous head-neck component vertex-impact testing that employed a fixed torso mass (16 kg) and a constraint on the motion of the T1 vertebra has produced severe injury at or above 3.1 m/s (Nightingale et al. 1996, 1997). A more recent study escrived vertex impacr experiments with four full-body PMHS in an impact conditions between 3.0 amd 3.6 m/s, with a goal of generating the same impact positioning and condition achieved by Nightingale in component testing (Nightingale et al. 1996, 1997; Kerrigan et al. 2014). These velocity conditions were also chosen in order to help fill the void of data identified by Viano and Parenteau (Viano & Parenteau 2008). However, the

study found that injuries were significantly less severe than in the Nightingale studies, with only one fracture in the full-body drop tests related to the first 100 ms after impact, and hypothesized these differences in injury severity were due to contraints on T1 (Nightingale et al., 1996, 1997).

This study aimed to expand on the study by Kerrigan et al. (2014) by subjecting five more PMHS to inverted vertex impact. Conditions were the same as the previous study, but tests were performed at 2.0 and 4.4 m/s to compare the results of these recent whole body tests to those of the literature ((Sances et al., 1981; Nusholtz, 1983; Yoganandan et al., 1991) that utilized similar velocities. Specific aims of the cyrrent study included determination whether injuries, in general, can be produced when impact velocity is 4.4 m/s, comparison of injury severity and type to those recorded in previous component and whole body tests, and to identify how abrupt changes in vertebral kinematics are represented in impact force data.

## TESTING METHODS

Five male PMHS were selected for this study; while all subjects were tested with a 4.4 m/s impact velocity; two subjects were tested at 2 m/s to examine the effect of impact velocity on spinal dynamics and repeatability of response (Table 1).

**Table 1.**
**Physical information and test matrix for each post-mortem human surrogate (PMHS) tested.**

| Subject Number | Age (years) | Height (mm) | Weight (kg) | Bone Density (DXA) | First Test (Impact Velocity) | Second Test (Impact Velocity) | Third Test (Impact Velocity) |
|---|---|---|---|---|---|---|---|
| *#582* | 71 | 1780 | 68.04 | 0.8 | 4.4 m/s (Test 6) | - | - |
| *#534* | 71 | 1715 | 93.16 | 0.8 | 2.0 m/s (Test 7) | 4.4 m/s (Test 8) | |
| *#606* | 62 | 1803 | 51.71 | -0.3 | 2.0 m/s (Test 9) | 2.0 m/s (Test 10) | 4.4 m/s (Test 11) |
| *#610* | 48 | 1721 | 61.69 | -2.6 | 4.4 m/s (Test 12) | - | - |
| *#693* | 47 | 1780 | 64.49 | -1.3 | 4.4 m/s (Test 13) | - | - |

### PMHS Preparation and Instrumentation

The PMHS were obtained and treated in accordance with the ethical guidelines established by the Human Usage Review Panel of the National Highway Traffic Safety Administration, and all testing and handling procedures were reviewed and approved by the Center for Applied Biomechanics Biological Protocol Committee and an independent Oversight Committee at the University of Virginia.

**PMHS Preparation** The upper extremities of each subject were removed at the sternoclavicular joint. Mounting plates for instrumentation cubes were screwed into the right and left sides of the parietal bones using wood screws. Three sets of mounting hardware were screwed into T1, T4, and T8, and static x-rays and geometric calculations were used to confirm that each mount was rigidly attached to the correct vertebra. After surgical preparation, each subject was wrapped in a thin layer of mechanically adhesive wrap (Coban, 3M, St. Paul, MN, USA) and outfitted with a tactical body harness (355 Extraction Harness, Yates Gear Inc, Redding, CA, USA). A post-preparation CT scan was taken to ensure no damage was done to the cervical spine and to confirm mount locations.

**Instrumentation** The instrumentation on the spine consisted of three blocks, rigidly attached to T1, T4, and T8 with the mounting hardware. Each block allowed for the attachment of three accelerometers (7264B-2000, Endevco, San Juan Capistrano, CA, USA) and three angular rate sensors (ARS-8K, DTS, Seal Beach, CA, USA). Two more of instrumentation blocks were also affixed to either side of the head onto the mounting plates. Other instrumentation used in the test included two load cells; one padded six-axis load cell (Denton B-3868-D, Humanetics Innovative Solutions, Plymouth, MI, USA) onto which the subjects landed, and another cable load cell that allowed for determination of drop release time. On the top plate of the six-axis load cell, a piece of 25.4 mm thick light-density closed-cell, polyvinyl chloride general purpose foam (V700 Series 1.00", Gaska Tape Inc., Elkhart, IN, USA), was adhered to the steel plate. This foam was used previously (Frechede et al. 2009) to mimic the foam used by Nightingale et al. (1996).

### Testing Area Setup and Procedures

Each subject was suspended in an upside-down seated position (Manary et al., 1998) using a system of strings and taut ties (small plastic pieces to adjust the length of each string). All of the strings were looped around a single carabineer, from which the cadaver was suspended. Multiple strings allowed for control over the position, and the subject's torso was rotated until the superior endplate of T1 was oriented at a 25 degree angle from parallel to ground, and the cervical spine was flexed until the Frankfurt plane was oriented parallel to the ground (Nightingale et al., 1996). The subject was positioned such that vertex of the head was centered over the padded load cell. Following final positioning, a ROMER arm scanner (ROMER Absolute Arm with Integrated Scanner, Hexagon Metrology, North Kingstown, RI, USA) was used to collect the orientation and position of all of the accelerometers, angular rate sensors, and the padded load cell onto which each subject landed. After recording this final position with the scans, the subject was released with a solenoid release mechanics to sustain impact with the load plate affixed to the floor.

X-Ray imagery was captured at 1000 Hz in all of the impact tests via positioning the subjects between an image intensifier connected to a high speed digital imager (GX-1, NAC Inc., Japan). Video images were also captured at 1000 Hz from lateral and superior views of the subjects.

A post-test CT was taken, followed by a dissection to confirmed the bony fracture seen in the CT scan and to display ligamentous and facet joint damage.

## DATA ANALYSIS

### Coordinate Transformations of Data

Head and T1 acceleration data were transformed to local coordinate systems (defined by anatomical landmarks) using the rigid body assumption. The vertebral and head coordinate systems were generated using CT imagery to find the location and orientation of the mount relative to vertebral anatomy. In the vertebral coordinate system, the y-axis was generated by creating a vector from the most lateral point of the left to the most lateral point of the right transverse process. The x-axis was defined to point from the most posterior point of the spinous process to a point on the y-axis such that the x- and y-axes were perpendicular. The z-axis was found by taking the cross product of the x and y vectors. The local head coordinate system was determined using 3 screws (right, left and posterior) that generated the plane in which the cg of the head laid. The y-axis was found by finding the vector of the location of the left screw, L and to the location of the right screw, R. Next the x-axis of the head was determined by finding the perpendicular line to the y-axis on which point P, the posterior of the head, lies. The positive x-axis was found my taking the cross product of the positive x-axis and the positive y-axis. After all of the local data had been found, time histories of the head and T1 local-to-global coordinate system transformations were determined from the angular rate data (Beard & Schlick, 2003).

### High Speed X-ray video analysis

Changes to the shape of cervical spine over the first 80 ms (2.0 m/s impact velocity tests) or 175 ms (4.4 m/s impact velocity tests) after impact were determined by tracking the motion of the connection between the vertebral body and the spinous process for each of the cervical vertebrae in each test using X-ray images. The times when abrupt changes in cervical curvature were seen were compared to the head/load plate loads to facilitate dynamic response analysis.

## RESULTS AND DISCUSSION

### Head Forces

The vertical force traces measured by the padded load cell during impact follow the general double peak shape seen in other studies, both full-body and component, that axially load the cervical spine (Figure 1). Comparing the force results from this test to the previous full-body tests in the literature, the duration, magnitude and peak forces attained during the test closely match (Sances et al., 1981; Nusholtz, 1983; Yoganandan et al., 1991). However, comparing to component tests, increasing the impact velocity by 38% (from 3.2 m/s to 4.4 m/s), resulted in an increased force of 200-250% (Nightingale et al., 1996, 1997). The previous whole body study showed similar peak forces as the component tests, yet no or only subtle injuries (Kerrigan 2014). If this were solely due to rate sensitivity, then it would be at a level that exceeds documented rate sensitivity for all other human tissues. The higher impact force is likely due more of the upper body mass being recruited in the initial impact because there is less time for it to move or articulate away from the load path.

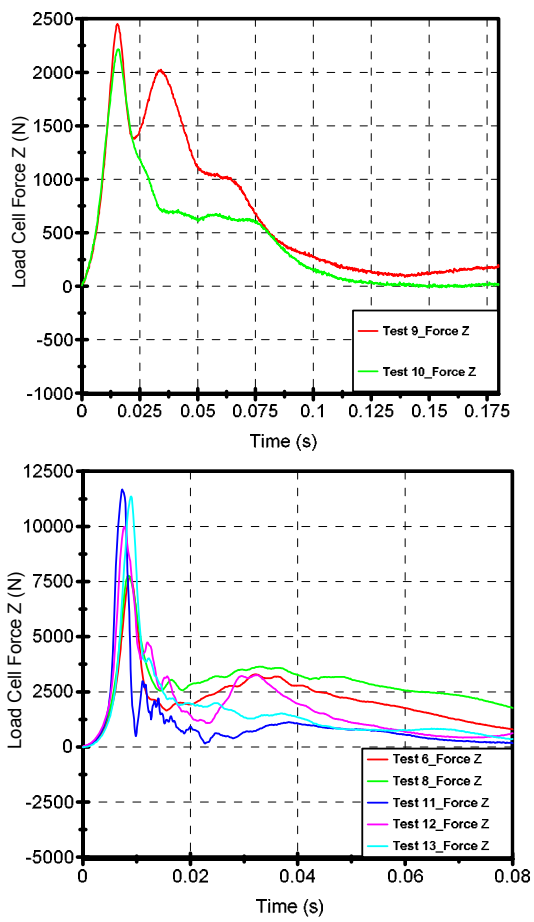


***Figure 1. Vertical force traces for each tests. The 2.0 m/s impact velocity tests are depicted in the top graph, and the 4.4 m/s impact velocity tests are depicted in the bottom graph***

**Kinematics of the torso, neck, and head**

Using high-speed X-ray video, it is possible to see the position of the cervical spine as a whole throughout the entire loading period resulting from the impact (both peaks in the vertical force trace). The relative positions of the cervical spine, torso, and head at different times during the vertical force trace are depicted in Figure 2.

In part 1, the PMHS has just initiated contact with the load cell; T1 looks as if it is 25 degrees from horizontal, as it was initially positioned, and the cervical spine is fairly straight with the exception of C1 and C2 (this is probably due to the initial position of the Frankfurt plane at 0 degrees). In part 2, the force trace shows a dramatic increase towards its maximum peak; the cervical spine remains in the same position, but begins to compress slightly. This is the only time during the test where the neck is in pure axial compression. At this time, the torso continues to translate downwards and the head remains fixed in its initial position. In part 3, the maximum Z-force is reached, and the curvature of the neck begins to increase, specifically around C3-C4. In part 4, the vertical force decreases as the neck continues to increase more and more in curvature. In other words, the load decreases at the geometry of the neck changes. In part 5, the vertical force increases once again, and the cervical spine begins to straighten as the head translates forward, and again, the torso continues to translate downward. In part 6, the force reaches a second peak as the neck straightens, and the head continues to translate even further forward, and the torso continues to move down. This puts the neck in shear loading, especially at the C7/T1 interface. In part 7, the Z-force is decreasing, and the bottom of the neck is in flexion with shear loading, the head continues to move forward, and begins to rotate up towards the torso. In 8, the head has almost left the load cell, and the head continues to rotate upwards, while the torso continues to translate downwards and also posteriorly. This rotation and translation of the head continue until the head leaves the load cell and the magnitude of the Z-force is zero.

As was noted before, these general kinematics occurred for every subject with the exception of Subject 582 in Test 6. In Test 6, the Subject's torso loaded the head and neck more vertically. This meant that the head was unable to translate forward and then rotate out of the way of the torso that was loading it.

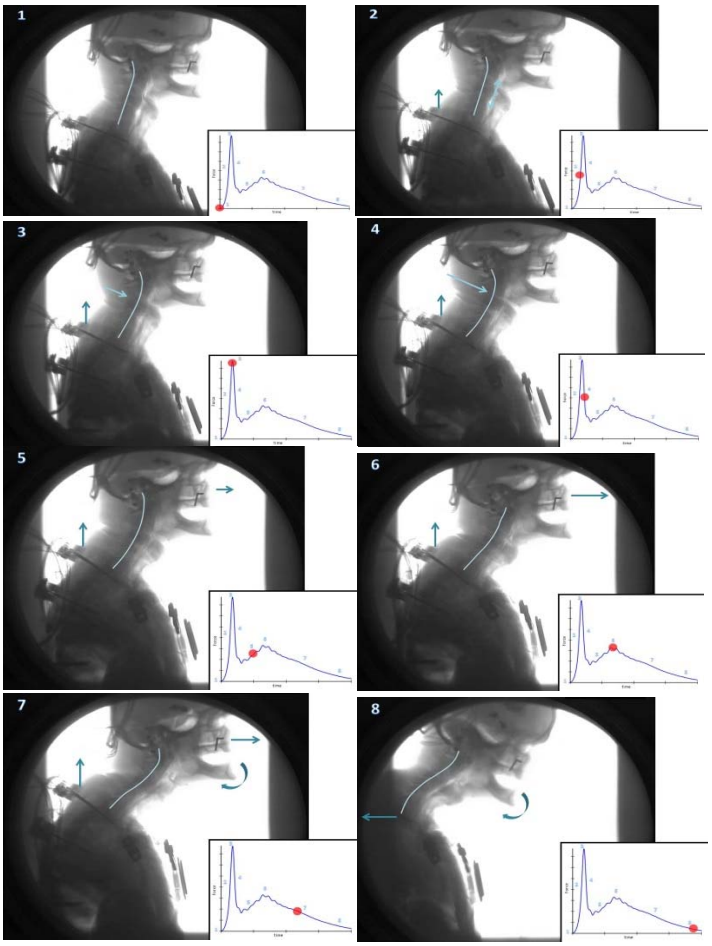


***Figure 2. Time step of X-ray video to show the kinematics of the cervical spine with respect to the force trace shape. A light blue curve is drawn along the cervical spine, connecting the location where the spinous process meets the body of each vertebra. Arrows are also shown to depict the general motion of the head and torso of the subject. This figure shows the representative general kinematics that all subjects underwent (with the exception of Subject 582). The red dot on the force trace of each image denotes the relative time at which each motion in the picture is occurring. Each image is also labeled in chronological order (1-8).***

**Injuries**

Table 2 is a collection of the injuries found in all of the subjects. It is very clear that most of the injuries occur in the lower cervical spine and thoracic spine and, it is important to note that only one compression injury in the upper cervical spine was attained during this test. All of the subjects did not attain bony fracture, but all were all injured during testing, most at the 4.4 m/s impact velocity.

**Table 2.**
**Location and type of injuries attained for each subject during testing.**

| Injury Location ↓ | Subject # 582 | Subject # 534 | Subject # 606 | Subject # 610 | Subject # 693 |
|---|---|---|---|---|---|
| **C1 Vertebra** | Anterior arch fracture | | | | |
| **C2 Vertebra** | | | | | |
| **C3 Vertebra** | | Two fractures in the vertebral body | | | |
| **C3/C4 Joint** | | | | Anterior longitudinal ligament tear | |
| **C4 Vertebra** | | | | | |
| **C5 Vertebra** | | | | | |
| **C6 Vertebra** | | | Acute fracture of inferior endplate | | |
| **C6/C7 Joint** | | | | Small tear in anterior longitudinal ligament | |
| **C7 Vertebra** | | | Acute fracture of superior endplate | | |
| **C7/T1 Joint** | | Supraspinous ligament tear<br>Interspinous ligament tear<br>Ligamentum flavum tear | Supraspinous ligament tear<br>Interspinous ligament tear<br>Facet disruption | Supraspinous ligament tear<br>Interspinous ligament tear<br>Ligamentum flavum tear<br>Partial tear of anterior longitudinal ligament<br>Facet disruption | Supraspinous ligament tear<br>Interspinous ligament tear<br>Partial tear of posterior longitudinal ligament |
| **T1 Vertebra** | Acute fracture of inferior endplate | Lamina fracture | | | |
| **T1/T2 Joint** | | | | | Facet disruption |
| **T2 Vertebra** | Acute fracture of inferior endplate<br>Acute fracture of superior endplate | Lamina Fracture | | | |
| **T3 Vertebra** | Acute fracture of superior endplate | | | | |
| **T4 Vertebra** | | Lamina Fracture | | | |
| **T5 Vertebra** | | Lamina Fracture | | | |

Most of the injuries at the C6, C7, T1 and T2 level were located anterior, suggesting they were flexion injuries. Given the mode of injury is flexion, and from the X-ray videos it is clear that the cervical spine does not go into flexion until the second peak of loading, it makes sense that these injuries occur during the second peak of the vertical force trace, not at the point of maximum vertical force. This suggests that simply measuring and then using a maximum force as an injury criterion would not be effective, as these injuries occur nowhere near the maximum force. These injuries are likely due to difference in stiffness between the neck and torso; more motion is allotted for the vertebrae in the cervical spine, and the resistance to motion of the more rigid thoracic spine could cause stress concentrations that resulted in fracture or excessive stretching of ligaments causing tearing.

The ligamentous injuries and fractures in C3 and C4 were located posterior, suggesting their mode of injury was extension. Extension of the cervical spine occurs during the unloading portion of the first peak of the vertical force trace, so it is likely that these extension injuries occurred just following the maximum measured force.

One injury is an outlier to this injury data set: the anterior arch fracture of C1 from subject 582. In the test of this subject, the head was unable to move away from the torso as it descended, and therefore the loading on the cervical spine due to the torso was directed more vertical than in the other tests. As seen in the time step videos in Appendix A, as well as Figure 3 the cervical spine remains straight for a longer portion of the test than in all of the other tests. It is likely that a higher axial force was experienced in the upper cervical spine in test 9, which explains this anterior arch fracture of C1. This injury is likely the only injury resulting from reaching a maximum vertical force where pure axial compression is the only load on the cervical spine.

Subject #606 attained an injury at the C7/T1 joint during test 9, the first 2.0 m/s impact velocity test for this subject. The injury could be seen on the high-speed X-ray video, and occurred after the 175 ms test time. The injury was not initially seen, so Test 10 (at 2.0 m/s impact velocity) and Test 11 (at 4.4 m/s impact velocity) were still performed. The magnitude of Z force between Test 9 and 10 are extremely close, suggesting that the first peak of loading is not affected by the C7/T1 extension injury. There is a distinct difference between the two tests as Test 10 lacks a distinct second peak; there is also a lack of a second peak in Test 11. The lack of the second peak in vertical force coupled with an extension injury further reinforces the idea that flexion injuries occur during the second peak, and that the prior damage to the C7/T1 joint allowed for greater motion between the cervical and thoracic spines, allowing the neck to more easily rotate away from the torso, and decreasing the vertical loading recorded by the load cell.

**Differences in kinematics between subjects**

Subject 582 had the largest divergence from the generalized kinematics and injuries explained above. Although this subject achieved an axial compression injury, the maximum force in Test 6 has the lowest magnitude of the 4.4 m/s impact velocity tests, yet Subject 582 has the second highest mass. Given all other subjects attained higher maximum forces, but no axial compression injuries, there was likely a difference in position of the cervical spine throughout impact, which could be seen through high speed X-ray imagery (Figure 3). One of the most significant discrepancies is the difference in the head position. In the top image, the head of Subject 582 is trapped almost directly under the torso, whereas in the bottom image, Test 12, the subject's head has translated to the right in the X-ray video, and the neck and torso still have room to translate downwards, because the head has moved out of the way. Another significant difference is the difference between the curvature of the cervical and thoracic spines between the two tests. There is a sharp bend between the cervical and thoracic spines in the bottom figure (the location where Subject 610 attained a flexion injury), whereas the curvature at this location in the top photo is much less severe.

Although the two subjects were initially positioned in the same manner, differences in kinematics and injuries are likely due to geometric differences in the thorax of each subject, which could change the anterior-posterior position of the center of mass of the torso, and thus change the direction of the force that loads the neck.

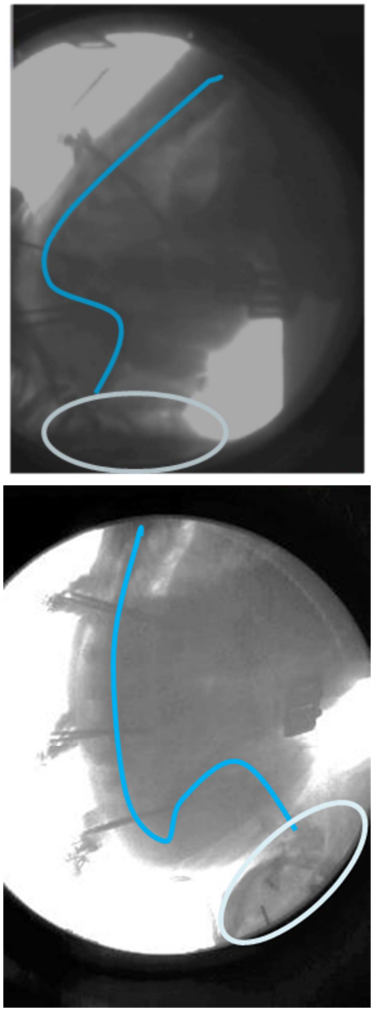

***Figure 3. Kinematic differences between the spine and head between Subject 582, Test 6 (top) versus Subject 610, Test 12 (bottom) both at 40ms after impact under the same velocity conditions. The blue line shows a trace of the cervical and thoracic spine shapes and the white circle shows the approximate location and orientation of the head.***

**Boundary Conditions of the Cervical Spine**

It is well established that cervical spine boundary conditions have a substantial effect on the injury tolerance and type in compressive loading (Nightingale et al., 1991). By performing full body-drop tests, one of these boundary effects can be measured in vitro, by measuring the motion of T1 using an instrumentation mount with three accelerometers and three angular rate sensors (Figure 4). There was substantial rotation of the T1 vertebra, especially in the roll (over a 15 degree change).

Given the magnitude of these rotations it is possible that the assumptions made for the boundary conditions by Nightingale in head-neck complex tests. Allowing T1 to only translate in the global Z direction drastically limits the motion that is seen in the full body. By restricting the motion of T1, more severe injuries could have been generated in the cervical spine at a lower impact velocity, and could have been created at different times or different locations than if T1 were allowed to be free to rotate.

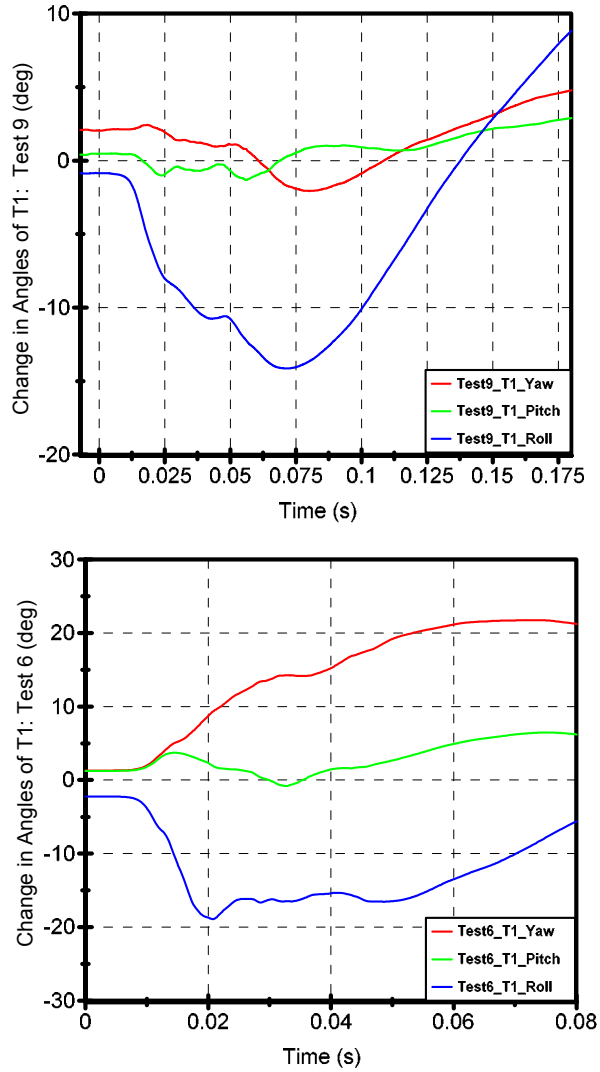


***Figure 4. Local vertebral coordinate system angular velocities depicting the motion of T1 during tests are shown. The plot on the top shows the x, y and z angular rates for a 2.0 m/s impact velocity test, and the plot on the bottom shows the same angular rates for a 4.4 m/s impact velocity test.***

## CONCLUSIONS

Five whole body PMHS were subjected to inverted vertex impacts at 2.0 m/s and 4.4 m/s to examine their response relative to other subjects tested at different velocity tests and component tests that constrained subject motion. The goals of this study included evaluation of whether a 4.4 m/s impact velocity was sufficient to cause injuries, comparison of injury severities and types to those seen in previous tests, and determination of how changes in vertebral kinematics are represented in impact force. The results of this study allowed the following conclusions to be drawn:

Results showed that:

- In general, the PMHS were injured at the 4.4 m/s impact velocity level
- The PMHS injuries generated in these tests were less severe than injuries produced in component test studies conducted at lower impact velocities around 3.2 m/s
- Substantially higher head forces (first peak) were generated in this study than in the previous whole body and component test studies at 3.2 m/s (7500-11500 N vs. 4500 N).

- Injuries, in general, do not occur as a result of the peak impact force; the peak head force does not indicate injury tolerance of the subject
- T1 rotates out of the way during the time period between initial impact, the peak force, and the time when the injury occurs, which suggests that constraining its motion will affect the load response and additionally the injury tolerance of the spine

A next steps in this research could be to evaluate how well existing ATDs represent human respinse by sunjecting ATDs to matched experiments. Aditionally, these data could be used to inform computational analyses aimed at evaluating human body computational models and/or using them to examine the effects of muscle tension on head/neck/torso response.

## REFERENCES


[1] Beard, D. A., and Schlick, T. (2003). Unbiased Rotational Moves for Rigid-Body Dynamics. Biophysical Journal, 85, 2973-2976.

[2] Frechede B; McIntosh A; Grzebieta R; Bambach M. (2009) Hybrid III ATD in inverted impacts: influence of impact angle on neck injury risk assessment. Annals of Biomedical Engineering, 37(7): 1403-1414.

[3] Kerrigan, J., Foster, J., Forman, J., Toczyski, J., Roberts, C., Crandall, J. (2014). Axial Compression Injury Tolerance of the Cervical Spine: Initial Results. Traffic Injury Prevention.

[4] Manary M., Reed M., Flannagan C., Schneider L. (1998). ATD Positioning Based on Driver Posture and Position. 42nd Stapp Car Crash Conference. 1-13.

[5] Matsushita T, Sato TB, Hirabayashi K, Fujimura S, Asazuma T, Takatori T. X-ray study of the human neck motion due to head inertia loading. Proceedings of the 38th Stapp Car Crash Conference, 55-64, 1994.

[6] Nightingale RW, Meyers BS, McElhaney J, Richardson WJ, Doherty BJ. (1991) The Influence of End Condition of Human Cervical Spine Injury Mechanisms. SAE 912915, Society of Automotive Engineers.

[7] Nightingale R., McElhaney J., Richardson W., Myers B. (1996). Dynamic responses of the head and cervical spine to axial impact loading. J Biomechanics, 29: 307–18.

[8] Nightingale R., McElhaney J., Camacho D., Kleinberger M., Winkelstein B., Myers B. (1997) The dynamic responses of the cervical spine: buckling, end conditions, and tolerance in compressive impacts. Proceedings of the 41st Stapp Car Crash Conference. Paper number 973344. 451-71.

[9] Nusholtz, G.., et al. (1983). Cervical spine injury mechanisms. No. 831616. SAE Technical Paper.

[10] Ridella, S., and A. Eigen. "Biomechanical investigation of injury mechanisms in rollover crashes from the CIREN database." proceedings of the 2008 International IRCOBI Conference, Bern, Switzerland. 2008.

[11] Sances Jr A, Myklebust J, Cusick JF, Weber R, Houterman C, Larson, SJ, Walsh P, Chilbert M, Prieto T, Zyvoloski M, Ewing C, Thomas D. (1981) Experimental Studies of Brain and Neck Injury. Proceedings of the 25th Stapp Car Crash Conference, Society of Automotive Engineers.

[12] Viano D., Parenteau C. (2008). Analysis of head impacts causing neck compression injury. Traffic Injury Prevention, 9(2):144-52.

[13] Yoganandan N, Pintar FA, Sances A Jr and Maiman DJ. (1991) Strength and kinematic response of dynamic cervical spine injuries, Spine, Vol. 16, No. 10S, pp. 511–517.

## APPENDIX A: STILL FRAME IMAGES OF TEST VIDEO

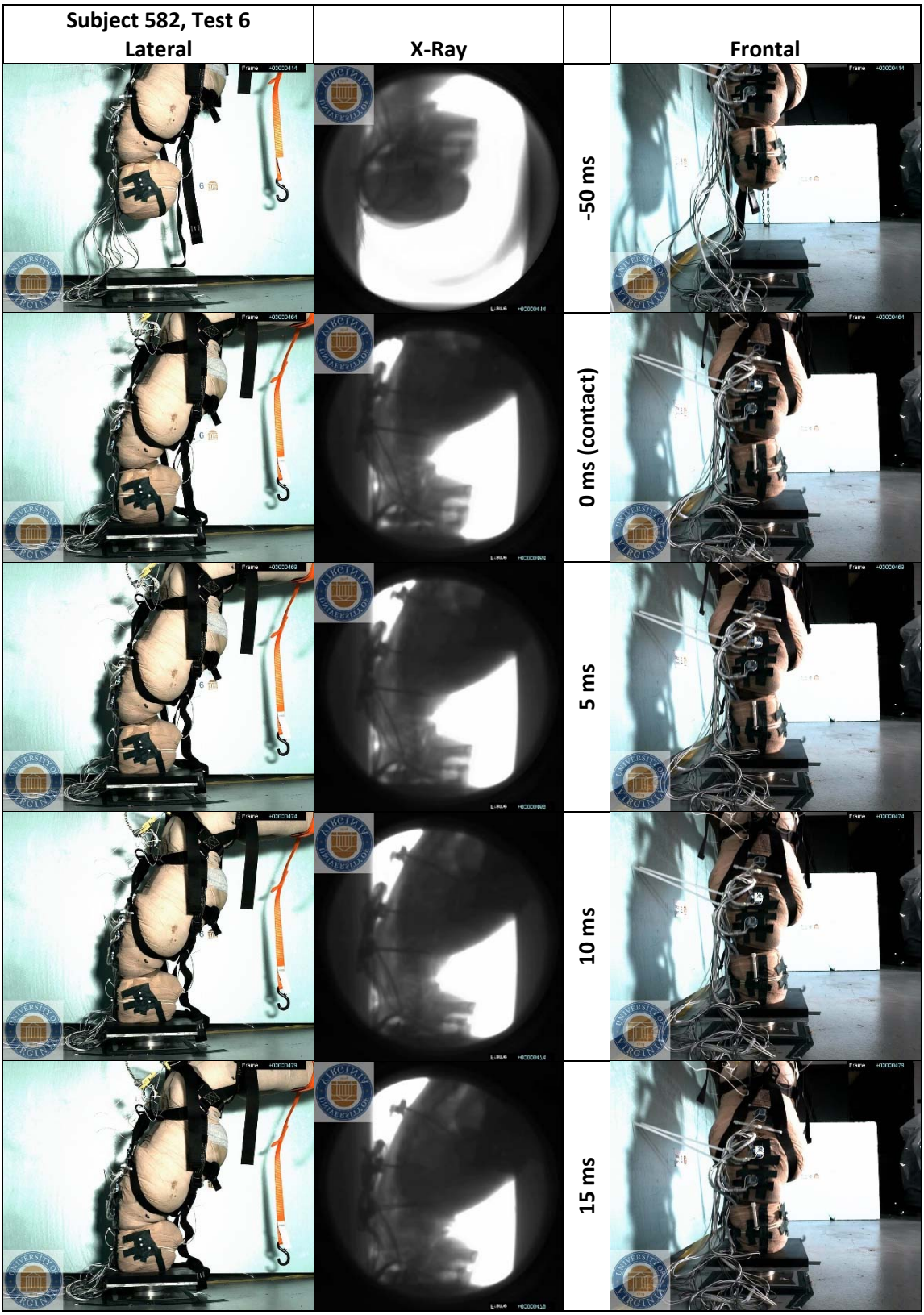

| Subject 582, Test 6<br>Lateral | X-Ray | | Frontal |
|---|---|---|---|
| 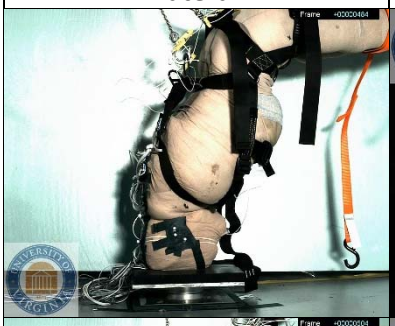 | | 20 ms | 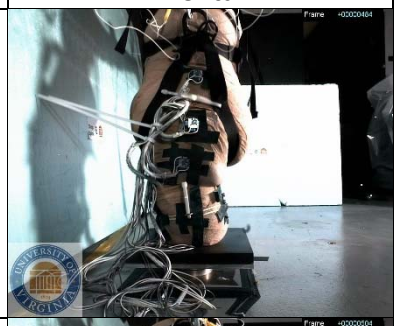 |
| | | 40 ms | |
| | 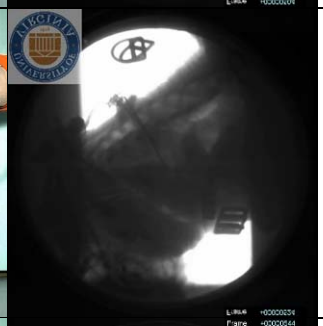 | 60 ms | |
| | | 80 ms | 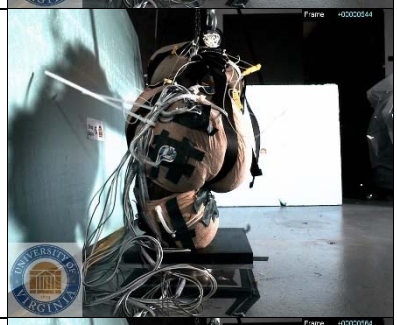 |
| | | 100 ms | |

| Subject 534, Test 8 Lateral | | Frontal |
|---|---|---|
| 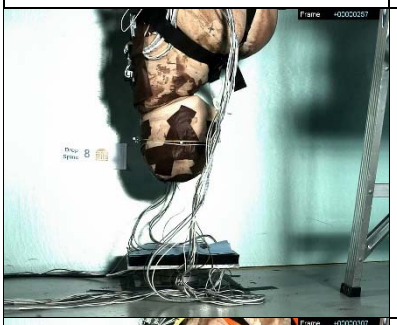 | -50 ms | 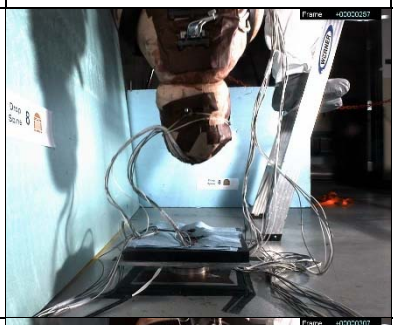 |
| | 0 ms (contact) | |
| | 5 ms | |
| | 10 ms | 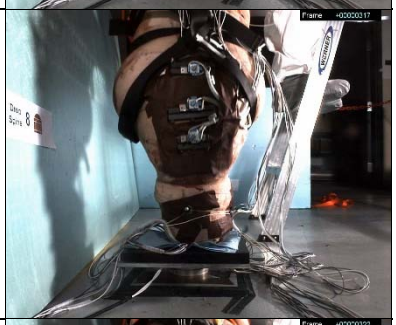 |
| | 15 ms | |

| Subject 534, Test 8<br>Lateral | | Frontal |
|---|---|---|
| 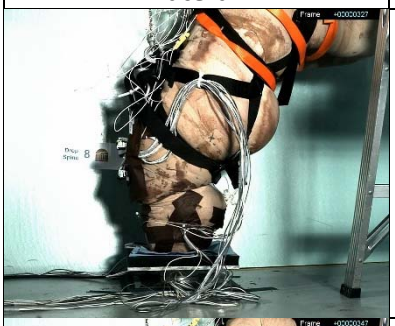 | 20 ms | 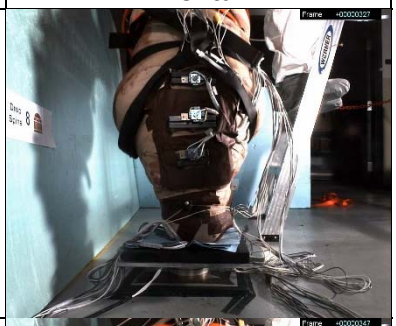 |
| | 40 ms | 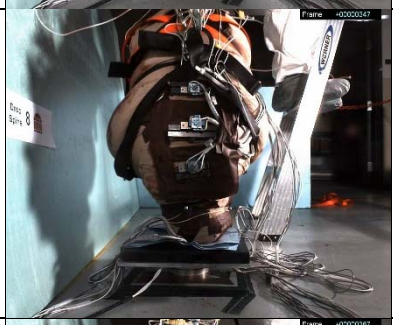 |
| | 60 ms | 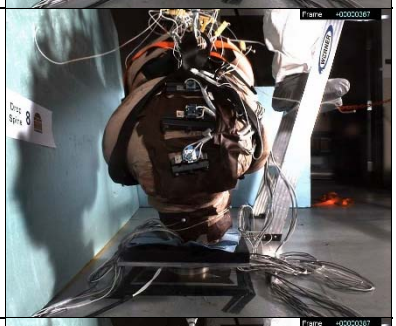 |
| | 80 ms | |
| | 100 ms | |

| Subject 606, Test 9<br>Lateral | X-Ray | | Frontal |
|---|---|---|---|
| 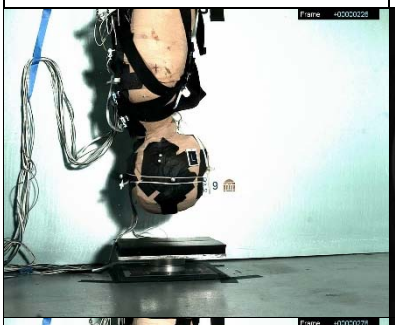 | | -50 ms | 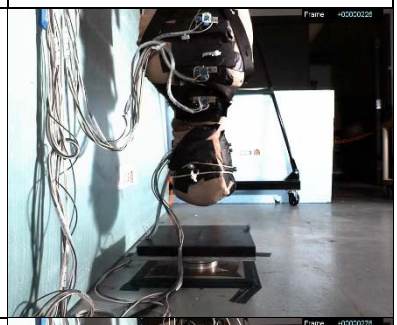 |
| | | 0 ms (contact) | |
| | | 5 ms | |
| 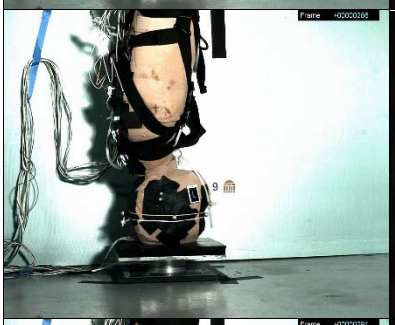 | | 10 ms | |
| 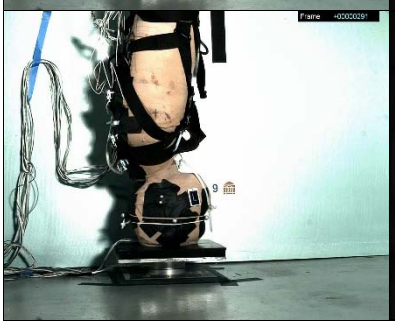 | | 15 ms | 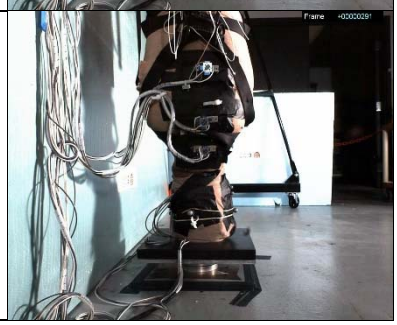 |

| Subject 606, Test 9<br>Lateral | X-Ray | | Frontal |
|---|---|---|---|
| 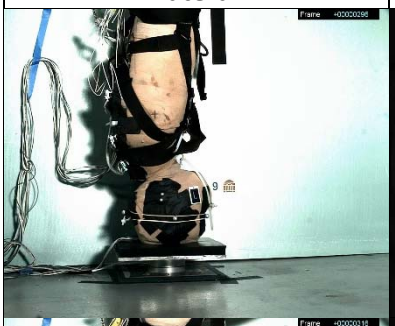 | | 20 ms | 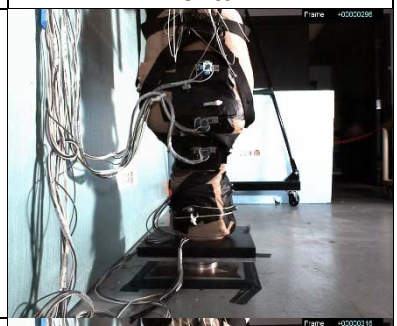 |
| 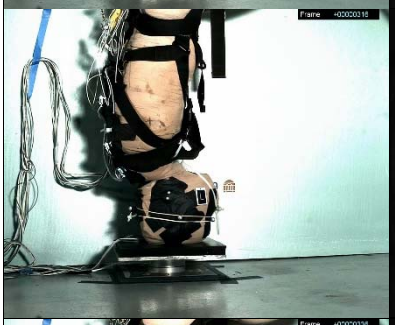 | 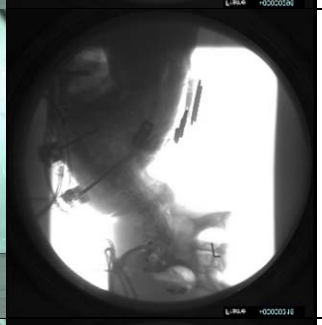 | 40 ms | |
| 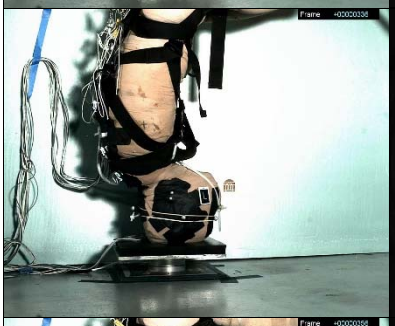 | | 60 ms | |
| 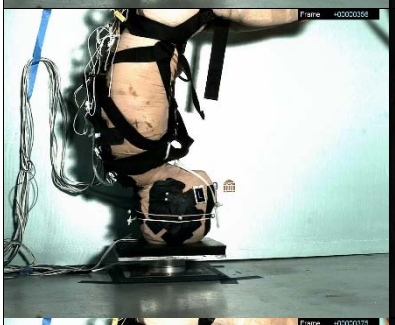 | 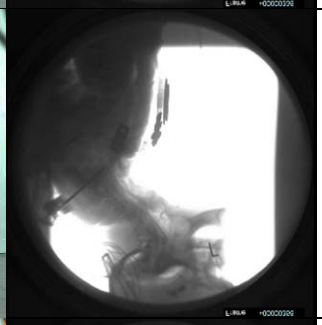 | 80 ms | |
| | | 100 ms | 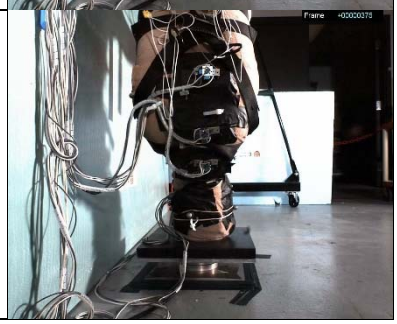 |

| Subject 606, Test 10<br>Lateral | X-Ray | | Frontal |
|---|---|---|---|
| 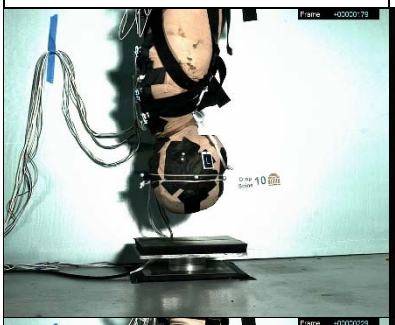 | 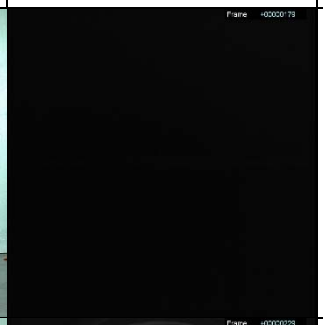 | -50 ms | 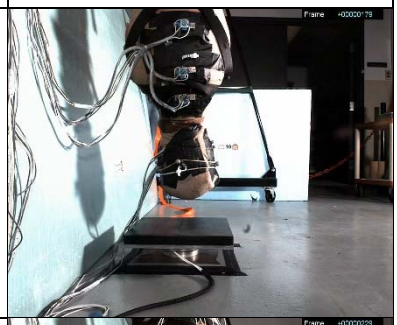 |
| | | 0 ms (contact) | |
| | | 5 ms | |
| | | 10 ms | 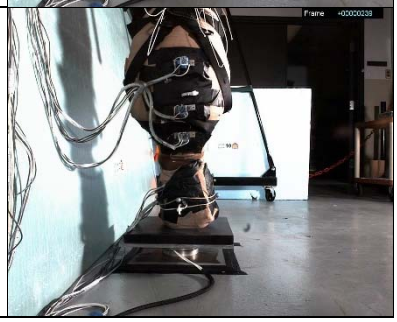 |

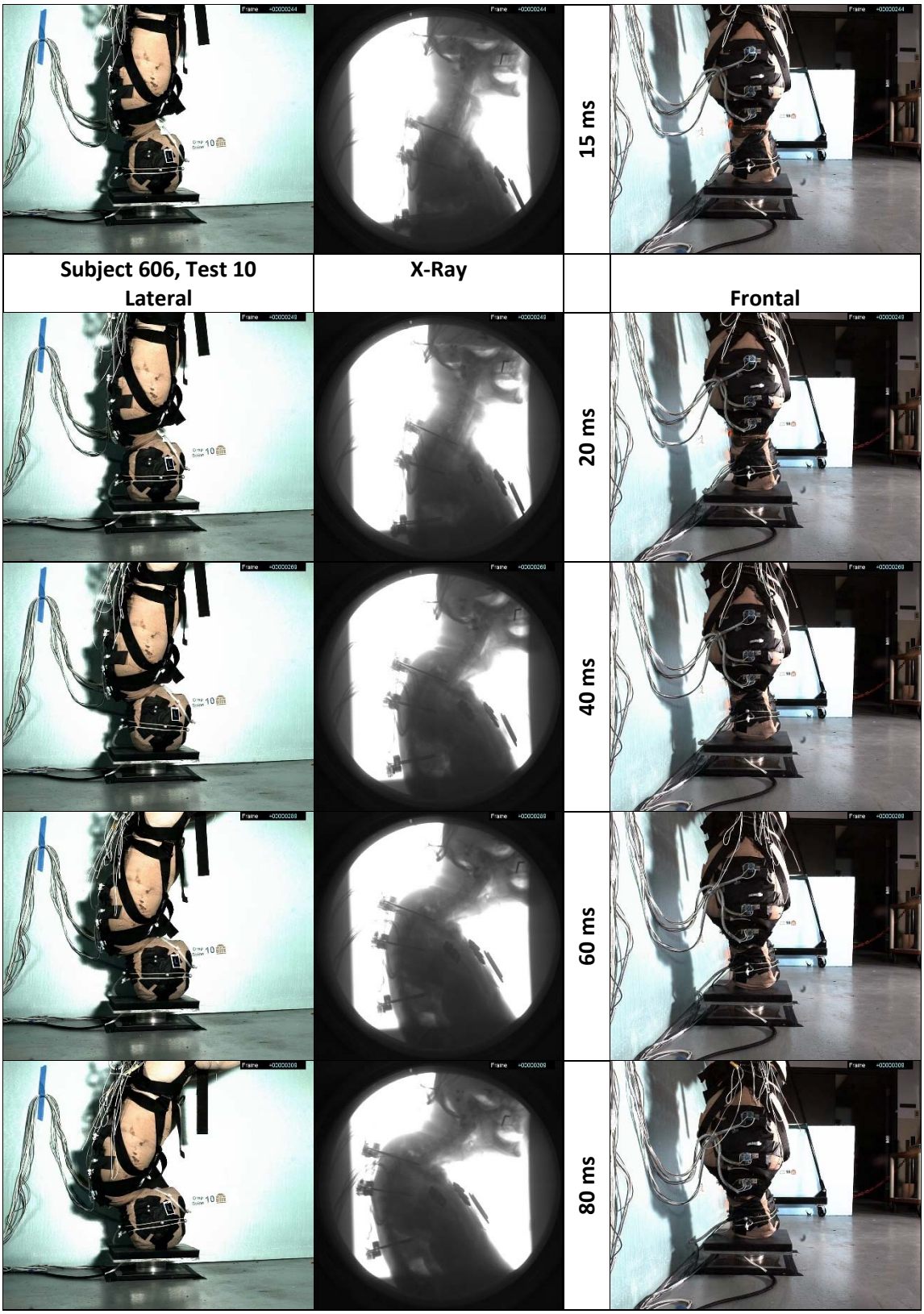
Subject 606, Test 10
Lateral
X-Ray
Frontal
15 ms
20 ms
40 ms
60 ms
80 ms

| Subject 606, Test 11 Lateral | X-Ray | | Frontal |
|---|---|---|---|
| 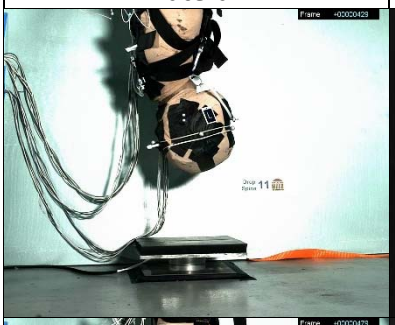 | | -50 ms | 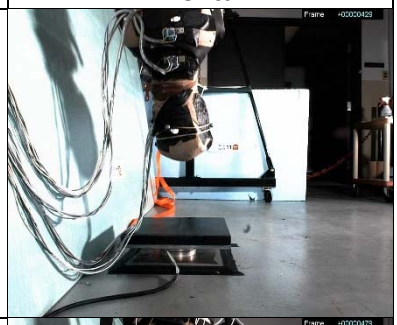 |
| | | 0 ms (contact) | |
| | | 5 ms | 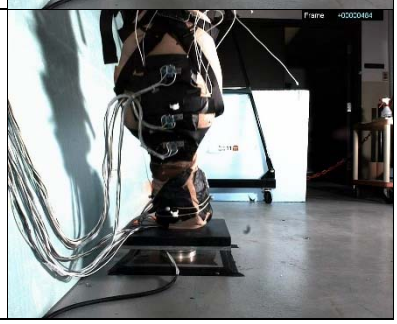 |

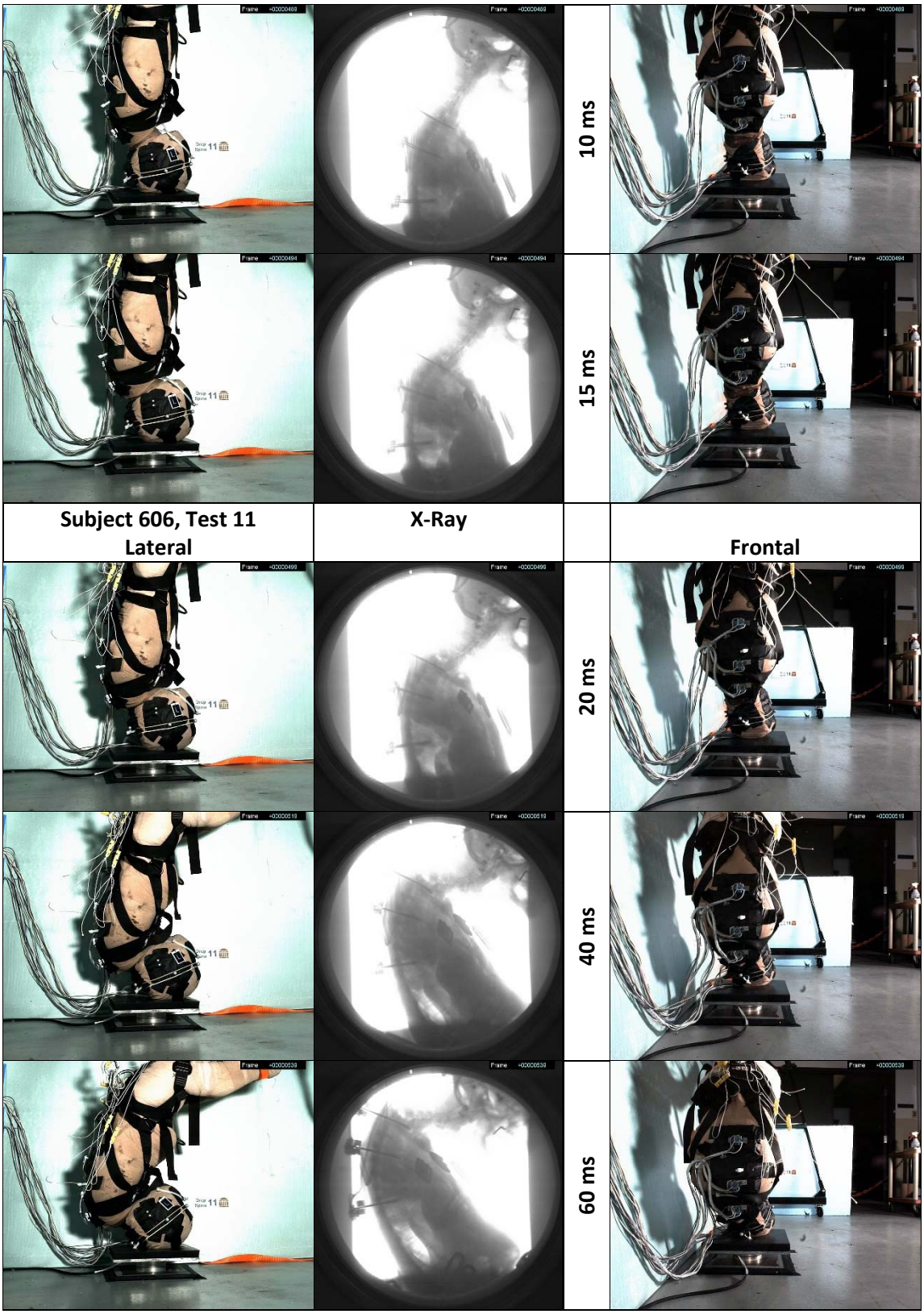
10 ms
15 ms
Subject 606, Test 11
Lateral
X-Ray
Frontal
20 ms
40 ms
60 ms

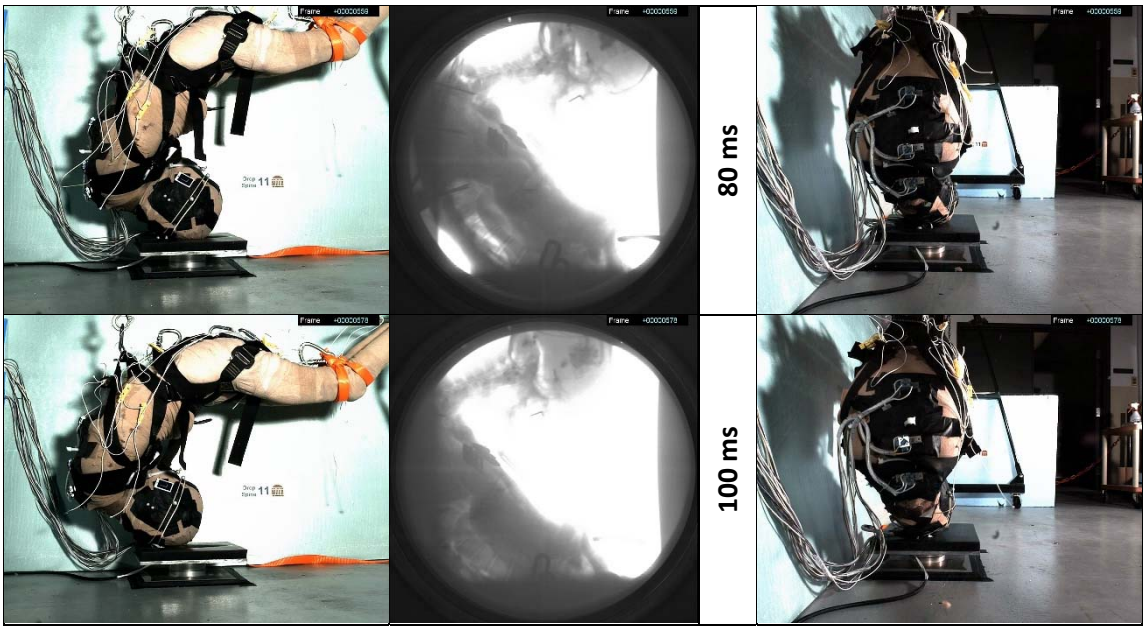
80 ms
100 ms

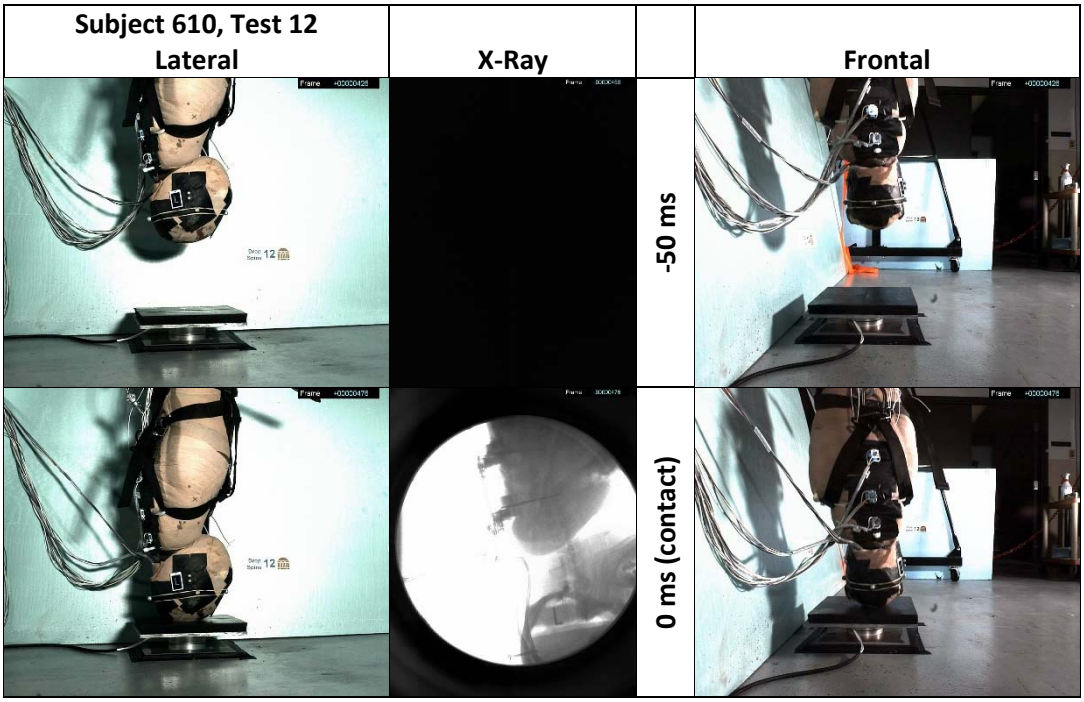
Subject 610, Test 12
Lateral
X-Ray
Frontal
-50 ms
0 ms (contact)

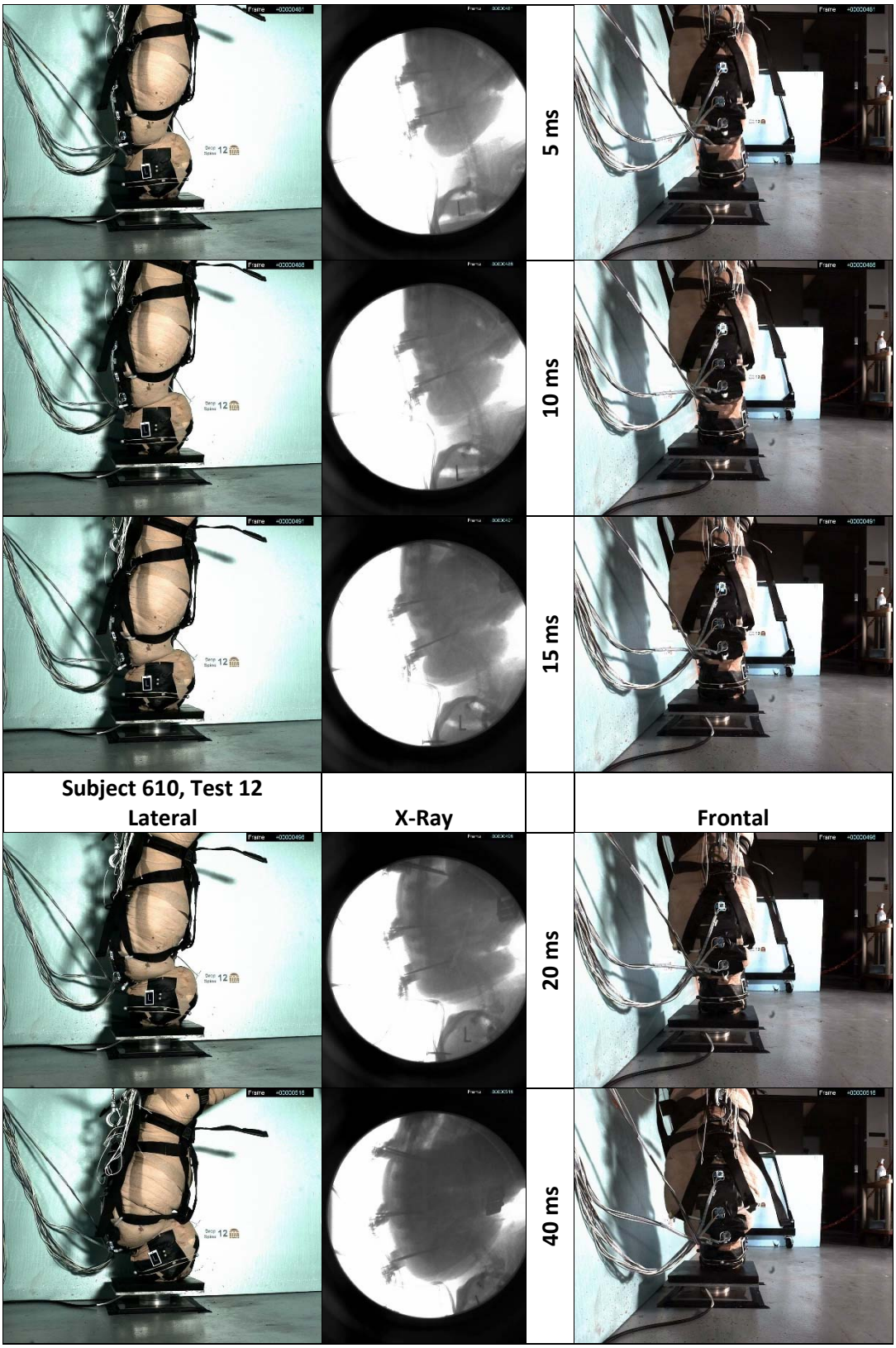
5 ms
10 ms
15 ms
Subject 610, Test 12
Lateral
X-Ray
Frontal
20 ms
40 ms

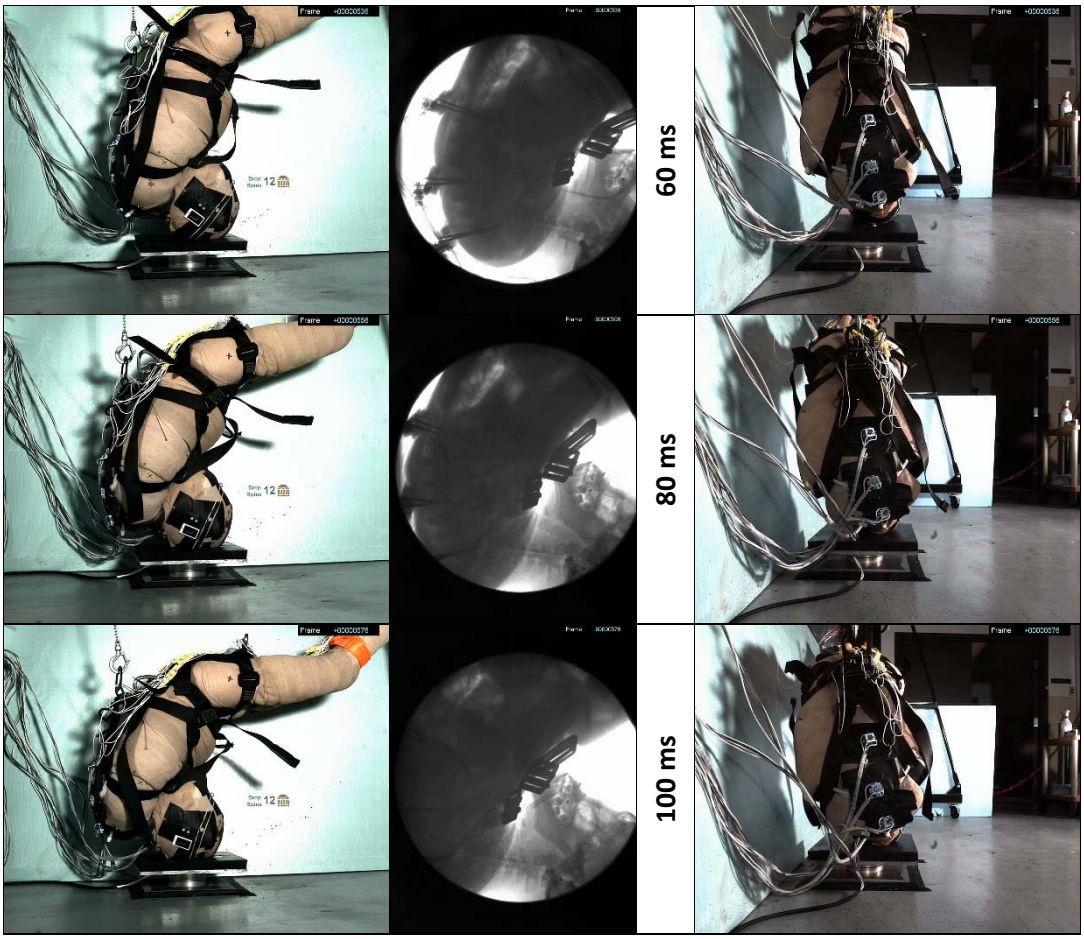


| Subject 693, Test 13 Lateral | X-Ray | | Frontal |
|---|---|---|---|
| 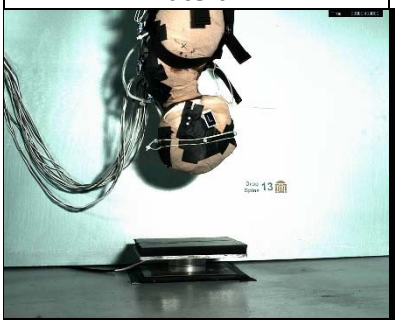 | 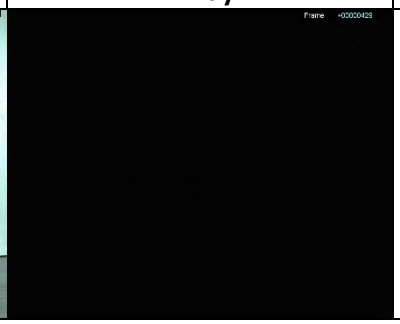 | -50 ms | 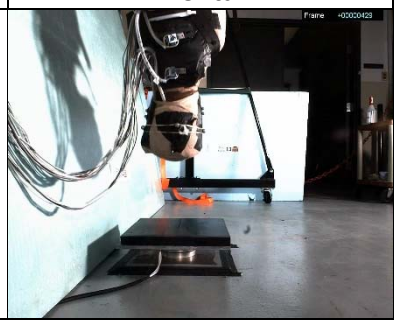 |

0 ms (contact)
5 ms
10 ms
15 ms
20 ms
Subject 693, Test 13
Lateral
X-Ray
Frontal

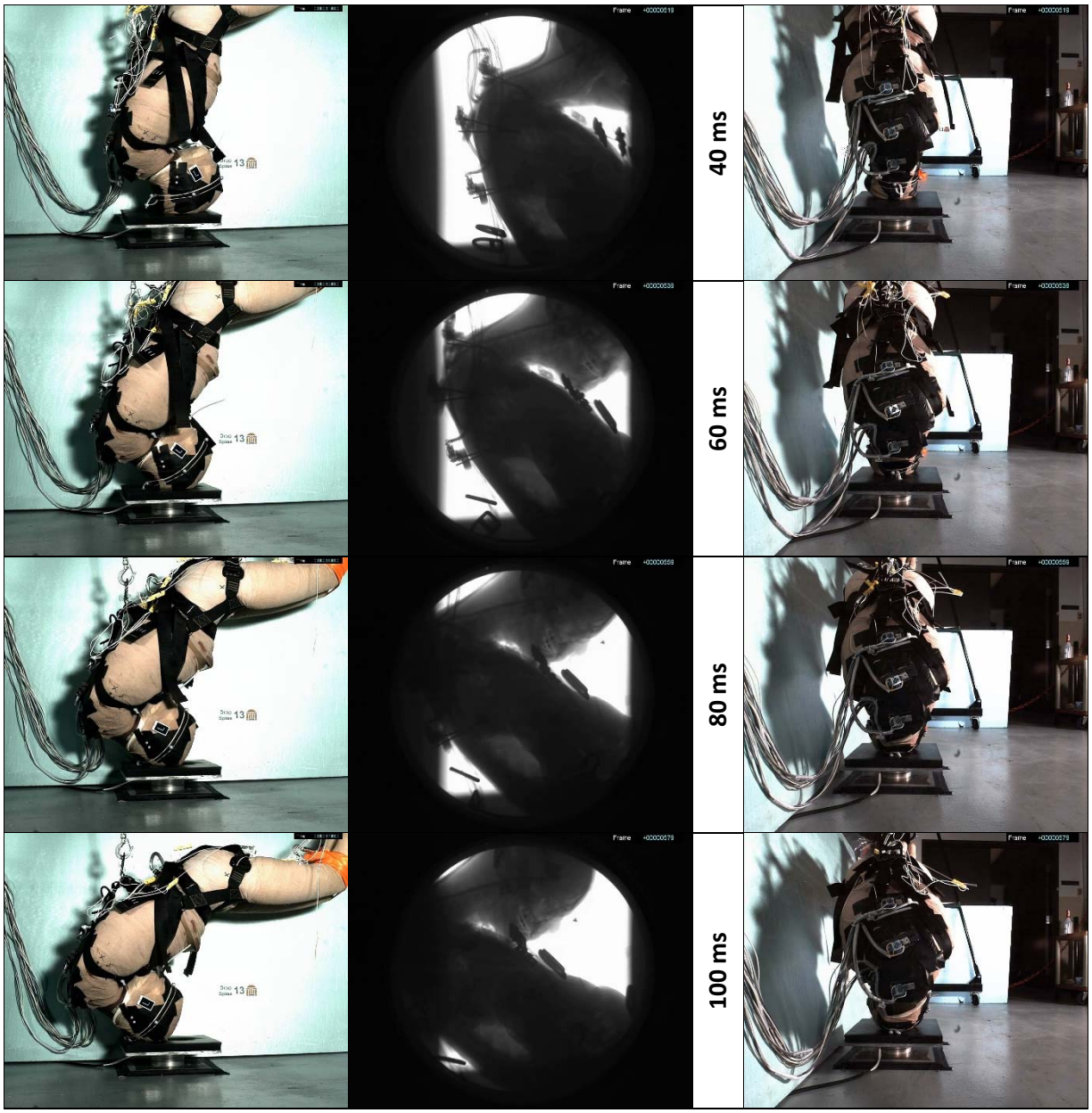
40 ms
60 ms
80 ms
100 ms

# COMPARISON OF HIC AND BrIC HEAD INJURY RISK IN IIHS FRONTAL CRASH TESTS TO REAL-WORLD HEAD INJURIES

**Becky Mueller**
**Anna MacAlister**
**Joe Nolan**
**David Zuby**
Insurance Institute for Highway Safety
United States

Paper Number 15-0272

## ABSTRACT

The Insurance Institute for Highway Safety (IIHS) has been measuring head injury criterion (HIC), a measure based on linear impact skull fracture data, to assess head injury risk in its front crash tests since 1995. In 2012, IIHS added instrumentation to measure brain injury criterion (BrIC), a rotationally based injury measure derived from animal data correlated to humans through computational modeling. BrIC is intended to complement HIC rather than replace it. Head injury risk associated with HIC and BrIC values measured with a Hybrid III dummy in 138 front crash tests was compared with real-world injury rates in similar frontal crash configurations calculated from the National Automotive Sampling System Crashworthiness Data System (NASS CDS) database.

NASS CDS identified 1.3-5 percent AIS3+ head injury rates in crashes similar to the test configurations. The mechanisms of injury represented by HIC and BrIC are a subset of all head injuries; therefore, the NASS-indicated head injury rates inherently may be an overprediction of injuries directly applicable to these formulas. In crash tests, HIC AIS3+ head injury risk ranged 0-22 percent and BrIC AIS3+ head injury risk ranged 3-85 percent. BrIC AIS3+ head injury risk greater than 50 percent was associated with a variety of head kinematic events including front airbag loading, head contact with instrument panel, and non-contact forward excursion.

The published injury risk curve for BrIC indicates that crash tests represent significantly higher serious head injury risk than observed in real-world crashes of similar configurations. Hybrid III may produce exaggerated measures of BrIC or, if accurate, the BrIC formula may need to be reexamined against the underlying animal test data to determine the limitations of BrIC, and the proposed injury risk curves need to be re-evaluated against real human injury risk. Despite its origins as an indicator of skull fracture risk, the range of HIC-based head injury risk observed in crash tests more closely reflects the real-world head injury rates than the range of BrIC-based head injury risk.

## INTRODUCTION

According to the U.S. Centers for Disease Control and Prevention, 17 percent of all traumatic brain injury (TBI) is caused by traffic crashes, and these have the highest proportion leading to death of all causes of TBI (Faul et al., 2010). Not only are motor vehicle crashes a frequent source of TBI, but TBI is a frequent outcome of crashes and the number of fatalities attributable to these injuries is second behind injuries of the chest (Eigen and Martin, 2005). This is the case despite great progress at reducing the risk of head injuries in crashes. Front airbags have been associated with a 29 percent reduction in the risk of head injury in front crashes (Kahane, 2015). Side airbags with head protection reduce the odds of dying in side crashes by 37 percent (McCartt and Kyrychenko, 2007). Nevertheless, it has been suggested that head injury risk in crashes has been increasing during the past decade (Takhounts et al., 2013).

In modern passenger vehicles, airbags provide the principal means of protecting the head from impacts with the vehicle interior because such impacts are possible even when seat belts are used. Canadian Motor Vehicle Safety Standard No. 208 limits linear acceleration of the head in crash tests with belted dummies as a way of ensuring that

passenger vehicles will be fit with airbags to protect a driver's head from impact against the steering wheel (Transport Canada, 2011). Similarly, linear accelerations of the head are limited in U.S. regulatory crash tests by requiring that the head injury criterion (HIC) remain below 1000 in unbelted front crash tests with both belted and unbelted dummies, in addition to side crashes against a rigid pole targeted at the dummy's head (Office of the Federal Register, 2011a, 2011b). HIC essentially is a measure of the linear impulse of the head's motion during a crash. It is largely based on the Wayne State Tolerance Curve (WSTC), which described a set of head impact experiments relating accelerations of cadaver skulls to the onset of skull fractures (Lissner et al., 1960, Society of Automotive Engineers, 1980). Skull fracture was used as an indicator of brain injury because a large proportion of people suffering fractures also are concussed (Melvin et al., 1993). Since its adoption as a regulatory limit in motor vehicle safety standards, HIC has been related to the risk of severe brains injuries — 4 and greater on the Abbreviated Injury Scale (AIS) — through the analyses of additional experiments with human surrogates (Mertz et al., 1996). Despite its widespread use for evaluating head injury risk in regulatory and consumer information crash tests, studies continue to reiterate that HIC was not developed as a comprehensive predictor of all head injuries, but rather an indication of translational-based skull fracture injuries involving impacts and not rotational-based injury mechanisms (Digges, 1998; Hess et al., 1980; Prasad and Mertz, 1985).

Head injuries remain a lingering concern to be addressed by further improvements in vehicle crashworthiness. Even among vehicle designs earning good ratings in the Insurance Institute for Highway Safety's (IIHS) moderate overlap front crash test, the head is the second most common seriously injured body region in front crashes (Brumbelow and Zuby, 2009). These head injuries often occurred in crashes with large deformations of the safety cage, but also were observed in crashes during which the safety cage remained largely intact, thereby suggesting a failure of the restraint system to protect the head from injury.

The IIHS small overlap front crash test illustrates one possible means by which occupants' heads are injured in front crashes of vehicles judged to provide good head protection. Especially in cases with large safety cage deformations, the dummy's head sometimes slides past the front airbag and impacts directly against the door, A-pillar, or instrument panel. This head injury mechanism also has been documented in real crashes (IIHS, 2012; Sherwood et al., 2009). HIC values in small overlap front crash tests with head impacts against the vehicle interior, however, indicate a relatively low risk of serious head injury, with values ranging from 82 to 651 and representing an AIS 3+ injury risk of essentially 0-14 percent. Observations like these raise the question about whether HIC is completely measuring TBI risk in crash tests.

Since the earliest studies of the biomechanics of brain injury, rotational motion of the head also has been hypothesized to create stresses and strains in the brain that manifest as the injuries observed in motor vehicle crashes (Melvin et al., 1993). Considerable effort has been expended on understanding the relationship between rotational movement of the head and TBI, but none have been widely employed in crash testing (Kimpara and Iwamoto, 2012; Kimpara et al., 2011, Newman et al., 2000). Recently, a measure of both linear and rotational accelerations has been developed for evaluating concussion risk in sports helmet testing (Rowson and Duma, 2012).

The National Highway Traffic Safety Administration (NHTSA) also has developed a brain injury criterion (BrIC) based on head rotational velocity that could be used in conjunction with HIC for a more complete evaluation of TBI risk in crash tests (Takhounts et al., 2011; Takhounts et al., 2013). The basis for BrIC is its correlation with measurements of strain in finite element (FE) brain models subjected to impacts. Specifically, maximum principal stress (MPS) and cumulative strain damage metric (CSDM) were highly correlated with BrIC when the measured head kinematics from head impact tests and crash tests were used as inputs to FE brain models. Both MPS and CSDM were related to AIS 4+ brain injury risk using data from animal experiments. The motions of the animals' head in these experiments were scaled to account for differences in size between the animal and human brains and then used as inputs to the FE brain models. Thus, the validity of BrIC as an indicator of human brain injury risk in crash tests depends on the validity of the scaling methods and the similarity of the head motions in the animal experiments to those experienced by occupants in motor vehicle crashes.

At least two studies have attempted to compare TBI risk predictions from crash tests with real-world injury experience. Prasad et al. (2014) found that BrIC values from NHTSA's oblique frontal crash tests estimate higher AIS 3+ brain injury risks compared with the actual rate of injury in similar real crashes. On average, BrIC values in NHTSA's crash tests suggest that the AIS 3+ injury risk was greater than 50 percent, compared with the real-world head injury rates in similar crashes of less than 2 percent. The Center for Applied Biomechanics at the University of Virginia has found that the correlations between BrIC and MPS and CSDM for various simulated tests are different from those reported by Takhounts et al. (2013) (Gabler et al., 2014). Of special concern is that these analyses show BrIC values from experimental pedestrian crashes indicate a 50 percent risk of AIS 2+ brain injury before the dummy's head impacts the vehicle, which seems an unrealistic assessment of pedestrian head injury risk.

## OBJECTIVE

The objective of this study is to expand the comparison of head injury risk predicted by BrIC in crash tests with real-world injury rates in similar crash configurations. In particular, injury risk based on HIC and BrIC measured with a Hybrid III dummy in IIHS moderate and small overlap front crash tests are compared with real-world head injury rates in similar frontal crashes. In addition, several crash tests with indications of possible head injury risks are examined in detail to ascertain the extent to which BrIC augments the evaluation of these risks provided by HIC.

## METHODS

### Crash Test Data

IIHS has conducted standardized moderate overlap front crash tests since 1995 and standardized small overlap front crash tests since 2012 as part of its crashworthiness evaluation program. The moderate overlap test involves crashing a new vehicle into a deformable barrier at 64 km/h with 40 percent of the vehicle's width on the driver side aligned with the barrier. The small overlap test also is conducted at 64 km/h but involves aligning 25 percent of the vehicle's width with a rigid barrier. In both tests, a midsize male Hybrid III dummy is seated in the driver seat. Detailed test protocols are available from the IIHS website (iihs.org).

Since 2012, driver dummies in IIHS moderate and small overlap tests have been equipped with sensors to measure the rotational movement of the head. Specifically, an orthogonal array of three angular rate sensors measures the rotational velocity about the head's center of gravity. The resulting dataset includes 17 moderate overlap and 121 small overlap crash tests of 2012-15 model year vehicles from which both HIC and BrIC can be calculated.

HIC is calculated according to Equation 1, where a(t) is the vector resultant linear acceleration at time t and $t_2 - t_1$ is the time interval during the crash that is no longer than 15 ms in duration and that maximizes the expression in brackets. HIC is related to the risk of AIS 4+ injury according to Equation 2 (Mertz et al., 1996) and to the risk of AIS 3+ injury according to Equation 3 (NHTSA, 1995).

(Equation 1): $$HIC_{15} = \left\{\left(\frac{1}{t_2-t_1}\int_{t_1}^{t_2} a(t)dt\right)^{2.5}(t_2-t_1)\right\}_{max}$$

(Equation 2): $$PR_{AIS4+} = Normal\left(\frac{HIC-1434}{430}\right)$$

(Equation 3): $$PR_{AIS3+} = \frac{1}{1+e^{\left(3.39+\frac{200}{HIC}\right)-0.00372*HIC}}$$

Angular velocity measurements are filtered to channel frequency class 60 according to Society of Automotive Engineers recommended practice J211 before calculating BrIC according to Equation 4, where $\omega_i$ is the single absolute value of the maximum magnitude velocity measurement about the $i^{th}$ axis

(x, y, z corresponding to posterior-anterior, laterally to the right, superior-inferior directions) during the test. BrIC is related to the risk of brain injury according to Equations 4 and 5 (Takhounts et al., 2013).

(Equation 3): $BRIC = \sqrt{\left(\frac{\omega_x}{66.25_{rad}}\right)^2 + \left(\frac{\omega_y}{56.45_{rad}}\right)^2 + \left(\frac{\omega_z}{42.87_{rad}}\right)^2}$

(Equation 4): $PR_{AIS3+} = 1 - e^{-\left(\frac{BRIC}{0.987}\right)^{2.94}}$

(Equation 5): $PR_{AIS4+} = 1 - e^{-\left(\frac{BRIC}{1.204}\right)^{2.94}}$

**Real-World Head Injuries**

Cases of real-world front crashes were obtained from the National Automotive Sampling System Crashworthiness Data System (NASS CDS) crash data collection program conducted and maintained by NHTSA. The NASS CDS sample contains more detail than is available from police crash reports because investigators visit the crash site, examine the vehicles involved, and collect injury data from hospital or coroner reports. The sample is intended to be representative of all tow-away crashes occurring in the United States. The total number of crashes investigated ranged from 4,000 to 5,600 during 2004-12, the years used in the study. Each case is assigned a sample weight, based on its likelihood of being investigated, that scale the individual crash observations to nationwide estimates.

The sample of NASS CDS crashes used in this study were intended to include damage and occupant patterns similar to IIHS small and moderate overlap test configurations. Consequently, only passenger vehicles (body type = 1-49) from model years 2000 and later that received a good rating in the IIHS moderate overlap test were included. Further restricting the case model year range to correspond exactly with the crash test model years (2012-15) likely would have yielded too few crashes for analysis. A broader group of front-damaged vehicles were chosen based on NASS classifications, and damage photographs were used to further categorize which cases reflect patterns similar to crash tests. Front crashes were identified as having damage to the frontal plane in the principal impact according to the crash deformation classification (CDC) as well as a principal direction of force (PDOF) between 30 degrees left of center and 30 degrees right of center. To further ensure the sample consisted of vehicles with damage similar to the crash tests, only vehicles with a vertical distribution of damage extending from the bumper to level of the hood were included. Thus, vehicles that underrode their crash partner or had significant damage to the undercarriage were excluded. Additionally, only vehicles with extent-of-damage classification of 3 or greater were included, as this is typical of the damage observed in the comparison crash tests. Vehicles involved in a rollover or fire were excluded because of the difficulty in identifying injury mechanisms. Finally, only drivers who were using lap/shoulder belts and not ejected from the vehicle were examined.

After obtaining the 880 cases meeting the NASS coding criteria, all remaining assessments of crash configurations and severity were based on photographs of vehicle damage. Vehicles with damage originating from the right side of the vehicle (right offset), both frame rails significantly engaged (full overlap), or narrow center damage were excluded because of their dissimilarity to comparison crash tests. Small or moderate overlap configurations were defined based on the extent to which the left longitudinal frame rail was engaged in the crash. If the left frame rail was not engaged or only minimally so, the subject vehicle was classified as having small overlap damage; if only the left frame rail was significantly

damaged, then the vehicle was classified as having moderate overlap damage. Severity, classified as less than, equal to, or greater than crash tests, was determined by comparing case photographs of exterior damage extent to example crash test photos of damage representing similar vehicles.

Crashes meeting the criteria for small and moderate overlap configurations, including an AIS 3+ head injured driver, were examined in detail to collect specific information about the injuries including their possible causation. Photographic evidence, medical records, and investigator notes were used to determine evidence of head contact with interior components.

## RESULTS

### Real-World Crashes

There were 880 frontal crashes involving good-rated passenger vehicles from model years 2000 and later. Of these, 343 cases (86,389 weighted) were determined to be small or moderate overlap configurations with damage offset to the driver side. There were no drivers with AIS 3+ head injuries in moderate and small overlap front crashes that were less severe than the IIHS tests in this sample; therefore, lower severity crashes were excluded from in-depth analysis. The final sample included 168 cases (17,276 weighted) of small or moderate overlap configurations with damage offset to the driver side at equal or greater severities. Most of the cases were of similar severity to the corresponding IIHS crash test, as the distribution of cases by severity and damage shows (Figure 1). Of these 168 cases, 51 drivers had a head injury of any severity. The distribution by AIS severity level of the most severe head injuries for these 51 drivers is shown in Figure 2. Among the crashes with driver head injuries at the AIS 3+ level, most were more severe than their corresponding IIHS crash test (Figure 3). Appendix A contains details about the head injuries for each of the 17 drivers injured at the AIS 3+ level.

Table 1 shows head injury rates (weighted data) for drivers exposed to front left offset crashes that were at least as severe as IIHS tests. The risk of sustaining a serious head injury is greater in front crashes with small overlap damage than those with moderate overlap damage. The AIS 4+ risk is lower than the AIS 3+ injury risk, but the difference is proportionally smaller among small overlap crashes. There were five drivers with skull fractures resulting in fracture rates (weighted data) of 0.2 and 0.9 percent for moderate and small overlap crashes, respectively. Two other drivers, both in moderate overlap crashes, had fractures limited to the facial bones.

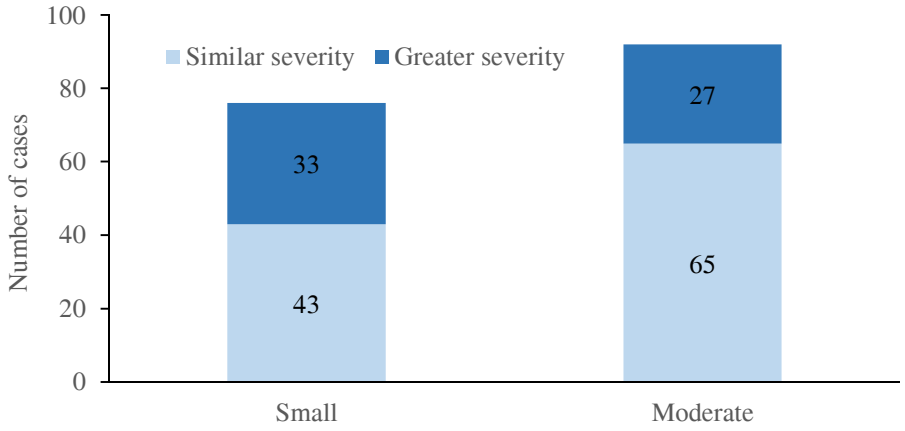


***Figure 1. Case distribution.***

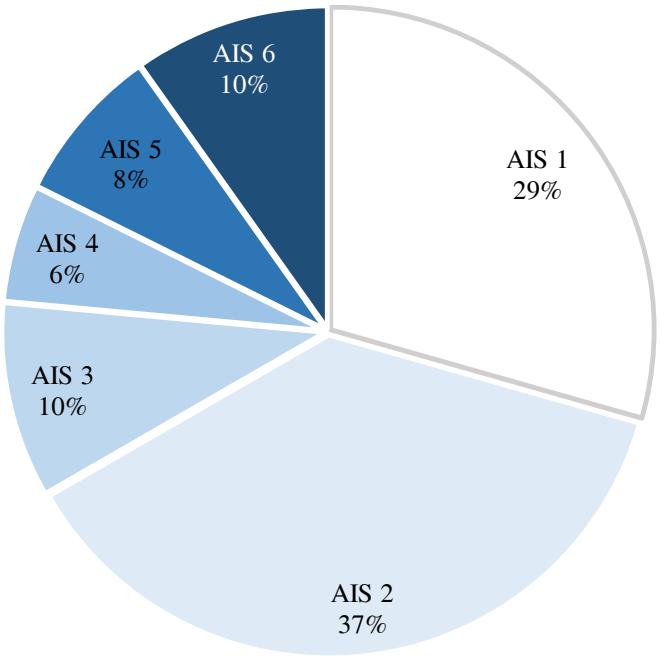


***Figure 2. Distribution of head injury severity for 51 head-injured drivers.***

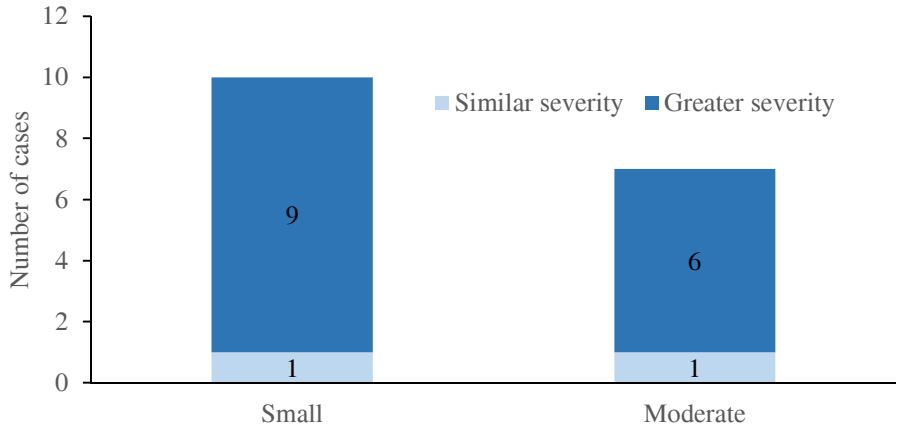


***Figure 3. Head injured cases.***

**Table 1.**
**Head injury rates for real-world crashes of equal or greater severity as IIHS tests.**

| | Moderate overlap (10,027) | Small overlap (7,249) |
|---|---|---|
| Skull fracture | | |
| Cases (weight) | 2 (21.84) | 3 (67.29) |
| Rate | 0.2% | 0.9% |
| AIS 3+ | | |
| Cases (weight) | 7 (117.21) | 10 (330.8) |
| Rate | 1.2% | 4.6% |
| AIS 4+ | | |
| Cases (weight) | 5 (67.11) | 7 (247) |
| Rate | 0.7% | 3.4% |

It is likely that the heads of all of the drivers injured at the AIS 3+ level made at least minimal contact with the driver airbag. Examination of the vehicle photographs, consideration of documented external injuries to the face and head, along with investigator-coded contact sources suggested that 10 of these drivers' heads also likely contacted some part of the vehicle interior other than the airbag — four in moderate overlap crashes and six in small overlap crashes. The other seven drivers' heads also may have contacted something besides the airbag, as the lack of contact evidence does not preclude its possibility.

**Crash Tests**

Table 3 shows the range and the average of HIC and BrIC values for each sample of crash tests. Appendix B contains details about the HIC and BrIC values calculated for each of the 128 crash tests. On average, HIC values were greater in moderate overlap crashes, but the highest HIC values were measured in small overlap tests. The average BrIC values were similar from the two different crash tests and, again, the highest measures were recorded in small overlap tests. Table 4 shows the average estimated injury risks associated with these measures. For both injury severity levels and both crash types, BrIC indicates a much higher risk of brain injury than HIC. BrIC suggests that the AIS 3+ injury risk is 6.5-13 times greater than predicted by HIC, and the AIS 4+ injury risk is 40-67 times greater than indicated by HIC. BrIC suggests that serious brain injury risks are greater in small overlap than moderate overlap crashes, while HIC suggests the opposite. Not surprisingly, HIC and BrIC are not highly correlated, as shown in Figure 4, although they are more so in small overlap than moderate overlap crash tests.

**Table 3.**
**HIC and BrIC: Moderate (n=17) and small overlap (n=121) front crash tests at 64 km/h.**

| | HIC | | BrIC | |
|---|---|---|---|---|
| | Moderate | Small | Moderate | Small |
| Minimum | 116 | 39 | 0.43 | 0.3 |
| Average | 259 | 173 | 0.64 | 0.69 |
| Maximum | 459 | 651 | 0.88 | 1.24 |

**Table 4.**
**Average brain injury risk based on HIC and BrIC measured in crash tests at 64 km/h.**

| | Skull/facial fracture risk | AIS 3+ risk | | AIS 4+ risk | |
|---|---|---|---|---|---|
| | HIC | HIC | BrIC | HIC | BrIC |
| Moderate overlap crash test (n=17) | 0.6% | 4.1% | 27% | 0.4% | 16% |
| Small overlap crash test (n=121) | 0.1% | 2.5% | 32% | 0.3% | 20% |

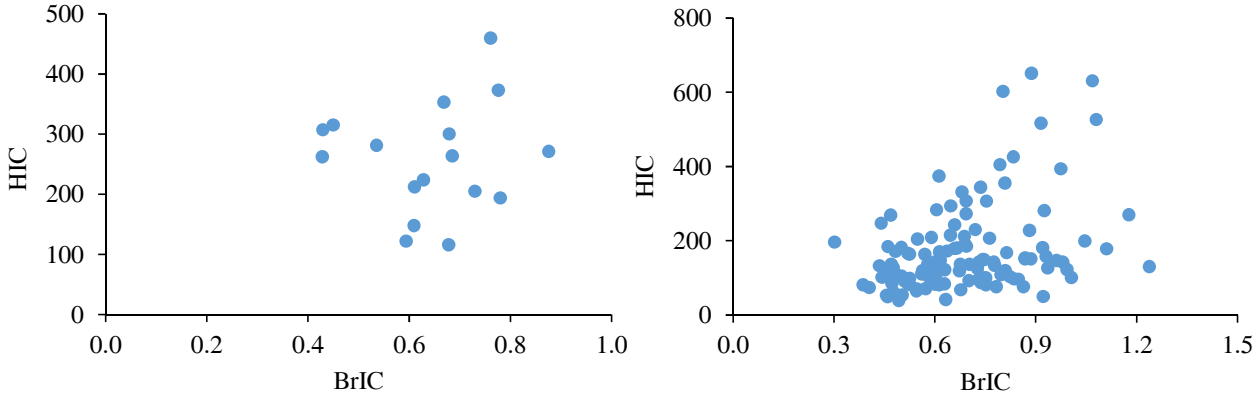


***Figure 4. HIC and BrIC values for moderate (left) and small overlap (right) crash tests.***

Associating HIC and BrIC with kinematic events provides some insight into the specific brain injury risks highlighted by each measure. Small overlap crash tests were used for this analysis because the moderate overlap tests lack the camera coverage necessary to identify kinematic events of the head. Three classes of events were defined for this analysis: airbag contact, hard contact, and unrestrained head motion. The HIC timeframe always encompassed the main contributing event, but choosing a contributing event for BrIC was not always straightforward, as each of the three peak rotational velocities may occur at different times during the crash. An approximate way of identifying the kinematic event most responsible for a particular BrIC value consists of using the event associated with the greatest peak. Ninety percent of tests had at least two components of BrIC occurring during the same event. Table 5 shows the HIC and BrIC values associated with three classes of kinematic events. The lowest values for HIC and BrIC were measured while the head was in contact with the airbag. The highest values for BrIC also occurred as a result of airbag contact, while the highest values for HIC occurred when the head impacted some interior surface other than the airbag. On average, HIC also was higher from hard contacts than the other classes of head motion. Free forward motion of the head after it slid off the airbag, on average, was associated with higher BrIC values than either contact with the airbag or hard interior surfaces.

**Table 5.**
**HIC and BrIC values for different kinematic events in 64km/h small overlap front crash tests.**

| | HIC | | | BrIC | | |
|---|---|---|---|---|---|---|
| | Airbag | Unrestrained motion | Hard contact | Airbag | Unrestrained motion | Hard contact |
| Minimum | 39 | 54 | 42 | 0.3 | 0.53 | 0.47 |
| Average | 163 | 172 | 205 | 0.66 | 0.77 | 0.72 |
| Maximum | 527 | 426 | 651 | 1.24 | 1.07 | 0.89 |

A close examination of 10 crash tests where the HIC timeframe included significant head impacts other than with the inflated airbag offers further insight into the ability of BrIC to augment the assessment of head injury risk based on crash tests. Table 6 shows the HIC and BrIC values, times associated with the three BrIC components, and non-airbag impacts between the dummy's head and vehicle interior. In all cases, the HIC time interval (not shown) includes the interior impact of interest. As before, HIC and BrIC are not highly correlated (0.24) (Figure 5) and, in every case, BrIC indicates a higher risk of AIS 3+ injury than HIC, with BrIC risk assessment ranging 2.4-58 times higher than HIC. In five tests, the greatest contributor (largest component peak) to BrIC occurs at a time greater than 4 ms from the impact highlighted within the HIC timeframe; therefore, BrIC cannot be associated with that impact. The correlation between HIC and BrIC among the remaining five tests is 0.60 (Figure 5), with BrIC indicating a risk ranging 2.2-23 times higher than HIC.

The sensitivity of HIC and BrIC to vehicle design changes was examined from comparison tests of three models that were redesigned or modified to improve small overlap front crashworthiness. The Mazda 6 was first evaluated for small overlap crashworthiness in model year 2012, and the full-model redesign was evaluated in model year 2014. In both tests, the Mazda 6 overall rating was acceptable. However, the earlier model received a restraints and kinematics score of marginal because the dummy's head slid off the driver airbag and impacted the door sill. The HIC in this test was 148, low enough that head protection was rated good. The full-model redesign in 2014 also received an acceptable overall rating even though the dummy's head remained in contact with the airbag during its forward excursion. Unfortunately, the head struck the steering wheel through the airbag, resulting in a HIC of 331, which was

**Table 6.**
**HIC and BrIC timing related to hard contacts.**

| Vehicle | Test ID | Hard contact source | Hard contact time | HIC | AIS 3+ | BrIC | AIS 3+ | BrIC peak component times x | y | z |
|---|---|---|---|---|---|---|---|---|---|---|
| 2012 Mazda 6 | CEN1220 | Door sill | 124 | 148 | 1% | 0.62 | 23% | 174 | **120*** | 135 |
| 2014 Mazda 6 | CEN1305 | Steering wheel through airbag | 122 | 331 | 6% | 0.68 | 29% | 139 | **124*** | 131 |
| 2014 Kia Forte | CEN1318 | Instrument panel | 122 | 355 | 7% | 0.81 | 43% | 176 | **110*** | 77 |
| 2013 Toyota RAV4 | CEN1319 | Instrument panel | 120 | 283 | 5% | 0.60 | 22% | 125 | **129*** | 132 |
| 2013 Toyota Prius C | CEN1328 | Instrument panel | 119 | 426 | 9% | 0.83 | 46% | 82 | **119*** | 84 |
| 2013 Toyota Yaris | CEN1331 | Instrument panel | 137 | 127 | 1% | 0.94 | 58% | 146 | **139*** | 122 |
| 2014 Ford Fiesta | CEN1343 | Instrument panel | 108 | 509 | 13% | 0.80 | 43% | 123 | **111*** | 87 |
| 2014 Fiat 500L | CEN1414 | A-pillar | 101 | 228 | 3% | 0.88 | 52% | 108 | 108 | **105*** |
| 2015 Hyundai Sonata | CEN1427 | Steering wheel through airbag | 105 | 405 | 8% | 0.79 | 42% | 123 | 109 | **115*** |
| 2015 Honda Fit | CEN1430 | Steering wheel through airbag | 87 | 651 | 22% | 0.89 | 52% | 102 | **92*** | 88 |

*Maximum individual component

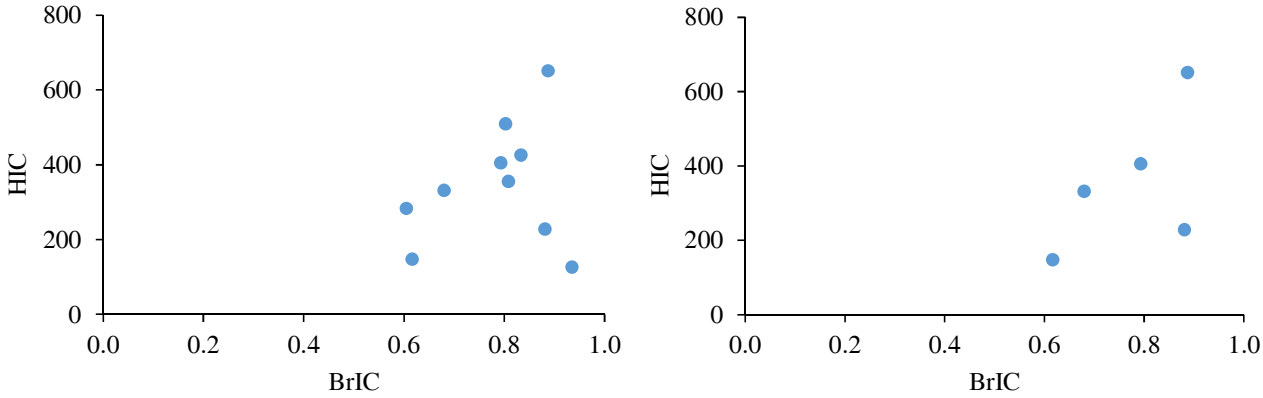


***Figure 5. Correlation of HIC and BrIC in all tests with head contacts (left) and tests where HID and BrIC both associated with hard contact (right).***

higher than in the test of the earlier design, and head protection was downgraded to acceptable because of a peak acceleration of 108 g despite the improved restraints and kinematics rating. The BrIC values for the two tests were similar, 0.62 and 0.68, despite differences in the head motions between tests.

The 2013 Honda Fit was rated poor overall because its safety cage collapsed in the small overlap test and the dummy's head struck the instrument panel after sliding off the airbag. This impact was associated with a HIC of 517, but the BrIC (0.92) recorded in this test was due to head motion occurring beforehand. The 2015 model was rated acceptable in the small overlap test, largely due to a greatly improved safety cage. However, the dummy's head struck the steering wheel through the airbag, resulting in a HIC of 651 and a BrIC of 0.89.

The Toyota RAV4 was first tested in model year 2013, receiving a poor overall rating, and then tested again in model year 2015 after it had been modified for better small overlap crashworthiness. In the test of the 2013 model, the dummy's head slid off the airbag and impacted against the instrument panel,

producing a HIC of 283 and a BrIC of 0.60. The modified design earned a good overall rating due largely to a stronger safety cage. In addition, the head impact against the instrument panel was eliminated, resulting in a lower HIC of 163 associated with the head's interaction with the airbag and a BrIC of 0.57.

Head impacts with the steering wheel through the airbag in tests of the 2015 Honda Fit and 2014 Mazda 6 were identified by HIC as more risky than impacts against the instrument panel and doorsill in the earlier models of each; however, the assessment of risk by BrIC was only slightly different between the newer and older designs. Similarly, HIC values suggest brain injury risk was halved with the modifications implemented in the 2015 RAV4 compared with the 2013 model, but the BrIC risk assessment was similar between the two designs.

## DISCUSSION

BrIC values measured in IIHS frontal offset crash tests estimated a much larger risk of brain injury than observed in real crashes with similar offset crash damage and at least the same damage extent. This overestimation is larger for moderate overlap front crashes (18 times) than small overlap ones (6 times), and about the same for both AIS 3+ and AIS 4+ injury levels. Only 16 of these 139 tests resulted in the dummy's head impacting a hard surface inside the vehicle, indicating that BrIC predicts high levels of serious and severe brain injury risk as a result of contacting only the airbag. This is contrary to the NASS CDS cases examined in this study in which at least 70 percent of those drivers with AIS 3+ brain injuries apparently impacted a hard surface in the vehicle.

HIC values measured in IIHS frontal offset crash tests indicated a much lower risk of serious and severe brain injuries than BrIC (Table 4). With the exception of AIS 3+ injury risk in moderate overlap crashes, these measures suggest a lower risk of brain injury than observed in the NASS CDS crashes with frontal offset crash damage. The estimated AIS 4+ injury risk in small overlap crash tests is less than one-tenth of that observed in real crashes with this damage pattern and at least the same damage extent. Skull fracture risk based on HIC (Mertz et al., 1996) overestimates injury risk in moderate overlap crash tests (0.6 percent) compared with what was observed in the real crash sample (0.2 percent), but the risk in small overlap crash tests (0.4 percent) is lower than that seen in real crashes (0.9 percent), though neither deviates significantly. The underestimation of skull fracture and brain injury risks in these crash tests is understandable given that nearly all of the NASS CDS sample have more damage than the test vehicles. The source of overestimation by BrIC is unknown.

While both BrIC and HIC estimate quite different head injury risks in frontal offset crash tests than observed in similar real crashes, the estimates from HIC are closer to the real injury rates. However, HIC indicates moderate overlap crashes present a higher head injury risk than small overlap crashes, while real crash data indicated higher injury rates in small overlap crashes. The relative risks estimated by HIC may better align with a larger sample of real crashes more comparable with the crash tests; however, it seems unlikely that they would yield brain injury rates as high as the BrIC estimates, as this crash sample included generally more severe impacts than the crash tests.

Even though BrIC appears to correctly assess the relative brain injury risk between these two crash types, it is unknown whether BrIC correctly identifies why small overlap crashes are more injurious. Table 5 shows that the majority of BrIC values were associated with the head's contact with the inflated airbag

and free motion of the head following airbag contact. In contrast, the average and highest values of HIC in these tests were associated with head impacts against hard surfaces in the vehicle interior, which is more consistent with real crash observations. Eight of the 17 NASS CDS cases had drivers with face or skull injuries not likely caused by contacting the inflated airbag or as a result of post-airbag forward motion alone. An additional two drivers were injured in ways that suggest their head's contacted something other than the airbag. The remaining drivers also may have impacted against something hard despite the lack of evidence recorded in the investigation file. It is unclear why BrIC brain injury risk estimates would be higher for seemingly more benign events than the head impacts that produced strong linear accelerations.

The lack of correlation between HIC and BrIC in the full crash test dataset suggests BrIC may be providing different indications of brain injury risk than HIC alone. However, the observations of the kinematic events associated with BrIC raise questions about whether BrIC is accurately identifying injurious events in a given crash test. For the five tests in which both HIC and BrIC could be associated with the same head impacts against the vehicle interior, HIC estimated an AIS 3+ injury risk of 2-20 percent and BrIC estimated a risk of 23-53 percent. While the BrIC estimates of brain injury risk were high relative to real crash injury rates, they may correctly indicate that the head impacts observed in these tests posed a greater brain injury risk than indicated by HIC.

BrIC seems insensitive to changes in vehicle design, while HIC makes distinctions. This is problematic for the process of developing countermeasures that can reduce BrIC in frontal crashes. Some of this insensitivity stems from the possibility that BrIC may be based on measurements from different times and events during the test. Takhounts et al. (2013) state that a time-based calculation of vector resultant rotation velocity did not yield a better correlation with measures of strain in the FE brain models than the formulation used here. As long as the time-based calculation still exhibits a reasonably strong correlation, its use may prove to be a better tool for evaluating head injury risks in crash tests than the version currently considered by NHTSA.

## CONCLUSIONS

Serious and severe brain injury risk estimates from offset crash tests based on BrIC are much higher than injury rates observed in a sample of crashes with similar damage type but greater severity. HIC appropriately estimates lower brain injury risk in tests less severe than real crashes with similar offset damage patterns. When both HIC and BrIC can be associated with the same head impact, the higher risk estimate from BrIC may be an indication that a brain injury risk exists that is not identified by HIC. It is not clear why BrIC predicts such high brain injury risks with contact between the head and airbag or free motion of the head afterward. If accurate, the injuries indicated by BrIC may be difficult to prevent except by reducing crash severity through the application of crash avoidance technologies.

## REFERENCES

Brumbelow ML, Zuby DS. 2009. Impact and injury patterns in frontal crashes of vehicles with good ratings for frontal crash protection. *Proceedings of the 21st International ESV Technical Conference* (CD-ROM) Washington, DC: National Highway Traffic Safety Administration.

Digges KH. 1999. Injury measurements and criteria. Keynote address at the Specialists' Meeting of the RTO Human Factors and Medicine Panel. *RTO Meeting Proceedings 20: Models for Aircrew Safety Assessment: Uses, Limitations, and Requirements*, pp. K2-1-5. Report no. RTO-MP-20. Quebec, Canada: Canada Communications Group Inc.

Eigen AM, Martin PG. 2005. Identification of real world injury patterns in aid of dummy development. Paper no. 05-0219. *Proceedings of the 19th International Technical Conference on the Enhanced Safety of Vehicles*. Washington, DC: National Highway Traffic Safety Administration.

Faul M, Xu L, Wald MM, Coronado VG. 2010. Traumatic brain injury in the United States; Emergency department visits, hospitalizations, and deaths, 2002-2006. Atlanta, GA: Centers for Disease Control and Prevention.

Gabler LF, Panzer MB, Crandall JR. 2014. On the application of BrIC to the biomechanics of various automotive impact scenarios. Presented at the 42nd International Workshop on Human Subjects for Biomechanical Research. San Diego, California.

Hess RL, Weber K, Melvin JW. 1980. Review of literature and regulation relating to head impact tolerance and injury criteria. Report no. UM-HSRI-80-52-l. Ann Arbor, MI: University of Michigan Transportation Research Institute.

Hodgson V, Thomas L. 1972. Effect of long-duration impact on head. SAE Technical Paper 720956. Warrendale, PA: Society of Automotive Engineers.

Insurance Institute for Highway Safety. 2012. Small overlap crashes: New consumer-test program aims for even safer vehicles. *Status Report* 47(6). Arlington, VA.

Kahane CJ. 2015. Lives saved by vehicle safety technologies and associated Federal Motor Vehicle Safety Standards, 1960 to 2012, Passenger cars and LTVs, with reviews of 26 FMVSS and the effectiveness of their associated safety technologies in reducing fatalities, injuries, and crashes. Report no. DOT HS 812 069. Washington, DC: National Highway Traffic Safety Administration.

Kimpara H, Iwamoto M. 2012. Mild traumatic brain injury predictors based on angular accelerations during impacts. Ann Biomed Eng. 40(1):114-26.

Kimpara H, Nakahira Y, Iwamoto M, Rowson S, Duma S. 2011. Head injury prediction methods based on 6 degree of freedom head acceleration measurements during impact. Int J Automot Eng 2:13-19.

Lissner HR, Lebow M, Evans FG. 1960. Experimental studies on the relation between acceleration and intracranial pressure changes in man. Surg Gynecol Obstet. 111:329-38.

McCartt AT, Kyrychenko SY. 2007. Efficacy of side airbags in reducing driver deaths in driver-side car and SUV collisions. Traffic Injury Prevention 8(2):162-170.

Melvin JW, Lighthall JW, Ueno K. 1993. Ch 12. Brain injury biomechanics. *Accidental Injury: Biomechanics and Prevention* (eds Nahum AM, Melvin JW), pp 268-291. New York: Springer-Verlag.

Mertz H, Irwin A. 1994. Brain injury risk assessment of frontal crash test results. SAE Technical Paper 941056. Warrendale, PA: Society of Automotive Engineers.

Mertz H, Prasad P, Nusholtz G. 1996. Head injury risk assessment for forehead impacts. SAE Technical Paper 960099. Warrendale, PA: Society of Automotive Engineers.

National Highway Traffic Safety Administration. 1995. Final economic assessment; FMVSS No. 201 Upper interior head protection. Washington, DC: U.S. Department of Transportation.

National Highway Traffic Safety Administration. 2008. Consumer information; New Car Assessment Program. Docket no. NHTSA-2006-26555. Federal Register 73(134): 40016-40050. Washington, DC: National Archives and Records Administration.

Newman JA, Shewchenko N, Welbourne E. 2000. A proposed new biomechanical head injury assessment function - the maximum power index. Stapp Car Crash J. 44:215-47.

Office of the Federal Register. 2011a. *Code of Federal Regulations*; Title 49 Transportation, Part 571 Federal Motor Vehicle Safety Standards, Standard No. 208 Occupant Crash Protection. Washington, DC: National Archives and Records Administration.

Office of the Federal Register. 2011b. *Code of Federal Regulations*; Title 49 Transportation, Part 571 Federal Motor Vehicle Safety Standards, Standard No. 214 Side Impact Protection. Washington, DC: National Archives and Records Administration.

Prasad P, Dalmotas D, German A. The field relevance of NHTSA's oblique research moving deformable barrier tests. *Stapp Car Crash J*. 58:175-196. Ann Arbor, MI: The Stapp Association.

Prasad P, Mertz HJ. 1985. The position of the United States delegation to the ISO Working Group 6 on the use of HIC in the automotive environment. SAE Technical Paper 851246. Warrendale, PA: Society of Automotive Engineers.

Research and Technology Organization, North Atlantic Treaty Organization. 1999. *RTO Meeting Proceedings 20: Models for Aircrew Safety Assessment: Uses, Limitations, and Requirements*. Report no. RTO-MP-20. Quebec, Canada: Canada Communications Group Inc.

Rowson S, Duma SM. 2013. Brain injury prediction: assessing the combined probability of concussion using linear and rotational head acceleration. Ann Biomed Eng. 41(5):873-82.

Sherwood CP, Nolan JM, Zuby DS. 2009. Characteristics of small overlap crashes. Proceedings of the 21st International Technical Conference on the Enhanced Safety of Vehicles (CD-ROM). Washington, DC: National Highway Traffic Safety Administration.

Society of Automotive Engineers. 1980. Human Biomechanics and Simulations Standards Committee, Standard J885B 198004. Warrendale, PA.

Takhounts EG, Craig MJ, Moorhouse K, McFadden J, Hasija V. 2013. Development of brain injury criteria (BrIC). Stapp Car Crash J. 57:243-66.

Takhounts EG, Hasija V, Ridella SA, Rowson S, Duma SM. 2011. Kinematic rotational brain injury criterion (BrIC). Proceedings of the 22nd International Technical Conference on the Enhanced Safety of Vehicles. Paper No. 11-0263. Washington, DC: National Highway Traffic Safety Administration.

Transport Canada. 2014. Motor Vehicle Safety Regulations; Schedule III: Canada Motor Vehicle Safety Standard No. 208 Occupant Protection in Frontal Impacts. Ottawa, Ontario.

Versace J. 1971. A review of the severity index. SAE Technical Paper 710881. Warrendale, PA: Society of Automotive Engineers.

## Appendix A. Head Injuries

**Table A-1. Real-world head injuries.**

| NASS-CDS case ID | Occupant ID | NASS case weight | Type of overlap | Impact side | Impact severity | Head MAIS | Evidence of head impact: External injuries | Evidence of head impact: Facial/Skull fractures | Evidence of head impact: Vehicle evidence | Number of AIS 3+ head injuries | List of AIS 3+ head injuries (AIS) |
|---|---|---|---|---|---|---|---|---|---|---|---|
| 200549156 | 58681 | 8.113 | Moderate | Near | Greater | 4 | — | — | Makeup on frontal airbag | 2 | R cerebrum hematoma (4), R cerebrum subarachnoid hemorrhage (3) |
| 200849138 | 90861 | 9.584 | Moderate | Near | Greater | 6 | Facial abrasions and contusions | Basilar skull, maxilla, mandible, nasal fractures | Steering wheel bent | 2 | Brain stem laceration (6), basilar skull fracture (4) |
| 200973074 | 102687 | 38.929 | Moderate | Near | Greater | 3 | Scalp and chin contusions | — | Bent steering wheel | 1 | Cerebrum brain swelling/edema (3) |
| 200981154 | 105483 | 27.983 | Moderate | Near | Greater | 4 | Chin laceration | Mandible fracture | Hair evidence on A-pillar | 2 | L cerebrum small hematoma (4), cerebrum brain swelling/edema (3) |
| 201149139 | | 12.26 | Moderate | Near | Greater | 6 | Forehead abrasions | Basilar skull, maxilla, mandible, zygoma fractures | — | 2 | Brain stem laceration (6), basilar fracture (3) |
| 201179125 | | 8.206 | Moderate | Near | Greater | 3 | — | Orbit, nasal fracture | — | 2 | L cerebrum hematoma (3), R cerebrum hematoma (3) |
| 201249063 | | 12.21 | Moderate | Near | Similar | 5 | Scalp contusions | — | — | 3 | Brain stem hemorrhage (5), cerebrum bilateral subdural small hematoma (4), R cerebrum contusion (3) |
| 200473241 | 49180 | 14.998 | Small | Near | Greater | 5 | Whole scalp contusions | Basilar and vault skull, maxilla, nasal, orbit fracture | Blood evidence on steering wheel and airbag | 12 | Multiple vault fractures (3), basilar skull fracture (4), multiple cerebrum hematoma (5,5,5), brain stem (5), cerebrum brain swelling/edema (5), cerebrum laceration (4), cerebrum contusion (3) |
| 200649023 | 68818 | 10.286 | Small | Near | Greater | 6 | Forehead, nose cheek abrasions | Basilar and vault skull | — | 3 | Brain stem laceration (6), basilar fracture (4), vault fracture (2) |
| 200705021 | 74218 | 118.769 | Small | Near | Greater | 6 | Whole face abrasions | Teeth fracture | — | 4 | L cerebrum subarachnoid hemorrhage (3), R cerebrum subdural hemorrhage (4), brain stem transection (6), cerebrum swelling (3) |
| 200943250 | 100508 | 42.007 | Small | Near | Greater | 4 | — | Basilar and vault skull, orbit and nasal fracture | Blood/bio evidence on frontal airbag | 13 | Multiple vault fractures (4), basilar fracture (4), multiple cerebrum subarachnoid hemorrhage (3), hematoma (4,5), contusion (3), brain swelling (5), R-L infarctions (3), brain stem laceration (5) |
| 200949089 | 101901 | 12.488 | Small | Near | Greater | 5 | — | — | Hair evidence on roof rail | 4 | Cerebrum hematoma (5), cerebrum brain swelling/edema (3), cerebrum contusion (3), L cerebrum subarachnoid hemorrhage (3) |
| 200975216 | 103812 | 29.106 | Small | Near | Greater | 3 | — | — | Bent steering wheel rim | 1 | Multiple L cerebrum contusion (3) |
| 200981007 | 105183 | 19.941 | Small | Near | Greater | 6 | — | — | — | 1 | Brain stem laceration associated with spinal cord laceration (6) |
| 200982010 | 105510 | 7.029 | Small | Near | Greater | 3 | — | — | Skin transfer evidence on frontal airbag | 2 | R cerebrum subarachnoid hemorrhage (3), L cerebrum subarachnoid hemorrhage (3) |
| 201206073 | | 28.992 | Small | Near | Greater | 4 | — | — | Bent steering wheel | 4 | R cerebrum subarachnoid hemorrhage (3), L cerebrum subarachnoid hemorrhage (3), cerebrum edema and compression (4), R cerebrum hematoma (3) |
| 200675096 | 71165 | 47.826 | Small | Near | Similar | 3 | Deep scalp laceration | — | Hair and blood evidence on A-pillar | 2 | L cerebrum contusion (3), R cerebrum subarachnoid hemorrhage (3) |

**Appendix B. Crash Test Data**

**Table B-1. Moderate overlap tests.**

| Vehicle model | Test ID | Class | BrIC | AIS 3 BrIC | AIS 4 BrIC | HIC | AIS 3 HIC | AIS 4 HIC | HIC contact source |
|---|---|---|---|---|---|---|---|---|---|
| 2013 Ford Escape | CEF1206 | Small SUV | 0.61 | 23% | 14% | 212 | 3% | 0.2% | Airbag |
| 2013 Dodge Dart | CEF1207 | Small car | 0.63 | 24% | 15% | 224 | 3% | 0.2% | Airbag |
| 2013 Nissan Altima | CEF1208 | Midsize car | 0.61 | 22% | 13% | 148 | 1% | 0.1% | Airbag |
| 2014 Mazda 6 | CEF1301 | Midsize car | 0.68 | 29% | 18% | 116 | 1% | 0.1% | Airbag |
| 2013 BMW X1 | CEF1302 | Small SUV | 0.88 | 51% | 33% | 271 | 4% | 0.3% | Airbag |
| 2013 Buick Encore | CEF1303 | Small SUV | 0.78 | 40% | 25% | 194 | 2% | 0.2% | Airbag |
| 2014 Fiat 500 L | CEF1304 | Small car | 0.68 | 29% | 18% | 300 | 5% | 0.4% | Airbag |
| 2014 Jeep Cherokee | CEF1305 | Midsize SUV | 0.73 | 35% | 21% | 205 | 3% | 0.2% | Airbag |
| 2013 Chevrolet Spark | CEF1306 | Minicar | 0.76 | 38% | 24% | 459 | 11% | 1.2% | Airbag |
| 2014 Maserati Ghibli | CEF1307 | Large car | 0.45 | 10% | 6% | 315 | 5% | 0.5% | Airbag |
| 2014 Mitsubishi Mirage | CEF1308 | Minicar | 0.69 | 30% | 18% | 264 | 4% | 0.3% | Airbag |
| 2014 BMW 2 Series | CEF1401 | Midsize car | 0.59 | 21% | 13% | 122 | 1% | 0.1% | Airbag |
| 2014 Nissan Rogue | CEF1402 | Small SUV | 0.67 | 28% | 17% | 353 | 7% | 0.6% | Airbag |
| 2015 Subaru WRX | CEF1403 | Small car | 0.78 | 40% | 25% | 373 | 7% | 0.7% | Airbag |
| 2014 Ford C-Max | CEF1404 | Small car | 0.43 | 9% | 5% | 307 | 5% | 0.4% | Airbag |
| 2014 Mazda 5 | CEF1405 | Small car | 0.43 | 9% | 5% | 262 | 4% | 0.3% | Airbag |
| 2014 Hyundai Veloster | CEF1406 | Small car | 0.54 | 16% | 10% | 281 | 4% | 0.4% | Airbag |

**Table B-2. Small overlap tests.**

| Vehicle model | Test ID | Class | Delta V | Peak Accel | Vehicle motion | BrIC | AIS 3 BrIC | AIS 4 BrIC | HIC | AIS 3 HIC | AIS 4 HIC | HIC contact source | BrIC contact source |
|---|---|---|---|---|---|---|---|---|---|---|---|---|---|
| 2012 Hyundai Sonata | CEN1219 | Midsize car | 47 | -34 | Translate | 0.99 | 64% | 44% | 123 | 1% | 0.1% | Airbag | Airbag |
| 2012 Mazda 6 | CEN1220 | Midsize car | 41 | -38 | Translate | 0.62 | 23% | 14% | 148 | 1% | 0.1% | IP | IP |
| 2012 Suzuki Kazashi | CEN1221 | Midsize car | 43 | -23 | Translate | 0.58 | 20% | 12% | 104 | 1% | 0.1% | Forward excursion | Forward excursion |
| 2013 Ford Escape | CEN1222 | Small SUV | 48 | -21 | Translate | 0.62 | 23% | 14% | 122 | 1% | 0.1% | Forward excursion | Forward excursion |
| 2012 Honda CR-V | CEN1223 | Small SUV | 44 | -26 | Translate | 0.73 | 35% | 22% | 102 | 1% | 0.1% | Forward excursion | Forward excursion |
| 2012 Nissan Rogue | CEN1224 | Small SUV | 50 | -27 | Translate | 0.39 | 7% | 4% | 82 | 0% | 0.1% | Airbag | Airbag |
| 2012 Kia Optima | CEN1225 | Midsize car | 44 | -32 | Translate | 0.46 | 11% | 6% | 53 | 0% | 0.1% | Airbag | Airbag |
| 2012 Jeep Patriot | CEN1226 | Small SUV | 48 | -24 | Translate | 0.75 | 37% | 23% | 81 | 0% | 0.1% | Forward excursion | Forward excursion |
| 2012 Mitsubishi Outlander Sport | CEN1227 | Small SUV | 48 | -34 | Translate | 0.52 | 15% | 9% | 84 | 0% | 0.1% | Airbag | Airbag |
| 2013 Subaru Legacy | CEN1228 | Midsize car | 56 | -28 | Rotate | 0.56 | 18% | 11% | 110 | 1% | 0.1% | Airbag | Airbag |
| 2012 Honda Accord | CEN1229 | Midsize car | 56 | -33 | Rotate | 1.11 | 75% | 55% | 178 | 2% | 0.2% | Airbag | Airbag |
| 2012 Nissan Maxima | CEN1230 | Midsize car | 61 | -23 | Translate | 0.54 | 17% | 10% | 65 | 0% | 0.1% | Airbag | Airbag |
| 2013 Nissan Altima | CEN1231 | Midsize car | 52 | -42 | Translate | 0.78 | 40% | 25% | 143 | 1% | 0.1% | Airbag | Airbag |
| 2012 Volkswagen Passat | CEN1232 | Midsize car | 56 | -37 | Rotate | 0.69 | 31% | 19% | 307 | 5% | 0.4% | Forward excursion | Forward excursion |
| 2012 Volkswagen Jetta | CEN1233 | Midsize car | 55 | -29 | Rotate | 0.69 | 30% | 19% | 191 | 2% | 0.2% | Forward excursion | Forward excursion |
| 2013 Honda Accord coupe | CEN1234 | Midsize car | 57 | -35 | Rotate | 0.98 | 62% | 43% | 142 | 1% | 0.1% | Airbag | Airbag |
| 2013 Jeep Wrangler | CEN1235 | Small SUV | 44 | -27 | Translate | 0.96 | 61% | 41% | 147 | 1% | 0.1% | Airbag | Airbag |
| 2013 Ford Fusion | CEN1236 | Midsize car | — | — | Translate | 0.50 | 14% | 8% | 54 | 0% | 0.1% | Forward excursion | Forward excursion |
| 2013 Hyundai Tucson | CEN1237 | Small SUV | 55 | -36 | Rotate | 0.93 | 57% | 38% | 158 | 2% | 0.2% | Forward excursion | Forward excursion |
| 2013 Honda Civic (coupe) | CEN1301 | Small car | 60 | -35 | Rotate | 0.76 | 38% | 24% | 207 | 3% | 0.2% | Airbag | Airbag |
| 2013 Honda Civic (sedan) | CEN1302 | Small car | 62 | -34 | Rotate | 0.97 | 62% | 42% | 394 | 8% | 0.8% | Airbag | Airbag |
| 2013 Subaru Forester | CEN1303 | Small SUV | 56 | -33 | Rotate | 0.48 | 12% | 7% | 127 | 1% | 0.1% | Airbag | Airbag |
| 2013 Volvo XC60 | CEN1304 | Midsize SUV | 43 | -21 | Translate | 0.51 | 14% | 8% | 91 | 1% | 0.1% | Airbag | Airbag |
| 2014 Mazda 6 | CEN1305 | Midsize car | 57 | -40 | Rotate | 0.68 | 29% | 18% | 331 | 6% | 0.5% | Airbag | SW through airbag |
| 2013 Mazda CX-5 | CEN1306 | Small SUV | 52 | -29 | Rotate | 0.73 | 35% | 21% | 95 | 1% | 0.1% | Airbag | Airbag |
| 2013 BMW X1 | CEN1307 | Small SUV | 51 | -26 | Rotate | 0.30 | 3% | 2% | 196 | 2% | 0.2% | Airbag | Airbag |
| 2013 Buick Encore | CEN1308 | Small SUV | 50 | -26 | Translate | 0.86 | 49% | 32% | 76 | 0% | 0.1% | Forward excursion | — |
| 2013 Volkswagen Tiguan | CEN1309 | Small SUV | 54 | -27 | Rotate | 0.74 | 35% | 22% | 87 | 0% | 0.1% | Forward excursion | Forward excursion |
| 2013 Hyundai Elantra | CEN1310 | Small car | 56 | -27 | Rotate | 0.65 | 26% | 16% | 215 | 3% | 0.2% | Airbag | Airbag |
| 2013 Buick Encore | CEN1311 | Small SUV | 53 | -31 | Rotate | 1.01 | 65% | 45% | 101 | 1% | 0.1% | Forward excursion | Forward excursion |
| 2013 Chevrolet Cruze | CEN1312 | Small car | 45 | -26 | Translate | 0.55 | 17% | 10% | 70 | 0% | 0.1% | Forward excursion | Forward excursion |
| 2013 Chevrolet Sonic | CEN1313 | Small car | 51 | -36 | Translate | 1.05 | 69% | 49% | 199 | 3% | 0.2% | Forward excursion | Forward excursion |
| 2013 Ford Focus | CEN1314 | Small car | 48 | -32 | Rotate | 0.78 | 40% | 25% | 133 | 1% | 0.1% | Airbag | Airbag |
| 2013 Nissan Sentra | CEN1315 | Small car | 47 | -28 | Rotate | 0.74 | 35% | 22% | 344 | 6% | 0.6% | Forward excursion | Forward excursion |
| 2013 Volkswagen Beetle | CEN1316 | Small car | 48 | -27 | Rotate | 0.65 | 26% | 16% | 294 | 5% | 0.4% | Forward excursion | Forward excursion |
| 2013 Kia Soul | CEN1317 | Small car | 40 | -25 | Translate | 0.60 | 22% | 13% | 83 | 0% | 0.1% | Forward excursion | Forward excursion |
| 2014 Kia Forte | CEN1318 | Small car | 47 | -27 | Rotate | 0.81 | 43% | 28% | 355 | 7% | 0.6% | IP | IP |
| 2013 Toyota RAV4 | CEN1319 | Small SUV | 45 | -24 | Translate | 0.60 | 22% | 13% | 283 | 5% | 0.4% | IP | IP |
| 2014 Scion tC | CEN1320 | Small car | 40 | -30 | Translate | 0.58 | 20% | 12% | 127 | 1% | 0.1% | Forward excursion | Forward excursion |
| 2013 Dodge Dart | CEN1321 | Small car | 36 | -33 | Translate | 0.63 | 24% | 15% | 84 | 0% | 0.1% | Airbag | — |
| 2013 Dodge Dart | CEN1322 | Small car | 42 | -43 | Translate | 0.46 | 11% | 6% | 184 | 2% | 0.2% | Airbag | Airbag |
| 2014 Mitsubishi Outlander | CEN1323 | Midsize SUV | 45 | -28 | Translate | 0.61 | 23% | 14% | 81 | 0% | 0.1% | Airbag | Airbag |
| 2013 Mazda 2 | CEN1324 | Minicar | 42 | -34 | Translate | 0.92 | 56% | 38% | 281 | 4% | 0.4% | Forward excursion | Forward excursion |

| Vehicle model | Test ID | Class | Delta V | Peak Accel | Vehicle motion | BrIC | AIS 3 BrIC | AIS 4 BrIC | HIC | AIS 3 HIC | AIS 4 HIC | HIC contact source | BrIC contact source |
|---|---|---|---|---|---|---|---|---|---|---|---|---|---|
| 2013 Fiat 500 | CEN1325 | Minicar | 46 | -29 | Rotate | 0.89 | 52% | 34% | 151 | 2% | 0.1% | IP | IP |
| 2014 Honda Odyssey | CEN1326 | Minivan | 54 | -31 | Rotate | 1.24 | 85% | 66% | 130 | 1% | 0.1% | Airbag | Airbag |
| 2013 Mercedes-Benz C class | CEN1327 | Midsize car | 51 | -28 | Rotate | 0.44 | 10% | 6% | 248 | 4% | 0.3% | Airbag | Airbag |
| 2013 Toyota Prius C | CEN1328 | Minicar | 50 | -31 | Rotate | 0.83 | 46% | 30% | 426 | 9% | 1.0% | IP | IP |
| 2013 Hyundai Accent | CEN1329 | Minicar | 44 | -24 | Translate | 0.80 | 42% | 27% | 108 | 1% | 0.1% | IP | IP |
| 2013 Kia Rio | CEN1330 | Minicar | 48 | -32 | Translate | 0.67 | 28% | 17% | 180 | 2% | 0.2% | Forward excursion | Forward excursion |
| 2013 Toyota Yaris | CEN1331 | Minicar | 54 | -27 | Rotate | 0.94 | 58% | 39% | 127 | 1% | 0.1% | IP | IP |
| 2014 Toyota Corolla | CEN1332 | Small car | 56 | -32 | Translate | 0.87 | 50% | 33% | 154 | 2% | 0.1% | Airbag | Airbag |
| 2014 Mercedes-Benz M class | CEN1333 | Midsize SUV | 55 | -27 | Rotate | 0.50 | 14% | 8% | 182 | 2% | 0.2% | Airbag | Airbag |
| 2014 Nissan Versa | CEN1334 | Minicar | 43 | -26 | Translate | 0.78 | 40% | 25% | 77 | 0% | 0.1% | Forward excursion | Forward excursion |
| 2013 Chevrolet Spark | CEN1335 | Minicar | 40 | -23 | Translate | 0.84 | 46% | 30% | 97 | 1% | 0.1% | Airbag | Airbag |
| 2014 Volvo XC90 | CEN1336 | Midsize SUV | 44 | -33 | Translate | 0.48 | 12% | 7% | 62 | 0% | 0.1% | Airbag | Airbag |
| 2014 Subaru Impreza | CEN1337 | Small car | 58 | -40 | Rotate | 0.44 | 9% | 5% | 133 | 1% | 0.1% | Airbag | Airbag |
| 2014 Infiniti Q50 | CEN1338 | Midsize car | 52 | -23 | Rotate | 0.55 | 17% | 10% | 204 | 3% | 0.2% | Airbag | Airbag |
| 2014 Acura MDX | CEN1339 | Midsize SUV | 60 | -28 | Rotate | 0.48 | 12% | 7% | 171 | 2% | 0.2% | Airbag | Airbag |
| 2013 Honda Fit | CEN1340 | Minicar | 53 | -26 | Rotate | 0.92 | 55% | 37% | 517 | 14% | 1.6% | IP | IP |
| 2014 Acura RLX | CEN1341 | Large car | 55 | -36 | Rotate | 0.87 | 50% | 33% | 151 | 2% | 0.1% | Airbag | Airbag |
| 2014 Mitsubishi Mirage | CEN1342 | Minicar | 43 | -31 | Rotate | 0.92 | 56% | 37% | 50 | 0% | 0.1% | Forward excursion | Forward excursion |
| 2014 Ford Fiesta | CEN1343 | Minicar | 48 | -31 | Rotate | 0.80 | 43% | 27% | 509 | 13% | 1.6% | IP | IP |
| 2014 Volvo S80 | CEN1344 | Large car | 43 | -20 | Translate | 0.44 | 10% | 6% | 102 | 1% | 0.1% | Airbag | Airbag |
| 2014 Mazda CX-5 | CEN1345 | Small SUV | 58 | -38 | Rotate | 0.92 | 56% | 37% | 181 | 2% | 0.2% | Airbag | Airbag |
| 2014 Mazda 3 | CEN1346 | Small car | 54 | -38 | Rotate | 0.59 | 21% | 12% | 209 | 3% | 0.2% | Airbag | Airbag |
| 2014 Toyota Prius | CEN1347 | Small car | 47 | -26 | Translate | 0.61 | 23% | 14% | 170 | 2% | 0.2% | Forward excursion | Forward excursion |
| 2014 Toyota Highlander | CEN1348 | Midsize SUV | 52 | -23 | Translate | 0.52 | 15% | 9% | 99 | 1% | 0.1% | Forward excursion | Forward excursion |
| 2014 Toyota Camry | CEN1349 | Midsize car | 46 | -28 | Translate | 0.73 | 34% | 21% | 125 | 1% | 0.1% | Airbag | Airbag |
| 2014 Chevrolet Equinox | CEN1401 | Midsize SUV | 33 | -19 | Translate | 0.46 | 11% | 6% | 49 | 0% | 0.1% | Airbag | Airbag |
| 2014 Ford Explorer | CEN1402 | Midsize SUV | 42 | -28 | Translate | 0.70 | 31% | 19% | 93 | 1% | 0.1% | Forward excursion | Forward excursion |
| 2014 Toyota 4 Runner | CEN1403 | Midsize SUV | 39 | -17 | Translate | 0.73 | 35% | 22% | 142 | 1% | 0.1% | Airbag | Airbag |
| 2014 Jeep Grand Cherokee | CEN1404 | Midsize SUV | 53 | -27 | Rotate | 0.64 | 25% | 15% | 172 | 2% | 0.2% | Airbag | Airbag |
| 2014 Honda Pilot | CEN1405 | Midsize SUV | 47 | -17 | Translate | 0.63 | 25% | 15% | 42 | 0% | 0.1% | Forward excursion | Forward excursion |
| 2014 Kia Sorento | CEN1406 | Midsize SUV | 43 | -23 | Translate | 0.66 | 27% | 16% | 179 | 2% | 0.2% | Forward excursion | Forward excursion |
| 2014 Nissan Rogue | CEN1407 | Small SUV | 46 | -24 | Translate | 0.69 | 31% | 19% | 185 | 2% | 0.2% | Airbag | Airbag |
| 2014 Mazda CX-9 | CEN1408 | Midsize SUV | 38 | -29 | Translate | 0.47 | 11% | 7% | 137 | 1% | 0.1% | Door sill | Doorsill |
| 2014 BMW 2 Series | CEN1409 | Midsize SUV | 51 | -23 | Translate | 0.47 | 11% | 7% | 269 | 4% | 0.3% | Airbag | Airbag |
| 2014 Mini Countryman | CEN1410 | Small car | 41 | -27 | Translate | 0.68 | 29% | 18% | 68 | 0% | 0.1% | Airbag | Airbag |
| 2014 Mitsubishi Lancer | CEN1411 | Small car | 48 | -34 | Rotate | 0.81 | 44% | 28% | 168 | 2% | 0.2% | Forward excursion | Forward excursion |
| 2014 Chevrolet Malibu | CEN1412 | Midsize car | 48 | -27 | Translate | 0.56 | 18% | 11% | 112 | 1% | 0.1% | Airbag | Airbag |
| 2015 Audi A3 | CEN1413 | Midsize car | 51 | -39 | Rotate | 0.82 | 45% | 29% | 103 | 1% | 0.1% | Airbag | Airbag |
| 2014 Fiat 500L | CEN1414 | Small car | 46 | -22 | Rotate | 0.88 | 52% | 34% | 228 | 3% | 0.3% | A-pillar | A-pillar |
| 2014 Hyundai Veloster | CEN1415 | Small car | 51 | -26 | Rotate | 0.75 | 37% | 23% | 100 | 1% | 0.1% | Forward excursion | Forward excursion |
| 2014 Nissan Juke | CEN1416 | Small car | 40 | -25 | Translate | 0.40 | 8% | 4% | 74 | 0% | 0.1% | Forward excursion | Forward excursion |
| 2015 Honda Fit | CEN1417 | Minicar | 51 | -36 | Rotate | 1.07 | 71% | 51% | 631 | 20% | 3.1% | Forward excursion | Forward excursion |
| 2015 Subaru WRX | CEN1418 | Small car | 52 | -27 | Rotate | 0.46 | 11% | 6% | 116 | 1% | 0.1% | Airbag | Airbag |
| 2015 Hyundai Genesis | CEN1419 | Large car | 61 | -32 | Rotate | 0.45 | 10% | 6% | 106 | 1% | 0.1% | Airbag | Airbag |

| Vehicle model | Test ID | Class | Delta V | Peak Accel | Vehicle motion | BrIC | AIS 3 BrIC | AIS 4 BrIC | HIC | AIS 3 HIC | AIS 4 HIC | HIC contact source | BrIC contact source |
|---|---|---|---|---|---|---|---|---|---|---|---|---|---|
| 2014 Ford C-Max | CEN1420 | Small car | 49 | -23 | Rotate | 0.69 | 30% | 18% | 212 | 3% | 0.2% | Forward excursion | Forward excursion |
| 2014 Mercedes-Benz E Class | CEN1421 | Large car | 60 | -38 | Rotate | 0.52 | 15% | 9% | 164 | 2% | 0.2% | A-pillar | A-pillar |
| 2015 Volkswagen GTI | CEN1422 | Small car | 55 | -27 | Rotate | 0.66 | 27% | 17% | 243 | 4% | 0.3% | Airbag | Airbag |
| 2014 Scion FR-S | CEN1423 | Small car | 50 | -32 | Translate | 0.57 | 19% | 11% | 71 | 0% | 0.1% | Airbag | Airbag |
| 2014 Mazda 5 | CEN1424 | Small car | 54 | -23 | Rotate | 0.63 | 24% | 15% | 122 | 1% | 0.1% | Forward excursion | Forward excursion |
| 2014 Chevrolet Volt | CEN1425 | Small car | 51 | -32 | Translate | 0.60 | 22% | 13% | 101 | 1% | 0.1% | Airbag | Airbag |
| 2014 Nissan Leaf | CEN1426 | Small car | 51 | -29 | Rotate | 0.85 | 48% | 31% | 96 | 1% | 0.1% | Forward excursion | Forward excursion |
| 2015 Hyundai Sonata | CEN1427 | Midsize car | 58 | -34 | Rotate | 0.79 | 42% | 26% | 405 | 8% | 0.8% | Airbag | SW through airbag |
| 2014 Scion xB | CEN1428 | Small car | 47 | -26 | Translate | 0.69 | 31% | 19% | 273 | 4% | 0.3% | Airbag | Airbag |
| 2014 BMW 5 Series | CEN1429 | Large car | 58 | -33 | Rotate | 0.47 | 12% | 7% | 86 | 0% | 0.1% | Airbag | Airbag |
| 2015 Honda Fit | CEN1430 | Minicar | 59 | -43 | Rotate | 0.89 | 52% | 34% | 651 | 22% | 3.4% | Airbag | SW through airbag |
| 2014 Infiniti Q70 | CEN1431 | Large car | 53 | -25 | Translate | 0.48 | 12% | 7% | 109 | 1% | 0.1% | Airbag | Airbag |
| 2015 Chrysler 200 | CEN1432 | Midsize car | 57 | -43 | Rotate | 0.67 | 29% | 17% | 119 | 1% | 0.1% | Airbag | Airbag |
| 2015 Subaru Legacy | CEN1433 | Midsize car | 58 | -31 | Rotate | 0.56 | 18% | 11% | 120 | 1% | 0.1% | Airbag | Airbag |
| 2015 Kia Soul | CEN1434 | Small car | 54 | -28 | Rotate | 0.61 | 23% | 14% | 374 | 7% | 0.7% | Airbag | Airbag |
| 2014 Lincoln MKS | CEN1435 | Large car | 44 | -26 | Translate | 0.53 | 15% | 9% | 82 | 0% | 0.1% | IP | IP |
| 2015 Kia Forte | CEN1436 | Small car | 56 | -44 | Rotate | 0.75 | 36% | 23% | 149 | 2% | 0.1% | IP | IP |
| 2015 Volkswagen Jetta | CEN1437 | Midsize car | 55 | -27 | Translate | 0.75 | 37% | 23% | 306 | 5% | 0.4% | Forward excursion | Forward excursion |
| 2014 Chrysler Town & Country | CEN1438 | Minivan | 48 | -23 | Translate | 0.72 | 34% | 21% | 230 | 3% | 0.3% | IP | IP |
| 2015 Toyota Sienna LE 4-door | CEN1439 | Minivan | 57 | -28 | Rotate | 0.57 | 19% | 11% | 118 | 1% | 0.1% | Forward excursion | Forward excursion |
| 2014 Mini Cooper | CEN1440 | Minicar | 43 | -33 | Translate | 0.52 | 15% | 9% | 166 | 2% | 0.2% | Airbag | Airbag |
| 2015 Kia Sedona | CEN1441 | Minivan | 59 | -26 | Rotate | 0.81 | 43% | 28% | 120 | 1% | 0.1% | Airbag | Airbag |
| 2015 Acura TLX | CEN1442 | Midsize car | 52 | -47 | Rotate | 0.70 | 32% | 19% | 136 | 1% | 0.1% | Airbag | Airbag |
| 2015 Honda Accord 2- door | CEN1443 | Midsize car | 55 | -23 | Rotate | 1.18 | 81% | 61% | 270 | 4% | 0.3% | Airbag | Airbag |
| 2015 Honda CR-V | CEN1444 | Small SUV | 49 | -25 | Translate | 0.68 | 29% | 18% | 137 | 1% | 0.1% | Airbag | Airbag |
| 2014 Nissan Quest | CEN1445 | Minivan | 53 | -17 | Rotate | 1.08 | 73% | 52% | 527 | 14% | 1.7% | Airbag | Airbag |
| 2015 Toyota Avalon | CEN1446 | Large car | 50 | -49 | Translate | 0.58 | 20% | 12% | 137 | 1% | 0.1% | Airbag | Airbag |
| 2015 Nissan Pathfinder | CEN1447 | Midsize SUV | 41 | -18 | Translate | 0.49 | 13% | 8% | 39 | 0% | 0.1% | Airbag | Airbag |
| 2015 Lexus RC | CEN1448 | Midsize car | 57 | -24 | Rotate | 0.50 | 14% | 8% | 105 | 1% | 0.1% | Airbag | Airbag |
| 2015 Lexus NX | CEN1449 | Small SUV | 48 | -25 | Translate | 0.74 | 36% | 22% | 150 | 2% | 0.1% | Airbag | Airbag |
| 2015 Lexus CT | CEN1450 | Small car | 45 | -30 | Translate | 0.60 | 22% | 13% | 142 | 1% | 0.1% | Airbag | Airbag |
| 2015 Toyota RAV4 | CEN1451 | Small SUV | 54 | -32 | Rotate | 0.57 | 19% | 11% | 163 | 2% | 0.2% | Airbag | Airbag |
| 2015 Toyota Prius V | CEN1452 | Midsize car | 58 | -41 | Translate | 0.62 | 23% | 14% | 193 | 2% | 0.2% | Airbag | Airbag |
| 2015 Kia Sedona | CEN1453 | Minivan | 61 | -25 | Rotate | 0.68 | 29% | 18% | 102 | 1% | 0.1% | Airbag | Airbag |

**Instrumentation Technique for Measuring Six Degrees of Freedom Head Kinematics in Impact Conditions using Six-Accelerometers and Three-Angular Rate Sensors (6aω Configuration) on a Lightweight Tetrahedron Fixture**

**Yun-Seok Kang**
Injury Biomechanics Research Center, The Ohio State University
USA

**Kevin Moorhouse**
National Highway Traffic Safety Administration, Vehicle Research & Test Center
USA

**John H. Bolte IV**
Injury Biomechanics Research Center, The Ohio State University
USA

Paper Number 15-0288

## ABSTRACT

The ability to measure six degree of freedom head kinematics in impact conditions (i.e. motor vehicle crashes and sport activities) plays an important role in injury assessment of the head/neck complex. Potential accuracy of head instrumentation schemes have recently been improved by using advanced angular rate sensors, so in this study an instrumentation technique for obtaining accurate head kinematics in impact conditions using an external fixture is proposed and validated. The methodology proposed in this study utilizes six accelerometers and three angular rate sensors (6aω) on a lightweight tetrahedron fixture (t6aω) originally designed for measuring head kinematics of post mortem human surrogates (PMHS) in car crash scenarios using a nine accelerometer array package (NAAP) configuration (tNAAP). A Hybrid III 50th percentile male anthropomorphic test device (ATD) head containing an internal nine accelerometer array package (iNAAP) was used to validate the t6aω method proposed in this study. The t6aω instrumentation was installed on a tetrahedron fixture which was attached externally to the Hybrid III ATD head, tested in direct contact tests of various severities, and then compared to data measured from the iNAAP of the Hybrid III ATD head which provided the kinematics gold standard to validate the proposed technique. Results indicate that angular acceleration obtained from the t6aω scheme was comparable to that determined from the iNAAP scheme in the head impact conditions, showing normalized root mean squared deviation (NRMSD) values less than 5%. Transformed linear acceleration from the t6aω to the center of gravity (CG) of the Hybrid III ATD head was also comparable to acceleration measured directly from the accelerometers at the CG, exhibiting less than 5% NRMSD. Accurate angular acceleration and velocity are important to obtain accurate transformed acceleration. Since the t6aω angular acceleration component of the transformed linear acceleration at an inaccessible point was shown to have equivalent accuracy to iNAAP (less than 5% error), and the angular velocity component of t6aω instrumentation should be more accurate than the tNAAP scheme (since it is directly measured by the ARS as opposed to using numerical integration as in tNAAP), the t6aω scheme should yield more accurate transformed linear acceleration at an inaccessible location than the tNAAP scheme. The proposed instrumentation should aid in the development and evaluation of head, neck and brain injuries in future testing.

## INTRODUCTION

Numerous measurement techniques for head kinematics in motor vehicle crashes and sports activities have been developed and evaluated [1-9], and the accuracy of angular kinematics, in particular, has been a challenge in developing these instrumentation techniques [1-4, 7]. The most frequent method to obtain accurate six degrees of freedom (6DOF) head kinematics is to use the nine accelerometer array (3-2-2-2) package (NAAP), in which angular acceleration can be calculated from simple algebraic equations [1]. Although the NAAP is capable of measuring angular acceleration accurately, single and double numerical integrations are required to obtain angular

velocity and displacement, which can particularly cause issues with the accuracy of the resulting displacement [5, 7]. Therefore, with the advent and availability of more advanced angular rate sensors (ARS), ARS combined with accelerometers have been recently employed to provide even more accurate angular velocity and displacement [5], since angular acceleration can still be obtained from algebraic equations, while angular velocity is directly measured from the ARS [7]. Therefore, six accelerometers and three ARS (6aω) should theoretically be capable of measuring more accurate 6DOF kinematics than NAAP, and this has been demonstrated for sensors installed inside an ATD head (i6aω versus iNAAP where "i" stands for internal) [7].

In order to measure 6DOF kinematics of the head of post mortem human surrogates (PMHS), an external fixture is typically used, and should be lightweight and stable against structural vibration. Previous studies evaluating head and brain injuries have used various external fixtures with nine accelerometers (NAAP) installed, such as a triangular pyramidal fixture [10] and a tetrahedral fixture [11]. Although the i6aω scheme has been validated inside a Hybrid III iNAAP head [7], its integrity with a lightweight/small external fixture should also be validated. Therefore, the objective of this study is to propose and validate a 6aω scheme installed on a lightweight tetrahedron fixture (t6aω, where "t" stands for tetrahedron).

## METHODS

### 6aω Scheme on a Lightweight Tetrahedron Fixture

An external tetrahedron fixture, similar to the one developed and validated (including its structural integrity and stability) by Yoganandan et al. [10], was utilized in this study. The t6aω scheme was implemented as shown in Figure 1. The edge length of the tetrahedron is approximately 6 cm, while the mass of the fixture is 72 grams without sensors and 96 grams with sensors attached. In order to obtain algebraic equations for angular acceleration of the t6aω scheme, the acceleration at each corner point (points A-B-C shown in Figure 1b) with respect to a body fixed coordinate system on the tetrahedron fixture was derived as Eqs (1) – (3).

$$a_{az'} = a_{0z'} + \omega_{x'}\,\omega_{z'}\rho_{ax'} - \dot{\omega}_{y'}\rho_{ax'} \tag{1}$$

$$a_{bx'} = a_{0x'} + \omega_{x'}\,\omega_{y'}\rho_{by'} - \dot{\omega}_{z'}\rho_{by'} \tag{2}$$

$$a_{cy'} = a_{0y'} + \omega_{y'}\,\omega_{z'}\rho_{cz'} - \dot{\omega}_{x'}\rho_{cz'} \tag{3}$$

where,
$\dot{\omega}$ : angular acceleration in the body fixed frame
$a$ : acceleration measured from accelerometers at each location
$\omega$ : angular velocity measured from ARS
$\rho$ : distance between accelerometers at vertex and accelerometers at points A, B, and C

Eqs (1) – (3) can now be expressed in terms of the angular accelerations, which are the only unknown variables under the proposed t6aω configuration, as in Eqs (4) – (6):

$$\dot{\omega}_{x'} = (a_{0y'} - a_{cy'}) / \rho_{cz'} + \omega_{ay'}\omega_{bz'} \tag{4}$$

$$\dot{\omega}_{y'} = (a_{0z'} - a_{az'}) / \rho_{ax'} + \omega_{cx'}\omega_{bz'} \tag{5}$$

$$\dot{\omega}_{z'} = (a_{0x'} - a_{bx'}) / \rho_{by'} + \omega_{cx'}\omega_{ay'} \tag{6}$$

The detailed procedure for deriving the kinematic equations with respect to the body fixed frame for the t6aω scheme is described in a previous study [7].

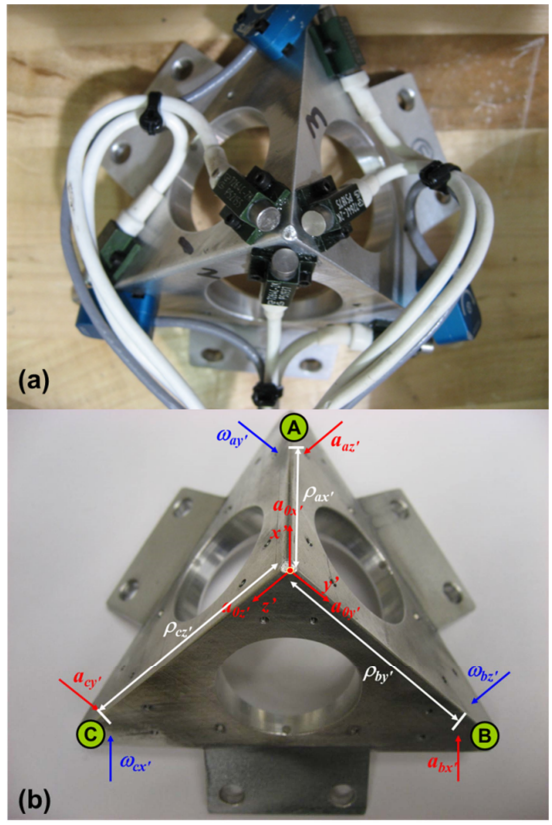


***Figure 1. (a) An external fixture with 6aω scheme and (b) body fixed coordinate system embedded on the tetrahedron fixture.***

**Test Configuration and Instrumentation**

Thirteen head impact tests were conducted to validate the proposed external instrumentation in a direct impact condition that usually yields high peak, short duration responses. The Hybrid III head/neck was fixed to an adjustable height table and a hydraulic ram impactor was used to deliver a severe head impact. The lower neck of the Hybrid III was fixed to the table after being rotated 30 degrees about the z direction according to SAE J211 (SAE, 2007), as shown in Figure 2, such that the impactor could collide with the head antero-laterally. The body fixed frame (x-y-z) on the Hybrid III head was defined as shown in Figure 2. In order to produce various severities and head injury criteria (HIC) values, the head was struck by the impactor without padding for five tests and with padding for eight tests. For the padded condition a one inch thick piece of gray "Ensolite SCC" foam was affixed to the head at the impact location. The Hybrid III iNAAP head was instrumented with nine accelerometers (Endevco 7264C 2K), while the t6aω scheme installed on the tetrahedron fixture was composed of six accelerometers (Endevco 7264C 2K) and three ARS (DTS ARS-18K). In addition to the t6aω scheme, a t3aω scheme on the tetrahedron fixture was also evaluated in this study. The t3aω scheme was composed of the three accelerometers at the origin (i.e. vertex of the fixture) and the three ARS at points A-B-C shown in Figure 1. Accuracy of the external instrumentation could be affected by any relative movement between the fixture and the head. To reduce the risk of relative motion, the tetrahedron fixture was screwed into the skull cap using six screws, as shown in Figure 2.

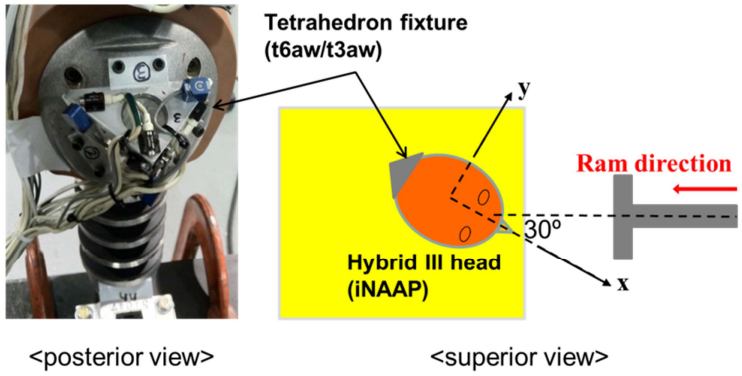


***Figure 2. Head impact test configuration***

**Data Analyses**

Data was sampled at 20,000 Hz. The consistency of the data measured from the accelerometers of the iNAAP was inspected by SIMon (version 4.0, NHTSA), which checked the integrity of the accelerometers, including instances of sensor malfunction and incorrect sensitivity [13, 14]. A 4th-order Butterworth low pass filter corresponding to appropriate SAE J211 channel filter classes (CFC) was applied to the data. For the iNAAP and t6aω schemes, the data recorded from the accelerometers and ARS were filtered at 1650 Hz (CFC1000). The angular velocity for the t3aω scheme was first filtered at 300 Hz (CFC180) and then numerically differentiated to obtain angular acceleration. Angular acceleration for the iNAAP was calculated by employing the procedure proposed by Padgaonkar et al. [1], while that for the t6aω was determined using Eqs (4) – (6). The kinematic data relative to the body fixed coordinate system on the external fixture was transformed to the body fixed coordinate system on the Hybrid III head using the procedure described by Kang et al. [7]. Origin locations and initial orientation of the body fixed coordinates for both the external fixture and the Hybrid III head were determined by digitizing points on the fixture and the head using a Faro arm device (Faro Arm Technologies, Lake Mary, FL). The normalized root mean squared deviation (NRMSD) shown in Eq (7) was used for quantitative evaluation of the proposed scheme. The NRMSD provided an average percent error over time between the iNAAP (i.e. gold standard) and kinematic data (linear acceleration and angular acceleration) obtained from the t6aω and t3aω. In addition to the NRMSD, percent differences of the peak values between the iNAAP and t6aω/t3aω schemes were also calculated since most injury criteria rely upon peak values.

$$NRMSD = \frac{\sqrt{\frac{1}{n}\sum_{i=0}^{n}(Y_i - Y_i')^2}}{Y'_{\max} - Y'_{\min}} \tag{7}$$

where:

- n is the total number of data points
- *Y'max* and *Y'min* represent the maximum and minimum values of the gold standard.
- *Yi* and *Y'i* are the i$^{th}$ data point obtained from the instrumentation scheme being evaluated and the i$^{th}$ data point obtained from the gold standard, respectively.

The angular velocity for the iNAAP was also computed using a single numerical integration, and then transformed to the coordinate system on the tetrahedron fixture so it could be compared to the angular velocity

directly measured on the tetrahedron by the ARS. For this evaluation the directly measured ARS were deemed as the gold standard for NRMSD calculation.

**RESULTS**

Three dimensional head motion was generated to validate the proposed instrumentation technique for measuring six degrees of freedom kinematics. Various impact severities were created randomly, ranging from HIC15 values of 319 to 1820. Many studies have looked at resultant linear and/or angular acceleration in their validation studies for instrumentation techniques [5, 6, 8, 10, 15, 16], likely due to the fact that transformation errors can be minimized by using the resultant acceleration. However, considering linear and angular kinematics in each component direction (x, y, and z) has been shown to be important in the prediction of brain injury [17]. Therefore, in this study linear and angular acceleration with respect to the body fixed frame on the tetrahedron fixture was transformed to the head coordinate system in x, y, and z axes at the center of gravity (CG) (Figure 2). When transforming the kinematics to the head CG coordinate system there can be some inherent transformation errors due to digitization of the tetrahedron fixture and ATD landmarks (e.g. OC joint and peripheral CG point). However, these transformation errors are likely to be small since both the tetrahedron and the ATD head have well-defined geometries. Figure 3 shows the linear and angular acceleration in x, y, and z axes for HImpact13, which resulted in a HIC15 value of 1820 (Table 1). NRMSD values were calculated for the first 40 ms after head contact for each test. Despite inherent transformation errors, the t6aω scheme yielded an average NRMSD of 1.8 ± 1.0% for the linear acceleration and 3.4 ± 0.9% for the angular acceleration, while the t3aω produced an average NRMSD of 5.6 ± 5.6% for the linear acceleration and 5.4 ± 1.4% for the angular acceleration for all thirteen tests (Tables 1 and 2). For the average peak value differences, the t6aω scheme yielded an average 5.3 ± 4.1% for the linear acceleration, 5.0 ± 4.8% for the angular acceleration and 2.4 ± 1.0% for $HIC_{15}$, while the t3aω produced an average 16.0 ± 21.7% for the linear acceleration, 14.0 ± 15.6% for the angular acceleration and 1.6 ± 1.3% for $HIC_{15}$ in all thirteen tests.

When evaluating the NRMSD values or peak value differences in Tables 1 and 2 it is important to consider the importance and/or magnitude of the signal being assessed, because in many cases the high percentage differences are simply a result of a low signal magnitude dominated by noise. Therefore, linear accelerations with a magnitude greater than 100g were highlighted in green in Table 1, and average NRMSD and peak value differences were calculated only using the highlighted linear accelerations with sufficient magnitude. Average NRMSD and peak value differences calculated in this manner were reduced for the t6aw configuration: 1.0 ± 0.8% for NRMSD and 2.9 ± 3.7% for peak value differences. The t3aw configuration showed even greater reduction in NRMSD and peak values differences: 1.4 ± 1.3% for NRMSD and 5.1 ± 6.6% for peak value differences.

Similarly in Table 2, angular accelerations with a magnitude greater than 3000 rad/s$^2$ were highlighted in yellow and the mean and standard deviation for only highlighted angular accelerations were calculated. Average NRMSD and peak value differences using only the highlighted angular accelerations were reduced to 3.1 ± 0.5% NRMSD and 3.7 ± 4.4% peak value differences for the t6aw, and 4.6 ± 1.2% NRMSD and 5.4 ± 6.5% peak value differences for the t3aw.

NRMSD and peak value differences for angular velocities are also shown in Table 2, and angular velocities with a magnitude greater than 1000 deg/s are highlighted in green. The average NRMSD for all thirteen tests was 4.6 ± 1.1%, while the average including only highlighted values was 5.0 ± 1.2%. For the average peak value differences in angular velocity, both mean values were less than 5% (4.7 ± 2.0% for all thirteen values and 4.3 ± 1.3% for only the highlighted values).

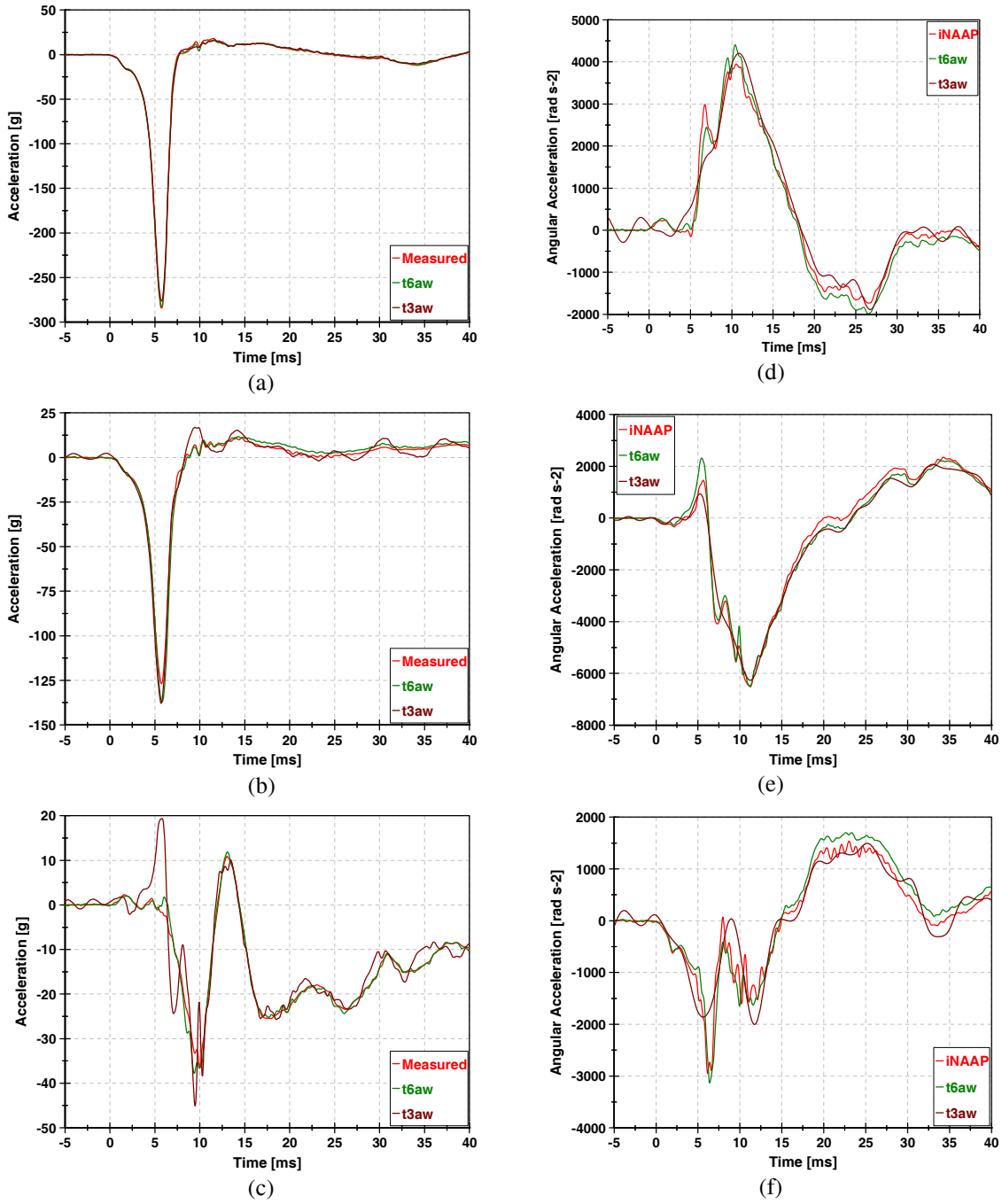


***Figure 3. Kinematics in HImpact13: linear acceleration in (a) x direction, (b) y direction, (c) z direction and angular acceleration in (d) x direction, (e) y direction, (f) z direction***
***Filter class: CFC1000 for accelerometers in all three schemes, CFC1000 for ARS in t6a$\omega$, and CFC180 for ARS in t3a$\omega$ due to numerical differentiation***

**Table 1.**
**NRMSD and peak value percent differences (t6aω vs. NAAP and t3aω vs. NAAP) for linear acceleration at CG and $HIC_{15}$**
**Gold standard: measured acceleration at CG**
**Highlighted cells: Acceleration > 100g**

| | Pad | $HIC_{15}$ | $HIC_{15}$ Peak difference (%) | | Axes | Linear acceleration NRMSD (%) | | Linear acceleration Peak difference (%) | |
|---|---|---|---|---|---|---|---|---|---|
| | | | t6aω | t3aω | | t6aω | t3aω | t6aω | t3aω |
| HImpact01 | No | 381 | 2.9 | 3.7 | x | 0.4 | 0.7 | 1.4 | 1.1 |
| | | | | | y | 2.1 | 4.4 | 6.9 | 20.7 |
| | | | | | z | 3.1 | 21.3 | 4.3 | 6.7 |
| HImpact02 | No | 633 | 1.9 | 1.6 | x | 0.4 | 0.8 | 2.1 | 2.8 |
| | | | | | y | 2.0 | 4.1 | 11.1 | 22.5 |
| | | | | | z | 3.1 | 17.6 | 15.9 | 128.2 |
| HImpact03 | No | 934 | 0.7 | 0.3 | x | 0.4 | 0.7 | 0.2 | 1.4 |
| | | | | | y | 1.9 | 4.3 | 2.9 | 20.1 |
| | | | | | z | 2.5 | 15.8 | 9.3 | 21.2 |
| HImpact04 | No | 1001 | 1.7 | 2.8 | x | 0.5 | 0.5 | 0.4 | 1.0 |
| | | | | | y | 1.9 | 4.0 | 7.5 | 21.3 |
| | | | | | z | 2.5 | 12.6 | 10.0 | 51.6 |
| HImpact05 | No | 1059 | 2.2 | 2.6 | x | 0.6 | 0.8 | 0.2 | 0.7 |
| | | | | | y | 1.8 | 3.8 | 6.4 | 16.4 |
| | | | | | z | 1.8 | 13.1 | 4.1 | 32.2 |
| HImpact06 | Yes | 319 | 4.4 | 4.1 | x | 0.5 | 0.7 | 0.4 | 1.2 |
| | | | | | y | 3.0 | 4.5 | 9.7 | 14.6 |
| | | | | | z | 3.4 | 13.7 | 6.4 | 12.6 |
| HImpact07 | Yes | 543 | 2.9 | 0.2 | x | 0.6 | 0.7 | 0.4 | 0.9 |
| | | | | | y | 2.5 | 3.0 | 8.0 | 9.7 |
| | | | | | z | 2.1 | 10.3 | 4.9 | 9.8 |
| HImpact08 | Yes | 846 | 2.7 | 1.3 | x | 0.7 | 0.8 | 1.9 | 2.9 |
| | | | | | y | 2.3 | 2.6 | 7.6 | 8.2 |
| | | | | | z | 2.4 | 8.8 | 9.1 | 29.8 |
| HImpact09 | Yes | 1153 | 2.9 | 1.4 | x | 0.4 | 0.6 | 0.1 | 1.1 |
| | | | | | y | 2.2 | 2.8 | 8.2 | 9.7 |
| | | | | | z | 2.1 | 8.9 | 5.5 | 23.9 |
| HImpact10 | Yes | 1183 | 3.0 | 0.3 | x | 0.5 | 0.6 | 0.5 | 1.6 |
| | | | | | y | 2.4 | 3.0 | 8.1 | 8.2 |
| | | | | | z | 2.3 | 9.7 | 4.9 | 20.8 |
| HImpact11 | Yes | 1421 | 3.2 | 0.7 | x | 0.5 | 0.6 | 0.8 | 2.1 |
| | | | | | y | 2.4 | 2.5 | 9.9 | 10.5 |
| | | | | | z | 2.8 | 8.5 | 3.9 | 14.3 |
| HImpact12 | Yes | 1432 | 1.0 | 0.2 | x | 0.5 | 0.7 | 0.6 | 2.7 |
| | | | | | y | 2.3 | 4.9 | 10.4 | 24.7 |
| | | | | | z | 4.0 | 14.0 | 11.9 | 29.2 |
| HImpact13 | Yes | 1820 | 1.8 | 1.5 | x | 0.4 | 0.6 | 0.6 | 2.8 |
| | | | | | y | 2.0 | 2.4 | 8.0 | 8.7 |
| | | | | | z | 2.0 | 8.4 | 3.8 | 23.9 |
| Total mean (SD) | N/A | 979 (439) | 2.4 (1.0) | 1.6 (1.3) | N/A | 1.8 (1.0) | 5.6 (5.6) | 5.3 (4.1) | 16.0 (21.7) |
| Highlighted mean (SD) | N/A | N/A | N/A | N/A | N/A | 1.0 (0.8) | 1.4 (1.3) | 2.9 (3.7) | 5.1 (6.6) |

**Table 2.**
**NRMSD and peak value percent differences for angular velocity (NAAP vs. ARS) and angular acceleration (t6aω vs. NAAP and t3aω vs. NAAP)**
**Gold standards: ARS for angular velocity; NAAP for angular acceleration**
**Highlighted cells: angular velocity > 1000 deg/s; angular acceleration > 3000 rad/s$^2$**

| | Pad | $HIC_{15}$ | Axes | Angular velocity | | Angular acceleration | | | |
|---|---|---|---|---|---|---|---|---|---|
| | | | | NRMSD (%) | Peak difference (%) | NRMSD (%) | | Peak difference (%) | |
| | | | | iNAAP | iNAAP | t6aω | t3aω | t6aω | t3aω |
| HImpact01 | No | 381 | x | 3.5 | 4.7 | 3.5 | 8.2 | 3.4 | 9.9 |
| | | | y | 3.9 | 4.0 | 3.3 | 7.1 | 1.7 | 5.7 |
| | | | z | 5.2 | 12.1 | 2.2 | 5.9 | 2.5 | 40.0 |
| HImpact02 | No | 633 | x | 3.9 | 2.0 | 3.8 | 8.2 | 3.8 | 8.6 |
| | | | y | 3.7 | 3.6 | 3.0 | 4.9 | 0.1 | 3.6 |
| | | | z | 4.5 | 8.7 | 3.1 | 6.0 | 14.2 | 29.3 |
| HImpact03 | No | 934 | x | 3.6 | 3.8 | 2.5 | 5.5 | 10.7 | 9.6 |
| | | | y | 4.0 | 5.5 | 2.1 | 4.5 | 1.1 | 0.0 |
| | | | z | 3.6 | 6.0 | 3.1 | 6.3 | 6.1 | 41.6 |
| HImpact04 | No | 1001 | x | 3.8 | 3.9 | 3.7 | 6.8 | 2.1 | 1.5 |
| | | | y | 4.6 | 4.2 | 2.8 | 4.4 | 0.7 | 3.7 |
| | | | z | 3.9 | 7.0 | 3.2 | 6.7 | 24.0 | 30.9 |
| HImpact05 | No | 1059 | x | 4.0 | 3.2 | 3.4 | 7.3 | 4.2 | 2.3 |
| | | | y | 4.7 | 4.9 | 3.0 | 5.5 | 1.8 | 0.0 |
| | | | z | 3.9 | 8.5 | 3.1 | 5.8 | 3.1 | 50.5 |
| HImpact06 | Yes | 319 | x | 4.0 | 2.9 | 2.9 | 3.8 | 9.0 | 1.8 |
| | | | y | 5.2 | 4.3 | 4.6 | 7.6 | 1.6 | 4.1 |
| | | | z | 4.0 | 4.2 | 6.4 | 6.4 | 2.2 | 3.3 |
| HImpact07 | Yes | 543 | x | 3.9 | 4.0 | 3.2 | 5.5 | 6.2 | 1.2 |
| | | | y | 5.7 | 4.0 | 2.6 | 3.4 | 0.9 | 0.9 |
| | | | z | 3.2 | 4.2 | 4.5 | 5.4 | 5.0 | 36.3 |
| HImpact08 | Yes | 846 | x | 4.7 | 7.0 | 3.0 | 4.6 | 9.8 | 9.9 |
| | | | y | 5.9 | 5.4 | 2.5 | 3.4 | 0.8 | 1.2 |
| | | | z | 4.1 | 3.4 | 4.6 | 4.5 | 9.5 | 31.9 |
| HImpact09 | Yes | 1153 | x | 5.0 | 5.1 | 3.1 | 3.8 | 8.9 | 6.6 |
| | | | y | 6.3 | 3.8 | 2.8 | 3.4 | 0.7 | 1.2 |
| | | | z | 3.6 | 3.5 | 4.9 | 5.5 | 4.8 | 26.3 |
| HImpact10 | Yes | 1183 | x | 5.1 | 4.3 | 3.2 | 4.5 | 4.2 | 8.8 |
| | | | y | 6.7 | 6.8 | 2.9 | 3.5 | 1.0 | 3.0 |
| | | | z | 3.7 | 1.8 | 5.3 | 6.1 | 6.7 | 34.7 |
| HImpact11 | Yes | 1421 | x | 5.7 | 3.9 | 3.7 | 5.0 | 7.9 | 8.6 |
| | | | y | 7.3 | 5.6 | 3.1 | 3.6 | 0.4 | 0.5 |
| | | | z | 4.3 | 3.8 | 5.1 | 5.2 | 3.5 | 23.8 |
| HImpact12 | Yes | 1432 | x | 3.8 | 3.6 | 3.9 | 6.5 | 2.4 | 6.4 |
| | | | y | 4.3 | 4.1 | 3.0 | 4.2 | 1.6 | 5.5 |
| | | | z | 4.1 | 6.9 | 2.7 | 5.6 | 10.2 | 50.0 |
| HImpact13 | Yes | 1820 | x | 5.8 | 3.9 | 3.1 | 4.6 | 11.6 | 6.4 |
| | | | y | 7.3 | 4.5 | 2.6 | 3.5 | 0.5 | 3.8 |
| | | | z | 4.1 | 1.3 | 4.6 | 6.2 | 6.2 | 32.1 |
| Total mean (SD) | N/A | 979 (439) | N/A | 4.6 (1.1) | 4.7 (2.0) | 3.4 (0.9) | 5.4 (1.4) | 5.0 (4.8) | 14.0 (15.6) |
| Highlighted mean (SD) | N/A | N/A | N/A | 5.0 (1.2) | 4.3 (1.3) | 3.1 (0.5) | 4.6 (1.2) | 3.7 (4.4) | 5.4 (6.5) |

## DISCUSSION

Various filtering classes for the instrumentation have been suggested to yield accurate head kinematics [2, 5, 7, 10, 11, 18]. The same filtering class (1650 Hz cutoff frequency, CFC1000) was applied to the accelerometers and ARS for both the t6aω (all six accelerometers and three ARS) and iNAAP (nine accelerometers) schemes. However, the t3aω scheme required a different filtering class due to numerical differentiation of the data measured from the angular rate sensors [2, 5, 7]. In order to determine the most appropriate filtering class for numerical differentiation in the t3aω scheme, different filtering cut-off frequencies were applied to the most severe impact tests: HImpact05 (with no padding and HIC15 value of 1059) and HImpact13 (with padding and HIC15 value of 1820) shown in Figure 4(a) and 4(b), respectively. Representative traces for both HImpact 05 and 13 are presented in Figure 4(c) and 4(d), respectively, where it can be seen that inaccuracies were inherent in the 100 Hz cut off frequency due to excessive signal attenuation, and also in the 500 Hz cut off frequency due to excessive noise. The NRMSD and peak value differences of the resultant angular acceleration between the iNAAP and t3aω were smallest at 300 Hz (CFC180) in the unpadded test (Figure 4a), consistent with what previous studies have used [4, 5]. Although the peak values were still smallest at 300 Hz in the padded test (Figure 4b), the NRMSD values were smallest at 400 Hz. For the most part, NRMSD and peak value differences in the padded test (HImpact13) were smaller than those in the unpadded test (HImpact05). Numerical differentiation errors in the t3aω scheme seem to be reduced in padded head impacts.

In a rigid body, the accuracy of the measured angular acceleration at a remote point affects the accuracy of the transformed linear acceleration at other locations which may be inaccessible (e.g., center of gravity of the head), because transformed linear acceleration is a function of both angular velocity and angular acceleration (Eqs 1 – 3). Therefore, accurate angular acceleration and velocity are important to obtain accurate transformed acceleration. Since the t6aω angular acceleration component of the transformed linear acceleration at an inaccessible point was shown to have equivalent accuracy to iNAAP, and the angular velocity component of t6aω instrumentation should be more accurate since it is directly measured by the ARS (as opposed to using numerical integration as in tNAAP), the t6aω should theoretically yield more accurate transformed linear acceleration at an inaccessible location than tNAAP.

Both 6aω and NAAP schemes use algebraic equations to compute angular acceleration [1, 7], which is numerically more stable and accurate than using nonlinear ordinary differential equations [19] and numerical differentiation of ARS [2, 5]. The NRMSD and peak value differences for the angular velocity determined from iNAAP were 4.6% and 4.7% (Table 2), which is generally acceptable, but the t6aω scheme should theoretically provide the most accurate six degrees of freedom head kinematics since the angular velocity is measured directly. The 6aω scheme should also provide more accurate angular displacement, and thus the most accurate six degrees of freedom head kinematics, both when installed inside an ATD head and when installed on an external fixture mounted to the outside of the head.

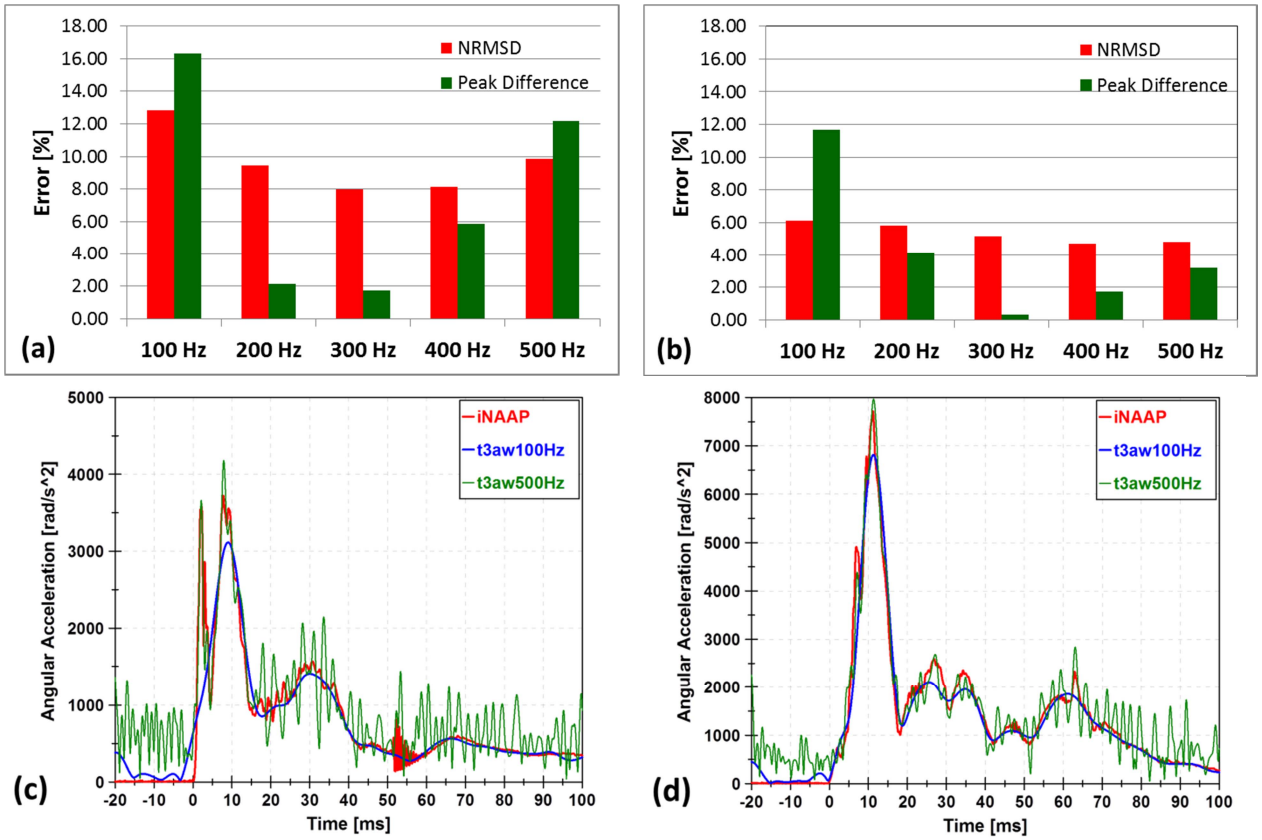


***Figure 4. NRMSD and peak difference of the angular acceleration between iNAAP and t3aω using different filtering classes: (a) HImpact05 (no pad impact), (b) HImpact13 (pad impact), (c) representative traces for HImpact05 (no pad impact), and (d) representative traces for HImpact13 (pad impact)***

## CONCLUSIONS

Six accelerometers and three angular rate sensors (6aω) installed on an external tetrahedron fixture (t6aω) were proposed and validated on a Hybrid III nine accelerometers array package (NAAP) head. Validation tests were conducted in various HIC15 levels (HIC15 of 319 to 1820). Quantitative comparison using the NRMSD and peak percent difference were made between each scheme evaluated (t6aω and t3aω) and the relevant gold standard (iNAAP). The proposed t6aω method appears to be capable of measuring accurate 6 DOF kinematics of the head in any severity of impact conditions. The results exhibited NRMSD less than 4% and peak percent difference less than 6% for both linear and angular acceleration. The proposed instrumentation should aid in the development and evaluation of head, neck and brain injuries in future testing.

## ACKNOWLEDGMENTS

The authors would like to thank Jim Stricklin and David Hyder from the Transportation Research Center, Inc. for their considerable support during test days.

## REFERENCES


[1] Padgaonkar, A., Krieger, K., King, A., 1975. Measurement of angular acceleration of a rigid body using linear accelerometers. Journal of Applied Mechanics 42, 552–556.
[2] Laughlin, D.R., 1989. A magnetohydrodynamic angular motion sensor for anthropomorphic test device instrumentation. Stapp Car Crash Journal, 33, 43 – 77.
[3] Nusholtz, G.S., 1993. Geometric methods in determining rigid-body dynamics. Exp. Mech. 33, 153–158.
[4] Martin, P.G., Hall, G.W., Crandall, J.R., Pilkey, W.D., Chou, C.C., Fileta, B.B., 1997. Measurement Techniques for Angular Velocity and Acceleration in an Impact Environment. SAE Paper 970575.
[5] Martin, P.G., Hall, G.W., Crandall, J.R., Pilkey, W.D., 1998. Measuring the Acceleration of a Rigid Body. Shock and Vibration 5, 211-224.
[6] Hanlon, E., Bir, C., 2010. Validation of a wireless head acceleration measurement system for use in soccer play. J. Appl. Biomech. 26, 424–31.
[7] Kang, Y.-S., Moorhouse, K., Bolte, J.H., 2011. Measurement of six degrees of freedom head kinematics in impact conditions employing six accelerometers and three angular rate sensors (6aω configuration). J. Biomech. Eng. 133, 111007.
[8] Rowson, S., Beckwith, J.G., Chu, J.J., Leonard, D.S., Greenwald, R.M., Duma, S.M., 2011. A six degree of freedom head acceleration measurement device for use in football. J. Appl. Biomech. 27, 8–14.
[9] Allison, M., Kang, Y., Maltese, M., Bolte, J., 2013. Validation of a Helmet-Based System to Measure Head Impact Biomechanics in Ice Hockey. Medicine and Science in Sports and Exercise, DOI: 10.1249/MSS.0b013e3182a32d0d.
[10] Yoganandan, N., Zhang, J., Pintar, F. A, Liu, Y., 2006. Lightweight low-profile nine-accelerometer package to obtain head angular accelerations in short-duration impacts. J. Biomech. 39, 1347–54.
[11] Hardy, W.N., Foster, C., Mason, M., Yang, K., King, A., Tashman, S., 2001. Investigation of Head Injury Mechanism Using Neutral Density Technology and High-Speed Biplanar X-ray. Stapp Car Crash Journal, 45, 337-368.
[12] SAE, 2007. Instrumentation for impact test, Part 1: Electronic instrumentation, SAE J211/1, Society of Automotive Engineers.
[13] Takhounts, E.G., Eppinger, R.H., Campbell, J.Q., Tannous, R.E., Power, E.D., Shook, L.S., 2003. On the Development of the SIMon Finite Element Head Model. Stapp Car Crash Journal, 47, 107-33.
[14] Takhounts, E.G., Hasija, V., Eppinger, R. H., 2009. Analysis of 3D Rigid Body Motion Using The Nine Accelerometer Array and the Randomoly Distributed in-plane Accelerometer Systems. In Proceedings of International Technical Conference on the Enhanced Safety of Vehicle, Stuttgart, Germany.
[15] Crisco, J.J., Chu, J.J., Greenwald, R.M., 2004. An Algorithm for Estimating Acceleration Magnitude and Impact Location Using Multiple Nonorthogonal Single-Axis Accelerometers. J. Biomech. Eng. 126, 849.
[16] Duma, S.M., Manoogian, S.J., Bussone, W.R., Brolinson, P.G., Goforth, M.W., Donnenwerth, J.J., Greenwald, R.M., Chu, J.J., Crisco, J.J., 2005. Analysis of real-time head accelerations in collegiate football players. Clin. J. Sport Med. 15, 3–8.
[17] Takhounts, E.G., Craig, M.J., Moorhouse, K., McFadden, J., 2013. Development of Brain Injury Criteria (BrIC). Stapp Car Crash Journal, 57, 243-66.
[18] Hardy, W.N., Mason, M., Foster, C.D., Shah, C.S., Kopacz, J.M., Yang, K.H., King, A.I., 2007. A Study of the Response of the Human Cadaver Head to Impact. Stapp Car Crash Journal, 51, 17-80.
[19] Becker, E., Willems, G., 1975. An experimentally validated 3-D inertial tracking package for application in biodynamic research. Stapp Car Crash Journal 19, 899-930.

# A STUDY OF BRAIN INJURY MECHANISMS IN VEHICLE CRASHES

**Takahiro Kikuchi**
**Atsushi Togawa**
**Daisuke Murakami**
**Kaoru Tatsu**
**Chinmoy Pal**
**Tomosaburo Okabe**
Nissan Motor Co., Ltd.
Japan

Paper Number 15-0207

## ABSTRACT

Brain injury has been researched since the 1940s and various methodologies have been discussed for evaluating brain injury risk in vehicle crash tests. In recent years, an angular velocity based brain injury criterion (BrIC) has been proposed by the National Highway Traffic Safety Administration (NHTSA) for use in regulatory or consumer vehicle safety assessment tests. One of the brain injury mechanisms can be explained by relative displacement between the brain and skull, resulting in brain deformation and strain. This paper states a hypothesis of this brain injury mechanism using a simple mass-spring-damper model. Then the hypothesis was verified by the Simulated Injury Monitor (SIMon) version 4.0, a finite element model of the human head developed by NHTSA, using a cumulative strain damage measure (CSDM) as the brain injury metric. In consequence, CSDM varies according to the input loadings, which have the same peak angular velocity but different levels of peak angular acceleration and loading durations. These results suggest that in order to evaluate brain injury risk accurately, an angular velocity based criterion may not always be sufficient and it may be necessary to consider the peak value of angular acceleration and the corresponding loading duration. This hypothesis was applied to NHSTA's research test data to prove its validity. It was found that brain injury risk predicted by CSDM can be comparatively lower than that predicted by BrIC and vice versa.

## INTRODUCTION

Brain injury is caused by either a direct contact force to the head or inertial loading from an indirect impact. In either case, the head undergoes both translational and rotational motion. Rotational motion of the head is purported to be the major factor of causing strain-induced brain injury [1-4]. CSDM is widely employed in this field as an injury metric for strain-related brain injury which is calculated by the fraction volume of brain which exceeds a prescribed strain level threshold. The accumulated volume fraction of damaged brain are thought to be related to diffuse axonal injury [2-4].

SIMon was used to examine the effect of head rotational motion on CSDM using NHTSA's research test data. Three variations of input to the skull were parametrically used: (i) both translational and rotational acceleration, (ii) only translational acceleration and (iii) only rotational acceleration. In both frontal and side impact tests, case (iii) showed that CSDM was approximately at the same level as that seen for the combined acceleration loading in case (i). By contrast, CSDM was almost zero in case (ii). These results indicated that rotational motion of head was the major contributor to CSDM [5].

In recent years, BrIC has been proposed as a brain injury predictor by NHTSA. It is calculated with Eq. (1).

$$\mathbf{BrIC} = \sqrt{\left(\frac{\omega_x}{\omega_{xc}}\right)^2 + \left(\frac{\omega_y}{\omega_{yc}}\right)^2 + \left(\frac{\omega_z}{\omega_{zc}}\right)^2} \tag{1}$$

where $\omega_x$, $\omega_y$ and $\omega_z$ are maximum angular velocities about the coronal, sagittal and transverse planes. $\omega_{xc}$, $\omega_{yc}$ and $\omega_{zc}$ are the critical angular velocities around each axis based on CSDM shown in Table 1.

**Table 1.**
**Critical angular velocity $\omega$ (rad/s) around each axis**

| | |
|---|---|
| $\omega_{xc}$ | 66.20 |
| $\omega_{yc}$ | 59.10 |
| $\omega_{zc}$ | 44.25 |

The heads of anthropomorphic test devices (ATDs) were impacted using a pendulum with and without a pad, and the resultant translational and rotational accelerations were measured. SIMon was used with translational and rotational data measured with the sensors on ATDs' heads to calculate CSDM and the maximum principal strain (MPS) on the brain. Risk curves for diffuse axonal injury were proposed with regard to BrIC [6].
The purpose of this study was to examine the effect of the peak value and loading duration of the angular acceleration on CSDM. The present hypothesis of brain injury is that the brain displacement depends on the peak angular acceleration and the loading duration, resulting in brain strain as a consequence. Firstly, brain displacement is explained with a simple mass-spring-damper model (simple model) in which physical paramaters are roughly estimated in reference to cadaveric experiments [7]. Loading pulses to the skull were parametrically input as sinusoidal functions which cover more than 95% of the loadings in 74 NHTSA research tests (Tabel A1) used in the literature [8]. The results were validated with SIMon. Secondly, NHSTA's reserch test data are applied to SIMon to calculate CSDM. The angular velocity based predictor, BrIC, is examined as to whether it is a rational predictor of CSDM, one of the brain injury metrics. Close examination of the plots of CSDM vs. BrIC can show that brain injury risk predicted by CSDM can be comparatively lower than that calculated by BrIC and vice versa. The reasons for this inversion are examined in terms of the peak and the duration of the resultant angular acceleration.

## METHODS

To examine the relationship between the relative displacement of brain and the loading pulse, a hypothesis for the mechanism of brain displacement is explained using a simple model as shown in Fig.1. Direct contact to the head or indirect inertial loading induces skull rotation indicated by the blue arrow in the left diagram, while the brain has a tendency to keep its position with respect to the inertial frame at $t = t_0$. After some delay ($\Delta t$) following the impact, the brain then starts to rotate (indicated by the green arrow in the right diagram), consequently producing relative displacement between the brain and skull ($\Delta Y$,$\Delta Z$), which induces brain deformation and strain.

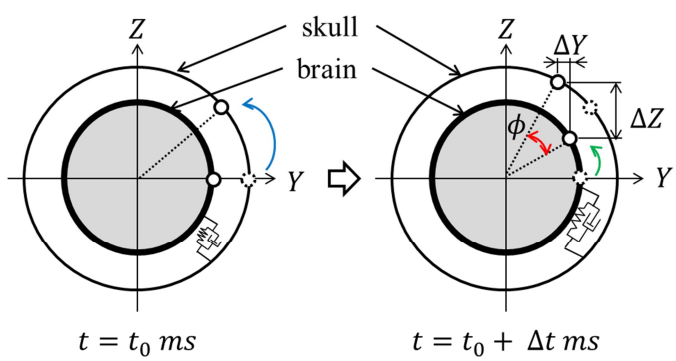


***Figure 1. A Simple Brain Displacement Model***

Assuming the input loading pulse to the head as a sinusoidal function [8-10], the equation of motion of the brain with respect to the skull, $\phi$ shown by red arrow in the right diagram, takes the form of Eq. (2).

$$\boldsymbol{I\ddot{\phi} + c\dot{\phi} + k\phi = A\Omega \sin \Omega t} \tag{2}$$

The steady-state solution of Eq.(2) can be expressed by Eq. (3).

$$\boldsymbol{\phi} = \frac{\mathbf{A\Omega}}{\sqrt{\left(\Omega_0^2-\Omega^2\right)^2+4\alpha^2\Omega}}\mathbf{sin}(\mathbf{\Omega t}+\boldsymbol{\delta}) \tag{3}$$

where, A: peak of the loading pulse, Ω: driving frequency, $\Omega_0$: undamped angular frequency of the oscillator and δ : induced phase change. It is seen that the peak relative angle of the brain with respect to the skull is a function of the amplitude of the driving force A and the driving frequency Ω which is the inverse of loading pulse duration. Coefficients of damper, c, and spring, k, were roughly estimated from the results of a cadaver head impact test C386-T6 in the literature [7] in which one of the test was conducted in the coronal plane and the specimen was impacted in the left-side temporal region.

To determine the loading pulse to the simple model, the peak values of both angular velocity and angular acceleration were investigated using 80 NHTSA research tests (Tabel A1) used in the literature [8]. The test data were for frontal impacts, side impacts with a moving deformable barrier (MDB), side impacts to a rigid pole and vehicle-to-vehicle side impacts. The ATDs used were the Hybrid-III 50th Male and the ES-2. Six out of 80 tests were excluded because the peak angular acceleration or the peak angular velocity in these tests were more than three standard deviations away from the mean value of those 80 tests. Fig.2 shows the peak angular velocity vs. peak angular acceleration of the 74 tests (blue dots). The red dots mean loading pulses which cover more than 95% of the tests as shown by shaded area in red. These three input pulses shown with the red dots were applied as the sinusoidal functions shown in Fig.3. For validation of the brain displacement results calculated with the simple model, CSDM was calculated by the SIMon version 4.0, using a strain threshold of 0.25 [6]. The loading pulses were the same as the ones used with the simple model and were applied around the coronal axis.

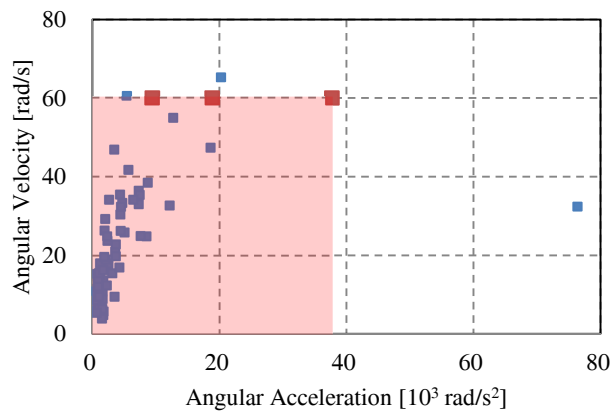


***Figure 2. Peak Angular Velocities and Angular Accelerations from 74 NHTSA Tests and Loading Pulses***

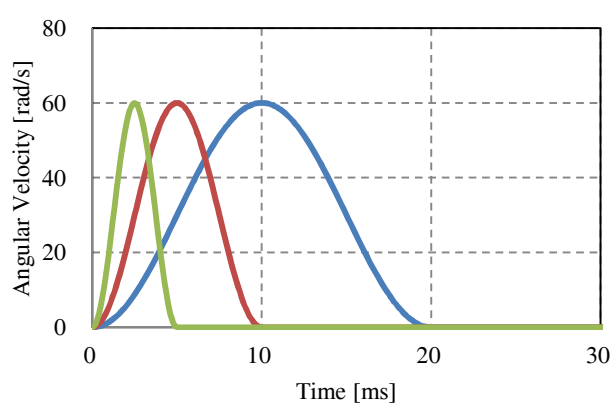


***Figure 3. Angular Velocities as Input Pulses***

In addition to the calculation above, the nine accelerometer data measured on ATDs' heads in 74 NHTSA research tests were applied to SIMon to calculate CSDM values under the loadings in vehicle crashes. BrIC was also calculated to examine whether it is a rational brain injury metric for predicting CSDM. In addition, the correlation between the angular acceleration and the gradient of CSDM, which is calculated from the difference of CSDM at time t and t+Δt (Δt=1ms), was examined by plotting their distributions with respect to time in order to estimate when and how much volume fraction of the brain exceeds the threshold strain level of 0.25.

## RESULTS

The relative displacements between the brain and skull calculated with the simple model are shown in Fig.4. The colors of curves correspond to the ones of the input loadings shown in Fig.3. The graph legend means the peak values of the angular acceleration of the input loading pulses. The results show that the relative displacements varied even though the peak angular velocities did not change as shown in Fig.3. The loading pulse having the longest loading duration due to the lowest peak acceleration shown with blue curve produces the largest relative displacement of the brain. This suggests that the longer is the loading duration due to the lower peak acceleration, the larger is displacement.

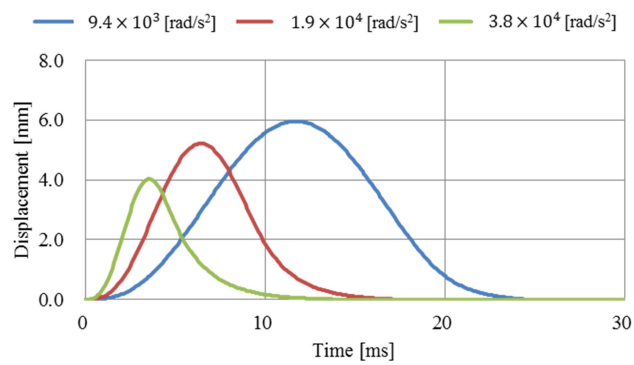


***Figure 4. Relative Displacement between the Brain and Skull calculated by Simple Model***

Fig.5 shows the time histories of CSDM calculated by SIMon using the same input pulses of the simple model shown in Fig.3. The legends of the graph correspond to the peak values of the angular acceleration of the input loading pulse. Referring to the blue curve, the CSDM value for the loading pulse having the longest loading duration and the lowest peak angular acceleration, reaches a level of 50% at around 25 ms. On the other hand, referring to the green curve, the CSDM value for the input loading having the shortest loading duration and the highest peak angular acceleration, reaches a level of 22% at around 10 ms.

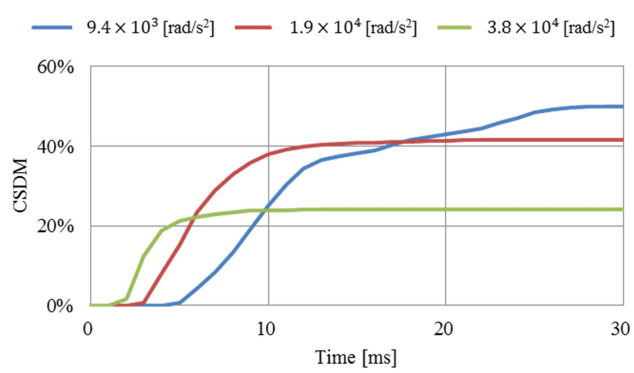


***Figure 5. CSDM Data calculated with SIMon***

Next, the above hypothesis obtained from the calculation by the simple model and SIMon was applied to NHSTA's research test data to prove its validity. In consequence, comparison of a pair of research tests (v03800 and v04292) shows that the brain injury risk predicted by CSDM can be comparatively lower than that calculated by BrIC and vice versa as shown Fig.6. The CSDM (Fig. 6a) and BrIC (Fig. 6b) values of these two tests, corresponding to their individual AIS 4+ brain injury risk curves, are plotted in blue and red squares on the dotted curves [6]. The CSDM value in the v03800 test is about two times higher than that of the v04292 test; while the BrIC value in v03800 is 0.05 lower than that in v04292.

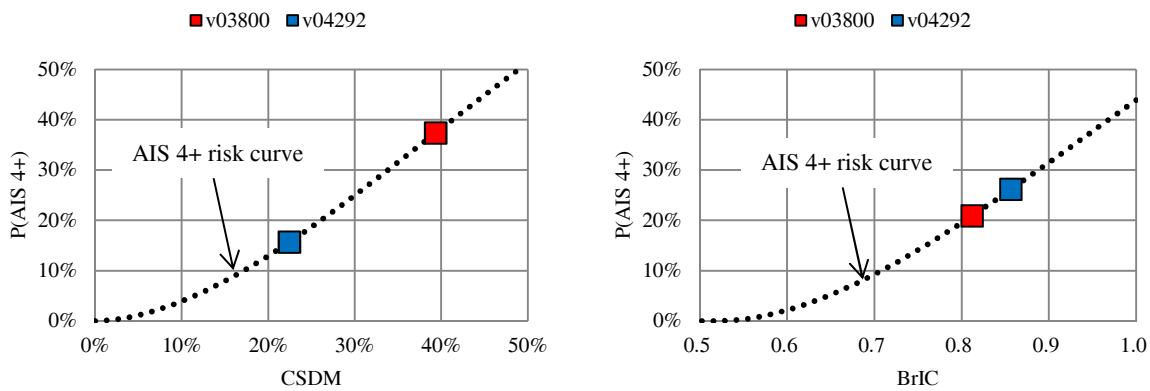


***(a)*** ***(b)***

***Figure 6. AIS 4+ Risk Curves for (a) CSDM and (b) BrIC based on CSDM of Brain Injuries***

Fig.7 shows time histories of the angular velocities and CSDM in (a) v03800 and (b) v04292. In both tests, the maximum angular velocities in the three axes are marked by dotted ellipses, which are used to calculate BrIC. Thorough observation of Fig.7 (a) shows the results for the v03800 test in which an increase of CSDM is seen after 50 ms. At nearly the same time, the angular velocity around the x-axis and y-axis changes from positive (A-A) to negative peak (B-B). Hence, the change in angular velocity, i.e. the angular acceleration in this period seems to cause the increase in CSDM from 0 to 39%. On the other hand, Fig. 7(b) shows the results for the v04292 test in which an increase of CSDM is seen around 50 ms (C-C). In this test, the value of the change in angular velocity may be about one half of that for v03800. The CSDM value is also about one half of that for v03800. These results suggest that the magnitude of the change in angular velocity seems to be related to the value of the CSDM.

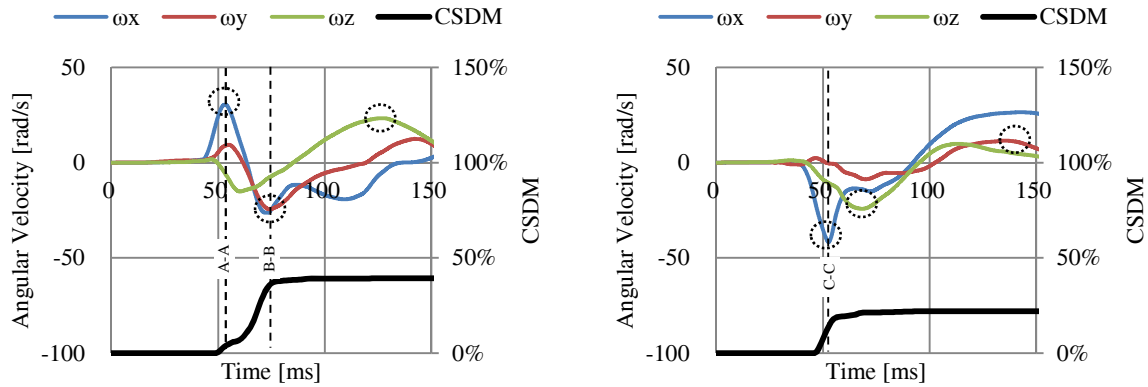


***(a)*** ***(b)***

***Figure 7. Angular Velocities and CSDM in (a) v03800 and (b) v04292***

Fig.8 shows CSDM versus BrIC plot of 74 tests. Among the tests results as marked in dotted ellipse as shown in Fig.8, the pair of tests, such as shown above in Fig.6 and Fig.7, can be seen frequently. For example, within one dotted ellipse, the lower right plots have relatively higher BrIC values than the upper left plots, while CSDM values of the lower right plots are lower than the ones of the upper left plots. The pair of tests shown above in Fig.6 and Fig.7 are marked in black.

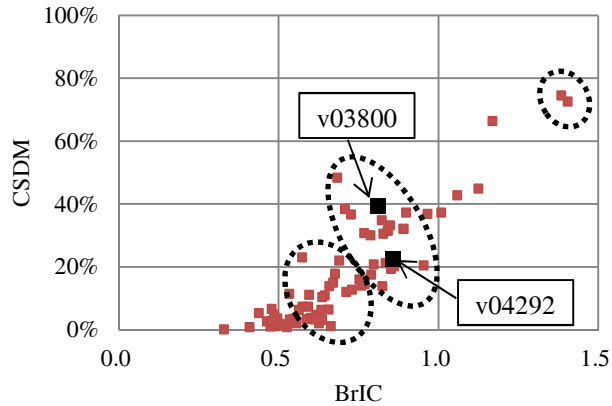


***Figure 8. CSDM versus BrIC of 74 tests calculated by SIMon***

Fig.9 shows time histories of the resultant angular acceleration and the volume fraction of the brain in 4 tests. The test numbers are shown below the corresponding graphs. These graphs show that the volume fraction of the brain that exceeds the strain level of 0.25 increases just after the resultant angular acceleration increases. These results suggest that the rate of change in CSDM might be influenced by the resultant angular acceleration.

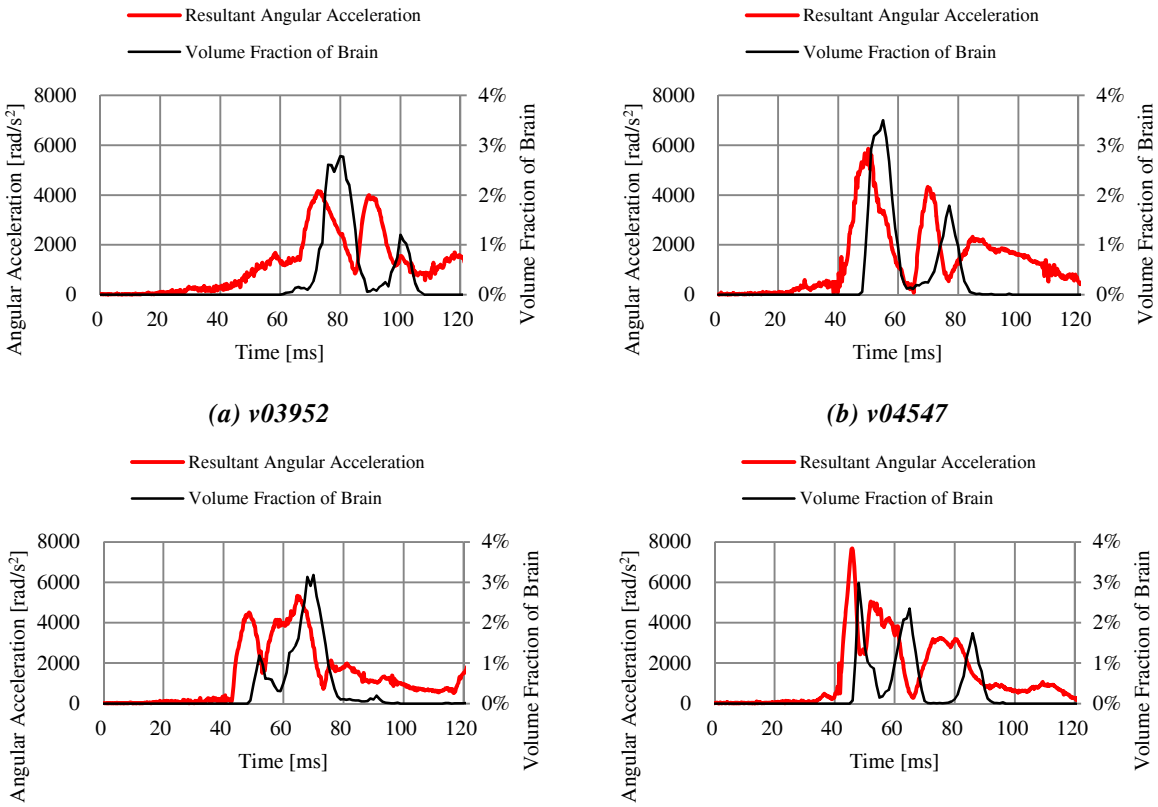


***(a) v03952***

***(b) v04547***

***(c) v03800***

***(d) v04380***

***Figure 9. Resultant Angular Acceleration and Volume Fraction of Bran in 4 tests***

## DISCUSSION

An injury criterion based only on angular velocity might not be an accurate brain injury metric for predicting CSDM values. The peak values of relative displacement between brain and skull calculated by simple model varied under the different loading pulses with the same peak angular velocity. The results of simple model were verified by FEM

based SIMon model. The CSDM values calculated by SIMon showed the same tendency as that of the simple model. In the vehicle crash test, BrIC, one of the angular velocity based injury criterion, not always accord with the predicted result based on CSDM value calculated by SIMon as shown in Fig.6 and Fig.7. The CSDM value in the v03800 test is approximately twice as large as the value in the v04292 test. However, the BrIC value in the former test hovers at a level of just 0.05 lower than that in the latter test. Such pairs of tests are found frequently as shown in Fig.8. Within one dashed ellipse in Fig.8, the lower right plots have relatively higher BrIC values than the upper left plots, but CSDM values of the lower right plots are lower than the upper left ones. This inversion of the relationship between CSDM and BrIC might lead to mislead consumers about the crash safety performance of vehicles, if the present BrIC estimation is used in regulatory or consumer vehicle safety assessment tests.
Presumably, one of the reasons why BrIC does not necessarily predict CSDM value is that BrIC considers only the absoulte peak angular velocity and does not take into account the peak value of angular acceleration and corresponding loading duration. The peak value and loading duration of angular acceleration might affect the relative displacement of the brain as shown Eq.(3) and Fig.4. This hypothesis was verified by SIMon as shown in Fig.5. The loading pulse having the longest loading duration due to the lowest peak acceleration produces the largest relative displacement of the brain and CSDM value. The gradient of CSDM with respect to time showed when and how much volume fraction of the damaged brain swelled. Fig.9 indicated that the volume fraction of the damaged brain increased with increasing resultant angular acceleration with some delay. These results suggest that the rate of change in CSDM might be influenced by the resultant angular acceleration.

## CONCLUSIONS

This study highlighted the importance of considering the peak value of angular acceleration and the corresponding loading duration when evaluating brain injury risk based on CSDM. In addition, an injury criterion based only on an angular velocity might cause misunderstanding of consumers about the crash safety of vehicles with respect to brain injury risk. More research is needed before adopting such criteria for evaluating brain injury risk in regulatory or consumer vehicle safety tests.

## REFERENCES

[1] Holbourn, A. H. S., 1943. "Mechanics of head injuries." Lancet 2:438-441.
[2] Bandak, F.A. and Eppinger, R.H. 1995. “A three-dimensional finite element analysis of the human brain under combined rotational and translational acceleration.” Proc. 38th Stapp Car Crash Conference, pp. 145-163.
[3] Bandak, F.A., 1995. “On the Mechanics of Impact Neurotrauma”, Journal of Neurotrauma 12, 4, pp.635-649
[4] DiMasi, F.P., Eppinger, R.H., Bandak, F.A., 1995. “Computational analysis of head impact response under car crash loadings.” Proc. 39th Stapp Car Crash Conference, pp. 425-438.
[5] Zhang, J., Yoganandan, N., Pintar, F. A., Gennarelli, T. A., 2006. “Brain Strains in Vehicle Impact Tests.” 50th Annual Proceedings Association for the Advancement of Automotive Medicine, Vol.50, pp. 1-12.
[6] Takhounts, E.G., Craig, T. J., Moorhouse, C. K., McFadden, J., Hasija, V., 2013. “Development of Brain Injury Criterion (BrIC).” Stapp Car Crash Journal, Vol. 57, pp. 243 - 266.
[7] Hardy, W.N., Mason, M.J., Foster, C.D., Shah, C.S., Kopacz, J.M. Yang, K.H., King, A.L., Bishop, J., Bey, M., Andrest, W., Tashman, S. 2007. "A Study of the Response of the Human Cadaver Head to Impact." Stapp Car Crash Journal, Vol. 51, pp. 17 - 80.
[8] Takhounts, E.G., Eppinger, R.H., Campbell, J.Q., Tannous, R.E., Power, E.D., Shook, L.S., 2003. “On the Development of the SIMon Finite Element Head Model.” Stapp Car Crash Journal, Vol. 47, pp. 107-133.
[9] Takhounts, E.G., Hasija, V., Ridella, S.A., Tannous, R.E., Campbell, J.Q., Malone, D., Danelson, K., Stitzel, J., Rowson, S., Duma, S., 2008. “Investigation of Traumatic Brain Injuries Using the Next Generation of Simulated Injury Monitor (SIMon) Finite Element Head Model.” 52nd Stapp Car Crash Conference.
[10] Zhang, L., Yang, K.H., Dwarampudi, R., Omori, K., Li, T., Chang, K., Hardy, W.N., Khalil, T.B., King, A.I, 2001. “ Recent advances in brain injury research: a new human head model development and validation.” Stapp Car Crash Journal, Vol. 45, pp. 369-394.
[11] Hardy, W.N., Foster, C., Mason, M., Yang, K., King, A., Tashman, S., 2001. “Investigation of head injury mechanisms using neutral density technology and high-speed biplanar X-ray.” Stapp Car Crash Journal, Vol. 45, pp. 337 – 368.

## Appendix

Table A1. NHTSA's research tests data.

| Frontal impact tests | | | Side impact tests | | |
|---|---|---|---|---|---|
| **Test Number** | **Occupant** | **Test Condition** | **Test Number** | **Occupant** | **Test Condition** |
| v04303 | Driver | Vehicle into barrier | v03800 | Driver | MDB into vehicle |
| v04242 | Driver | Vehicle into barrier | v04551 | Driver | MDB into vehicle |
| v04205 | Passenger | Vehicle into barrier | v03875 | Driver | MDB into vehicle |
| v04273 | Driver | Vehicle into barrier | v03899 | Driver | MDB into vehicle |
| v04198 | Driver | Vehicle into barrier | v03818 | Driver | Vehicle into pole |
| v03897 | Driver | Vehicle into barrier | v04547 | Driver | MDB into vehicle |
| v04266 | Passenger | Vehicle into barrier | v04380 | Driver | MDB into vehicle |
| v04247 | Driver | Vehicle into barrier | v03845 | Driver | Vehicle into pole |
| v03916 | Driver | Vehicle into barrier | v04497 | Driver | Vehicle into pole |
| v04081 | Passenger | Vehicle into barrier | v04547 | Passenger | MDB into vehicle |
| v04264 | Passenger | Vehicle into barrier | v03898 | Driver | Vehicle into pole |
| v03901 | Passenger | Vehicle into barrier | v04551 | Passenger | MDB into vehicle |
| v04250 | Driver | Vehicle into barrier | v03799 | Passenger | MDB into vehicle |
| v04251 | Driver | Vehicle into barrier | v04380 | Passenger | Vehicle into pole |
| v04215 | Passenger | Vehicle into barrier | v03820 | Driver | Vehicle into pole |
| v04237 | Passenger | Vehicle into barrier | v04456 | Passenger | MDB into vehicle |
| v04080 | Driver | Vehicle into barrier | v03819 | Passenger | MDB into vehicle |
| v04205 | Driver | Vehicle into barrier | v04378 | Driver | Vehicle into pole |
| v04090 | Driver | Vehicle into barrier | v04292 | Driver | Vehicle into vehicle |
| v04264 | Driver | Vehicle into barrier | v04498 | Driver | Vehicle into pole |
| v04090 | Passenger | Vehicle into barrier | v03803 | Passenger | MDB into vehicle |
| v04223 | Passenger | Vehicle into barrier | v03802 | Driver | Vehicle into pole |
| v04267 | Passenger | Vehicle into barrier | v04292 | Passenger | Vehicle into vehicle |
| v04215 | Driver | Vehicle into barrier | v03803 | Driver | MDB into vehicle |
| v04242 | Passenger | Vehicle into barrier | v04482 | Driver | Vehicle into vehicle |
| v04259 | Driver | Vehicle into barrier | v03800 | Passenger | MDB into vehicle |
| v03987 | Driver | Vehicle into barrier | v04471 | Driver | Vehicle into pole |
| v03915 | Driver | Vehicle into barrier | v04313 | Driver | Vehicle into pole |
| v04255 | Passenger | Vehicle into barrier | v03819 | Driver | MDB into vehicle |
| v04235 | Driver | Vehicle into barrier | v04086 | Driver | MDB into vehicle |
| v04235 | Passenger | Vehicle into barrier | v04284 | Driver | Vehicle into pole |
| v04265 | Passenger | Vehicle into barrier | | | |
| v04292 | Passenger | Vehicle into barrier | | | |
| v04240 | Driver | Vehicle into barrier | | | |
| v04237 | Driver | Vehicle into barrier | | | |
| v04259 | Passenger | Vehicle into barrier | | | |
| v04198 | Passenger | Vehicle into barrier | | | |
| v03915 | Passenger | Vehicle into barrier | | | |
| v03952 | Driver | Vehicle into barrier | | | |
| v03901 | Driver | Vehicle into barrier | | | |
| v04241 | Driver | Vehicle into barrier | | | |
| v04252 | Driver | Vehicle into barrier | | | |
| v03952 | Passenger | Vehicle into barrier | | | |

**GLOSSARY**

ATD: anthropomorphic test device
BrIC: brain injury criteria
CSDM: cumulative strain damage measure
MPS: maximum principal strain
NHTSA: National Highway Traffic Safety Administration
SIMon: Simulated Injury Monitor

**Occupant Behavior and Brain Injury in NHTSA Oblique Test**

**Jeong Keun, Lee**
Hyundai Mobis
Republic of Korea

**Hyo bae, Lee**
**Hun hee, Jeong**
Hyundai Mobis
Republic of Korea

Paper Number 15-0397

## ABSTRACT

The National Highway Traffic Safety Administration (NHTSA) found that a large number of fatalities occurred in crashes involving poor structural interaction between the striking and the struck vehicles, such as corner impacts, oblique crashes, or impacts with narrow objects.
NHTSA proposed the oblique test that can reproduce vehicle crush, occupant kinematics, and risk of injury in vehicle-to-vehicle crashes, an offset impact between a research moving deformable barrier (RMDB) and a stationary vehicle at a 15 degree angle.
Recent research for NHTSA oblique test with THOR ATD showed the lateral movement of both occupants, so that the driver's head contact with door or between door and steering wheel. For the far-side occupant, the head contact with center IP and the brain injury risk predicted using BrIC is higher than SOI.
The objective of this paper is to investigate and understand the effect of airbag performance on the occupant kinematics and related injury during NHTSA oblique tests. This paper focuses on effect of various airbag parameters corresponding to the dynamic stiffness.
The research integrated the injury analysis with a crash testing and computer simulation. MADYMO was used to create a NHTSA oblique test environment. Both 50th percentile THOR ATD and Hybrid III in MADYMO were respectively used to simulate occupant kinematics and injuries for the driver and passenger occupant. Airbag models for curtain airbag and passenger airbag are used in the simulations in order to understand the effect of various restraint system concepts on occupant kinematics and injuries.
In this paper, driver side airbag and passenger side airbag are investigated for both near-side occupant and far-side occupant. CAE models are used to show their advantages and limitations. Further enhancements are proposed to improve the correlation of these occupant models. Passenger side airbag and driver side airbag are investigated to reduce the brain injury and head contact with compartment. NHTSA oblique test case is used to demonstrate the effectiveness of the airbag variations.
Limitations of the current airbag model used for NHTSA oblique test were highlighted. Vent hole was modified to improve the head injury.
For reducing the brain injury risk of occupant in an NHTSA oblique test, it was found counter measures which didn't cause head rotation was effective.

## INTRODUCTION

The past several years, most vehicles have achieved the good ratings in the IIHS frontal tests, and NHTSA's frontal NCAP. This aroused the IIHS and NHTSA to investigate further test configurations for frontal impacts in order to improve the occupant safety. The Small Overlap Impact (SOI) test shown in Figure 1 has been introduced by IIHS, that is a 64 km/h frontal crash test in which 25% of the front-end of a vehicle is overlaped by a rigid barrier. The vehicle structural performance, restraints and dummy kinematics, and dummy injury measures are used to rate the vehicle's overall safety performance as Good, Acceptable, Marginal or Poor. Four groups of dummy injury ratings utilize the instrumentation in the dummy's head and neck, chest, hip and thigh, and legs and feet. The vehicle structural rating is based upon the pre-test and post-test measurements of seven various locations. Prior to the designing a NHTSA oblique test, shown in Figure 1, the NHTSA investigated fatal frontal crashes in the NASS database in which the occupants were belted non-ejected and the vehicles were equipped with frontal airbags. A large number of fatalities occurred in crashes involving poor structural interaction between the striking and the

struck vehicles in the report published in 2009[1]. On the other hand, full-frontal or offset-frontal impacts with good structural interaction ended in less fatalities, unless the crashes were of extreme severity or the occupants were exceptionally vulnerable. As a result of the NHTSA study, the agency stated its intent to further analyze small overlap and oblique frontal crashes [2]. NHTSA had conducted a large number of frontal crash tests, and developed a moving deformable barrier crash test, shown in Figure 1. The ″research" moving deformable barrier (RMDB) impacts the target vehicle at 90 kph (56 mph) and the stationary vehicle is positioned such that the angle between the RMDB and the vehicle is 15 degrees and the overlap is 35 percent on the driver side of the vehicle[3]. The RMDB's mass is 2490.7 kg (5491 lb.).

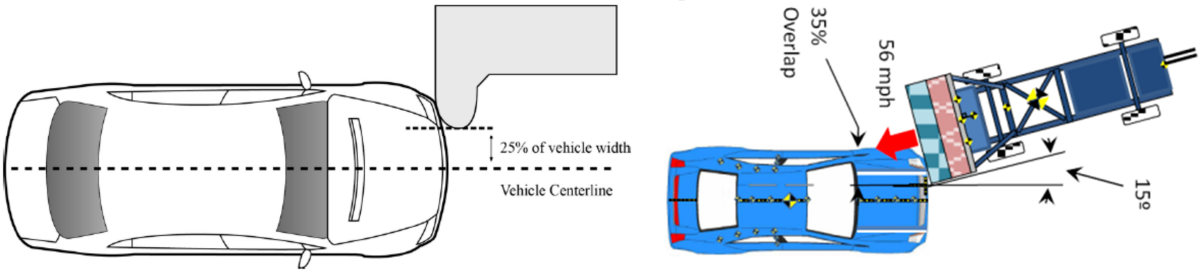


***(a) IIHS Small Overlap*** ***(b) NHTSA RMDB***

***Figure1. Scheme of IIHS Small Overlap and NHTSA RMDB.***

The hybrid III frontal crash test dummy is developed at 1970's and the development of an advanced frontal crash test dummy with improved biofidelity under frontal impact conditions and with expanded injury assessment capabilities is needed. Under these circumstances, in 2001 an advanced frontal crash test dummy THOR (Test Device for Human Occupant Restraint) - Alpha version was developed in the United States[4]. After the THOR Alpha, later upgraded to the THOR-NT in 2005. A modification package ("Mod Kit") intended to enhance the biofidelity, repeatability, durability, and usability of the THOR was introduced in 2011 and installed as an upgrade kit on the NHTSAowned fleet of THOR-NT ATDs[5]. Recent research showed that THOR dummy injury measures are closer to those of the post mortem human surrogates (PMHS) than the Hybrid III By continuous improvement of THOR dummy[6]. Comparing responses of the THOR and the Hybrid III with the same conditions, the upper body of the THOR moved forward more, compared to the Hybrid III, and the torsion about the z-axis was also larger than the Hybrid III. As a result, the head acceleration of the THOR and the Hybrid III showed different responses. NHTSA Oblique RMDB crash tests included an anthropomorphic test device (ATD) seated in the driver (near-side) and passenger(far-side) position. These ATDs are a 50$^{th}$ percentile male THOR. Due to the test configuration of NHTSA Oblique RMDB, both side occupants responses in NHTSA's tests showed rotational head velocities and resulted in high risk of brain injury. Rotational motion of the head can cause the brain injury and rotational kinematics experienced by the head may cause axonal deformations large enough to induce their functional deficit[7].

## OBJECTIVES

The objectives of this study are:

1. Estimate the CAE simulation method of the oblique RMDB test for correlation refer to the dummy kinematics and the brain injury comparision between CAE result and test data.
2. Compare the dummy injury responses between THOR and Hybrid III in Oblique RMDB tests.
3. Estimate the sensitivity of the brain injury to different parameters of airbag .

## METHODOLOGY

A correlated NHTSA NCAP model was used to build a NHTSA oblique RMDB baseline model. Modeling method for RMDB occupant analysis was constructed using both deceleration method and rigid body motion method as shown in Figure 2. The deceleration method is commonly used modeling method for FMVSS208 and NHTSA NCAP. The rigid body motion method is constructed by using the test motion of the tested vehicle. Structural intrusion data was extracted from a full vehicle test. The vehicle intrusion at struck side during test was used to replicate the vehicle test and to correlate the low extremity injuries and dummy kinematics. Hybrid III 50th percentile dummy was used first as a driver and a passenger occupants in order to compare the injury responses of THOR and Hybrid III dummy. This model used driver side airbag, passenger side airbag, curtain airbag, retractor and pre-tensioner as a restraint system.

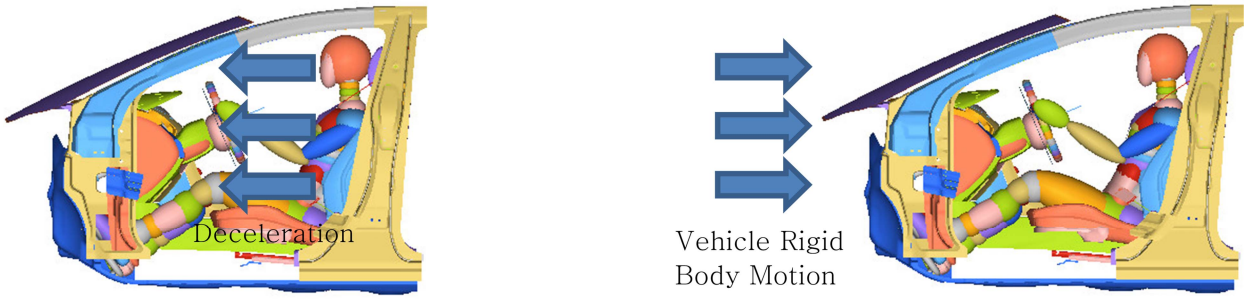


***Figure2. Occupant Simulation Modeling Methods for RMDB.***

Both baseline models used for this study demonstrated good correlation with NHTSA Oblique RMDB test. Validation index is unique index for evaluating the injury correlation rating of CAE model. Validation indices for the deceleration method and the rigid body motion method are 89 and 90 points respectively. This means both modeling methods give the similar injury response in peak and phase. For NHTSA Oblique RMDB test condition, occupant kinematics of the rigid body motion method showed better correlation with the test. This occupant kinematic correlation is shown in Figure 3.

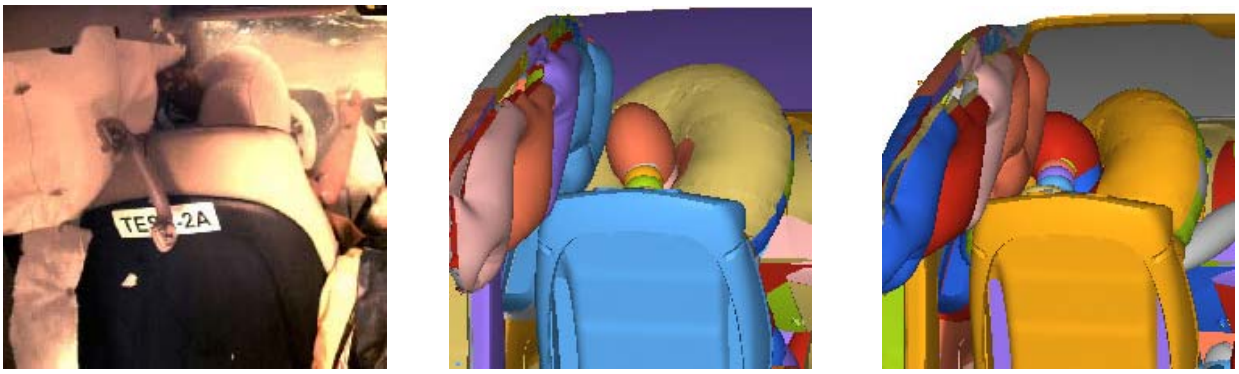

***(a) Test*** ***(b) Simulation w/Deceleration*** ***(c) Simulation w/Rigid Body Motion***

***Figure3. Dummy Kinematics.***

With this correlated model using the rigid body motion method, further study was conducted in order to understand the injury trends and occupant kinematics with variation of parameters. The passenger side occupant kinematics of the rigid body motion method showed good correlation with the test in Figure 4.

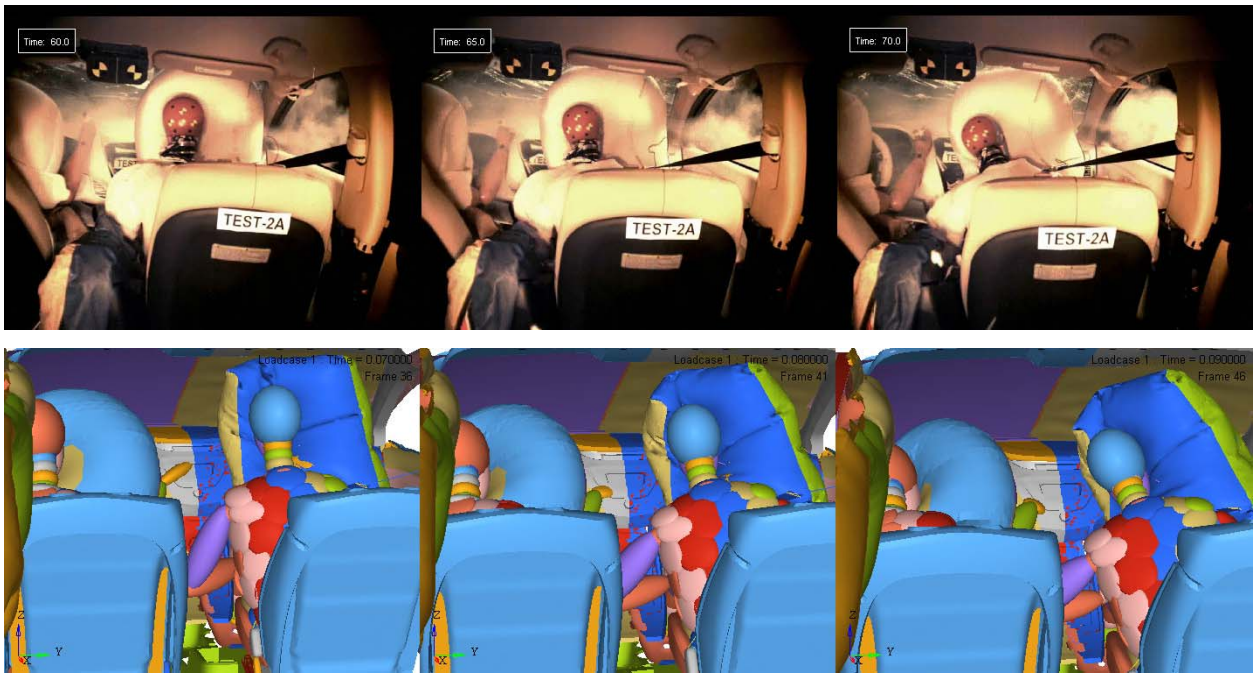


***Figure4. Comparison of Passenger Dummy Kinematics between Test and Simulation.***

**RESULTS**

This study evaluated the kinematic and the brain injury responses of a THOR and the 50th percentile Hybrid III in the NHTSA Oblique RMDB frontal impact condition. The 50th percentile Hybrid III dummy is replaced by the THOR in the baseline model and then compared with the test results and the injury tendency. It was observed from the CAE simulation result data that the brain injury of the THOR dummy tended to increase about 30~51% with respect to the Hybrid III dummy. Figure 5 compares injuries for THOR dummy and Hybrid II dummy. BrIC values were higher for THOR dummy in both driver and passenger. This increasing tendency of the brain injury is also observed in the tests. The differences of neck joints between THOR dummy and Hybrid III dummy caused the increasing of the BrIC.

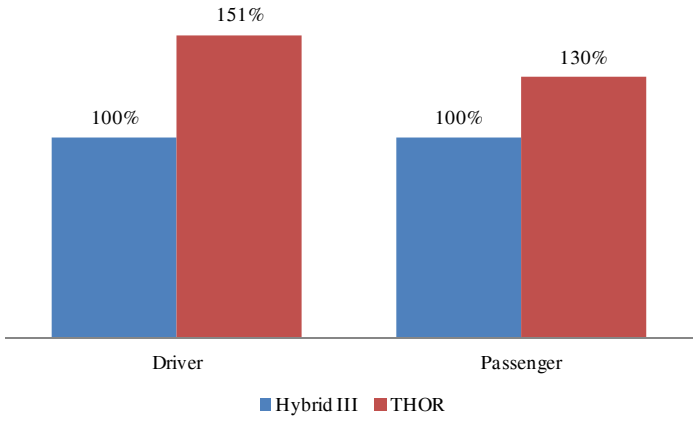


***Figure5. BrIC Response of THOR and Hybrid III***

The purpose of this parameter study was to understand the effectiveness of the restraint system based on airbag's internal pressure. To achieve this, airbag's outer vent was varied at every 5 mm step.

Figure 6 compares internal pressure and BrIC for various vent hole size. Outer vent hole size variation analysis showed that as internal pressure decreased, BrIC is increased. Head X travel and Y rotational velocity were increased with decrease in internal pressure level of DAB. Since DAB's reaction force was reduced, it allowed dummy head and chest to travel farther increasing the dummy's forward movement.

From the internal pressure analysis of PAB, it was observed that with decrease in internal pressure level of PAB, BrIC was decreased slightly. It was seen at the lowest level of BrIC for 60mm outer vent. The lower internal pressure result in decreasing Z rotational velocity of the passenger's head.

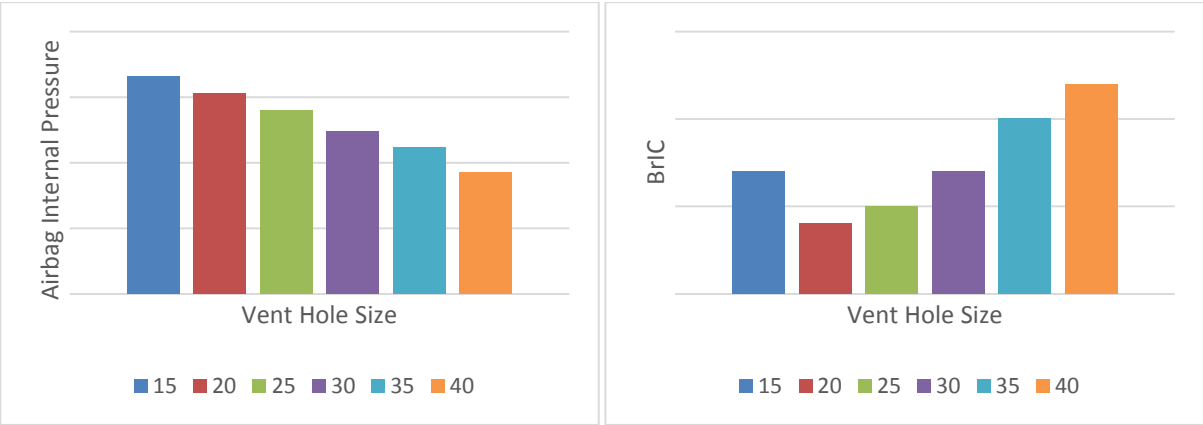


***Figure6. Driver BrIC w.r.t Outer Vent Size.***

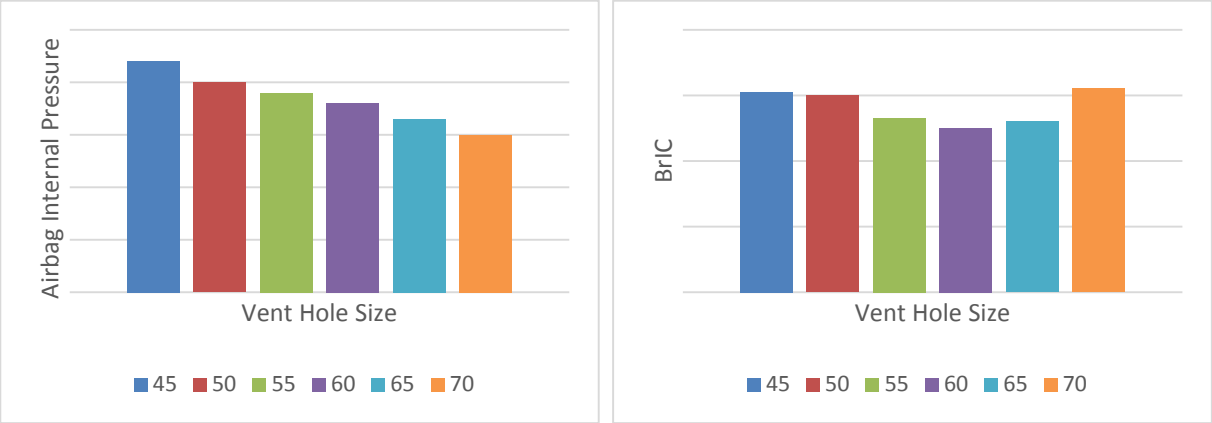


***Figure7. Passenger BrIC w.r.t Outer Vent Size.***

## CONCLUSIONS

1. For dummy injury response, there is slight difference between the deceleration method and the rigid body motion method. The rigid body motion method for CAE modeling gives better correlation in dummy kinematics with the test both driver side and passenger side occupants.

2. It was observed from CAE simulation result data that the brain injury of the THOR dummy tended to increase about 30~51% with respect to the Hybrid III dummy. This increasing tendency of the brain injury is also observed in the tests.
3. Head rotational velocity depends on the internal pressure of the airbag, the pressure stratage should be used for major component of BrIC. The strategy for achieving highest injury rating in NHTSA NCAP should be modified to meet the NHTSA Oblique RMDB BrIC requirements.

**REFERENCES**

[1] Bean, J., Kahane, C. K., Mynatt, M., Rudd, R. W., Rush, C. J. and Wiacek, C. 2009. "Fatalities in Frontal Crashes Despite Seat Belts and Air Bags- Review of All CDS Cases- Model and Calendar Years 2000-2007 – 122 Fatalities." Report No. DOT HS 811 102. US DOT, Sept. 2009.

[2] Saunders, J., Craig, M. and Parent, D. 2012. "Moving Deformable Barrier Test Procedure for Evaluating Small Overlap/Oblique Crashes." SAE World Congress, Paper No. 2012-01-0577.

[3] Saunders, J. and Parent, D. 2013. "Assessment of an Oblique Moving Deformable Barrier Test Procedure." Paper No.: 13-0402, 23rd ESV Conference, Seoul, Korea.

[4] Haffner M., Eppinger R., Rangarajan N., Shams T., Artis M., Beach D. 2001. "Foundations and Elements of the NHTSA THOR Alpha ATD Design," Proceedings of the 17th International Technical Conference on the Enhanced Safety of Vehicles.

[5] Daniel P. Parent, Matthew Craig, Stephen A. Ridella, Joseph D. McFadden. 2013. ), "Thoracic Biofidelity Assessment of the THOR mod kit ATD", Paper No.: 13-0327, 23rd ESV Conference, Seoul, Korea.

[6] Greg Shaw, David Lessley, Joe Ash, Jeff Crandall and Dan Parent. 2013. "Response Comparison for the Hybrid III, THOR Mod Kit with SD-3 Shoulder, and PMHS in aSimulated Frontal Crash" Paper No.: 13-0130, 23rd ESV Conference, Seoul, Korea.

[7] Erik G. Takhounts, Matthew J. Craig, Kevin Moorhouse, Joe McFadden and Vikas Hasija. 2013. "Development of Brain Injury Criteria (BrIC)" Stapp Car Crash Journal, Vol. 57, 243-266

# PROPOSAL FOR A MODIFIED THOR LOWER ABDOMEN INCLUDING ABDOMINAL PRESSURE TWIN SENSORS

**Sabine Compigne**
Toyota Motor Europe NV/SA
Belgium

**Mitsutoshi Masuda**
Toyota Motor Corporation
Japan

**Gaëtan Hanen**
**Philippe Vezin**
**François Bermond**
Université de Lyon, Université Claude Bernard Lyon 1, IFSTTAR, LBMC UMR_T 9406
France

Paper Number 15-0216

## ABSTRACT

This paper presents the evaluation of a modified THOR-NT lower abdomen which includes two abdominal pressure twin sensors (APTS®) as replacement for the displacement measurements. Further small changes such as the addition of small masses in front of the abdomen have also been made to better mimic the response of the PMHSs under seat belt loading. As a result, the biofidelity of the prototype abdomen was improved compared to THOR-NT standard abdomen. The addition of the small masses succeeded in increasing the initial peak force of the force-penetration response under seat belt tests. In rigid bar impacts, the prototype force-deflection response stayed longer in the corridor. The pressure measurement was repeatable and discriminated the various impact speeds as well as the impact direction. The pressure peaks were proportional to force and penetration peaks. This study demonstrates the feasibility of introducing the APTSs into THOR lower abdomen and makes proposals for further biofidelity enhancements.

## INTRODUCTION

The Test Device for Human Occupant Restraint (THOR) is an advanced anthropomorphic test device designed to represent the automotive occupants in the sophisticated restraint systems, such as force-limited three-point belts and air bags. The first THOR version, THOR alpha, was released in 2000. Since then the dummy version has evolved into THOR-NT (NHTSA, 2005), THOR Mod Kit (Ridella et al., 2011) and THOR Metric (Parent, 2014). The current study focuses on the THOR lower abdomen which design has not changed along THOR versions except for the instrumentation. THOR abdomen biofidelity specifications are defined for a 6.1 m/s rigid-bar test simulating an impact to the lower rim of the steering wheel as previously tested by Cavanaugh et al. (1986) on Post Mortem Human Subjects (PMHSs). However, the seatbelt is reported nowadays as the most common abdominal injury source of belted occupants involved in a frontal collision (Huelke et al., 1993; Klinich et al., 2008). Rear seat occupants are especially concerned since they are reported to have a significantly higher rate of sustaining a moderate or severe abdominal injury compared to front seat occupants (Lamielle et al., 2006; Martin et al., 2010; Frampton et al., 2012). Several biomechanical studies investigated swine (Miller et al., 1989; Kent et al., 2008) or human abdomen responses (Hardy et al., 2001; Trosseille et al., 2002; Foster at al., 2006; Lamielle et al., 2008) under seatbelt loading which allow the evaluation of the dummy response. Some of the mentioned biomechanical studies investigated various abdominal injury predictors such as abdominal compression, belt tension, penetration speed, viscous criterion, force "viscous criterion", work of belt tension. Arterial and venous pressure peaks have also been proposed to serve as injury predictor of abdominal organs (Miller et al., 1989; Ruan et al., 2005; Kremer et al. 2011). Beillas et al. (2012) demonstrated the ability to measure pressure inside child Q-dummy abdomen using the Abdominal Pressure Twin Sensors (APTS®). The APTSs could detect injurious abdominal loading for child Q3 and Q6 dummies with an estimated risk of sustaining an AIS3+ abdominal injury of 50% at 1.09 bars. Hanen et al. (2011, 2012), Masuda et al. (2012) investigated the introduction of the APTSs inside the THOR lower abdomen. This paper presents the results of the prototype delivered in 2012 and developed from THOR-NT dummy version.

## MATERIAL AND METHOD

### THOR lower abdomen prototype

THOR-NT lower abdomen is made of two foam blocks and of an internal mounting weld assembly enclosed in a Cordura nylon bag. Two DGSPs (Double Gimbaled String Potentiometer) go through two holes in the foam blocks. They are attached to the rear on each side of the spine to mounting brackets and to the front of the abdominal bag. The DGSPs measure the three dimensional displacements of the two points on the bag surface. The whole lower abdomen assembly can be accessed by opening a zipper placed on the abdomen bag (NHTSA, 2005) (Figure 1).

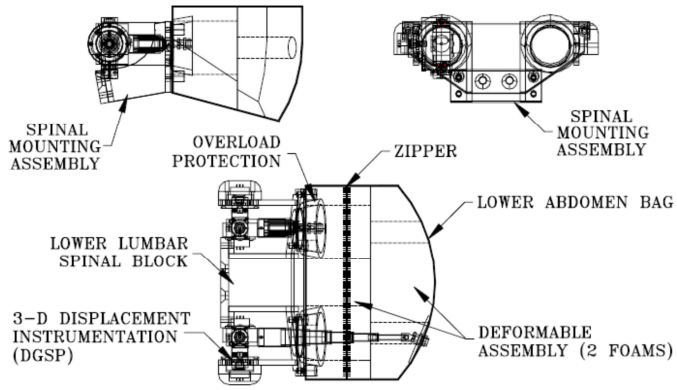


***Figure 1. THOR-NT lower abdomen assembly (NHTSA, 2005).***

The THOR lower abdomen prototype is made from THOR-NT abdomen components. An exploded view of the prototype assembly is shown in Figure 2. New front and rear foam blocks were ordered without holes as DGSPs are not used anymore. Instead two new vertical holes of 51 mm diameter with center axes spaced by 90 mm were made in the front foam block to receive the APTSs (Figure 3). The APTSs (version 2) were inserted with their caps downwards. The version 2 is composed of a 50 mm diameter soft polyurethane bladder filled with paraffin oil. The APTS has one cap through which oil is entered using a pressure column to provide consistent filling conditions. Pressure measures are made by XPR30 subminiature pressure sensors (Measurement Specialties, Les Clayes, France) placed in the balled cap at the interface with the oil (Beillas et al., 2012). Mounting brackets to the spine and abdomen internal plate geometries were simplified. The brackets allow a simpler mounting and dismounting of the entire abdomen assembly from the spine (Figure 4, Figure 5). The wires of the APTSs exit from the bottom of the front foam, go through two cuts made in the rear foam and finally pass through the holes of the modified internal plate and the abdomen bag.

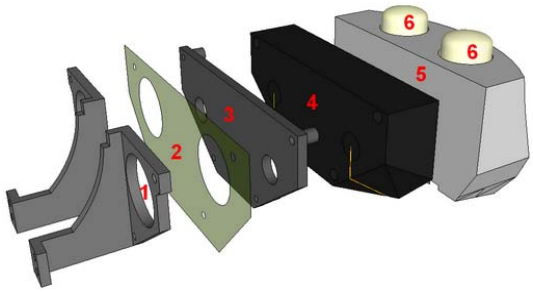


***Figure 2. Abdomen prototype exploded view: (1) Right and left modified mounting brackets (2) Cordura bag (3) Modified internal plate (4) Rear foam block (5) Front foam block (6) Right and left APTSs.***

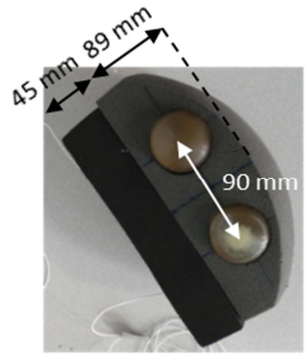


***Figure 3. Top view of abdomen prototype equipped with the APTSs (dimensions measured from dummy parts) .***

***Figure 4. Standard (top) and modified (bottom) abdomen internal plate.***

***Figure 5. Standard (top) and modified (bottom) mounting bracket to the spine.***

Fifteen steel cylinders of 30 mm diameter and 10 mm thickness are attached to the front of the abdomen bag using a Velcro® layer (Figure 6). They represent an additional mass of 825 g. The total mass of the prototype with the attachment brackets is 3.12 kg (THOR-NT abdomen assembly is 2.60 kg). The prototype abdominal depth is 292 mm and 282 mm without the small masses. This has to be compared with the THOR-NT abdominal depth of 265 mm. The abdomen prototype can similarly be mounted on THOR Mod Kit and THOR-Metric thanks to similar lower abdomen/spine assemblies between the dummies.

***Figure 6. Abdomen prototype assembly with the small masses attached to the Cordura bag.***

**Test set-ups**

The abdomen prototype response was evaluated under rigid bar impact and seatbelt loading as performed previously by Hanen at al. (2011) on THOR-NT standard abdomen. Its response was compared to available Post Mortem Human Subject (PMHS) corridors and standard THOR-NT abdomen response re-analysed from Hanen et al. (2011). Additional tests at various speeds (1 to 6.1 m/s) and different impact angles (0° and 20°) were performed to evaluate the sensitivity of the APTS measurement.

**Rigid bar impact** The THOR-NT dummy equipped with the abdomen prototype was submitted to 32 kg impactor tests according to Cavanaugh et al. (1986) test set-up. The impactor was equipped with a 25 mm diameter rigid bar of length 300 mm. Initial impact speed was varied from 1 to 6.1 m/s. The dummy was placed on a table covered by a Teflon® sheet with outstretched legs. The lumbar spine joint was in slouch position (9° between lumbar bracket and pelvis bracket) and the back was unsupported. The hands were attached at the head level. The table height was adjusted to align the rigid bar with the line joining the centers of the attachment nuts of the DGSPs (Figure 7).

The impactor was instrumented with a 20 kN SEDEME SAM-load cell and a 100 g ENTRAN EGCS-S067 uniaxial accelerometer. A light gate measured the impact speed just prior to the contact between the impactor bar and the dummy. The THOR dummy pelvis was instrumented with a 250 g ENTRAN EGAS-S077B three-axis accelerometer. A laser ODS 1150 (900 mm range, 0.1 mm resolution) was positioned in the back of the dummy and measured its pelvis displacement. Data acquisition was made at 20 kHz using Kistler acquisition system and channels were filtered according to SAE J211 using a low pass band Butterworth filter (CFC180 for the accelerations, pressures and laser displacement, CFC600 for the force).
Two high-speed cameras (Photron SA3 black and white) recorded the impact at a rate of 2000 frames/s with a resolution of 1024×1024 pixels. One camera filmed the overall scene and the other one was placed perpendicular to the dummy sagittal plane to measure the impactor and dummy pelvis displacements using Motion Track® software. The time "zero" was identified on the video by a flash which was lit up when the rigid bar came in contact with the dummy suit.
Impact force could be obtained by multiplying the impactor longitudinal acceleration by its mass (32 kg) or by the impactor load cell once corrected for the mass placed in front of the sensor (2.62 kg). Consistency of the force response obtained by these two means was checked. Abdomen penetration was measured as the difference between the impactor displacement and the one of the dummy pelvis obtained by the video analysis. Consistency with other measurements (difference of the double integration of impactor and dummy pelvis longitudinal accelerations) was also checked.
Abdominal penetration measured from the video was re-sampled using linear interpolation at 20 kHz to draw the force-penetration response.

**Seatbelt loading** The THOR-NT dummy equipped with the abdomen prototype was submitted to seatbelt loading according to Foster at al. (2006) test set-up. The dummy was seated on the floor covered by a Teflon® sheet with the legs outstretched and the back against a vertical rigid plate. The dummy lumbar spine joint was in slouch position and its arms were attached to the vertical structure at the head level. The seatbelt was wrapped around the abdomen at mid height and guided from the lateral aspects of the dummy abdomen. The same pretensioner systems as in Foster et al. (2006) study were used and denoted similarly Type A, B and C. Type B and C consisted of a single pretensioner (at different levels of pretension, respectively) whereas Type A consisted of two Type B pretensioners. In addition to Foster's configurations, two Type C pretensioners were also tested. In the case of a single pretensioner system, the webbing was attached on itself using a clamp whereas in the case of a dual pretensioner system, a webbing piece was wrapped around the dummy and its extremities were sewn to each pretensioner webbing. The longitudinal position of the pretensioner support was adjusted to set an initial small tension inside the webbing (10 to 20 N) (Figure 8).
Two 500 g ENTRAN EGAS-S077D uniaxial accelerometers were mounted on each side of the webbing together with two 16 kN MEAS EL20-S458 seatbelt load cells. The same laser as in the rigid bar impact was positioned in front of the dummy and targeted the dummy umbilicus. The dummy pelvis was instrumented with a 250 g ENTRAN EGAS-S077B three-axis accelerometer. Data acquisition was made at 20 kHz using Kistler acquisition system and channels were filtered according to SAE J211 using a low pass band Butterworth filter (CFC180 for the accelerations, pressures and laser displacement, CFC600 for the force).
Two Photron high-speed cameras recorded the impact at a rate of 2000 frames/s. One camera was placed in front of the dummy and the other one was placed to the right of the dummy, perpendicular to the dummy sagittal plane to record the seatbelt and the dummy pelvis displacements. Motion Track® software was used to perform the video analysis. The time "zero" was identified on the video by a flash which was lit up when firing the pretensioner.
Applied force to the abdomen was obtained by adding the forces recorded by both seatbelt load cells. Abdomen penetration was measured as the difference between the seatbelt displacement at dummy umbilicus level and the displacement of the dummy pelvis obtained by the video analysis. Consistency with other measurements (abdominal displacement measured by the laser and pelvis displacement obtained by the double integration of the pelvis longitudinal acceleration) was also checked.
Abdominal penetration measured from the video was re-sampled using linear interpolation at 20 kHz to draw the force-penetration response.

The prototype abdomen responses were overlaid in each test configuration with THOR-NT standard abdomen and, when available, with PMHS corridors. Dummy responses under rigid-bar impacts were compared with Cavanaugh et al. (1986) and Hardy et al. (2001) PMHS corridors defined using average force-penetration responses firstly filtered at 100 Hz and CFC60 respectively and scaled to a 76 kg subject using Eppinger

(1976) equal-stress/equal-velocity technique. Dummy responses under seatbelt loadings were compared with Foster et al. (2006) PMHS corridors defined using average force-penetration responses firstly filtered at CFC600 and scaled to a 78 kg subject using Eppinger (1976) equal-stress/equal-velocity technique.
In all studies, the corridors were calculated from the average response plus and minus one standard deviation. The linear approximations of corridors established in Hardy's and Foster's papers are used here. Cavanaugh's corridor was digitised from the paper.

***Figure 7. Rigid bar impact test set-up.***

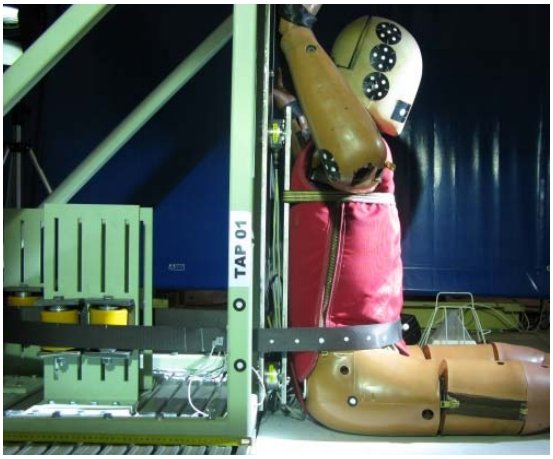


***Figure 8. Seatbelt loading test set-up.***

**Test matrices** Rigid bar impacts were performed with impact speeds ranging from 1 to 6.1 m/s. Each test condition was at least repeated twice. Oblique impacts at 20° towards the right side of the dummy were also conducted at 3 m/s impact speeds to assess directional sensitivity. One test at 3 m/s was performed without the prototype front masses to quantify their effect. The prototype abdomen response was compared to the standard abdomen one at 3 and 6.1 m/s impact speeds (Table 1).

***Table 1. Rigid bar impact test matrix.***

| Test Id (Prototype abdomen) | Velocity (m/s) | Impact angle (°) | Test Id (Standard abdomen, Hanen et al., 2011) |
|---|---|---|---|
| TME82, 83 | 1 | 0 | NA |
| TME84, 85 | 2 | 0 | NA |
| TME79, 80, 81[(1)] | 3 | 0 | TME02, 03 |
| TME77, 78, 88, 89 | 3 | 20 | NA |
| TME90, 91 | 4 | 0 | NA |
| TME92, 93 | 5 | 0 | NA |
| TME94, 95 | 6.1 | 0 | TME04, 05 |

[(1)]The masses in front of the abdomen were removed.

Seatbelt tests were conducted according to Table 2. Four loading conditions were applied to the abdomen. Each test condition was at least repeated twice. The prototype abdomen response was compared to the standard abdomen one under Type B and C test conditions.

***Table 2. Seatbelt test matrix.***

| Test Id (Prototype abdomen) | Loading type | Test Id (Standard abdomen) |
|---|---|---|
| TAP39, TAP40 | C | TAP04, TAP05 |
| TAP41, TAP42, TAP47[(2)] | B | TAP02, TAP03 |
| TAP43, TAP44 | 2×C | NA |
| TAP45, TAP46 | A (2×B) | NA |

[(2)]The masses in front of the abdomen were removed.

## RESULTS

### Prototype biofidelity

**Rigid bar impact** Figure 9 shows the force-time and the penetration-time responses of the standard and the prototype abdomen under 6.1 m/s rigid bar impact. The changes in force-time slopes and small peaks were correlated with the events observed on the video. Overall, the force peaks recorded for the standard abdomen are higher than those of the prototype abdomen and the penetration peaks are slightly higher for the prototype.
The first slope of the force curve of the standard abdomen is related to the abdomen jacket and front foam compression whereas in the prototype, the addition of the small masses gives first a steeper rise of the force during approximately the first 10 mm of penetration. At around 13 ms, the impactor hits the pelvis flesh of the dummy equipped with the standard abdomen. The effect of this contact is visible on the force slope of the standard abdomen due to the stiffness difference between the front abdomen foam and the pelvis flesh. At the moment the impactor slides over the flesh pelvis, the force drops suddenly for the standard abdomen and the penetration continues to increase. The impactor starts to move the dummy at around 27-30 ms, almost 10 ms after the force peak.
The contact with the pelvis flesh happened later with the prototype abdomen (at around 21 ms, 8 ms later than the standard abdomen). The compression of the APTS which happened in addition to the flesh compression increased more gradually the force before the impactor contacts the pelvis flesh. The force peak and the start of the dummy motion happened almost at the same time. The penetration peak occurred around 6 ms after the force peak due to the fact that the impactor continued to move inside the dummy after going above the pelvis flesh. By looking at the movie, this phenomenon was related to the impactor rigid bar mounting which was not sufficiently reinforced to avoid the impactor upwards bending due to the abdomen /pelvis reaction force (Figure 10). The movie showed that the impactor bar slid along the pelvis flesh whereas for the standard abdomen, a significant compression of the pelvis flesh was seen before the impactor could ride above it. For the prototype abdomen, it is expected that such ride off the pelvis flesh may not happen for a more rigidly mounted impacting face and therefore, the maximum penetration would correspond to the maximum force and would likely be lower.

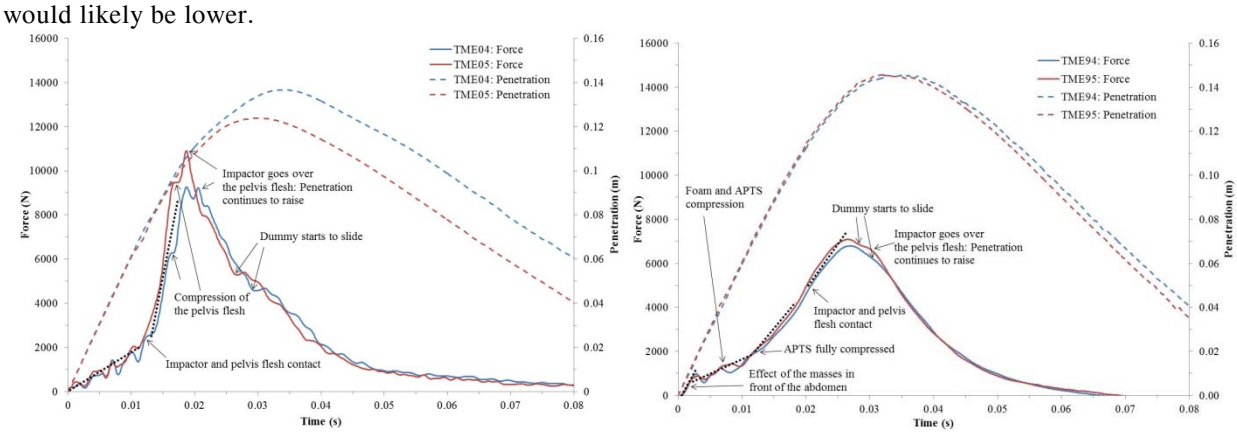


***Figure 9. Force-time and Penetration-time responses of the standard (left) and the prototype (right) abdomen for 6.1 m/s rigid bar impact.***

The difference in time for the impactor contact with the pelvis flesh between the standard and the prototype abdomens was mainly due to their abdomen width difference. Figure 11 shows both abdomens in front of the impactor. By looking at the jacket profile, it is visible that the prototype abdomen protrudes more outside of the pelvis flesh. The small masses and the APTS increase the prototype depth whereas in the standard abdomen, the DGSPs attached at the front of the abdomen bag compress the front foam. Approximately an additional 45 mm penetration was measured at the time of impactor-pelvis contact in the case of the prototype compared to the standard abdomen.

*Figure 10. Impactor rigid-bar upwards bending.*

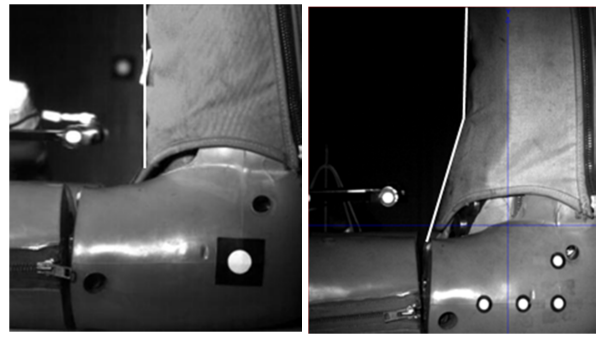

*Figure 11. Depth of standard abdomen (left) and prototype abdomen (right).*

Figure 12 and Figure 13 show the force-penetration responses of the two abdomens. Peak values are reported in Table 3. At 3 m/s, no contact was recorded between the impactor and the pelvis flesh for the dummy equipped with the prototype abdomen. On the opposite, this contact occurred at around 33 ms (88 mm penetration) with the standard abdomen. This increased the force peak (Figure 12). At 6.1 m/s, the prototype abdomen response stayed a bit longer in the PMHS corridors. This was due to a later contact with the pelvis flesh (at 119 mm penetration compared to 80 mm for the standard abdomen). Before that point, between 90 and 120 mm penetration (front foam block and APTS were fully compressed), the response of the prototype exceeds the upper bound of the PMHS corridor which seems to highlight a too stiff response of the abdomen rear foam block (Figure 13).

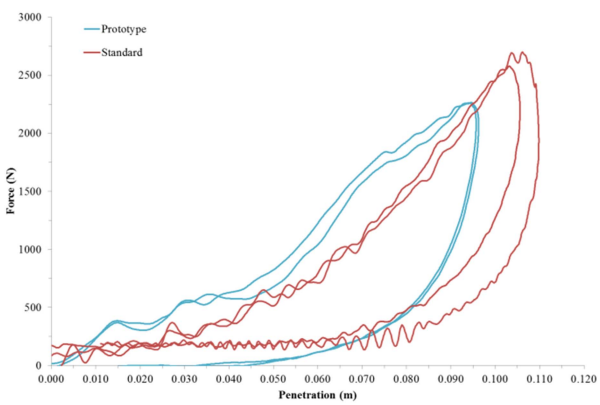


*Figure 12. Force-penetration of the standard (in red) and prototype (in blue) abdomens at 3 m/s rigid bar impact.*

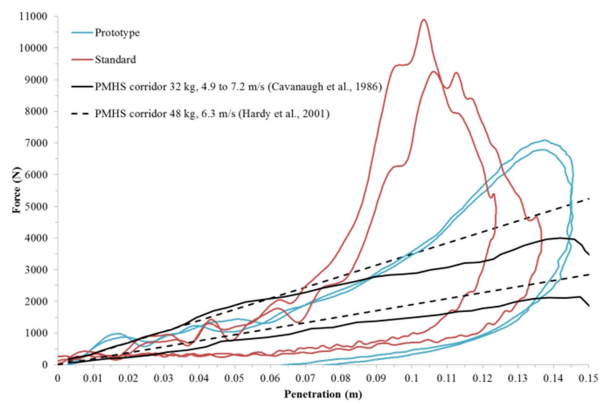


*Figure 13. Force-penetration of the standard (in red) and prototype (in blue) abdomens overlaid with the scaled PMHS corridor at 6.1 m/s rigid bar impact.*

*Table 3. THOR-NT and Prototype peak values under rigid-bar impacts.*

| | Force Peak (N) | | Penetration Peak (mm) | |
|---|---|---|---|---|
| **Velocity (m/s)** | **NT** | **Prototype** | **NT** | **Prototype** |
| 3 | 2578 / 2699 | 2263 / 2265 | 106 / 110 | 96 / 96 |
| 6.1 | 9255 / 10902 | 6791 / 7088 | 137 / 124 | 146 / 146 |

**Seatbelt loading** Figure 14 and Figure 15 overlay the force-penetration responses of the standard THOR-NT abdomen, the prototype abdomen, the responses of a single PMHS (for Type C) and the PMHS corridors as defined by Foster et al. (2006) (for Type B and A). On Figure 14, the large force variations seen from 8 to 12 mm penetration were attributed to the left seatbelt sensor. The reason for these sudden variations is unknown and could not be checked from the video as the camera was on the right side of the dummy. Generally, the force measured at the webbing is increased for the prototype compared to the standard abdomen. However, this increase is still not sufficient to match PMHS responses. The penetration is also much lower than that of the PMHSs (Table 4). Foster et al. (2006) obtained 25%, 35% and 55% PMHS abdominal compression for

pretensioner Type C, B and A respectively, whereas 8%, 20% and 28% abdominal compression was reached with the abdomen prototype (292 mm abdominal depth is considered for the abdomen prototype). The standard abdomen gave similar compression to the prototype: 6% and 18-19% under pretensioner Type C and B (265 mm abdominal depth is considered for THOR-NT).

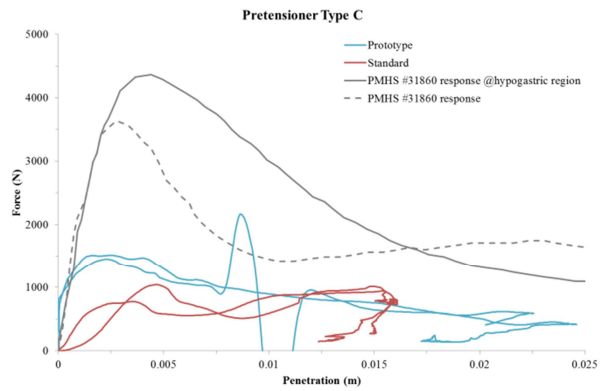


***Figure 14. Force-penetration response of the standard and prototype abdomen compared to Foster et al. (2006) PMHS scaled responses (seatbelt load CFC180 versus penetration CFC60) for pretensioner Type C.***

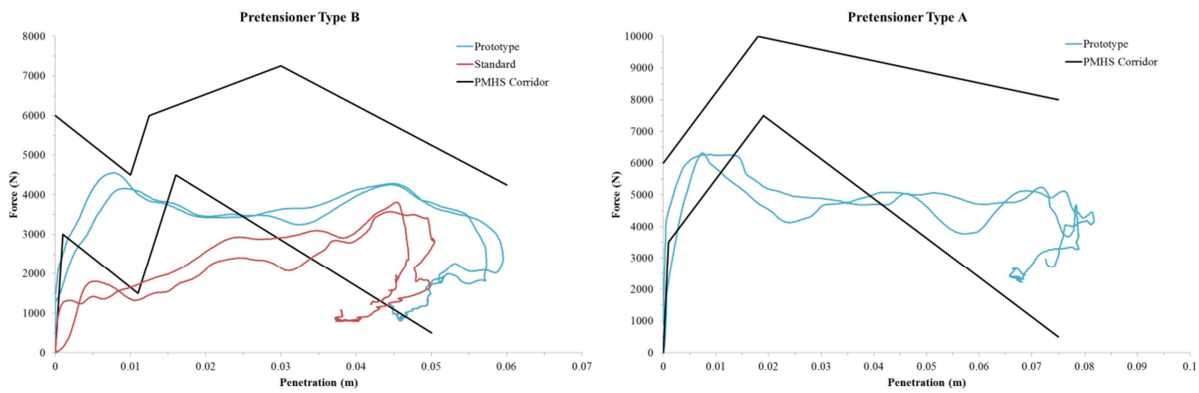


***Figure 15. Force-penetration response of the standard and prototype abdomen compared to Foster et al. (2006) PMHS scaled corridors for pretensioners Type B (left) and A (right, only prototype).***

***Table 4. THOR-NT, Prototype and PMHS peak values under pretensioners Type C, B, A.***

| | Force Peak (N) | | | Penetration Peak (mm) | | |
|---|---|---|---|---|---|---|
| **Loading Type** | **NT** | **Prototype** | **PMHS (Scaled)** | **NT** | **Prototype** | **PMHS (Scaled)** |
| C | 939 / 1039 | 1451 / 1513 | 4363 / 3636 | 16.1 / 15.9 | 24.6 / 22.6 | 63.6 / 66.1 |
| B | 3573 / 3811 | 4257 / 4551 | 5593/5128/6726 | 50.4 / 47 | 57.3 / 59.5 | 97.6/93.6/107.4 |
| A | NA | 6318 / 6265 | 8289 / 7938<br>9737 / 9370 | NA | 78.9 / 81.8 | 123.6 / 112.1<br>153.2 / 128.5 |

**<u>Effect of the APTS and small masses</u>** Force-compression responses of the standard abdomen, of the prototype abdomen without the small masses, and of the prototype with the small masses are compared in Figure 16 and Figure 17 under rigid bar impact and pretensioner loading respectively. Compression is considered here to take into account the differences in abdomen depth between the THOR-NT (265 mm), the prototype without the small masses (282 mm) and the prototype abdomen (292 mm). Starting from the THOR-NT response, the addition of the APTS and of the small masses allowed the gradual increase of the force. The compression of the three abdomens is similar under the Type B seatbelt loading and smaller for the prototype under the 3 m/s rigid bar impact.

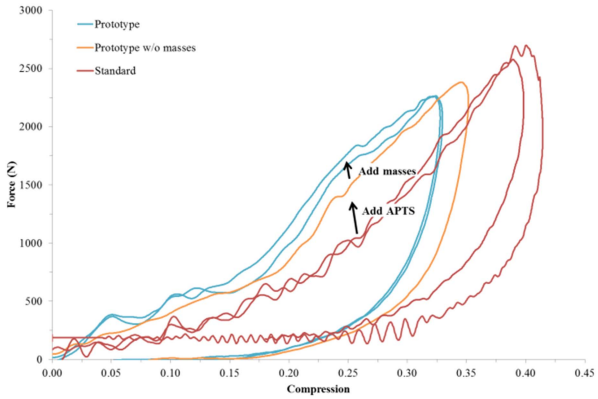


***Figure 16. Force-compression responses of THOR-NT abdomen, prototype without small masses and prototype under 3 m/s rigid bar impact.***

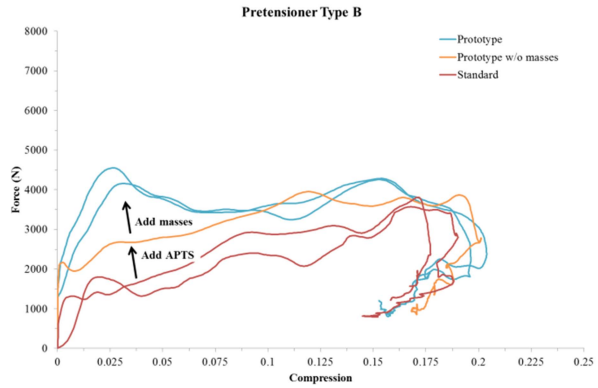


***Figure 17. Force-compression responses of THOR-NT abdomen, prototype without small masses and prototype under pretensioner Type B loading.***

**Sensitivity to speed**

Figure 18 shows the force-penetration responses of the prototype abdomen under 32 kg rigid-bar impacts and for speed variations between 1 and 6.1 m/s. The force and the penetration peaks raise with increasing speed. The force peaks vary between 400 and 7100 N and the penetration peaks vary between 46 mm and 145 mm. The loading slope also increases with the increased penetration at higher speed due to the compression of abdomen components. The contact between the rigid-bar and the pelvis flesh only occurred at 6.1 m/s. For 4 and 5 m/s impacts, the rigid bar rode over the pelvis flesh without touching it. This explains why the penetration peak occurred after the force peak. This kind of behaviour would not be expected with a reinforced rigid bar and in that case, the loading force would increase with a steeper slope up to the peak. Figure 19 overlays the force-penetration responses of the prototype for the various pretensioner types. The average retraction speeds of the seatbelt measured by video analysis using the targets placed on the side of the webbing are mentioned in the figure key. The retraction speed varied from 6.5 to 16 m/s. A first force peak is observed on all the curves at the very beginning of the penetration (at 2 and 10 mm for the slower and the higher retraction speed respectively). For Type B and A, this initial peak is followed by a decrease in force and a plateau almost up to the maximum penetration. For Type C and 2C, the force decreases after the initial peak until the maximum penetration. The force and the penetration peaks are increased with the retraction speed. A large jump in absorbed energy (area under force-penetration curves) is seen between Type 2C and B from 50 to 200 J.

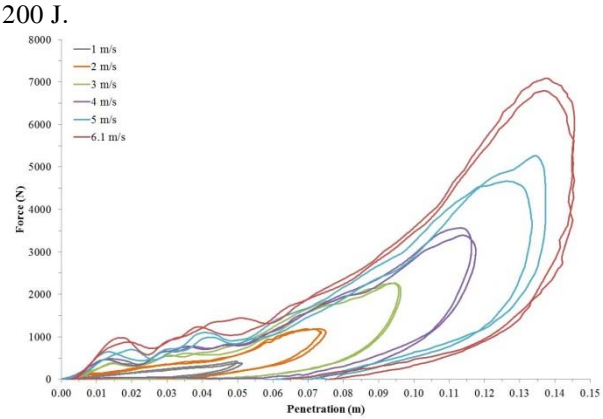


***Figure 18. Prototype abdomen force-penetration responses under 32 kg rigid-bar impacts for impact speed ranging from 1 to 6.1 m/s.***

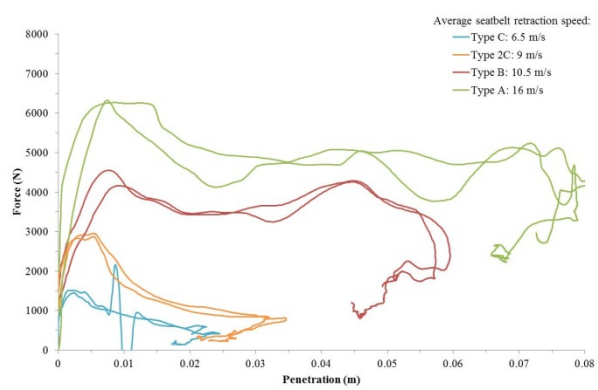


***Figure 19. Prototype abdomen force-penetration responses under pretensioners Type C, 2C, B and A.***

**APTS measurements**

Figure 20 to Figure 23 show APTS pressure versus abdomen penetration for rigid bar impacts and seatbelt loading. Under seatbelt loading, the pressure peaks are observed at the beginning of the penetration. The APTS pressure peaks occur between 10 mm (pretensioner Type C) and 35 mm (pretensioner Type A) penetration. Figure 24 and Figure 25 reveal that pressure peaks are synchronized with force peaks in the case of the prototype without the small masses and delayed by around 4 ms in the case of the prototype. Indeed, with the little masses, the first force peak is linked to the masses inertia whereas there is little abdomen penetration.

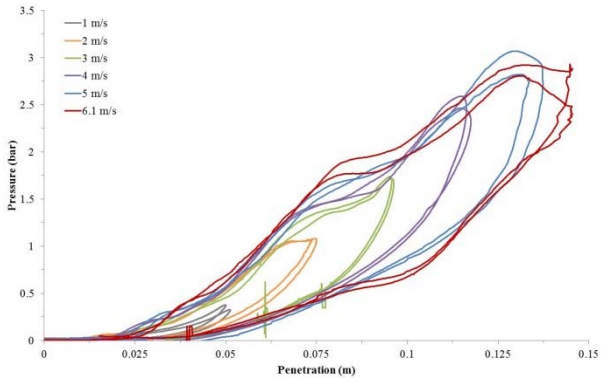


***Figure 20. Left APTS pressure versus abdomen penetration for rigid-bar impacts from 1 to 6.1 m/s.***

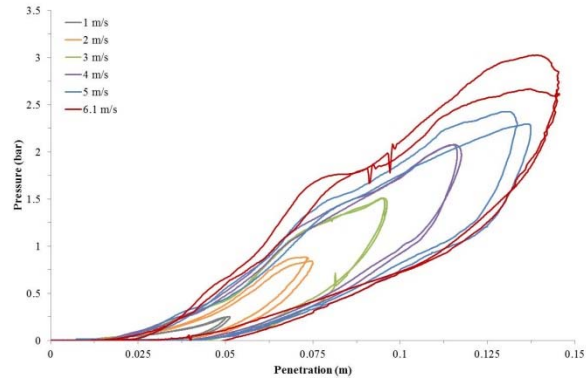


***Figure 21. Right APTS pressure versus abdomen penetration for rigid-bar impacts from 1 to 6.1 m/s.***

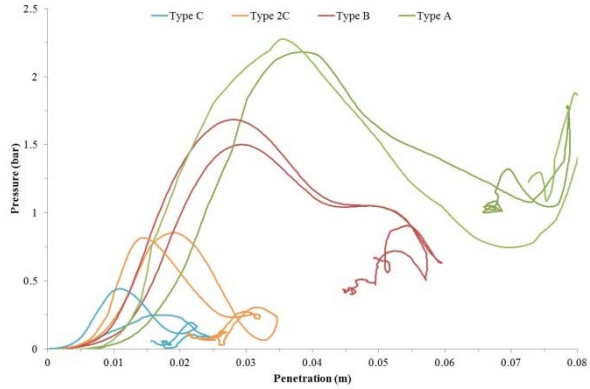


***Figure 22. Left APTS pressure versus abdomen penetration for seatbelt loading using pretensioner Type C, 2C, B and A.***

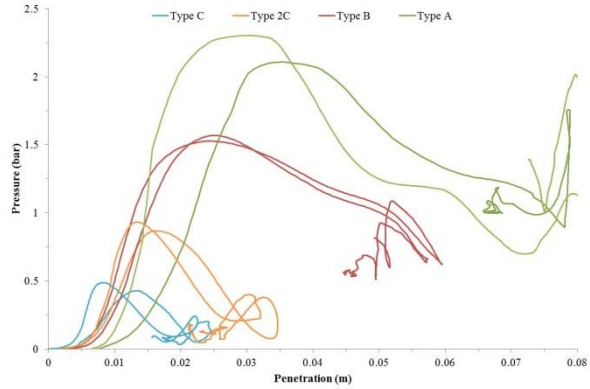


***Figure 23. Right APTS pressure versus abdomen penetration for seatbelt loading using pretensioner Type C, 2C, B and A.***

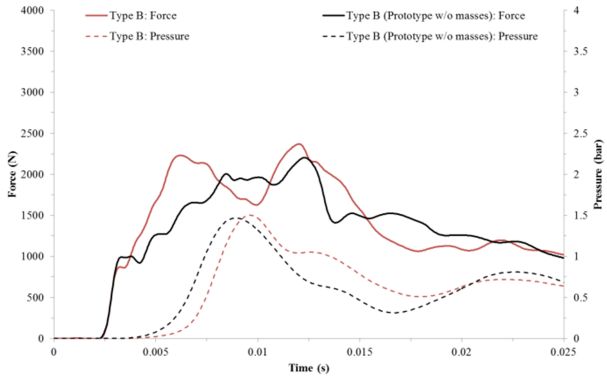


***Figure 24. Left seat belt force (y-axis1) and left APTS pressure (y-axis2) versus abdomen penetration for pretensioner Type B.***

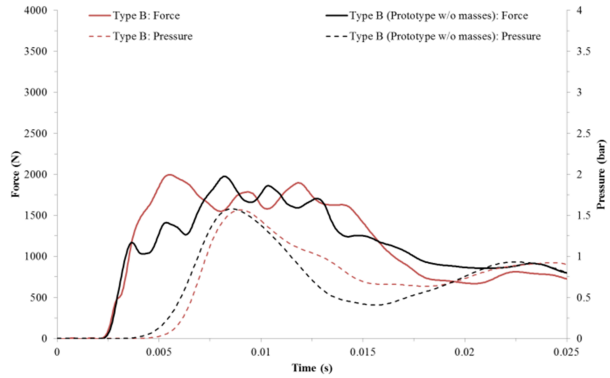


***Figure 25. Right seat belt force (y-axis1) and right APTS pressure (y-axis2) versus abdomen penetration for pretensioner Type B.***

Rigid-bar impacts performed with the dummy rotated by 20° to its left side, exposing more the right APTS, showed the ability of the APTS to discriminate the loading direction. Almost twice higher pressure peaks were recorded by the right APTS (Figure 26).

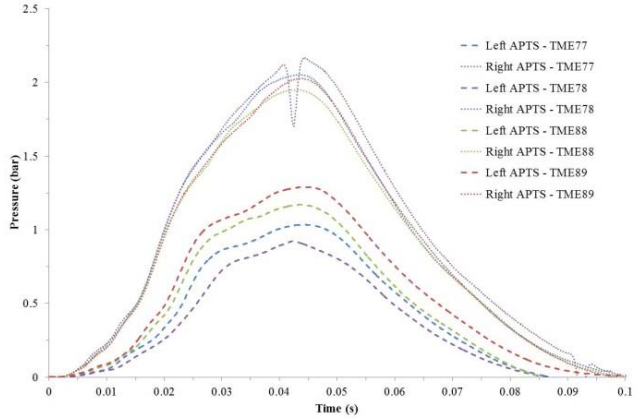


***Figure 26. Left and right APTS pressure for 20° rigid-bar impacts at 3 m/s (4 tests).***

## DISCUSSION

**Biofidelity** The prototype biofidelity was improved under rigid-bar impacts thanks to the addition of the small masses and the higher stiffness of the APTS compared to the front foam. The increased abdominal depth in the prototype made the contact between the rigid-bar and the pelvis flesh occurring later than with the THOR-NT abdomen. In the THOR-Mod Kit and THOR-Metric (most recent version of THOR released by NHTSA), the pelvis flesh at the antero-superior iliac spine (ASIS) are shortened by 20 mm. It is therefore expected that such contact with the rigid-bar impact will not occur anymore. It will remain that the stiffness observed between 90 and 120 mm penetration is still higher than PMHS corridors. This might be solved by changing the abdominal rear foam block properties.

The human response under the seatbelt/pretensioner loading is much more challenging to mimic. The force can be increased, but not to a sufficient level compared to PMHS. The penetration remains lower than that of the PMHSs. A comparison between the prototype and the average scaled PMHS response under pretensioner Type B gives further insight into these differences compared to the corridor (Figure 27-Left). A similar curve shape is in fact observed but it appears that the force plateau after the initial force peak is longer for the prototype (around during 15 mm penetration compared to 5 mm for the PMHSs). A second higher force plateau exists for the PMHS response whereas the penetration of the prototype is stopped. It is therefore necessary to reduce the first plateau in the prototype and increase the force between 20 and 50 mm penetration. This might be done by changing the front foam characteristics to a stiffer material.

Finally, the first force peak should be at the really beginning of the impact (Figure 27). This should be achieved by placing the small masses inside the dummy suit instead of the surface of the abdomen Cordura bag.

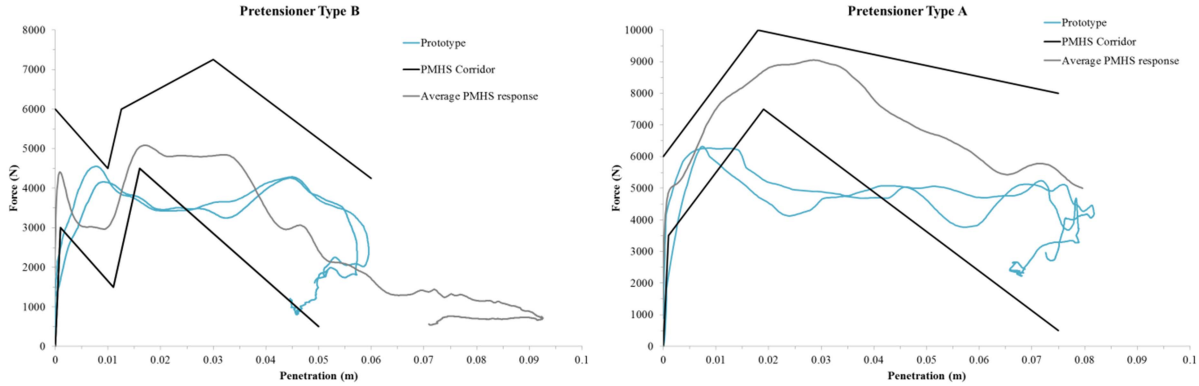


***Figure 27. Force-penetration response of the prototype compared to Foster et al. (2006) PMHS corridors and average PMHS response scaled with Eppinger technique (Lebarbé, 2011)(Left: Type B, Right: Type C).***

**Instrumentation** The abdomen prototype is equipped with two APTSs. In THOR-Mod Kit and THOR-Metric, the pelvis ASISs are equipped with load cells (Ridella et al., 2011). This will provide information on the lap belt and the pelvis interaction in addition to the lap belt and abdomen interaction given by the APTS. The pressure peaks measured by the APTSs corresponded to the force and the penetration peaks measured under the rigid-bar impacts (Table A 1). Under the seatbelt loading, the pressure peak corresponded to the force peak in the prototype without the small masses (Figure 24 and Figure 25). In the prototype (including the small masses), this is not the case as explained earlier. Regarding the penetration peak, there is always a significant time delay (around 10 ms) between the pressure and the penetration peaks as between the force and the penetration peaks (Table A 2). The pressure curves follow force history curve shapes.

**Injury prediction** Cavanaugh et al. (1986) PMHS tests led to abdominal AIS4 injuries for speeds higher than 6 m/s. In Foster et al (2006) study, only tests with pretensioner Type A created AIS2 to AIS3 abdominal injuries. In these two test configurations, the APTS pressure peaks were above 2.7 bars and 2 bars respectively. Beillas et al. (2012) estimated a threshold of 1 bar for the child Q-dummies. This is of course not possible to compare since the tolerance of adult and child is certainly different and since the dummy abdomen designs are also different.

## CONCLUSIONS

The APTSs already used in 3 and 6 years old Q-dummies were introduced into THOR lower abdomen front foam block. Small masses were added on the abdomen Cordura bag and the assembly was mounted on THOR-NT dummy. The response of the abdomen prototype was then compared to the THOR-NT abdomen and to PMHS corridors under 6.1 m/s rigid-bar impact and Foster's seatbelt/pretensioner loadings. Generally, the force-penetration response of the prototype was closer to PMHS response and the APTS pressures accounted well for the impact severity as measured by external force measurements or dummy abdominal penetration. Along the analysis, below proposals were made to further improve the abdomen response:

1. Moving the small masses inside the dummy suit to create earlier the initial peak force seen on PMHS responses,
2. Changing rear foam block properties to a softer material to allow a larger penetration and a lower force after 90 mm penetration,
3. Increasing front foam stiffness to raise further force up to 50 mm penetration,
4. Proceeding with 2/ and 3/ above might lead to using a single lower abdominal foam block since the front foam is too soft and the rear foam is too stiff.

In the component tests performed in this study, the interaction between the pelvis flesh and the rigid-bar or the seatbelt webbing influenced largely the results. This could be easily identified in the rigid-bar tests but less easily in the seatbelt tests. The THOR-Metric is equipped with ASIS load cell and its pelvis flesh has been shortened by around 20 mm. Together with the prototype abdomen, THOR-Metric will allow measurement of the load applied to the pelvis and to the abdomen, discretely.

Interaction between the lower abdomen and the upper torso will need to be considered. Evaluation in sled tests highlighted that further work is also needed to understand the influence of the dummy kinematics on the pressure measurements.

## REFERENCES

Beillas P., Alonzo F., Chevalier M-C., Lesire P., Leopold F., Trosseille X., Johannsen H. (2012) Abdominal twin pressure sensors for the assessment of abdominal injuries in Q dummies : In-dummy evaluation and performance in accident reconstruction. Stapp Car Crash Journal 56: 387-410.

Cavanaugh J. M., Nyquist G. W., Goldberg S. J., King A. I. (1986) Lower abdominal tolerance and response. Proceedings of 30th Stapp Car Crash Conference, pp. 41-63, SAE technical paper No 861878. Society of Automotive Engineers, Warrendale, PA.

Eppinger R. H. (1976) Prediction of thoracic injury using measurable experimental parameters. Proceedings of 6th international ESV Conference, p. 770. Washington, DC, USA. 1976.

Foster C. D., Hardy W. N., Yang K. H., King A. I. (2006) High-speed seatbelt pretensioner loading of the abdomen. Stapp Car Crash Journal 50: 27-51.

Frampton R., Lenard J., Compigne S. (2012) An in-depth study of abdominal injuries sustained by car occupants in frontal crashes. Proceedings of 56th Association for the Advancement of Automotive Medicine, Chicago, Illinois. October, 2012.

Hanen G., Bermond F., Compigne S., Masuda M. (2011) Contribution to the improvement of crash test dummies in order to decrease abdominal injuries in road accidents. Proceedings of 22nd international ESV Conference, Paper No 11-0218. Washington, DC, USA. June 13-16, 2011.

Hanen G, Vezin P., Bermond F., Masuda M., Compigne S. (2012) A pressure-based abdominal insert for THOR-NT. JSAE Annual Congress, Pacifico Yokohama, Japan. May 2012.

Hardy W. N., Schneider L. W., Rouhana S. W. (2001) Abdominal impact response to rigid-bar, seatbelt, and airbag loading. Stapp Car Crash Journal 45: 1-31.

Huelke D. F., Mackay G. M., Morris A. (1993) Intraabdominal injuries associated with lap-shoulder belt usage. SAE paper n°930639.

Kent R., Stacey S., Kindig M., Woods W., Evans J., Rouhana S. W., et al. (2008) Biomechanical response of the pediatric abdomen, Part 2: Injuries and their correlation with engineering parameters, Stapp Car Carsh Journal 52: 135-166.

Klinich K. D., Flannagan C. A., Nicholson K. et al. (2008) Abdominal injury in motor vehicle crashes. UMTRI technical report UMTRI-2008-40.

Kremer M. A., Gustafson HM, Bolte J. H., Stammen J., Donnelly B. (2011) Pressure-based abdominal injury criteria using isolated liver and full-body post-mortem human subject impact test. Stapp Car Crash Journal 55: 317-350.

Lamielle S., Cuny S., Foret-Bruno JL., Petit P., Vezin P., Verriest JP., Guillemot H. (2006) Abdominal injury patterns in real frontal crashes: Influence of crash conditions, occupants seat and restraint systems. Association for the Advancement of Automotive Medicine, Chicago, Illinois. October 16-18, 2006.

Lamielle S., Vezin P., Verriest JP., Petit P., Trosseille X., Vallancien G. (2008) 3D deformation and dynamics of the human cadaver abdomen under seatbelt loading. Stapp Car Crash Journal 52: 267-294.

Lebarbé M. (2011) Contribution to the definition of biofidelity corridors in frontal impact for an adult male 50th percentile – Abdomen. ACEA report Revision 9. September 2011.

Martin JL., Lardy A., Compigne S. (2010) Specificities of rear occupant protection: Analysis of French accident data. Proceedings of IRCOBI Conference, Hanover. September 2010.

Masuda M., Compigne S. (2012) Dynamic response of the THOR-NT: Thorax and Abdomen. SAE 2012. Government/industry meeting. Washington, DC, USA. January 25-27, 2012.

Miller M.A. (1989) The biomechanical response of the lower abdomen to belt restraint loading. Journal of trauma 29 (11): 1571-1584.

National Highway Traffic Safety Administration, THOR-NT user manual 50% male frontal dummy, Revision 2005.1, Report No: GESAC-05-02, U.S. Department of Transportation, Washington, DC, March 2005.

Parent D. P. (2014) Applications of the THOR ATD in NHTSA research. . SAE 2014. Government/industry meeting. Washington, DC, USA. January 22-24, 2014.

Ridella S. A., Parent D. P. (2011) Modifications to improve the durability, usability and biofidelity of the THOR-NT dummy. Proceedings of 22nd international ESV Conference, Paper No 11-0312. Washington, DC, USA. June 13-16, 2011.

Ruan J. S., El-Jawahri R., Barbat S., Prasad P. (2005) Biomechanical analysis of human abdominal impact responses and injuries through finite element simulations of a full human body model. Stapp Car Crash Journal 49: 343-366.

Trosseille X., Le-Coz JY., Potier P., Lassau JP. (2002) Abdominal response to high-speed seatbelt loading. Stapp Car Crash Journal 46: 71-79.

**APPENDIX I**

*Table A 1. Peak values and timing in rigid-bar impacts.*

| | | Rigid-bar impact | | | |
|---|---|---|---|---|---|
| **Impact speed (m/ss)** | **Test Id** | **Force (N) @ Time (ms)** | **Penetration (mm) @ Time (ms)** | **Left Pressure (bar) @ Time (ms)** | **Right Pressure (bar) @ Time (ms)** |
| 1 | TME82 | 384@75 | 51@84 | 0.33@79.2 | 0.25@76.9 |
| | TME83 | 419@73.3 | 50@79.5 | 0.38@75.2 | 0.25@75.2 |
| 2 | TME84 | 1183@44.2 | 74@55 | 1.1@51.3 | 0.9@50.4 |
| | TME85 | 1185@47.1 | 75@56.5 | 1.1@51.8 | 0.8@51.1 |
| 3 | TME79 | 2263@41.8 | 96@47 | 1.7@43.6 | 1.5@43 |
| | TME80 | 2265@41.8 | 96@47 | 1.7@44 | 1.5@42.4 |
| 4 | TME90 | 3563@35.3 | 116@40.5 | 2.6@36.9 | 2.1@37.3 |
| | TME91 | 3389@36 | 118@42.5 | 2.5@36.7 | 2.1@37.4 |
| 5 | TME92 | 4661@30.9 | 134 @38 | 2.8@34.5 | 2.4@33.3 |
| | TME93 | 5261@33.7 | 137@39 | 3.1@30.8 | 2.3@35.4 |
| 6.1 | TME94 | 6791@27 | 146@35 | 2.8@25 | 3.0@28 |
| | TME95 | 7088@26.6 | 146@32 | 2.9@33.7 | 2.7@26.3 |

*Table A 2. Peak values and timing in seatbelt loading.*

| | | Seatbelt loading | | | | |
|---|---|---|---|---|---|---|
| **PT** | **Test Id** | **Left Force (N) @ Time (ms)** | **Left Pressure (bar) @ Time (ms)** | **Right Force (N) @ Time (ms)** | **Right Pressure (bar) @ Time (ms)** | **Penetration (mm) @ Time (ms)** |
| Type C | TAP39 | 563@4.6 | 0.25@11.6 | 888@4.5 | 0.43@9.9 | 17@20.5 |
| | TAP40 | 730@6.1 | 0.44@10.6 | 917@4.6 | 0.49@9.3 | 23@19 |
| Type B | TAP41 | 2370@12 (*) | 1.5@9.6 | 1996@5.5 | 1.6@9 | 57@16.5 |
| | TAP42 | 2479@12.2 (*) | 1.7@9.7 | 2278@5.7 | 1.5@9.3 | 60@17 |
| Type 2C | TAP43 | 1616@5.1 | 0.85@8.6 | 1346@5.2 | 0.87@8.2 | 35@17 |
| | TAP44 | 1592@4.5 | 0.82@9.2 | 1315@5.3 | 0.9@8.8 | 32@16.5 |
| Type A | TAP45 | 3492@3.8 | 2.2@7.9 | 2832@3.7 | 2.1@7.6 | 79@23 |
| | TAP46 | 3480@3.8 | 2.3@7.4 | 3166@4.8 | 2.3@6.8 | 82@16.5 |

(*) This time corresponds to the second peak force. The first one is slightly lower but occurs at 6 ms.

# DEVELOPMENT OF A HIGH ENERGY SIDE IMPACT DUMMY

**Zhenwen Wang**
Humanetics Innovative Solutions, Inc.
USA

**Donald Sherman**
Wayne State University
USA

**Nickolas Kloppenborg**
S-E-A Ltd.
USA

**Cynthia Bir**
University of Southern California
USA

Paper Number 15-0116

## ABSTRACT

A high energy side impact dummy (HE-SID) was developed for special vehicle development used for law enforcement and VIP protections subjected to improvised explosive device (IED). MIL-SID, i.e. ES-2 ATD with Hybrid III head/neck and MIL-LX design, was used to develop the test rig and define inputs to mimic the IED test conditions. It was found that the MIL-SID shoulder and rib modules were not durable enough to survive the impact during the testing. In addition, the shoulder biofidelity was lacking and requires improvement. A new shoulder structure was designed to improve the shoulder biofidelity. Finite element analysis was conducted to optimize the shoulder design according to the target biofidelity as defined by a series of 12 PMHS shoulder impacts. The MIL-SID shoulder cam design was replaced with a single shoulder rib integrated with damping materials. A 3D deflection measurement system was developed to measure the shoulder deflections. The 3D deflection measurement system consists of a linear potentiometer and two rotary potentiometers. An algorithm was developed to calculate the deflections at its shoulder joint attachment location. Hardware was fabricated and retrofitted in a MIL-SID for verification and validation. The preliminary test shows that the thorax durability issue was addressed. The ATD was able to withstand numerous tests without any damage. The new shoulder design demonstrated good biofidelity under high energy test conditions.

## INTRODUCTION

Mines have been a major threat for military vehicles and their occupants since World War I [Radonic, 2004]. Improvised Explosive Devices (IEDs) were one of the major threats in Mideast conflict in the last two decades. In peacekeeping and peace-enforcing, occupant safety has the highest priority. Military and law enforcement personnel are becoming more aware that, apart from vehicle integrity, personnel safety is crucial in operations where IEDs pose a threat. In the past 15 years, national and international projects for the improvement of the mine protection of several military vehicles have been performed to study the injury mechanisms under the IED. To systematically approach the issue, HFM-090/TG25, a team of experts developed an injury assessment methodology for light armored and logistic vehicles landmine protection systems [RTO TR-HFM-090]. Hybrid III anthropomorphic test devices (ATD) and ES-2RE were specified for the injury assessment surrogates [RTO TR-HFM-148]. ES-2RE is used for lateral loading test conditions. MIL-SID is an ES-2RE design with the Hybrid III 50$^{th}$ percentile ATD head, neck and MIL-LX lower extremities. The MIL-LX leg provides superior biofidelity and instrumentation capability for under-body blast test.

Shoulder injury is the one of the major injuries for occupant injuries from side impact. The most common injury in low-speed automotive impacts is distal clavicle fracture [Bolte et al 2003]. The Post Mortem Human Subjects (PMHS) tests conducted in the Bolte study are conducted at 4.4 m/s for majority of the tests. Two of the tests were conducted at 7.6 m/s velocity. The duration of the impact was slightly over 60 milliseconds. In loading conditions generated from IED detonation in the lateral direction, the impact velocity can be as high as 27 m/s [Lebarbe et al 2013], and the duration of the impact is near 10 milliseconds. Clavicle fracture was rare in high speed tests. Instead, it was found that humerus, coracoid process and scapula fractures were present frequently. Lebarbe observed that that there was a good correlation between the force, impact speed and injury. It was observed that the force alone was not sufficient to predict the injuries. He also noticed the shoulder deflection was associated with the humerus and scapular fractures. In the current MIL-SID design, the ATD shoulder structure does not have the capability of measuring the shoulder deflection. There is a need to develop an ATD that has the ability to measure shoulder deflection for injury prediction. In this paper, a new shoulder design was developed and can be retrofitted into the MIL-SID dummy. The revised ATD is named High Energy Side Impact Dummy (HE-SID). HE-SID has a shoulder design that provides motion with a degree of freedom in vertical direction. It also has a 3D linear potentiometer in the shoulder structure to provide deflection measurement in x, y and z directions.

## METHOD

### HE-SID Design

The design of HE-SID was developed from MIL-SID. Three major changes were conducted in the design: 1) the thoracic rib durability improvement, 2) the shoulder complex, 3) arm flesh thickness.

The existing MIL-SID was tested using a high rate loading condition (20 m/s, 50 mm deflection) to determine a baseline response. For the thoracic rib module, several durability issues were found from the high rate testing. The potentiometer shaft for the rib module was pulled out of its housing during the rib rebound. The rib module rubber stops were sheared off during the initial loading phase. The housing bracket for the rail bent during testing. Under such loading conditions, the thoracic rib model spring was bottoming out. The strong rebound requires a large travel distance to damp out the energy. This additional travel distance exceeded the travel range of the potentiometer and caused damage. The strong rebound also generated higher force and sheared off the rubber stops.

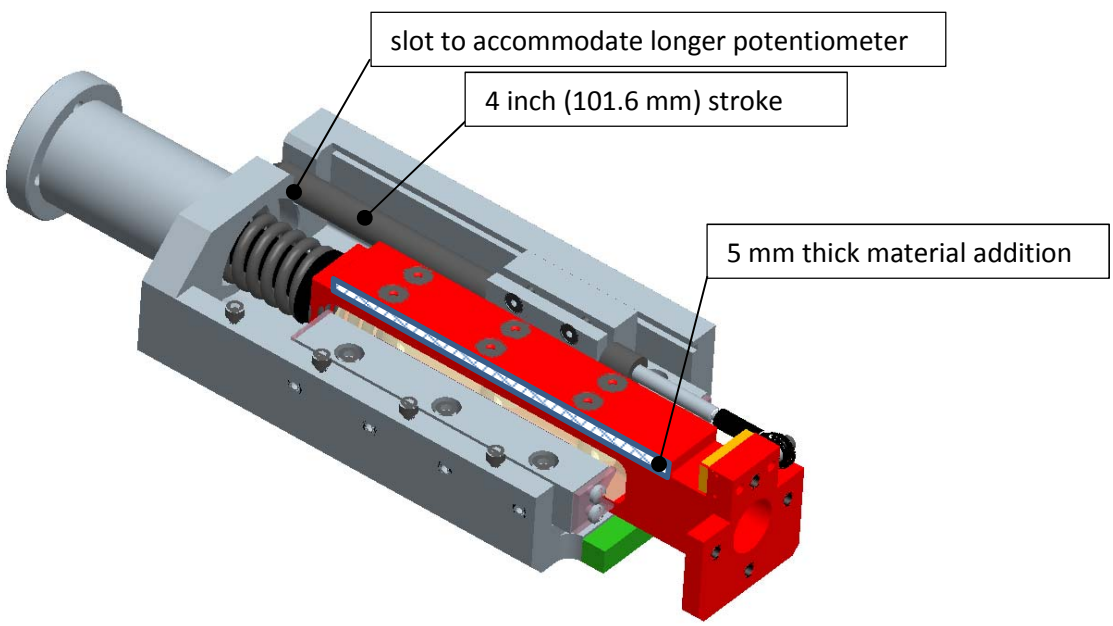


Figure 1, Thoracic rib module design changes - 4 inch potentiometer and stronger rail mounting bracket

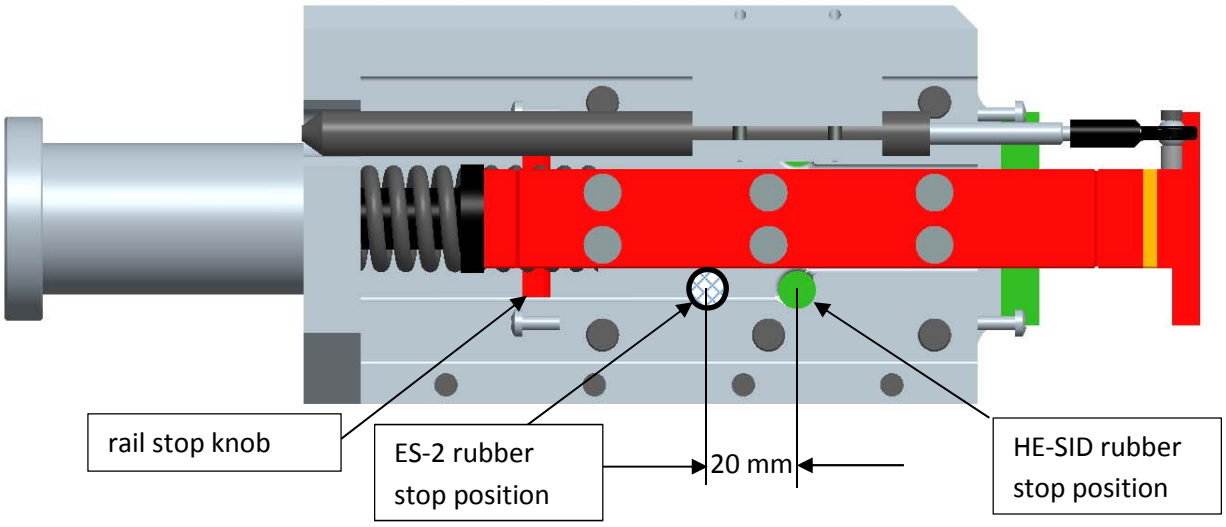


Figure 2, Thoracic rib model rubber stop shifted by 20 mm

To address the above durability issues, design changes were made accordingly. A 4-inch (101.6 mm) stroke potentiometer was chosen to replace the 3-inch (76.2 mm) stroke potentiometer, shown in Figure 1. The 4-inch potentiometer had a longer barrel, which required a slot cutout on the guidance bracket to accommodate the additional length and allow enough space for cable exit. When installed, the 4-inch potentiometer shaft was compressed back by 25 mm more to allow additional motion for the rebound. The rubber stops were shifted laterally toward the struck side by 20 mm to allow more energy dissipation before the rail stop knob engages with the rubber stop. The design was proven to effectively address the durability issue in testing.

Test results show the MIL-SID shoulder stiffness is much higher than that of PMHS shoulder. It was desired to improve the ATD shoulder biofidelity. The MIL-SID shoulder structure limits the range of motion in its horizontal plane. The shoulder has a leaf spring and a shoulder cam. When the shoulder is impacted, it rolls inboard. No vertical or posterior range of motion is allowed in the design, shown in Figure 3. In addition, the MIL-SID shoulder design does not provide the ability to measure the shoulder deflection and acceleration in the shoulder joint.

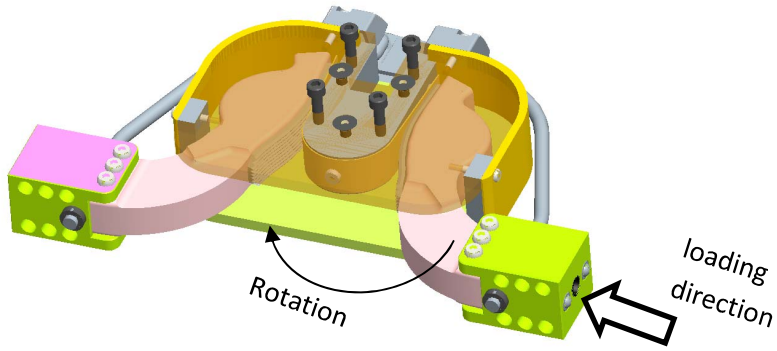


Figure 3, ES-2 shoulder design

It was desired to have a new shoulder design that was able to provide a long range of motion not only in the lateral direction, but also in the vertical and posterior directions. Due to the budget and time limitation, the project would not permit the exploration of a more complex design, such as the THOR-SD3. It was proposed to develop a simple

solution similar to the SID-IIs design – a steel shoulder rib with damping material. 3D shoulder deflection measurement was also desired to develop deflection based injury criteria. Considering the constraints above, a shoulder girdle was designed as shown in Figure 4. The design consists of a spring steel rib with the blue damping material developed in the WorldSID program, an interface bracket for the MIL-SID arm, a linear potentiometer and two rotary potentiometers system to provide 3D calculation of the shoulder joint motion, and a triaxial block for 3 linear accelerometers to measure the acceleration in X, Y and Z directions.

The linear potentiometer range of motion was designed to allow ±32° rotation in the transverse plane (rotation along z axis), and ±90° rotation in coronal plane (along the x axis). The design is shown in Figure 4.

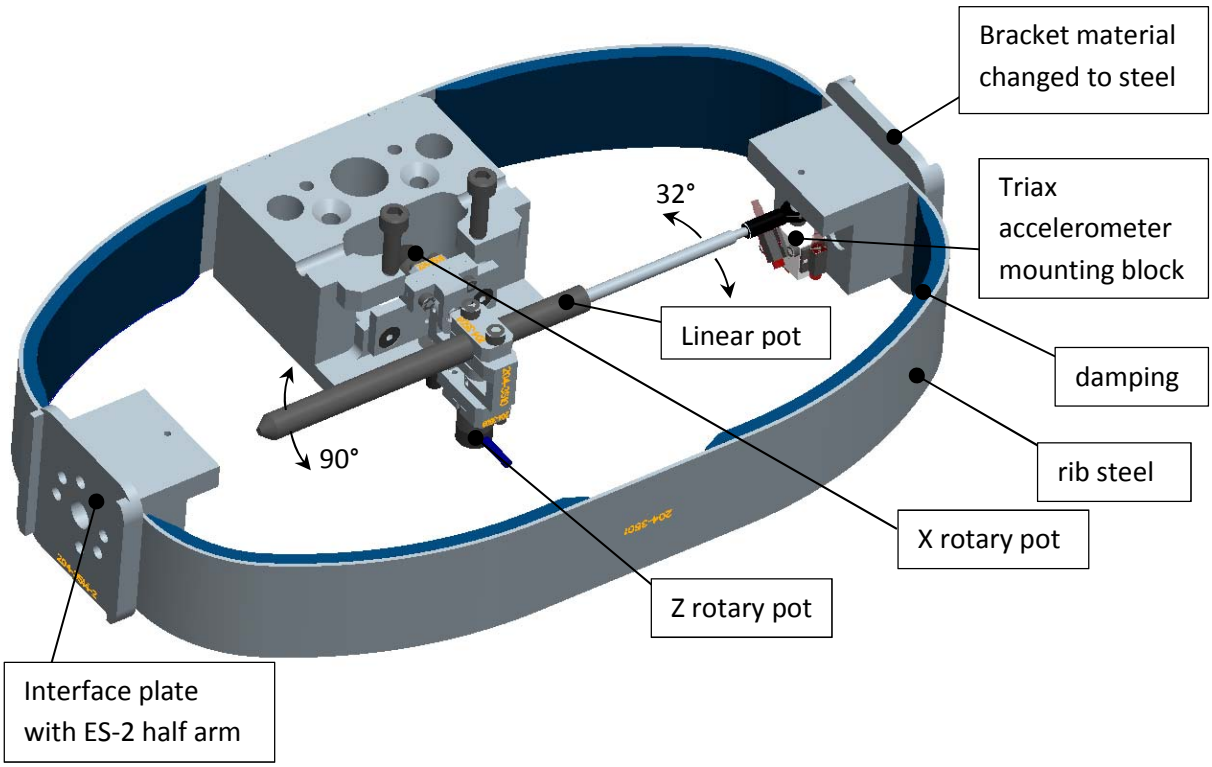


Figure 4, HE-SID shoulder design

Arm flesh provides damping to the skeletal structure of the shoulder. The flesh plays an import rule to mitigate the load. It is important to have a representative flesh in the ATD design. To gain knowledge of the flesh thickness, 8 PMHS MRI images were evaluated; the average flesh thickness at the glenohumeral joint was measured to be 14.3 mm with a standard deviation of 4.8 mm. The MIL-SID arm flesh thickness, shown in Figure 5, is between 27-35 mm, which is much thicker than that in human beings.

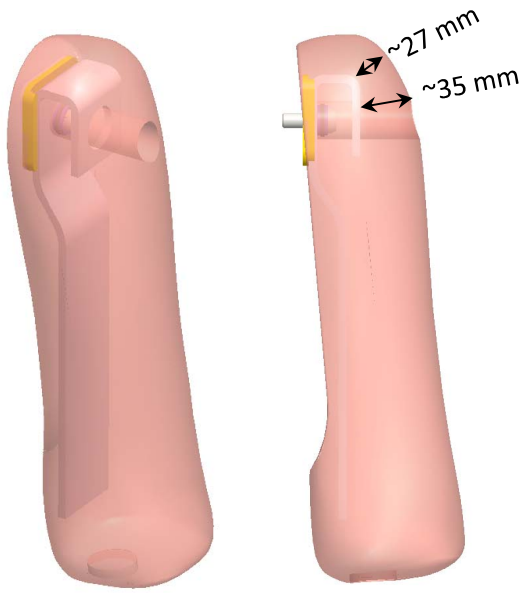


Figure 5, ES-2 arm flesh thickness near acromion

In order to bring the flesh thickness closer to human thickness values, a nylon insert was designed and attached to the existing MIL-SID arm bone in proximal humerus, which brought the thickness to approximately 15 millimeters, shown in Figure 6. In addition, the edges of the block were rounded to provide a smooth profile in order to minimize the potential damages to the ATD flesh during the impact.

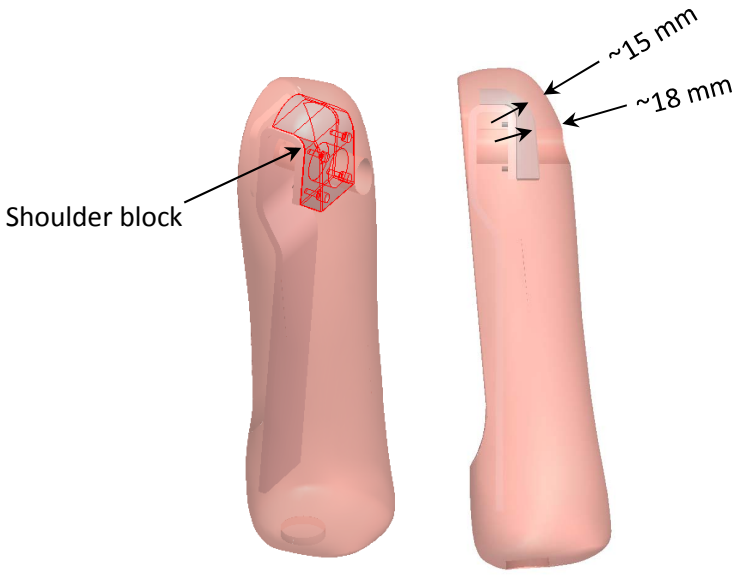


Figure 6, HE-SID arm design

**Shoulder Joint Location**

The MIL-SID shoulder joint is defined by where the shoulder is located in driving posture, which is in a forward (anterior) position relative to that of a (passively seated?) human. HE-SID was designed to represent the impact scenario of a passenger occupant. The shoulder joint center was aligned with the thorax to reflect the real shoulder joint position of the occupants. The HE-SID arm position is shown in Figure 7. The distance between the two

positions is 46.5 mm. The HE-SID shoulder position allows the arm to have more realistic arm/thorax engagement during the impact.

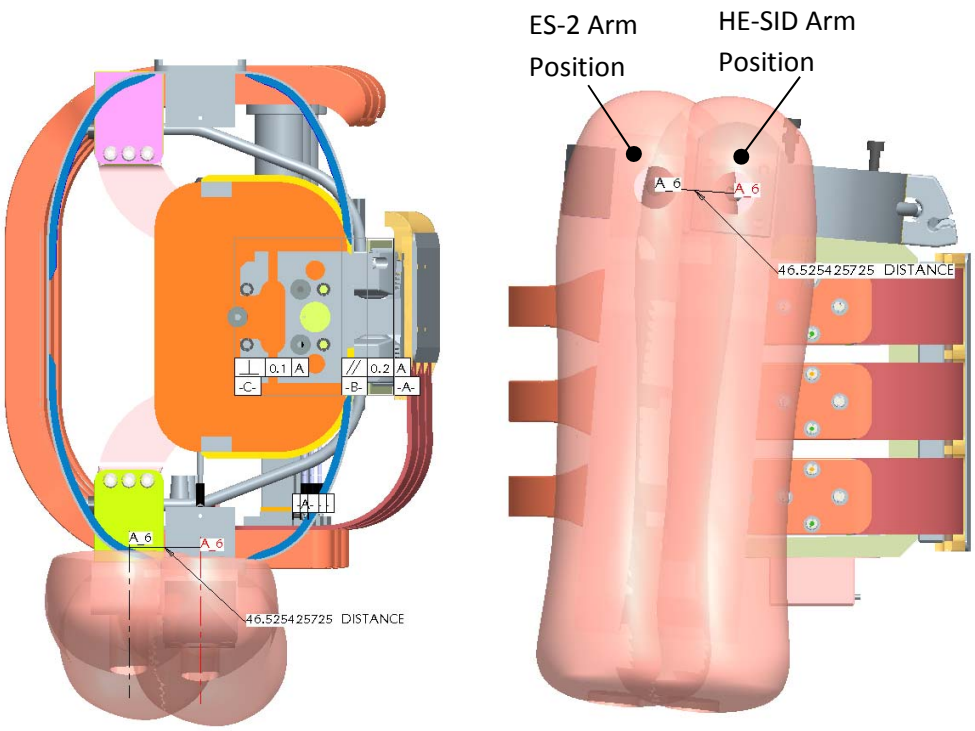


Top View Side View

Figure 7, ES-2 and HE-SID arms overlayed for position comparison

**Shoulder Deflection Calculation**

In the HE-SID shoulder design, a linear potentiometer and two rotary potentiometers were designed in the shoulder to provide the capability for the shoulder joint motion calculations in all three directions. The initial position is aligned with the ATD shoulder local coordinate system, shown in Figure 8.

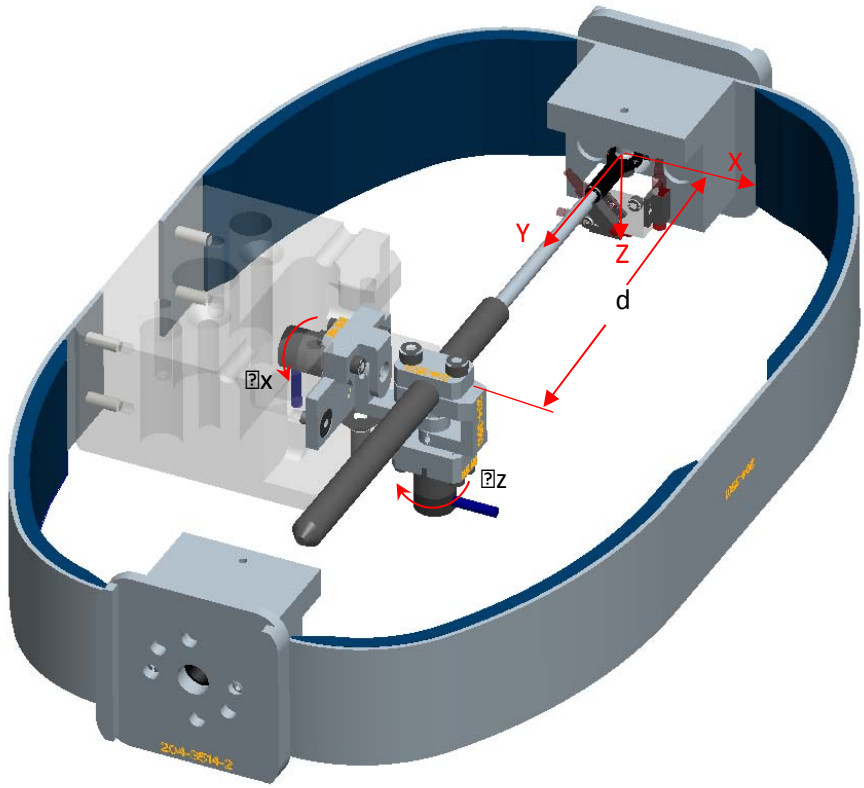


Figure 8, Shoulder deflection measurement system

The calculation can be carried out with the following formula

$$d_x = (d_0 + d_{pot}) * \sin(\theta_z)$$

$$d_y = (d_0 + d_{pot}) * \cos(\theta_z)$$

$$d_z = (d_0 + d_{pot}) * \sin(\theta_x)$$

Where:

$d_0$ is the initial distance (pre-impact condition) between the rotary pot pivot center to the linear pot rod end pivot center.

$d_{pot}$ is deflection at the rod end pivot center of the linear potentiometer attached to the rib.

$\theta_x$and $\theta_z$ are the rotation angles of the two rotary potentiometers from their initial ( pre-impact) positions.

For a brand new rib assembly, the rib was very close to the designed orthogonal planes. $d_0$ is very close to the designed dimension of 129.66 mm. If the rib is off the orthogonal planes due to small permanent deformation, the rotary potentiometer offset from its orthogonal position and $d_0$ at the deformed condition can be measured and taken into consideration in the calculation for better calculation accuracy.

After the above calculation, the data can be filtered according to SAE J211 filter class recommendation if appropriate. The absolute deflection time history in X, Y and Z directions can be calculated by subtracting its pre-impact values from $d_x$, $d_y$ and $d_z$.

**Finite Element Analysis**

Preliminary PMHS test results were used to evaluate the biofidelity of the HE-SID design. Finite Element models were built to analyze the design for durability, biofidelity and sensitivity to the shoulder impactor alignment.

Quasi-static analysis was conducted for the rib rail mounting bracket with AutoDesk Inventor 2012 Professional (stress results from LS-DYNA). The MIL-SID design with aluminum 6061-T6 was loaded until it yielded. The stress distribution is shown in Figure 9. The same load was applied to the HE-SID design, which has 5 mm additional thickness with aluminum 7075-T6 material, shown in Figure 10.

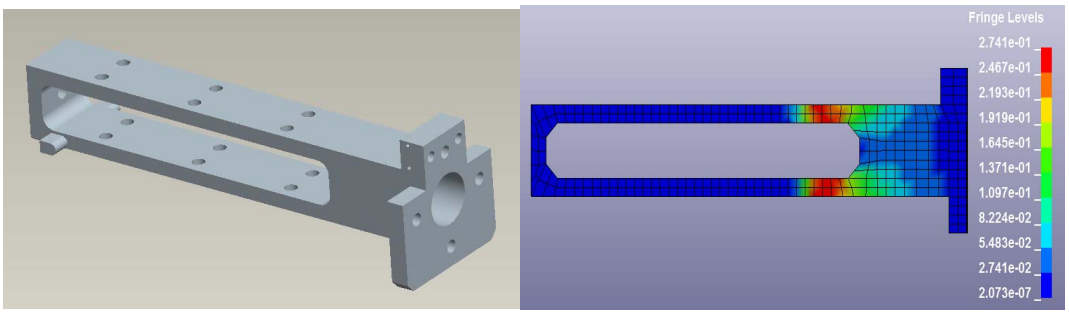


Figure 9, Load to yield for the ES-2 rail mounting bracket

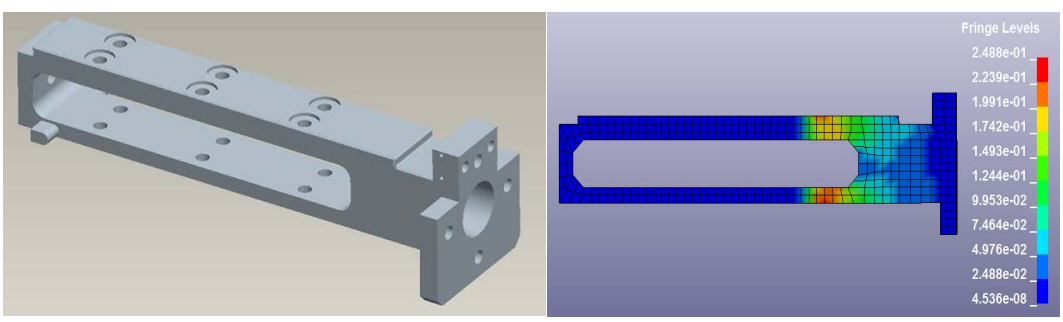


Figure 10, HE-SID rail mounting bracket stress distribution with the same load to yield ES-2

The analysis is summarized in Table 1. HE-SID rib module rail mounting bracket strength was increased by approximately 90%.

Table 1 Stress analysis results of the thoracic rib module rail mounting bracket

| ATD | Materials | Load | Max Von Mises Stress | Yield Stress |
|---|---|---|---|---|
| ES-2 | Aluminum 6061-T6 | 5.2 KN | 274 MPa | 276 MPa |
| HE-SID | Aluminum 7075-T6 | 5.2 KN | 264 MPa | 503 MPa |

Stress analyses were conducted for the shoulder rib to analyze the durability of the rib. For spring steel 1095, the Von Mises stress is well below the yield stress level for 60 mm compression, which is well above the estimated shoulder injury threshold.

In PMHS tests, the center of the impactor is aligned with the glenohumoral joint. Due to the irregular geometry in the shoulder girdle, the alignment is critical for achieving consistent test results. An FEA study was conducted to investigate the sensitivity of the impactor alignment with the ATD shoulder. Two positions were analyzed for comparison – 1) the impactor center is aligned with the ATD shoulder joint pivot center, 2) the impactor center is aligned with the ATD shoulder corresponding to the human glenohumoral joint.

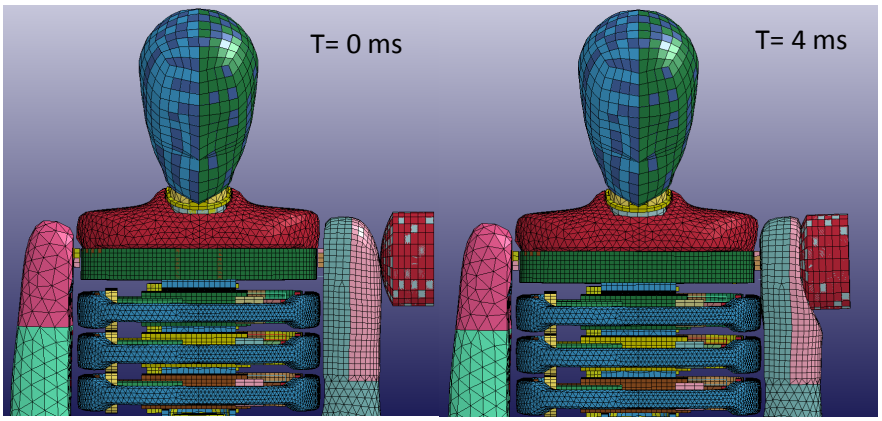


Figure 11, Shoulder impactor aligned with shoulder joint pivot center

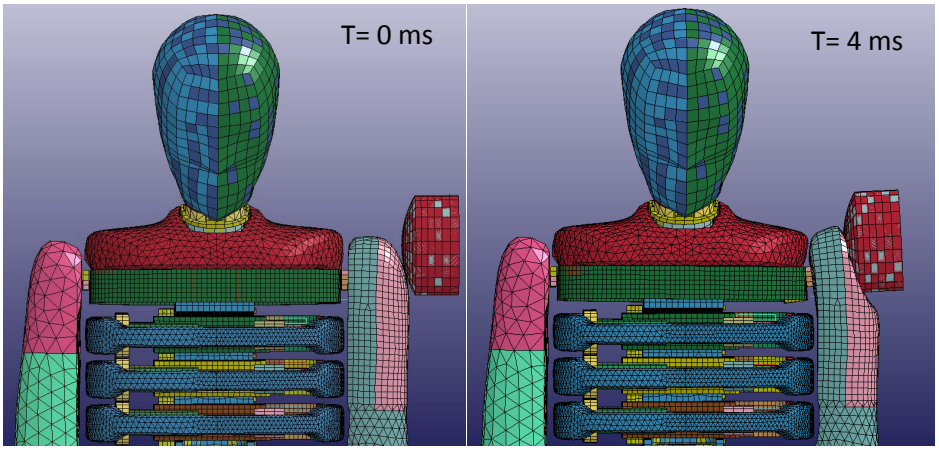


Figure 12, Shoulder impactor aligned with glenohumoral joint

From the kinematics analysis, it was observed that the HE-SID upper torso does not move much at all when the shoulder was maximally compressed (~50 mm). This is consistent with the observation in PMHS impact tests. Due to its impact speed and high energy impact, the PMHS and ATD upper torso remains its position due to its inertia. The deformation happened mainly in the local girdle of the shoulder, shown in Figure 11 and Figure 12. The low reaction of the torso kinematics is also evidenced by the relatively low T1 displacement, less than 3.5 mm in both cases.

Between the two alignment positions, a large deflection difference, up to 14 mm from both skeleton or arm flesh, was observed. It is important to align the impactor with glenohumeral joint for ATD biofidelity validation and verification test so that the results are comparable.

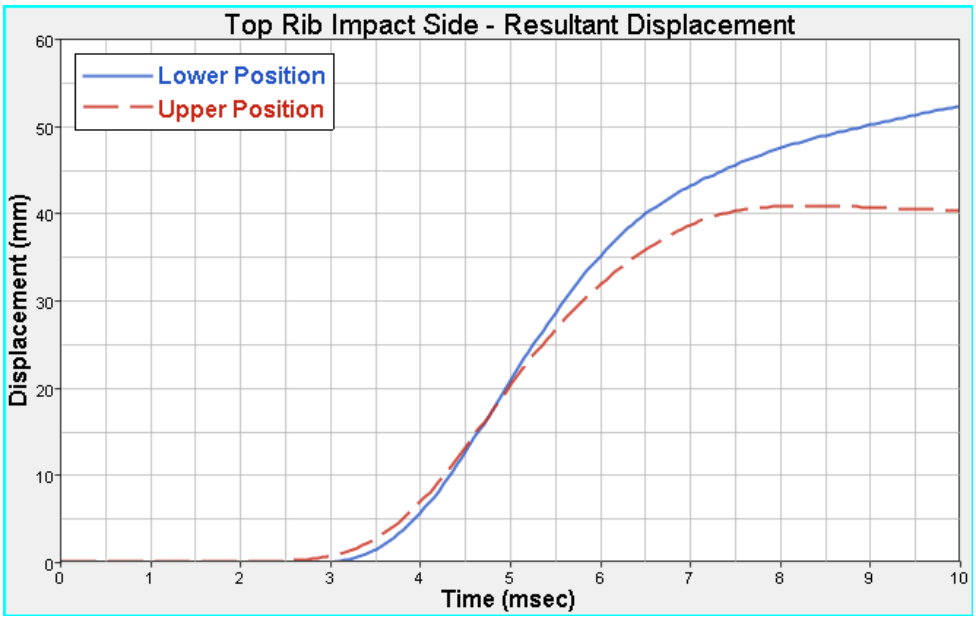


Figure 13, Deflection from ATD linear potentiometer measurement

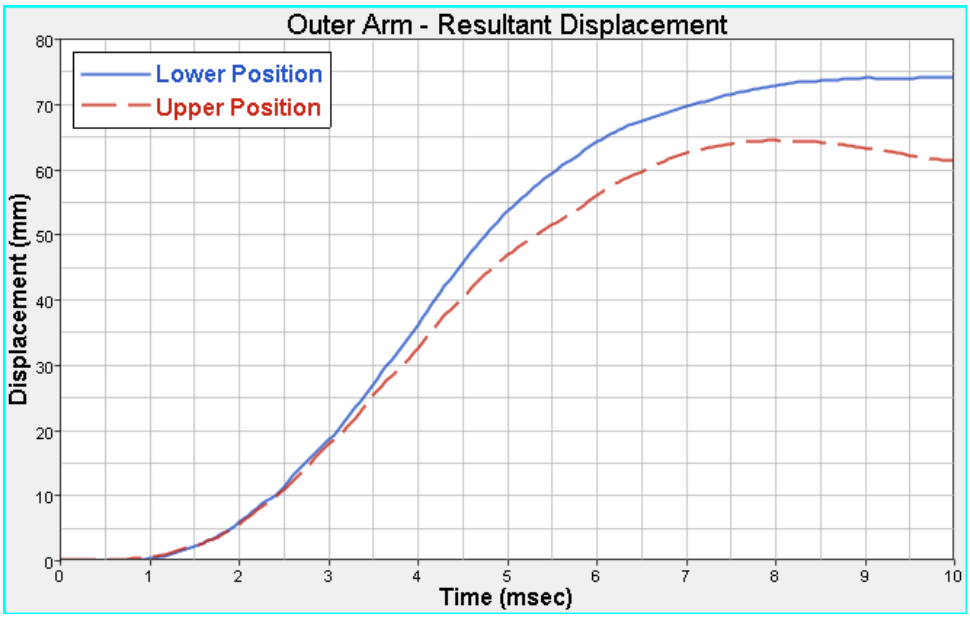


Figure 14, Deflections from the exterior arm flesh measurement

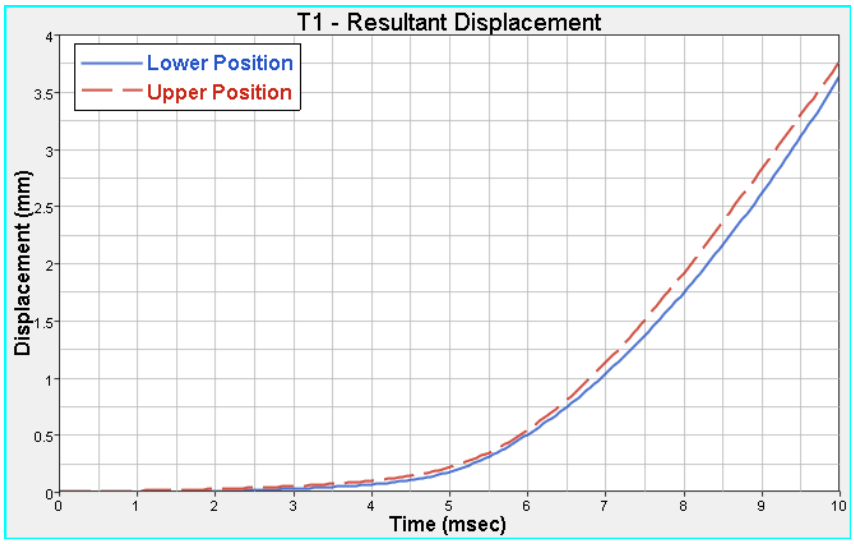


Figure 15, T1 Accelerations

## RESULTS

### Durability

Upon the completion of the HE-SID design, prototype ATD hardware was fabricated for validation and verification testing. After the first test, it was found that the shoulder rib was bent. The rib was brought to Humanetics for analysis and it was discovered that the spring steel was not properly heat treated. A second rib was treated with the proper heat treat process and the rib survived numerous impact tests without damage. No durability issue was observed for the thoracic rib module. The thoracic rib potentiometer was functioning well without any issue. The analysis and the design successfully addressed the MIL-SID durability issue.

### ATD Responses

The prototype HE-SID was tested in the same rig that was developed for PMHS tests to verify the ATD biomechanical response. A series of 12 PMHS were tested to develop a biofidelity guideline and also the injury criteria. The force-deflection relationship of the PMHS tests is summarized in Figure 16, Figure 17 and Figure 18. The ATD demonstrates that the biomechanical parameters are similar to those of the PMHS. Specifically, the third test in the series aligns well with the PMHS corridors. Additional testing will need to be completed to fully characterize the variance shown in the initial test series.

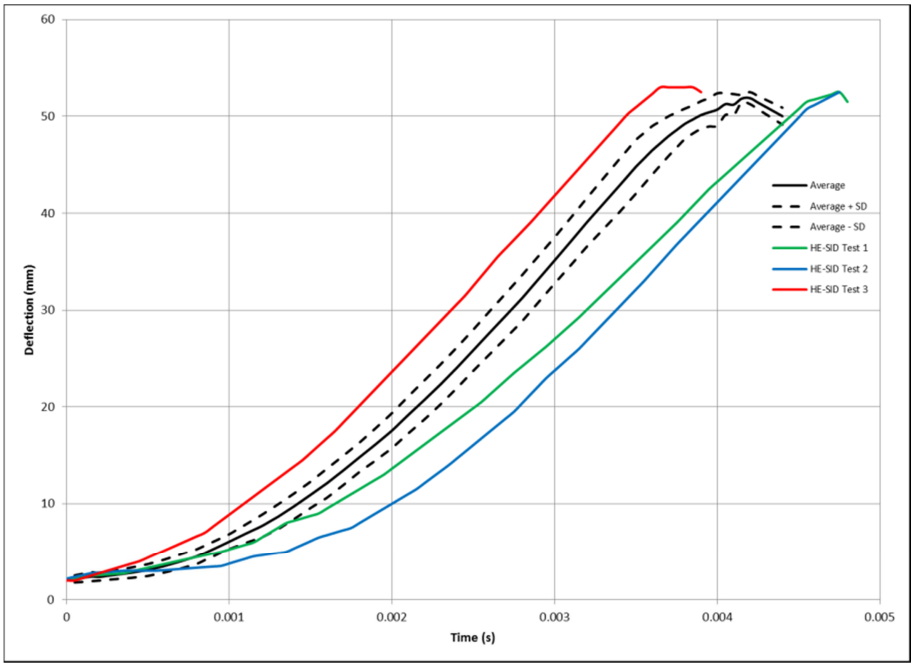


Figure 16, ATD and PMHS shoulder deflection comparison

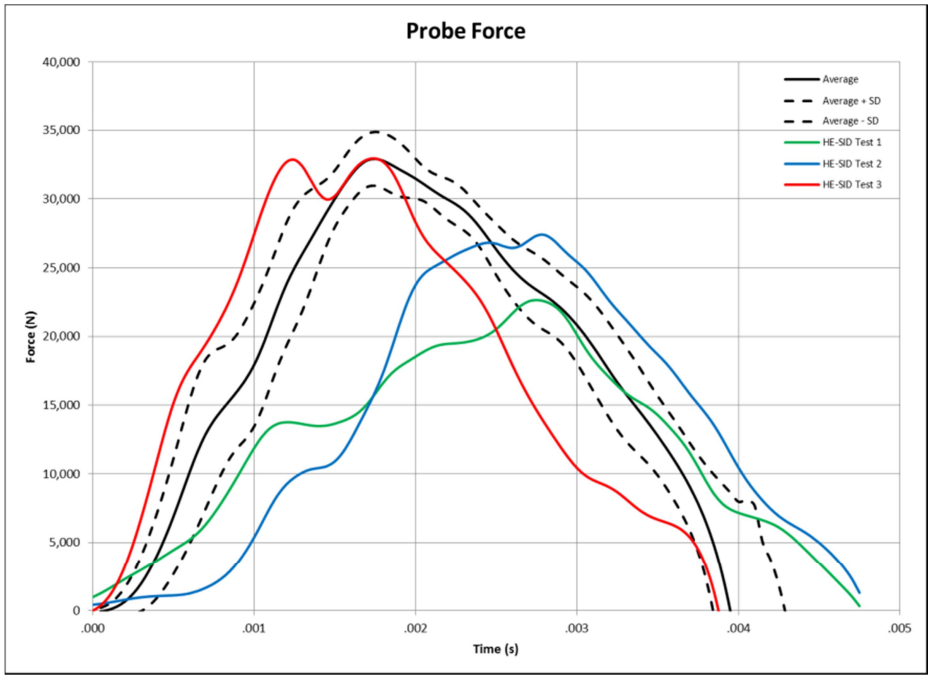


Figure 17, HE-SID and PMHS shoulder probe force comparison

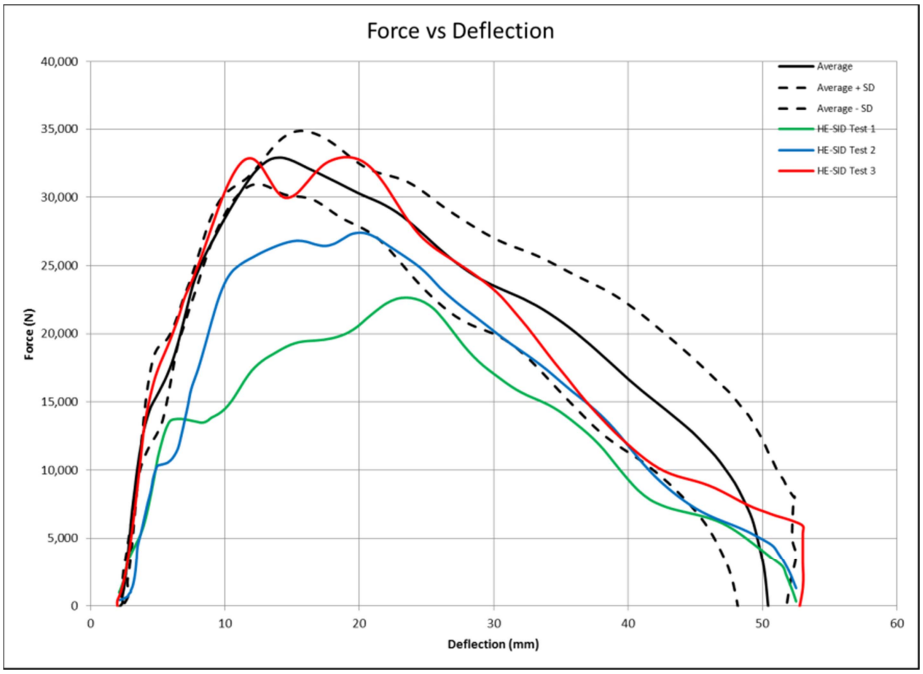


Figure 18, HE-SID and PMHS force vs deflection comparison

## CONCLUSIONS

HE-SID was developed to address the need for a durable and biofidelic ATD in high speed testing for injury predictions. The design is based on the ES-2RE design with improved durability of the rib modules and a new shoulder design. The HE-SID shoulder design allows motion in more degrees of freedom and also offers a 3D deflection measurement ability with a linear potentiometer and two rotary potentiometers. The shoulder joint of the HE-SID is located closer to the anatomical location and the arm skin thickness now resembles that of the human. The testing of the prototype design shows good durability at the high impact speed. Compared to PMHS shoulder response, the ATD shows similar results to human response. Further testing will be conducted to evaluate the HE-SID biomechanical response and injury criteria will be developed accordingly in the future.

## REFERENCES

Bolte IV, J., Hines, M.H., McFadden, J.D., and Saul, R.A., 2000. Shoulder response characteristics and injury due to lateral glenohumeral joint impacts, 44th Stapp Car Crash Journal.

Bolte IV, J., Hines, M. H., Herriott, R.G., McFadden, J.D., Donnelly, B.R., 2003. Shoulder impact response and injury due to lateral and oblique loading, 47th Stapp Car Crash Journal.

Lebarbe, M., Lafont, D., Uriot, J., Potier, P., Baudrit, P., Vallencien, G., 2013. Study of the shoulder response to a high speed – short displacement lateral impact using PHMS and ES-2re, IRCOBI Conference, Gothenburg, Sweden, September 11-13.

TR-HFM-090, Final Report of HFM-090 Task Group 25, 2007. Test methodology for protection of vehicle occupants against anti-vehicular landmine effects.

Radonić, V., Giunio, L., Biočić, M., Tripković, A., Lukšić, B. and Primorac, D., 2004. Injuries from Antitank Mines in Southern Croatia, in Military Medicine, Vol. 169, April, pp. 320-324.

# IMPACT RESPONSES OF THOR MOD KIT UNDER DIFFERENT CONDITIONS IN SLED TESTS AND VEHICLE CRASH TESTS

**Masayuki Yaguchi**
**Koshiro Ono**
Japan Automobile Research Institute
Japan

**Mitsutoshi Masuda**
**Hidetoshi Sokusai**
**Yoshinao Kusayama**
**Kazunobu Ogaki**
Japan Automobile Manufacturers Association, Inc.
Japan

Paper Number 15-0339

## ABSTRACT

In order to contribute to the development and improvement of the THOR dummies, the impact responses of the THOR Mod Kit were compared with the THOR-NT and the Hybrid III, based on the kinematic and dynamic responses to different conditions in the frontal sled and vehicle crash tests. In a 56 km/h frontal sled test where a dummy was installed on the driver seat of a white body, the responses of the THOR Mod Kit with SD3 shoulder to the differences of the seating procedures and restraint conditions were evaluated comparing with the THOR-NT and the Hybrid III. Moreover, two crash tests using a small passenger car at 55 km/h FWRB and 64 km/h ODB corresponding to JNCAP conditions were conducted, and the responses of the THOR Mod Kit were compared with that of the Hybrid III.
Difference of seating procedure affected the responses of the thoracic deflection, abdominal deflection, and iliac force, etc. Compared with the THOR-NT, the THOR Mod Kit clearly showed difference on each measurement location and the forward displacement of its shoulder on the unrestrained side was more pronounced. Regardless of the D-ring positions, the shoulder belt slippage didn't occur in the Hybrid III, whereas belt slippage occurred in the THOR Mod Kit when the D-ring was at the lowest position. When the load limiter force of the seatbelt was higher, forward displacements of the thorax became smaller in both the THOR Mod Kit and the Hybrid III and the neck flexion of the THOR Mod Kit became larger. Accompanying the difference of kinematics, the responses of the head acceleration, neck force and thoracic deflection also differed. In both the FWRB and ODB tests, the maximum rotation angle of the ankle eversion exceeded the preliminary IARV for the THOR at the rebound phase, not at the intrusion phase.
From the results above, it turned out, that the THOR Mod Kit response to the difference in seating procedure was more sensitive than that of the THOR-NT. The sensitivity of the THOR Mod Kit to the D-ring position was higher than that of the Hybrid III, and that the difference of load limiter affected the difference of kinematics and dynamic responses of the upper body in both the THOR Mod Kit and the Hybrid III.

## INTRODUCTION

While the Hybrid III is widely used in regulation and assessment in various countries, it has been expected that a more advanced dummy with higher biofidelity and higher measurement ability will be developed to advance the occupant protection performance of vehicles. From this background, the advanced frontal crash test dummy – THOR (Test device for Human Occupant Restraint), was developed. In 2001, the THOR-Alpha was released [1], and the THOR-NT, which had improved biofidelity, anthropometry, and durability from the THOR-Alpha, was introduced in 2005 [2].
Many researchers had a great interest in the THOR dummy, and further improvements on the biofidelity, repeatability, reproducibility, durability and usability of the THOR-NT were discussed under the SAE THOR Evaluation Task Force Group. Based on discussions in the THOR Task Force, the THOR Task Force Design Team investigated necessary improvements on the specifications of the THOR, drafted a development plan for a short-

term improvement of the THOR, and in 2010 the THOR Mod Kit, which added modifications to each component of the THOR-NT by utilizing the latest biomechanical data was manufactured [3]. At about the same time in Europe, the THORAX Project, the seventh framework program of the European Union, was initiated to perform studies on thoracic injury mechanisms considering the diversity of factors such as age, gender and the physique of the occupants in traffic accidents. In order to reflect the project's efforts to improve the THOR, research and development for the THOR's thorax were performed. The NHTSA had evaluated the THOR Mod Kit in collaboration with individual organizations from the U.S., Europe, and Japan, and they also developed the THOR Metric which redesigned all components based on the metric system.
Under these circumstances, JAMA/JARI has continuously conducted evaluation tests and proposed activities aimed at contributing to the development and improvement of the THOR dummies. In this study, the impact responses of the THOR Mod Kit were compared with the THOR-NT and the Hybrid III, based on the kinematic and dynamic responses to different conditions in the frontal sled and vehicle crash tests.

## THOR MOD KIT DUMMY

The THOR Mod Kit is a dummy which has added modifications to each component of the THOR-NT by utilizing the latest biomechanical data in order to further improve the biofidelity, repeatability, reproducibility, durability and usability of the THOR-NT. The SD3 shoulder, upgraded by the EU THORAX project from the original SD2 shoulder developed by Chalmers University of Technology, had been installed onto this dummy [4][5].

## SLED TEST

In order to contribute to the research and development of the THOR, sled tests of the THOR Mod Kit were conducted in different test conditions and its performance was evaluated. This included a comparison between its responses and that of the THOR-NT and the Hybrid III. In the test, a dummy was installed on the driver seat of a white body of sedan-type vehicle fixed on a sled. The sled was launched rearward so as to reach the maximum speed of 56 km/h. For the restraint system, the front air bag, seatbelt with force limiter and a double pretensioner at the retractor and outer lap belt anchorage were used.

### Comparative Conditions for Evaluation of the Dummy Dynamic Responses

To evaluate the influences on kinematic and dynamic responses of the THOR Mod Kit in different test conditions, the following three comparative conditions were considered and five sled tests were conducted. The data of the THOR Mod Kit from these tests are placed in the NHTSA biomechanics database. The NHTSA test numbers which correspond to these tests are shown in Table 1. Furthermore, the test results of the THOR Mod Kit were compared with those of the THOR-NT and the Hybrid III.

(1) Difference of the seating procedure

(2) Difference of the D-ring position

(3) Difference of the seatbelt load limiter

**Table1. Matrix of the sled tests.**

| NHTSA Biomechanics Database Test No. | Test Parameter for THOR Mod Kit | | | | Other Dummy Data | |
|---|---|---|---|---|---|---|
| | Sled G Pulse | Seat Belt | | Seating Procedure | THOR-NT | Hybrid III |
| | | D-ring Position | Load Limiter | | | |
| 11185 | 35 mph | Highest | N | FMVSS 208 | □ | □ |
| 11186 | 35 mph | Highest | N | UMTRI | □ | □ |
| 11187 | 35 mph | Highest | N | MP-30 | □ | □ |
| 11188 | 35 mph | Lowest | N | UMTRI | | □ |
| 11190 | 35 mph | Highest | N＋α(2kN) | UMTRI | | □ |

**Dummy Seating Procedure**

The dummy positioning was subject to the following three seating procedures:

(1) FMVSS 208; specified for the Hybrid III,

(2) UMTRI (the University of Michigan Transportation Research Institute); the seat position depends on the driver occupant size, geometry of steering wheel and accelerator pedal, and range of seat adjustment [6],

(3) MP-30; according to the FMVSS 208 procedure basically, only the seat slide was adjusted 30 mm forward from the mid position.

With respect to the seating posture of the THOR Mod Kit in different seating procedures, the right view photographs and the position plot of each body region in the X-axis (horizontal) and Z-axis (vertical) coordinate are shown in Figure 1. As the seat position differs among the three seating procedures, the positions of the head C.G., shoulder, H-point and knee in each procedure varied accordingly.

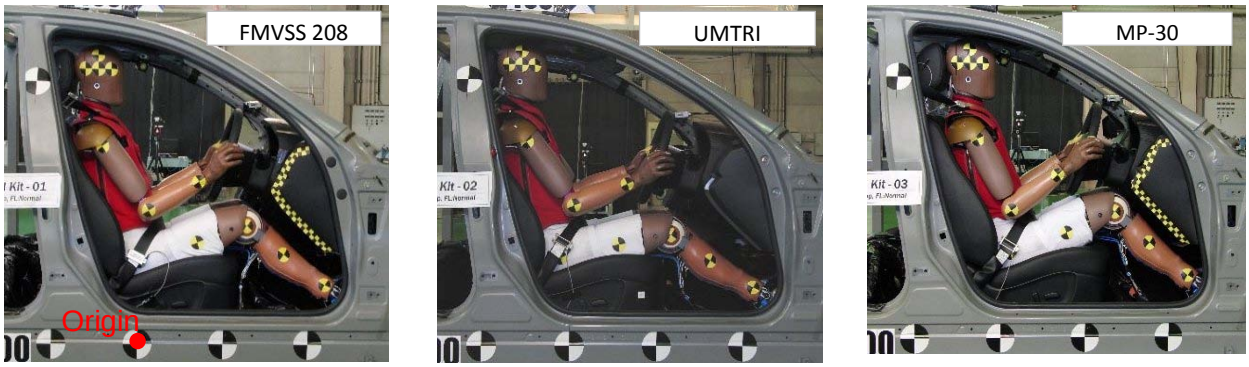


| Seat Slide: Mid | Seat Slide: 49 mm rearward* | Seat Slide: 30mm forward* |
|---|---|---|
| Seat Lifter: Lowest | Seat Lifter: 16 mm upward* | Seat Lifter: Lowest |

* Relative Positions to FMVSS 208

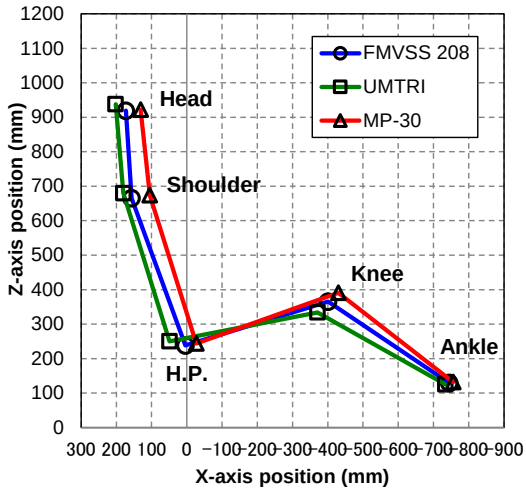


***Figure 1. Seat positions and THOR Mod Kit's seating posture in the three seating procedures.***

## VEHICLE CRASH TEST

In order to evaluate the performance of the THOR Mod Kit, two high-speed frontal crash tests corresponding to JNCAP condition were conducted using a small passenger car as the representative of Japanese cars. One was a 55 km/h Full Width Rigid Barrier (FWRB) test. Another was a 64 km/h Offset Deformable Barrier (ODB) test. The data from these crash tests are placed in the NHTSA biomechanics database. The NHTSA test numbers which correspond to these tests are shown in Table 2. Based on these test results, the response, measurement ability, and durability were compared between the THOR Mod Kit and the Hybrid III. The THOR Mod Kit and the Hybrid III were installed on the driver seat and front passenger seat of the small passenger car. Since the Hybrid III was seated in the front passenger seat merely as a weight dummy, the measurements for the Hybrid III were not taken. Take note that the Hybrid III measurements used in this paper are from JNCAP tests. For the restraint system, the test vehicle was equipped with airbag and the seat belt had pretensioner and load limiter.

**Table2. Vehicle crash tests in this study.**

| NHTSA Biomechanics Database | Test Condition |
|---|---|
| 11204 | 55 km/h FWRB |
| 11205 | 64 km/h ODB |

### Dummy Positioning

Figure 2 shows the comparison of the seating posture between the THOR Mod Kit and the Hybrid III in the FWRB and ODB tests. Since the THOR Mod Kit and the Hybrid III differ in structure and in dimension, the position coordinates of each body region differed in each dummy. Compared with the Hybrid III, the THOR Mod Kit was positioned more rearward and upward in the head, more forward and upward in the shoulders, more upward in the Hip-Point (H.P.), and more forward and upward in the knees. Although the H.P. of THOR Mod Kit could be placed at almost the same position as the H.P. of the Hybrid III in the X-axis, it was not possible to lower the H.P. of the THOR Mod Kit to the HP level of Hybrid III in the Z-axis due to the difference in length of the lower legs.

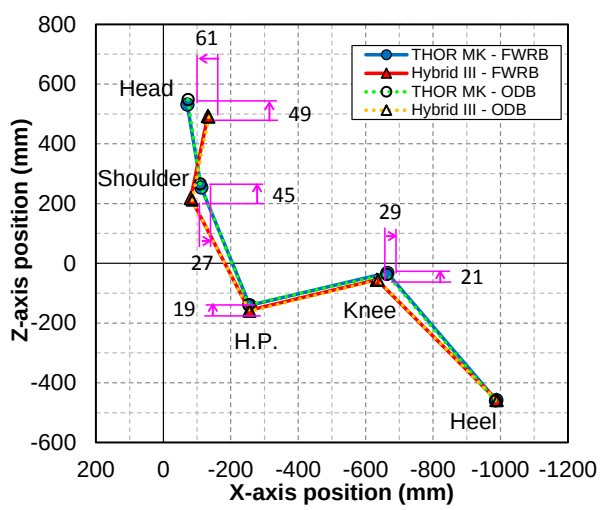


*Figure 2. Seating posture of the THOR Mod Kit and the Hybrid III.*

## RESULTS

### Comparison of Dummy Responses with Different Seating Procedures in Sled Test

Figures 3 shows the comparison of the thoracic deflections, lower abdomen deflections and iliac forces between the THOR Mod Kit and the THOR-NT. With respect to the four point thoracic deflections of the THOR-NT, there was little difference among the three seating procedures, whereas for the THOR Mod Kit, the upper right and lower left deflections in the FMVSS 208, which the seat belt had passed through a closer point to the dummy centerline, indicated smaller responses than those from the other two seating procedures. Because both the lower abdomen deflections (left and right) and the iliac forces (left and right) of the THOR Mod Kit indicated larger responses than those of the THOR-NT, it appears that the THOR Mod Kit improved with regard to sensitivity to seat belt compression compared with the THOR-NT. These differences in dummy responses are believed to be because of the following reasons: the thoracic and abdominal deflection measurement systems of the THOR Mod Kit were changed from the CRUX and the DGSP in the THOR-NT, respectively, to the IR-TRACC systems, and the iliac load cells were also redesigned.

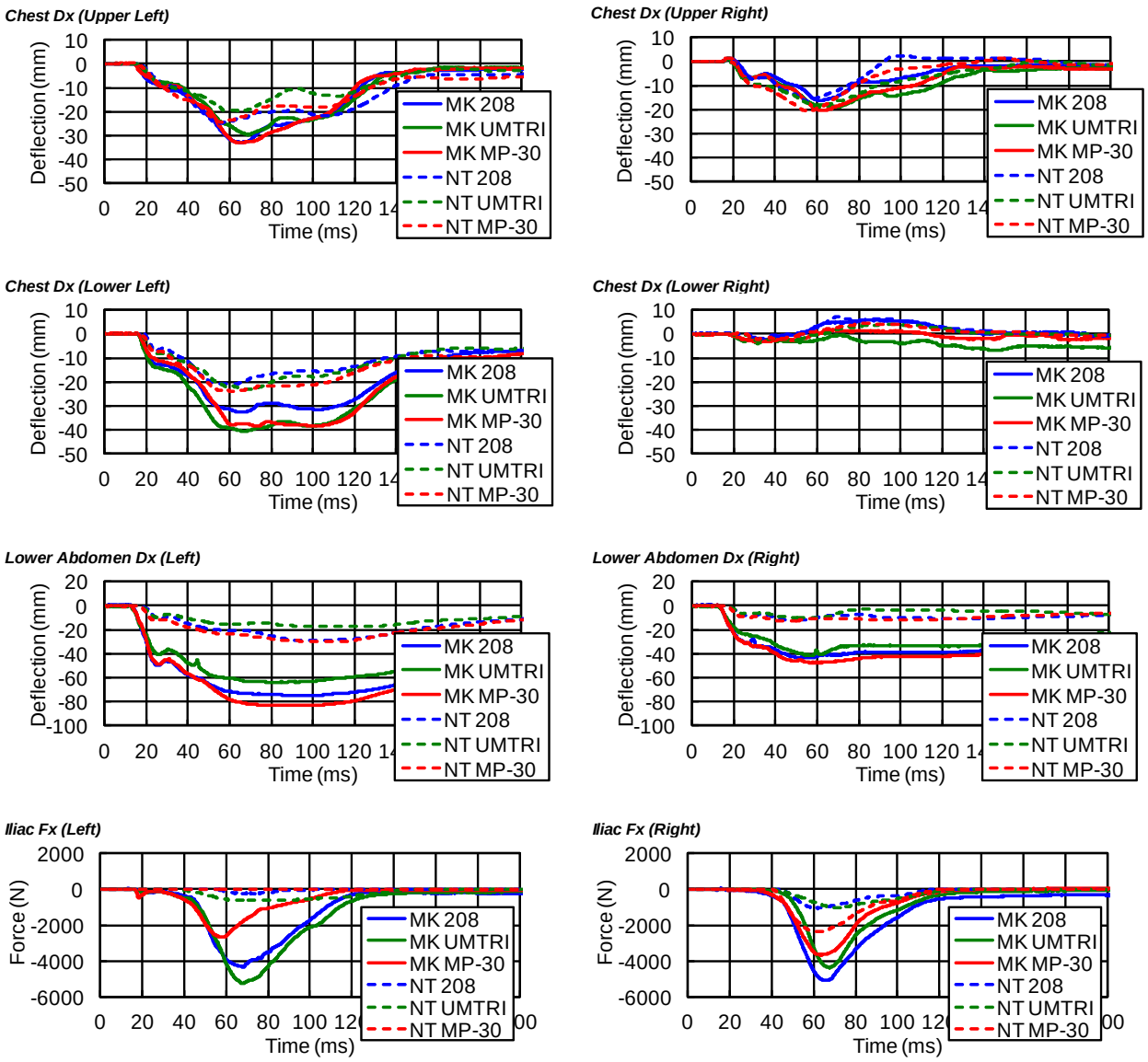


***Figure 3. Thoracic deflections, lower abdomen deflections, and iliac forces of the THOR Mod Kit and the THOR-NT.***

Figure 4 shows the difference in forward movement of the shoulder between the THOR Mod Kit and the THOR-NT in FMVSS 208. The forward movement of the right shoulder was approximately equivalent between the two dummies, whereas the left shoulder of the THOR Mod Kit indicated a larger forward movement than that of the THOR-NT. The left shoulder of the THOR Mod Kit moved forward more than its thorax after approximately 60 ms, and the forward movement at 100 ms was considerably large.

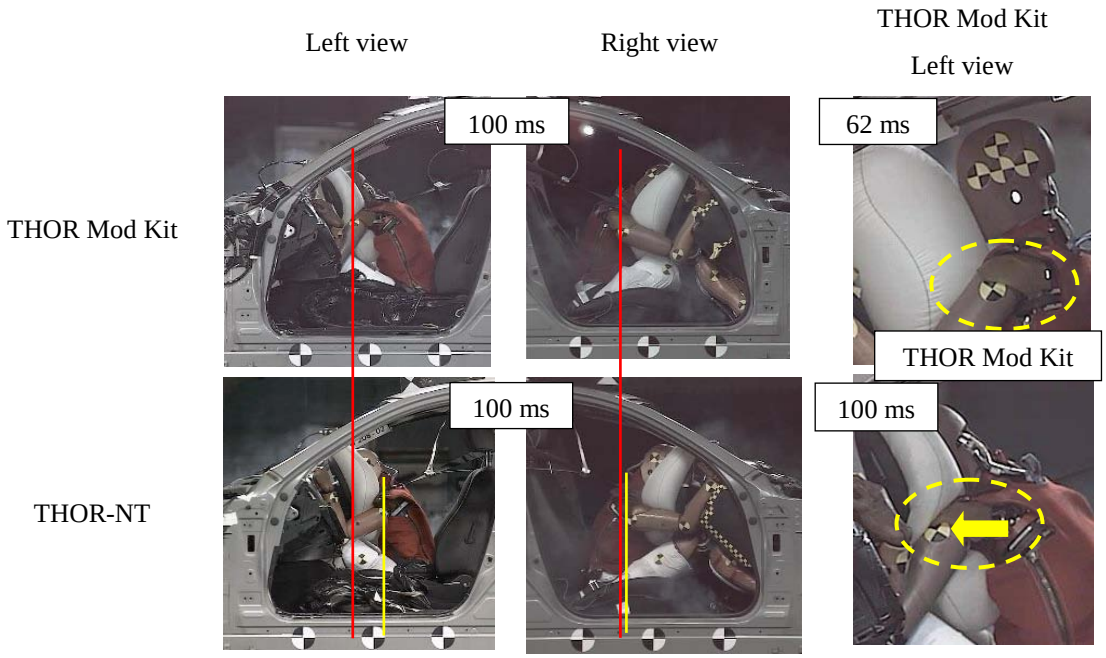


***Figure 4. Difference of shoulder forward displacements between the THOR Mod Kit and the THOR-NT in the FMVSS 208 seating procedure.***

**Comparison of Dummy Responses at Different D-ring Positions in Sled Test**

Based on the captured images from the high-speed video camera, the comparison of the kinematics for the THOR Mod Kit and the Hybrid III at different D-ring positions (load limiter - normal) is shown in Figure 5. Regardless of the D-ring position, shoulder belt slippage didn't occur in the Hybrid III, whereas belt slippage occurred in the THOR Mod Kit when the D-ring was at the lowest position. The belt path on the shoulder of the THOR Mod Kit had passed outward compared with that of the Hybrid III because of the difference in shoulder height between the dummies. Furthermore, the shoulder structure of the THOR Mod Kit with SD3 differs from that of the Hybrid III. These differences are presumed to bring about this phenomenon of slippage or non-slippage of the shoulder belt between the dummies.

Figure 6 shows the comparison of the head accelerations and thoracic deflections respectively of the THOR Mod Kit with respect to difference of the D-ring position (load limiter - normal). The peak acceleration in the X-axis indicated a higher value in the highest D-ring position than in the lowest D-ring position, whereas the peak acceleration in the Y-axis indicated the opposite result to that of the result in the X-axis. Since the seat belt slippage from the shoulder occurred in the case of the lowest D-ring position, the torsion of the dummy upper body about the Z-axis became large and the head lateral acceleration increased. Therefore, it seems that the head acceleration measurements of the THOR Mod Kit are able to sensitively respond to the difference of its own kinematics. Since in the lowest D-ring position the seat belt slippage occurred due to the effect of the seat belt path and the belt strongly compressed the right side of the thorax, the deflection on the thoracic upper right indicated larger values than in the highest D-ring position. It demonstrated that the THOR Mod Kit has high sensitivity to the seat belt path and has a high measurement ability utilizing the multi-point deflection measurements.

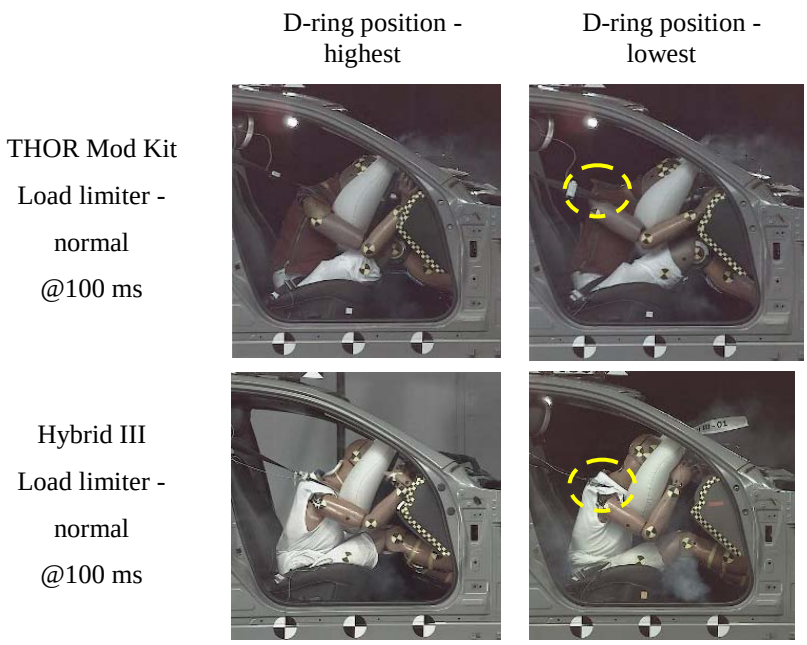


***Figure 5. Comparison of kinematics for the THOR Mod Kit and the Hybrid III at different D-ring positions.***

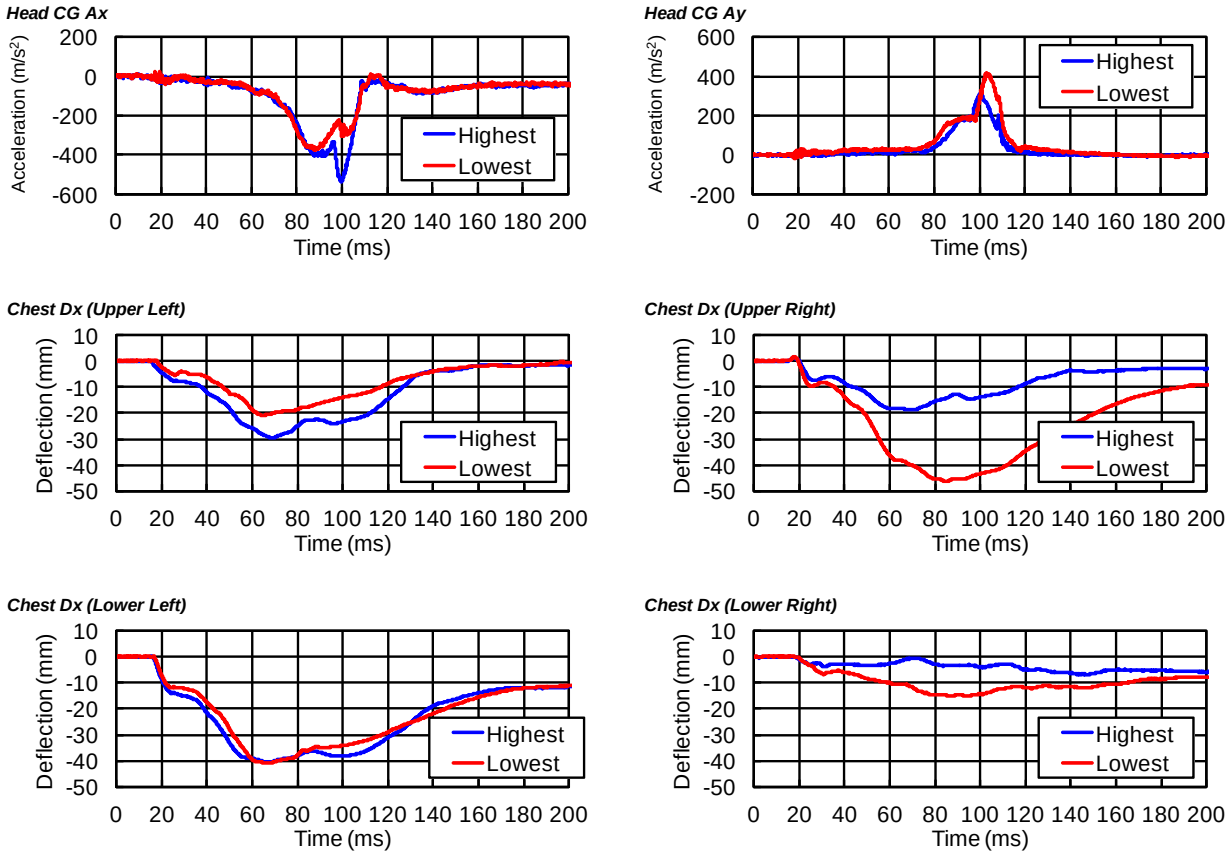


***Figure 6. Head accelerations (X- and Y-axes) and thoracic deflections (UL, UR, LL, LR) of the THOR Mod Kit.***

**Comparison of Dummy Responses with Different Seat Belt Load Limiter in Sled Test**

Comparison of the kinematics for the THOR Mod Kit and the Hybrid III with different load limiter forces (where the D-ring position was at the highest position) is shown in Figure 7. When the load limiter force was higher, the forward movement of the upper body of both the THOR Mod Kit and the Hybrid III was smaller than with a normal load limiter.

Figure 8 shows the comparison of the head resultant acceleration and Figure 9 shows the neck tensile force and the thoracic deflection, respectively, for the THOR Mod Kit and the Hybrid III with different load limiter forces (D-ring position was at the highest position). When the load limiter force was higher, the head accelerations of both dummies indicated lower values, while their thoracic deflections indicated larger values, compared with a normal load limiter. For the neck tensile force, the THOR Mod Kit indicated a higher value with a higher load limiter force than with a normal load limiter but there was little difference in the Hybrid III, because the neck flexion of the THOR Mod Kit became larger but that of the Hybrid III differed only slightly when the load limiter force was higher.

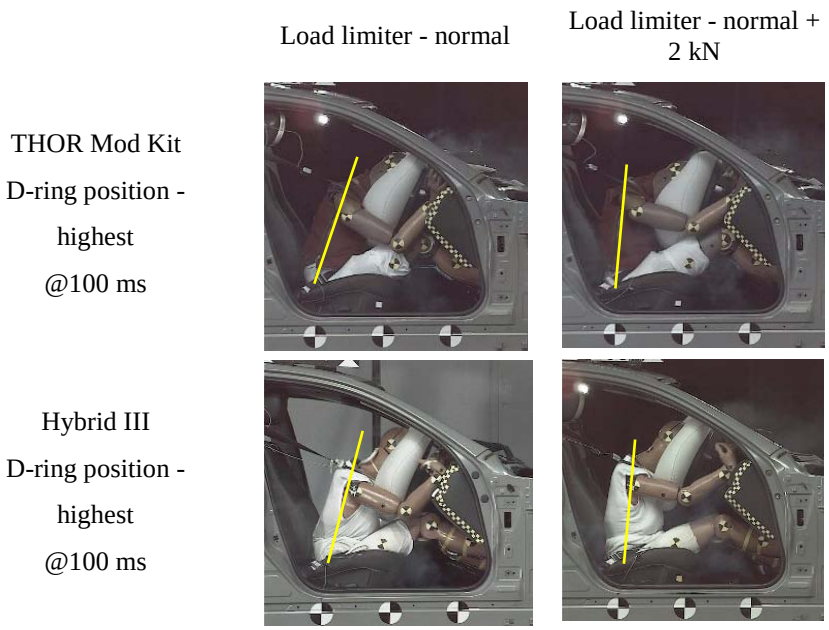


***Figure 7. Comparison of kinematics for the THOR Mod Kit and the Hybrid III with different load limiter forces.***

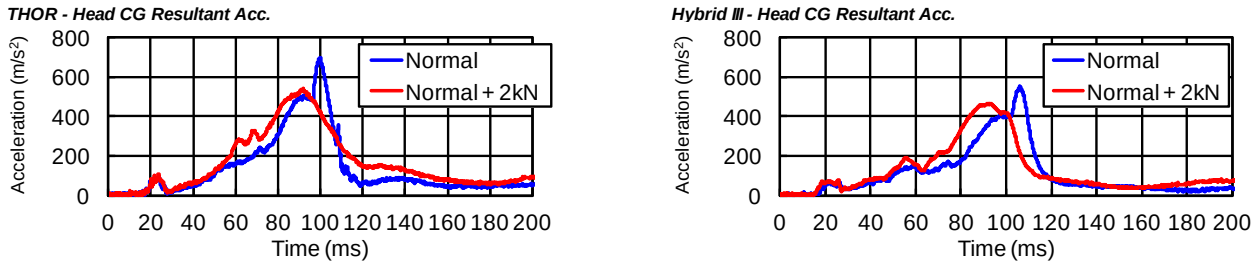


***Figure 8. Head accelerations of the THOR Mod Kit and the Hybrid III.***

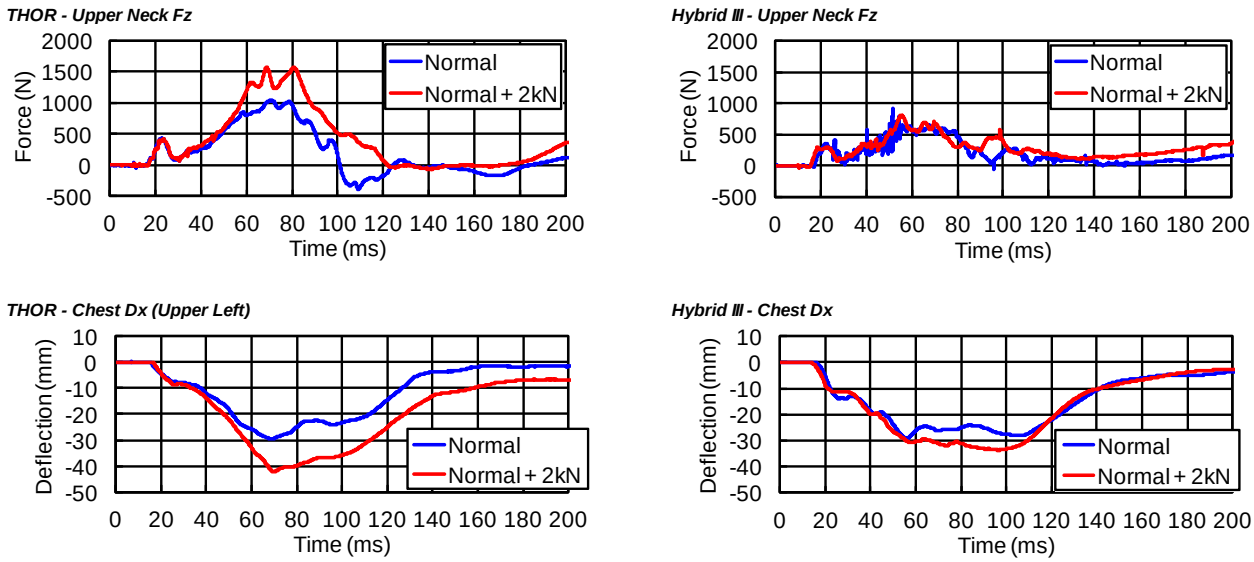


***Figure 9. Neck forces and thoracic deflections of the THOR Mod Kit and the Hybrid III.***

**Kinematics of the THOR Mod Kit with SD3 Shoulder in ODB Test**

Figure 10 shows the captured images from a high speed camera behind the dummies and Figure 11 shows some measurement curves of the THOR Mod Kit. After the left elbow of the THOR Mod Kit came in contact with the instrument panel at approximately 90 ms, its left shoulder moved rearward and upward because of the rebound of its upper body after 100 ms. At 120 ms, the right shoulder moved forward and torsion of the upper body occurred. T1 acceleration rapidly increased at 90 ms because the force was transmitted to the spine by the contact between the left elbow and the instrument panel. Furthermore, the force in Y-axis and moment about X-axis on the spine and the head angular velocity about Z-axis rapidly varied at 100 ms because of the upper body torsion.

| 80 ms | 90 ms | 100 ms | 120 ms |
|---|---|---|---|
| | Left elbow hit to dashboard | Left shoulder is pushed to rearward and upward | Right shoulder (belted side) move forward and torso is twisted |

***Figure 10. Kinematics of the upper body of the THOR Mod Kit in the ODB test.***

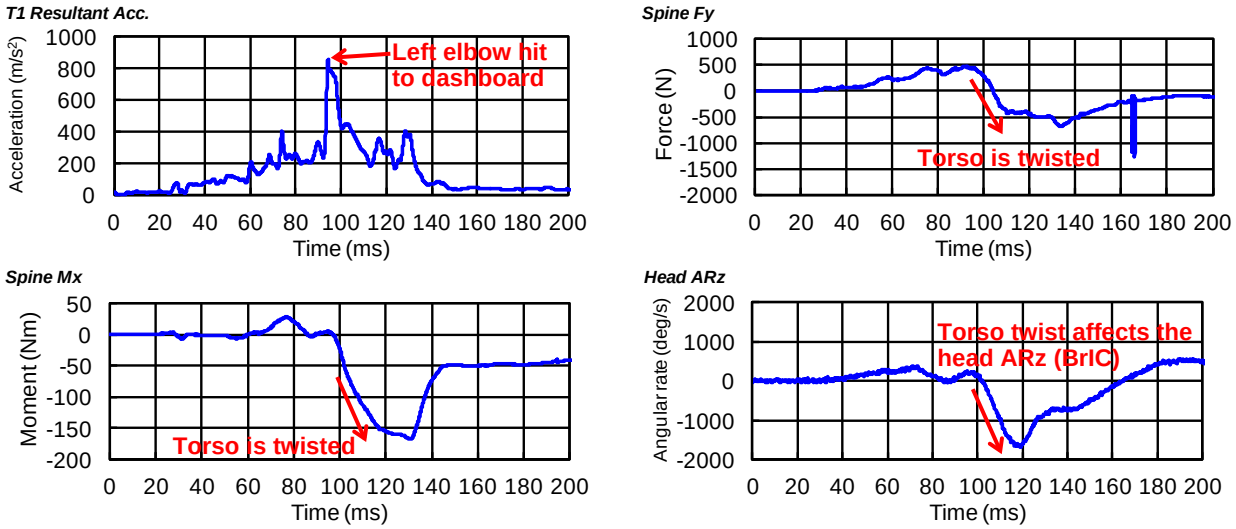


***Figure 11. Measurement curves of the THOR Mod Kit in the ODB test.***

**Ankle Rotation Responses of the THOR Mod Kit in the FWRB and ODB Tests**

Figure 12 shows the kinematics of the ankles of the THOR Mod Kit from a high speed camera on the floor of the driver side and Figure 13 shows the measurement curves of the right ankle rotation. In both the FWRB and ODB tests, the ankles of the THOR Mod Kit indicated eversion responses. A angle of the ankles in the FWRB test reached the maximum at about 80 ms, while in the ODB tests it reached the maximum at about 100 ms, and their values exceeded the preliminary reference value of 35 degrees. They were in the rebound phase of the vehicle after 63 ms in the FWRB test and in that after 90 ms in the ODB test.

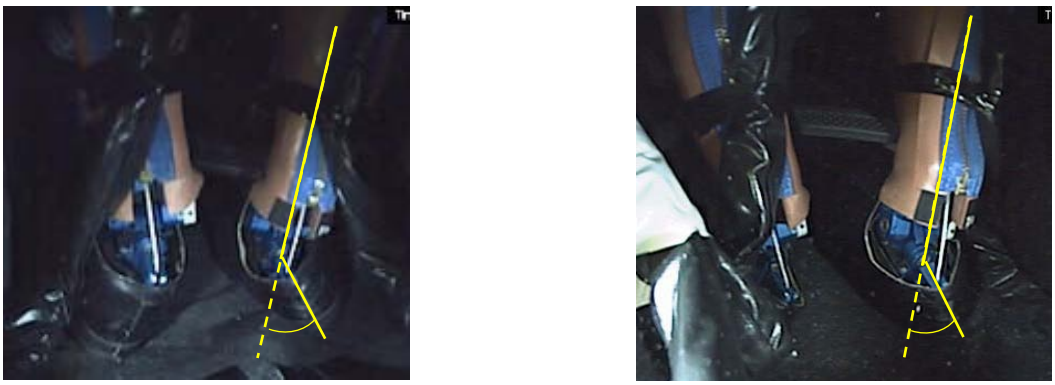

***Figure 12. Kinematics of the ankles of the THOR Mod Kit in the FWRB and ODB tests.***

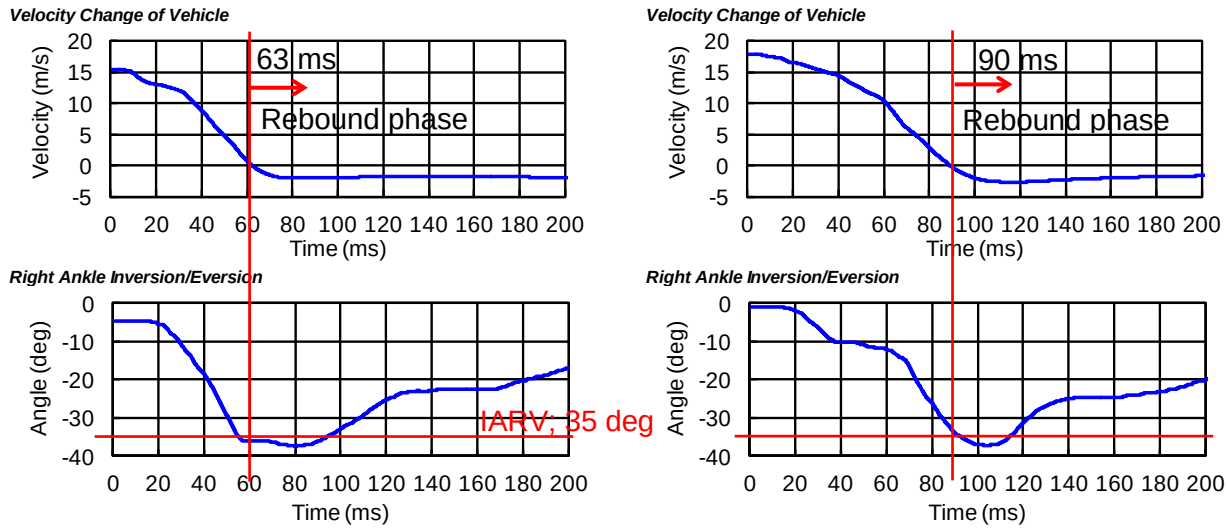


(a) FWRB test (b) ODB test

***Figure 13. Measurement curves of the right ankle of the THOR Mod Kit in the FWRB and ODB tests.***

**Comparison of the Injury Measures in the FWRB and ODB Tests**

The preliminary injury assessment reference values (IARVs) for the THOR [7][8] and the injury measures of the THOR Mod Kit and the Hybrid III obtained from the FWRB and ODB tests are shown in the APPENDIX. In the preliminary IARVs for the THOR, the kinematic rotational brain injury criterion (BRIC), abdominal deflection, acetabulum force, and ankle rotation are newly proposed, compared with the IARVs for the Hybrid III specified in FMVSS 208 and UN/R94. BRIC has been developed to estimate the risk of brain injury due to the rotation of the skull and is calculated by angular velocity and angular acceleration of the head center of gravity as shown in Eq. (1). The IARV of BRIC is 0.89, which corresponds to a 30% risk of AIS 3+ traumatic brain injury [9]. Furthermore, in 2013, the updated BrIC was developed [10]. As shown in Eq. (2), although the new BrIC is calculated only by angular velocity of the head center of gravity, the IARV has not been proposed yet as the study still in progress.

In the FWRB test, most of the injury measures of both dummies were less than the preliminary IARVs, however, the eversion on the right ankle of the THOR Mod Kit exceeded the reference value of 35 degrees. The moment My on the left upper tibia of the THOR Mod Kit was not measured because there was a disconnected wire problem on the load cell sensor (moment My) of the left upper tibia before the test. Due to that problem, calculating the tibia index was not done. In the ODB test, most of the injury measures of both dummies were less than the preliminary IARVs, however, the eversion on the right ankle of the THOR Mod Kit exceeded the reference value of 35 degrees.

Figure 14 shows a ratio of the injury measures of the THOR Mod Kit and the Hybrid III relative to the provisional IARVs in the FWRB and ODB tests. In the FWRB test, although the HIC 36 of both dummies were less than the reference value, the value of the Hybrid III was 285, whereas that of the THOR Mod Kit was 521. The THOR Mod Kit was approximately 1.8 times higher than the Hybrid III. For the neck tensile force, the THOR Mod Kit also indicated higher values than the Hybrid III. It is presumed that the contact force between the head and the steering wheel was larger because the upper body forward displacement and neck flexion of the THOR Mod Kit were larger than those of the Hybrid III. Among the four thoracic points of the THOR Mod Kit, the deflection at the upper left was the largest, which was approximately 1.4 times of the deflection at the chest center of the Hybrid III. The chest 3 ms clip G was almost the same between the two dummies. Compressive forces on the left and right femurs indicated higher values in the THOR Mod Kit than in the Hybrid III. The tibia index for the left tibia of the THOR Mod Kit was lower but that of its right tibia was higher than those of the Hybrid III. Particularly, on the right-lower tibia, the THOR Mod Kit indicated a tibia index of 0.56, which was 2 times over compared with a tibia index of 0.2 in the Hybrid III. In the ODB test, although the HIC 36 of both dummies were less than the reference value, the value of the Hybrid III was 263, whereas that of the THOR Mod Kit was 510. The THOR Mod Kit was approximately 1.9 times higher than the

Hybrid III. For the neck tensile force, the THOR Mod Kit also indicated higher values than the Hybrid III. Among the four thoracic points of the THOR Mod Kit, the deflection at the upper left was the largest, which was approximately 1.4 times of the deflection at the chest center of the Hybrid III. The chest 3 ms clip G was almost the same between the two dummies. Compressive forces on the left and right femurs indicated higher values in the THOR Mod Kit than in the Hybrid III. The tibia index for the left and right tibias of the THOR Mod Kit indicated higher values than those of the Hybrid III. Particularly, on the right-lower tibia, the THOR Mod Kit indicated a tibia index of 0.83, which was about 4 times higher compared with the tibia index of 0.2 in the Hybrid III.

$$BRIC = \frac{\omega_{max}}{\omega_{cr}} + \frac{\alpha_{max}}{\alpha_{cr}} \qquad \textbf{(1)}$$

$\omega$ = angular velocity at head CG , $\alpha$ = angular acceleration at head CG , max = maximum resultant value

cr = critical value for THOR, $\omega_{cr} = 63.5\ rad/s,\ \alpha_{cr} = 19501\ rad/s^2$

$$BrIC = \sqrt{\left(\frac{\omega_x}{\omega_{xC}}\right)^2 + \left(\frac{\omega_y}{\omega_{yC}}\right)^2 + \left(\frac{\omega_z}{\omega_{zC}}\right)^2} \qquad \textbf{(2)}$$

$\omega_x, \omega_y, \omega_z$ = maximum angular velocities about X-, Y-, Z-axes, $\omega_{xC}, \omega_{yC}, \omega_{zC}$ = critical angular velocities

$\omega_{xC} = 66.25\ rad/s$ (Average of CSDM and MPS), $\omega_{yC} = 56.45\ rad/s$ (Average of CSDM and MPS )

$\omega_{zC} = 42.87\ rad/s$ (Average of CSDM and MPS )

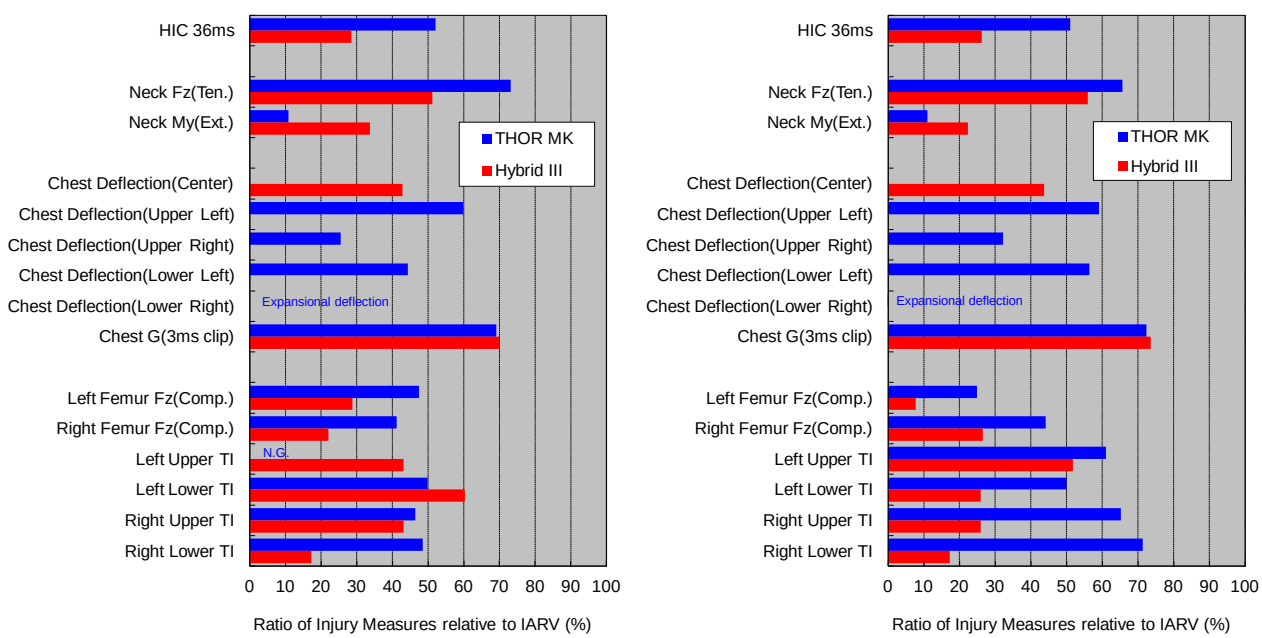


(a) FWRB (b) ODB

***Figure 14. Ratio of the injury measures of the THOR Mod Kit and the Hybrid III in the FWRB and ODB tests relative to preliminary IARVs.***

## DISCUSSION

### Shoulder Belt Slippage with Difference of D-ring Position in Sled Test

Regardless of the D-ring positions, the shoulder belt slippage didn't occur in the Hybrid III, whereas belt slippage occurred in the THOR Mod Kit when the D-ring was at the lowest position. Further verification of the biofidelity of the shoulder kinematics between the Post-Mortem Human Subjects (PMHS) and the ATD (Anthropomorphic Test Device) is needed.

### Difference between the Left and Right Shoulder Movements in Sled Test

From the image of the high speed camera, it was observed that the difference between the left and right shoulder movements of the THOR Mod Kit was large. How the seat belt restrains the shoulder, which is an important to design the specification of the seat belt and its location. Since the sensitivity of the shoulder restraint performance to the D-ring position was high in a series of tests, further verification for the shoulder motion is needed.

### Kinematics of the THOR Mod Kit with SD3 Shoulder in ODB Test

From the image of the high speed camera and some measurement curves of the dummy, it was presumed that the torsion of the upper body of the THOR Mod Kit occurred because its left elbow came in contact with the instrument panel, and this kinematics affected some measurement curves of the dummy. However, as for that, in the future, it needs to verify by comparing the dummy responses under the different condition, for instance, with and without the instrument panel. Furthermore, it is necessary to verify whether this dummy kinematics is human like in this test mode.

## CONCLUSIONS

In order to contribute to the development and improvement of the THOR dummies, the impact responses of the THOR Mod Kit were compared with those of the THOR-NT and the Hybrid III, based on the kinematic and dynamic responses to different conditions in the frontal sled and vehicle crash tests. From the results of this research, it turns out that:

- The response of the THOR Mod Kit to the difference of seating procedure was more sensitive than that of the THOR-NT
- The sensitivity of the THOR Mod Kit to the D-ring position was higher than that of the Hybrid III
- The difference of load limiter affected the difference of kinematics and dynamic responses of the upper body in both the THOR Mod Kit and the Hybrid III
- As for durability of the THOR in two JNCAP test conditions, there was no dummy failure and unusual mode.
- As for the relation between the contact between the elbow of dummy and the instrument panel and the increase of the spine moment about the X-axis in the ODB test, further verification by re-testing etc is needed.
- In both the FWRB and ODB tests, the eversion on the ankle of the THOR Mod Kit exceeded IARV at the rebound phase of the vehicle.

## REFERENCES

[1] Haffner M., et al. “Foundations and Elements of the NHTSA THOR Alpha ATD Design,” Proceedings of the 17th International Technical Conference on the Enhanced Safety of Vehicles, 2001

[2] Shams T., et al. “Development of THOR-NT: Enhancement of THOR Alpha-the NHTSA Advanced Frontal Dummy,” Proceedings of the 19th International Technical Conference on the Enhanced Safety of Vehicles, 2005

[3] Ridella S., et al. “Modifications to Improve the Durability, Usability and Biofidelity of the THOR-NT Dummy,” Proceedings of the 22nd International Technical Conference on the Enhanced Safety of Vehicles, 2011

[4] Törnvall F., “A New Shoulder for the THOR Dummy Intended for Oblique Collision,” Chalmers University of Technology, 2008

[5] Lemmen P., et al. “An Advanced Thorax-Shoulder Design for the THOR Dummy,” Proceedings of the 23rd International Technical Conference on the Enhanced Safety of Vehicles, 2013

[6] IIHS “Guidelines for Using the UMTRI ATD Positioning Procedure for ATD and Seat Positioning (Version V)”, 2004

[7] Saunders J., et al. "NHTSA’s Test Procedure Evaluations for Small Overlap/Oblique Crashes," Proceedings of the 22nd International Technical Conference on the Enhanced Safety of Vehicles, 2011

[8] Saunders J., et al. "Assessment of An Oblique Moving Deformable Barrier Test Procedure,” Proceedings of the 23rd International Technical Conference on the Enhanced Safety of Vehicles, 2013

[9] Takhounts E., et al. “Kinematic Rotational Brain Injury Criterion (BRIC),” Proceedings of the 22nd International Technical Conference on the Enhanced Safety of Vehicles, 2011

[10] Takhounts E., et al. “Development of Brain Injury Criteria (BrIC),” Stapp Car Crash Journal, Vol. 57 (November 2013), pp. 243-266

## APPENDIX

### Table A1. Preliminary IARVs for the THOR and the injury measures in the FWRB test.

| | | IARV | Ref | THOR Mod Kit | Hybrid III |
|---|---|---|---|---|---|
| Head | BRIC(Previous Version) | 0.89 | [8] | 0.54 | No sensor |
| | BrIC(Latest Version) | TBD | [10] | 0.50 | |
| | HIC 36ms | 1000 | [8] | 520.8 | 284.8 |
| | HIC 15ms | 700 | [8] | 376.4 | - |
| | 3ms clip (G) | 80 | [7] | 59.7 | - |
| Upper Neck | Tension Force (N) | 2520 | [8] | 1842.1 | 1290 |
| | Compression Force (N) | 3640 | [8] | 234.9 | - |
| | Flexion at OC (Nm) | 48 | [7] | 1.5 | - |
| | Extension at OC (Nm) | 72 | [7] | 7.8 | 24.3 |
| Chest | Deflection(Center) | 63 | [8] | No sensor | 27.0 |
| | Deflection(Upper Left) (mm) | | | 37.7 | No sensor |
| | Deflection(Upper Right) (mm) | | | 16.1 | |
| | Deflection(Lower Left) (mm) | | | 27.9 | |
| | Deflection(Lower Right) (mm) | | | -9.5 | |
| | 3ms clip (G) | 60 | [8] | 41.5 | 42.0 |
| Abdomen | Deflection (mm) | 90 | [8] | 69.6 | No sensor |
| Acetabulum | Left Resultant Force (N) | 3316 | [8] | 1486 | No sensor |
| | Right Resultant Force (N) | | | 1042 | |
| Femur | Left Femur Force (N) | 9040 | [8] | 4288 | 2600 |
| | Right Femur Force (N) | | | 3725 | 2000 |
| Tibia | Left Upper Tibia Index | 1.16 | [8] | Sensor N.G. | 0.5 |
| | Left Lower Tibia Index | | | 0.58 | 0.7 |
| | Right Upper Tibia Index | | | 0.54 | 0.5 |
| | Right Lower Tibia Index | | | 0.56 | 0.2 |
| Ankle | Left Inversion/Eversion (deg) | 35/35 | [8] | 26.6 | No sensor |
| | Left Dorsiflexion/Plantarflexion (deg) | | | 16.1 | |
| | Right Inversion/Eversion (deg) | | | 37.4 | |
| | Right Dorsiflexion/Plantarflexion (deg) | | | 14.8 | |

**Note**
**Currently all IARVs are preliminary.**
**Negative value in chest deflection means chest expansion.**
**Hybrid III measurements are from JNCAP tests.**

### Table A2. Preliminary IARVs for the THOR and the injury measures in the ODB test.

| | | IARV | Ref | THOR Mod Kit | Hybrid III |
|---|---|---|---|---|---|
| Head | BRIC(Previous Version) | 0.89 | [8] | 0.60 | No sensor |
| | BrIC(Latest Version) | TBD | [10] | 0.72 | |
| | HIC 36ms | 1000 | [8] | 510.1 | 262.7 |
| | HIC 15ms | 700 | [8] | 291.5 | - |
| | 3ms clip (G) | 80 | [7] | 53.0 | - |
| Upper Neck | Tension Force (N) | 2520 | [8] | 1653.5 | 1410 |
| | Compression Force (N) | 3640 | [8] | 803.3 | - |
| | Flexion at OC (Nm) | 48 | [7] | 1.6 | - |
| | Extension at OC (Nm) | 72 | [7] | 7.9 | 16.1 |
| Chest | Deflection(Center) | 63 | [8] | No sensor | 27.5 |
| | Deflection(Upper Left) (mm) | | | 37.2 | No sensor |
| | Deflection(Upper Right) (mm) | | | 20.3 | |
| | Deflection(Lower Left) (mm) | | | 35.5 | |
| | Deflection(Lower Right) (mm) | | | -17.8 | |
| | 3ms clip (G) | 60 | [8] | 43.4 | 44.1 |
| Abdomen | Deflection (mm) | 90 | [8] | 68.7 | No sensor |
| Acetabulum | Left Resultant Force (N) | 3316 | [8] | 1121 | No sensor |
| | Right Resultant Force (N) | | | 1485 | |
| Femur | Left Femur Force (N) | 9040 | [8] | 2247 | 700 |
| | Right Femur Force (N) | | | 3995 | 2400 |
| Tibia | Left Upper Tibia Index | 1.16 | [8] | 0.71 | 0.6 |
| | Left Lower Tibia Index | | | 0.58 | 0.3 |
| | Right Upper Tibia Index | | | 0.76 | 0.3 |
| | Right Lower Tibia Index | | | 0.83 | 0.2 |
| Ankle | Left Inversion/Eversion (deg) | 35/35 | [8] | 33.5 | No sensor |
| | Left Dorsiflexion/Plantarflexion (deg) | | | 23.2 | |
| | Right Inversion/Eversion (deg) | | | 37.2 | |
| | Right Dorsiflexion/Plantarflexion (deg) | | | 21.5 | |

**Note**
**Currently all IARVs are preliminary.**
**Negative value in chest deflection means chest expansion.**
**Hybrid III measurements are from JNCAP tests.**